Hybrid Silicon-Photonic Circuits with Second-Order Optical Nonlinearities

Zur Erlangung des akademischen Grades eines

Doktors der Ingenieurwissenschaften (Dr.-Ing.)

von der KIT-Fakultät für Elektrotechnik und Informationstechnik des
Karlsruher Instituts für Technologie (KIT)

angenommene

Dissertation

von

Clemens Kieninger, M. Sc.

geboren in

Aalen, Deutschland

Tag der mündlichen Prüfung: 04. Dezember 2020
Hauptreferent: Prof. Dr. Christian Koos
Korreferent: Prof. Dr. Dr. h. c. Wolfgang Freude
                                          Prof. Dr. Shiyoshi Yokoyama

Table of Contents

Kurzfassung

Die integrierte Optik ermöglicht die Miniaturisierung diskreter photonischer oder elektro-optischer (EO) Komponenten und die Kombination dieser Bauelemente in komplexen photonischen integrierten Schaltungen (engl. photonic integrated circuit, PIC) auf kompakten Mikrochips. Die Silizium-Photonik (SiP) ist eine sehr attraktive Plattform für die photonische Integration, da sie ausgereifte Herstellungsprozesse aus der Mikroelektronik nutzen kann. Damit eröffnet die Silizium-Photonik die Möglichkeit zur kostengünstigen Massenproduktion von photonischen Chips mit hoher Ausbeute und Reproduzierbarkeit. Darüber hinaus erlaubt der große Brechungsindexkontrast zwischen dem als Wellenleiterkern dienendem Silizium (Si) und dem als Mantelmaterial verwendeten Siliziumdioxid die Herstellung von Wellenleitern mit kleinen Querschnitten und kleinen Krümmungsradien, was die Integrationsdichte im Vergleich zu anderen Materialplattformen erhöht. Die Silizium-Photonik hat jedoch einen entscheidenden Nachteil: Aufgrund seines inversionssymmetrischen Kristallgitters besitzt Silizium keine Nichtlinearität zweiter Ordnung. Folglich sind Bauelemente wie optische Frequenzkonverter, optische Logikgatter, verschränkte Photonenquellen und vor allem elektro-optische Modulatoren, welche auf dem Pockels-Effekt basieren, auf der SiP-Plattform nicht ohne Weiteres realisierbar. Die hybride Integration von Silizium-Nanowellenleitern mit anderen Materialien, die eine Nichtlinearität zweiter Ordnung aufweisen, ist daher für die Erweiterung des Portfolios von SiP-Bauelementen von entscheidender Bedeutung. In dieser Arbeit werden zwei Ansätze für die hybride Integration in SiP-Schaltungen untersucht.

Der erste Ansatz stütz sich auf hocheffiziente organische EO Materialien, die mit siliziumphotonischen Wellenleiterstrukturen in einem Back-End-of-Line-Prozess kombiniert werden, um sogenannte Silicon-Organic Hybrid (SOH) EO Modulatoren zu realisieren. In dieser Arbeit werden SOH-Modulatoren demonstriert, die neue Rekorde in Bezug auf Modulationseffizienz, optische Einfügungsdämpfung und demonstrierte Datenrate definieren. Darüber hinaus wird die thermische Langzeitstabilität dieser Bauelemente bei 85 °C validiert.

Der zweite Ansatz beruht auf neuartigen anorganischen Nanolaminat-Dünnfilmen, die durch Atomlagenabscheidung (ALD) gewachsen werden. Aufgrund des frühen Forschungsstadiums wurden diese Materialien nicht direkt auf SiP-Chips, sondern auf Glassubstraten gewachsen und durch die Erzeugung der zweiten Harmonischen (SHG) charakterisiert. In dieser Arbeit werden SHG-Charakterisierungstechniken für Nanolaminate untersucht und ein neues Nanolaminat vorgestellt. Perspektivisch könnte ALD allerdings auch für die Beschichtung von SiP-Chips verwendet werden. Das konforme ALD-Wachstum bietet sich hierbei an, um präzise definierte Schichtfolgen auch auf komplexen Wellenleiterstrukturen mit hoher Reproduzierbarkeit abzuscheiden.

Diese beiden Ansätze werden in der vorliegenden Arbeit näher beschrieben.

Kapitel 1 gibt eine Einführung in die integrierte Optik und erläutert die Notwendigkeit der Hybridintegration von optisch-nichtlinearen Materialien zweiter Ordnung in SiP-Schaltungen.

Kapitel 2 fasst den theoretischen Hintergrund, führt die für diese Arbeit relevanten Aspekte der nichtlinearen Optik ein und gibt einen Überblick über verschiedene Klassen von nichtlinearen Materialien zweiter Ordnung. Darüber hinaus wird der Stand der Technik von Mach-Zehnder-Modulatoren auf der SiP-Plattform vorgestellt.

In *Kapitel 3* wird die sehr hohe Modulationseffizienz von SOH-Modulatoren demonstriert. Dabei wird ein Mach-Zehnder-Modulator diskutiert, bei dem das Produkt aus π-Spannung und Länge nur 0,32 Vmm beträgt. Im Vergleich zu modernsten SiP-Modulatoren stellt dieser Wert eine Verbesserung um mehr als eine Größenordnung dar. Diese hohe Effizienz ermöglicht eine optische Signalerzeugung mit einer Datenrate von 40 Gbit/s unter Verwendung sehr kleiner Peak-to-Peak Treiberspannungen von nur 140 mV$_{pp}$.

Kapitel 4 stellt einen kompakten SOH-Modulator mit einer optischen Dämpfung des Phasenschiebers von unter 1 dB vor – dies entspricht dem niedrigsten Wert der jemals für einen ultra-schnellen SiP-Modulator veröffentlicht wurde. Der Nutzen dieses Bauteils für schnelle und effiziente optische Datenübertragung wird in einem Experiment demonstriert, bei dem vierstufige Pulsamplitudenmodulations-Signale (PAM4) bei 100 GBd erzeugt

werden. Die hierfür verwendeten Treiberspannungen sind kompatibel mit typischen Spannungspegeln, die von energieeffizienten und hochgradig skalierbaren Complementary Metal-Oxide-Semiconductor-(CMOS-)Bauteilen erzeugt werden können.

Kapitel 5 demonstriert die thermische Langzeitstabilität von SOH-Modulatoren gemäß den Telcordia-Normen für die Lagerung bei hohen Temperaturen. Die Bauelemente werden bei 85 °C für insgesamt 2700 h gelagert, und es zeigt sich, dass die π-Spannung nach einem schnellen anfänglichen Anstieg auf ein konstantes langzeitstabiles Niveau konvergiert. Weiterhin wird gezeigt, dass die Lagerung bei 85 °C keinen negativen Einfluss auf die Leistungsfähigkeit der Bauteile bezüglich der optischen Datenübertragung hat. Dazu wurde eine optische Datenübertragung mit einem SOH-Bauteil durchgeführt, das zuvor für 2700 h bei 85 °C gelagert wurde. Mit dieser Demonstration wird eines der letzten verbleibenden Hindernisse auf dem Weg zum technischen Einsatz von SOH-Bauteilen adressiert: Die Stabilität der zugrundeliegenden organischen Materialien.

In *Kapitel 6* werden zwei verschiedene Techniken zur Messung von SHG von anorganischen Nanolaminaten und zur Bestimmung der zugehörigen Elemente des $\chi^{(2)}$-Tensors untersucht. Die Vor- und Nachteile der beiden Methoden werden verglichen und die Quellen für Messfehler identifiziert.

Kapitel 7 stellt ein neuartiges binäres Nanolaminatmaterial vor, das auf abwechselnden Schichten aus Zinkoxid und Aluminiumoxid basiert. Die ermittelte Nichtlinearität zweiter Ordnung ist mehr als dreimal so groß wie bei zuvor veröffentlichten ternären Nanolaminaten.

Kapitel 8 fasst die Themen dieser Arbeit zusammen und gibt einen Ausblick auf zukünftige Arbeiten zu SOH-Modulatoren und Nanolaminat-Dünnfilmen.

Preface

Integrated optics enables the miniaturization of conventional discrete photonic or electro-optic (EO) components and the combination of these devices in advanced photonic integrated circuits (PIC) on compact micro-chips. Silicon photonics (SiP), in particular, is a highly attractive platform for photonic integration because it can use mature manufacturing processes developed for silicon (Si) microelectronics. Thus, SiP opens up the possibility for cost-effective mass production of photonic chips with high yield and reproducibility. Furthermore, the large refractive index contrast between Si waveguide cores and the silicon-dioxide cladding allows fabricating nanophotonic waveguides with small cross sections and small bending radii, thereby increasing integration density as compared to other material platforms. However, silicon photonics has a distinct drawback: Due to its inversion symmetric crystal lattice, unstrained Si does not have any second-order nonlinearity. Consequently, devices like optical frequency converters, all-optical logic gates, entangled photon sources, and most importantly Pockels-type electro-optic (EO) modulators are challenging to realize in Si. Hybrid integration of materials featuring a second-order nonlinearity is hence instrumental for expanding the portfolio of SiP devices. In this work, two material approaches to hybrid integration in SiP circuits are investigated:

The first approach relies on highly efficient organic EO materials, which are combined with standard SiP chips in a back-end-of-line process to realize so-called silicon-organic hybrid (SOH) EO modulators. In this thesis, SOH devices are realized, which define new records in terms of modulation efficiency, optical insertion loss, and demonstrated data rate. Furthermore, long-term thermal stability of SOH devices at 85 ° is shown.

The second approach exploits novel inorganic nanolaminate thin-films grown by atomic layer deposition (ALD). Due to the early stage of research, these materials have not yet been grown directly on SiP chips but on glass substrates, and the performance is tested by second-harmonic generation (SHG). In this thesis, SHG characterization techniques for nanolaminates are investigated and a new nanolaminate is presented. In the future, ALD could also be used for the

coating of SiP chips. The conformal ALD growth would lend itself to coating of advanced modulator geometries, which are, *e.g.*, based on Si-slot waveguides.

These approaches are described in more detail in the following chapters.

Chapter 1 gives an introduction to integrated optics and elaborates the need for hybrid integration of second-order nonlinear materials in SiP circuits.

Chapter 2 summarizes the theoretical background of nonlinear optics as relevant to this work and gives an overview of various classes of second-order nonlinear materials. In addition, state-of-the-art SiP Mach-Zehnder modulators are reviewed.

Chapter 3 demonstrates ultra-high in-device EO activity in an SOH Mach-Zehnder modulator. The device has a π-voltage-length product of only 0.32 Vmm, outperforming standard SiP modulators by more than an order of magnitude. The high modulation efficiency allows signalling at 40 Gbit/s using small peak-to-peak drive voltages of only 140 mV$_{pp}$.

Chapter 4 introduces a compact SOH modulator with sub-1 dB optical phase-shifter loss. This is the lowest value ever reported for a high-speed SiP modulator. The high-speed performance of the device is demonstrated by generating 4-level-pulse-amplitude-modulation-(PAM4-)signals at 100 GBd using complementary-metal-oxide-semiconductor-(CMOS-)compatible drive voltages.

Chapter 5 demonstrates long-term thermal stability of SOH modulators according to Telcordia standards for high-temperature storage. The devices are stored at 85 °C for 2700 h, and we find that the π-voltage converges to a constant long-term stable level after a rapid initial increase. High-speed signalling at 40 Gbit/s is demonstrated using a device which was stored for 2700 h at 85 °C. This demonstration addresses one of the last remaining obstacles on the way to industrial use of SOH components: The stability of the underlying organic materials.

Chapter 6 investigates two different techniques to measure SHG from inorganic nanolaminates and to determine the associated elements of the $\chi^{(2)}$ tensor. The

advantages and disadvantages of the two methods are compared and the sources for measurement errors are identified.

Chapter 7 introduces a novel binary nanolaminate material based on alternating layers of zinc oxide and aluminium oxide. The determined second-order nonlinearity is more than three times larger than for previously published ternary nanolaminates.

Chapter 8 summarizes the topics of this thesis and gives an outlook for future work on SOH modulators and nanolaminate thin-films.

Achievements of the present work

In this thesis, we investigate two approaches to implement second-order nonlinearities on the silicon photonic (SiP) platform:

The first approach relies on the concept of silicon-organic hybrid (SOH) integration, which is mainly used to realize high-speed low-power electro-optic (EO) modulators. In this work, the performance of SOH Mach-Zehnder modulators (MZM) is improved to new record values in terms of EO activity, modulation efficiency, optical insertion loss, and achieved data rates. Furthermore, systematic reliability tests are performed, which represents an important step towards large-scale industrial application of SOH devices.

The second approach is based on thin-film nanolaminates grown by atomic layer deposition. A detailed comparison of two measurement techniques to determine the nonlinearity of these thin-films is presented. Furthermore a novel nanolaminate with best in-class nonlinearity is realized.

The key achievements of this work cover the following aspects:

Demonstration of record-high in-device EO activity for a high-speed Pockels-type modulator: The highly efficient organic EO material JRD1 is implemented in SOH modulators, and the poling conditions of the material are optimized. We realize an EO figure of merit of $n^3 r_{33} = 2300$ pm/V, corresponding to an estimated electro-optic coefficient of $r_{33} = 390$ pm/V, which is the highest value ever reported for a high-speed modulator based on the Pockels effect.

Demonstration of the lowest π-voltage-length product for a modulator based on low-loss waveguides: Based on organic materials with highest EO activity, SOH modulators with a record-low π-voltage-length product of $U_\pi L = 0.32$ Vmm are realized. As compared to $U_\pi L$ of standard SiP modulators this value represents an improvement by an order of magnitude and is furthermore the lowest value ever reported for a modulator based on low-loss dielectric waveguides. The high modulation efficiency enables on-off keying

(OOK) signaling at 40 GBd using peak-to-peak drive voltages of only 140 mV$_{pp}$.

Demonstration of compact low-loss SOH modulators: The high modulation efficiency of SOH modulators is exploited to realize SOH phase shifters with a length of only 280 µm without unduly increasing the π-voltage. The devices have a phase shifter insertion loss of only 0.7 dB, which is the lowest value ever reported for a high-speed SiP modulator. The low loss makes SOH MZM not only attractive for conventional optical communications, but also for emerging applications in the fields of quantum optics.

Highest line rate achieved with a sub-millimeter long SiP MZM: We use an SOH MZM with 280 µm long phase shifters to generate line rates up to 200 Gbit/s by using PAM4 signaling. This represents the highest line rate ever reported for a SiP MZM shorter than 1 mm. To drive the device, we use CMOS-compatible voltage levels.

First demonstration of long-term thermally stable SOH modulators: We integrate a side-chain EO polymer with a high glass-transition temperature in SOH modulators and perform systematic storage experiments at 85 °C according to Telcordia standards. The devices show a stable π-voltage after storage at 85 °C for thousands of hours. This is a major breakthrough towards the industrial adoption of SOH modulators.

Systematic comparison of two measurement techniques for second-harmonic generation (SHG) from thin nonlinear films: We compare two measurement techniques, which were recently developed to determine the second-order nonlinearity of nanolaminates. The techniques rely both on SHG and feature distinct advantages and disadvantages. These differences are investigated in detail, and the main sources of measurement errors are identified, which provides helpful guidance for researchers in the field on thin nonlinear films.

Highest nonlinearity in a nanolaminate material grown by atomic layer deposition (ALD): We use ALD to grow a novel binary nanolaminate based on alternating layers of zinc oxide (ZnO) and aluminum oxide (Al$_2$O$_3$). The intermediate Al$_2$O$_3$ layers ensure a well-defined orientation of the ZnO

crystallites. This is essential for the comparatively high nonlinearity, which is three times larger than for previously demonstrated ternary nanolaminates.

1 Introduction: Silicon photonics and the need for hybrid integration

Over the last 25 years fiber-optic communications had an enormous impact on our everyday life: Access to information has become ubiquitous, and the amount of shared information continues to grow exponentially – with transformative impact on the way we live, work, and learn. Photonic integrated circuits (PIC) made a major contribution to the technological foundation of these transformation processes: Combining a multitude of distinct photonic or optoelectronic components on a compact chip, PIC offer unprecedented functionalities and performance in transmission, reception, and processing of optical data signals and are thus key to powerful information and communication infrastructures. In principle, photonic integration leverages similar advantages as integrated microelectronics: Integrated components are realized at a fraction of the size of their discrete counterparts, which enables dense integration, power-efficient operation, and low-cost mass production by advanced wafer-scale processes. Conventionally, indium phosphide (InP) has been the best-established material platform for PIC. The portfolio of available integrated components ranges from passive waveguides to power splitters and electro-optic (EO) modulators, which are used to encode information on an optical carrier [1,2]. Furthermore, the direct bandgap of InP allows monolithic fabrication of laser sources, semiconductor optical amplifiers (SOA), and photodetectors. However, the material is mechanically rather fragile and the wafer diameters are currently limited to only (50…100) mm [3,4]. Furthermore, InP waveguides are grown by epitaxy, which is prone to form defects, dramatically reducing the yield. When additionally taking into account that indium is a rare material, it becomes apparent that InP-based PIC are quite expensive. This deficiency can be overcome by silicon photonics (SiP). This technology can rely on high-yield fabrication processes with tight process control, which were established by the Si microelectronic industry. In addition, the existing infrastructure of CMOS-foundries with outdated technology nodes can be reused. This enables fabrication of SiP PIC on wafers with diameters up to 300 mm [5], which allows for cost-efficient mass production. Furthermore,

Si offers a high index contrast with respect to its oxide. This allows for small waveguide cross sections with tight bends, thereby enabling compact SiP chips with high integration density.

However, Si as a platform for photonic integration has two major drawbacks: First, its indirect bandgap prohibits efficient light emission, which is key to lasers and optical amplifiers. Second, due to its inversion-symmetric crystal lattice, unstrained bulk Si does not exhibit any second-order nonlinearity [6]. As a consequence, devices such as optical parametric amplifiers, ultra-fast optical gates, sources for entangled photons used in quantum optics, and most importantly EO modulators based on the Pockels-effect are not available in Si. Pockels-effect modulators are particularly attractive for applications in the field of optical communications as these devices provide pure phase modulation at high operation speed. Conventional SiP modulators are based on the free-carrier plasma-dispersion effect [7], where a modulation of the refractive index is induced by varying the concentration of free carriers. However, the free-carrier density affects also the optical attenuation, which results in amplitude-phase coupling and chirp of the modulated optical signal. Furthermore, all-Si modulators are subject to fundamental trade-offs, which makes it challenging to realize devices that simultaneously exhibit high energy efficiency, low optical insertion loss, and high-speed operation [8]. A way to circumvent these trade-offs is the hybrid co-integration of second-order nonlinear materials in SiP circuits. Lithium niobate ($LiNbO_3$) is a popular candidate for hybrid integration due to its widespread industrial acceptance and its enormous commercial success in discrete EO modulators. However, current concepts to integrate $LiNbO_3$ into SiP circuits either deviate strongly from established SiP fabrication process flows [9–12], or the performance of the hybrid SiP devices [13] does not exceed the one of standard all-Si modulators. An attractive alternative is barium titanate ($BaTiO_3$), which offers a much larger EO coefficient. However, growing this material still requires rather complex processes, which are currently limited to fabrication of rather simple SiP phase shifter structures with limited modulation efficiency [14]. In contrast to this, organic EO (OEO) materials with optimized EO properties can be integrated in advanced SiP phase shifter structures based on Si slot waveguides. The OEO material can be applied to the SiP chip in a back-end-of-line process, which requires only a minimum adaption of established SiP fabrication steps. The resulting silicon-organic

hybrid (SOH) modulators outperform standard SiP modulators in terms of energy efficiency and achieved data rates [15–18].

In this thesis, the performance of SOH Mach-Zehnder modulators (MZM) is further improved, leading to experimental demonstrations of several record-high parameters. In Chapter 3, we integrate a highly efficient OEO material in an SOH MZM and demonstrate the highest in-device EO activity for a high-speed Pockels-type modulator. This results in π-voltage-length products of only 0.32 Vmm, which represents the lowest value ever reported for a modulator based on low-loss dielectric waveguides. The high modulation efficiency allows driving the modulator with peak-to-peak voltages of only 140 mV$_{pp}$ at symbol rates of 40 GBd. Besides modulation efficiency, an essential requirement for EO modulators is low optical insertion loss. While standard SiP modulators suffer from an inherent trade-off between modulation efficiency and optical loss, we show that SOH MZM can overcome this problem: In Chapter 4, we realize compact devices with phase-shifter lengths of 280 μm and low optical insertion loss of only 0.7 dB, which is the lowest value ever reported for a high-speed SiP modulator. We further demonstrate the high-speed performance of the device and show PAM4 signaling at 100 GBd, resulting in line rates of 200 Gbit/s, the highest value ever reported for a SiP modulator smaller than 1 mm. Despite these record performance parameters, SOH modulators are not yet used in commercial applications. The main reason for that is the alleged lack of stability of the organic materials, *e.g.*, with respect to elevated temperatures. This topic is addressed in Chapter 5: In the presented work, we follow Telcordia testing protocols and investigate the impact of high-temperature storage at 85 °C on SOH MZM which are clad by an EO polymer with high glass-transition temperature. We find that the devices remain stable after an initial burn-in period. This underlines the potential of SOH EO modulators for industrial applications.

An additional challenge for SOH MZM is photo-oxidation of the organic material [19,20], which could potentially require a hermetic package of the device to exclude oxygen. An inorganic and thus inherently photo-chemically stable EO material, which, in addition, is compatible with standard SiP process flows, would thus be highly desirable. In Chapters 6 and 7, we therefore also investigate novel nanolaminate materials based on metal oxides [21,22]. These

nanolaminates are grown by atomic layer deposition (ALD) and can be applied to the SiP chips as a thin coating. Furthermore, the ALD growth is conformal such that the material could potentially be implemented in advanced phase-shifter structures based on slot waveguides. However, these materials are still in an early research stage, requiring iterative approaches to optimize growth parameters. For efficient experimental investigations, the materials are therefore not grown on SiP chips, but on cheap glass substrates, and the associated second-order nonlinearity is characterized by second-harmonic generation (SHG). In Chapter 6, we compare two SHG measurement methodologies, which were particularly developed to measure the nonlinearity of nanolaminates [21,22]. We discuss the differences of the techniques and specify criteria which help to decide which method is better suited for specific nanolaminates. In Chapter 7, we introduce a novel binary nanolaminate based on the two constituents zinc oxide (ZnO) and aluminum oxide (Al_2O_3). By adapting the thickness of the individual layers, we tailor the orientation and the size of ZnO crystallites, and we achieve a nonlinearity which is three times larger than that achieved for previous nanolaminates.

2 Theoretical and technological background

This chapter summarizes the theoretical background, which is essential to understand the present work. This includes the relevant background in the field of nonlinear optics, as well as an overview of second-order nonlinear optical materials, ranging from traditional single-crystalline materials over thin-film materials grown by atomic layer deposition to organic materials. Finally, the state of the art of electro-optic (EO) modulators realized on the silicon photonic (SiP) platform is briefly discussed.

2.1 Fundamentals of nonlinear optics

In this section, basic physical relations of nonlinear optics are summarized. The structure and nomenclature loosely follows the textbook *Nonlinear Optics* of E. G. Sauter [23].

2.1.1 Nonlinear electric polarization

During the propagation of light in a medium, the electric field strength $\vec{E}$ of the light field excites electric dipoles leading to a polarization $\vec{\mathcal{P}}$ of the medium. Linear optics describes the regime in which the electric-field dependence of the polarization can be described by a linear relationship. However, this linear relation is merely an approximation for small electric field strengths. In general, also higher order terms which depend nonlinearly on the electric field, contribute to the overall polarization of the medium. We can thus write

$$\vec{\mathcal{P}} = \vec{\mathcal{P}}^{(1)} + \vec{\mathcal{P}}^{(2)} + \ldots, \tag{2.1}$$

where $\vec{\mathcal{P}}^{(1)}$ denotes the linear polarization that depends linearly on the electric field $\vec{E}$ and $\vec{\mathcal{P}}^{(2)}$ denotes the second-order nonlinear polarization where the electric field $\vec{E}$ enters quadratically. All higher-order contributions are neglected within the scope of this thesis. In the following, we give an explicit

expression for the vector components $i \in \{1,2,3\}$ of the polarization $\vec{\mathcal{P}}(\vec{x},t)$ at location $\vec{x}$ and time t of a medium which is time-invariant, local in space and homogeneous. $\vec{\mathcal{P}}(\vec{x},t)$ takes the form of a Volterra series where the input is given by the electric field $\vec{E}(\vec{x},t)$ and the Volterra kernels are given by the linear and second-order nonlinear response functions of the medium $\chi_{ij}^{(1)}(\tau_1)$ and $\chi_{ijk}^{(2)}(\tau_1,\tau_2)$ with $i,j,k \in \{1,2,3\}$. These quantities are tensors of the rank 2 and 3, respectively. Using Einstein notation, we find

$$
\begin{aligned}
\mathcal{P}_i(\vec{x},t) = \epsilon_0 \int\limits_{-\infty}^{\infty} d\tau_1 \; \chi_{ij}^{(1)}(\tau) E_j(\vec{x},t-\tau_1) \\
+ \epsilon_0 \int\limits_{-\infty}^{\infty} d\tau_1 \int\limits_{-\infty}^{\infty} d\tau_2 \; \chi_{ijk}^{(2)}(\tau_1,\tau_2) E_j(\vec{x},t-\tau_1) E_k(\vec{x},t-\tau_2).
\end{aligned}
\tag{2.2}
$$

Here, ϵ_0 is the vacuum permittivity and $\tau_{1,2}$ are time integration variables. The first term on the right-hand side of Eq.(2.2) corresponds to the linear polarization $\vec{\mathcal{P}}^{(1)}(\vec{x},t)$, and the second term describes the second-order nonlinear polarization $\vec{\mathcal{P}}^{(2)}(\vec{x},t)$. Note that the orientation of the coordinate system, which defines the directions associated with the indices $i,j,k \in \{1,2,3\}$, is typically chosen such that $\chi_{ijk}^{(2)}$ takes a simple form. For uniaxial crystals, $e.g.$, the 3-axis is typically chosen to coincide with the optic axis of the crystal.

In the following, we take a closer look at the second-order nonlinear polarization $\vec{\mathcal{P}}^{(2)}(\vec{x},t)$. Compared to Eq. (2.2), a much simpler form of this expression is found if we assume that the electric field $\vec{E}(\vec{x},t)$ of the optical wave can be represented as a superposition of monochromatic waves with S different frequencies ω_s and corresponding complex time domain amplitudes $\underline{\vec{E}}(\vec{x},\omega_s)$ given by

$$
\vec{E}(\vec{x},t) = \frac{1}{2} \left(\sum_{s=1}^{S} \underline{\vec{E}}(\vec{x},\omega_s) e^{j\omega_s t} + \text{c.c.} \right).
\tag{2.3}
$$

The term c.c. denotes the complex conjugate of the first expression and ensures that the electric field $\vec{E}(\vec{x},t)$ is a real quantity. Using the notation

$$\underline{\vec{E}}(\vec{x}, -\omega_s) = \underline{\vec{E}}^*(\vec{x}, \omega_s)$$
$$\omega_{-s} = -\omega_s \qquad , \tag{2.4}$$
$$\omega_0 = 0$$

Eq. (2.3) can be further simplified to

$$\vec{E}(\vec{x}, t) = \frac{1}{2} \sum_{s=-S}^{S} (1 + \delta_{s0}) \underline{\vec{E}}(\vec{x}, \omega_s) e^{j\omega_s t} , \tag{2.5}$$

where we have introduced the Kronecker delta defined by

$$\delta_{ij} = \begin{cases} 1 \text{ for } i = j \\ 0 \text{ for } i \neq j \end{cases} . \tag{2.6}$$

The correction factor $(1 + \delta_{s0})$ doubles the complex amplitude for the zero-frequency component, which avoids a situation in which a DC electric field is associated with an amplitude of $\underline{\vec{E}}(\vec{x}, \omega_0) / 2$. Substituting Eq. (2.5) in Eq. (2.2) we find for the second-order nonlinear polarization

$$\mathcal{P}_i^{(2)}(\vec{x}, t) = \frac{1}{4} \epsilon_0 \sum_{s_1, s_2 = -S}^{S} (1 + \delta_{s_1 0})(1 + \delta_{s_2 0}) \chi_{ijk}^{(2)}(\omega_\Sigma : \omega_{s_1}, \omega_{s_2}) \\ \times \underline{E}_j(\vec{x}, \omega_{s_1}) \underline{E}_k(\vec{x}, \omega_{s_2}) e^{j(\omega_{s_1} + \omega_{s_2})t} \tag{2.7}$$

where $\chi^{(2)}(\omega_\Sigma : \omega_{s_1}, \omega_{s_2})$ corresponds to the two-dimensional Fourier transform of $\chi^{(2)}(\tau_1, \tau_2)$ given by

$$\chi^{(2)}(\omega_\Sigma : \omega_{s_1}, \omega_{s_2}) = \int_{-\infty}^{\infty} \int_{-\infty}^{\infty} \chi^{(2)}(\tau_1, \tau_2) e^{-j\omega_{s_1}\tau_1} e^{-j\omega_{s_2}\tau_2} d\tau_1 d\tau_2. \tag{2.8}$$

Here, ω_Σ corresponds to the sum frequency $\omega_\Sigma = \omega_{s_1} + \omega_{s_2}$ at which the polarization oscillates. Similar to Eq. (2.5), the polarization $\vec{\mathcal{P}}^{(2)}$ can be expressed as a sum of monochromatic waves with R distinct frequencies ω_r and corresponding complex time-domain amplitudes

$$\vec{\mathcal{P}}^{(2)}(\vec{x}, t) = \frac{1}{2} \sum_{r=-R}^{R} (1 + \delta_{r0}) \underline{\vec{\mathcal{P}}}^{(2)}(\vec{x}, \omega_r) e^{j\omega_r t}. \tag{2.9}$$

Comparing this expression with Eq. (2.7), a relation between amplitudes of the electric field at frequencies ω_{s_1} and ω_{s_2} and amplitudes of the second-order nonlinear polarization at frequency $\omega_r = \omega_{s_1} + \omega_{s_2}$ can be found [23]

$$\underline{\mathcal{P}}_i^{(2)}(\vec{x},\omega_r) = \frac{1}{2}\epsilon_0 \sum_{\mathbb{S}(\omega_r)} \frac{(1+\delta_{s_1 0})(1+\delta_{s_2 0})}{(1+\delta_{r0})} \chi_{ijk}^{(2)}(\omega_r : \omega_{s_1}, \omega_{s_2})\underline{E}_j(\vec{x},\omega_{s_1})\underline{E}_k(\vec{x},\omega_{s_2}),$$

(2.10)

where the quantity $\mathbb{S}(\omega_r)$ indicates a summation over all permutations of frequencies $\omega_{s_1}, \omega_{s_2}$ which amount in sum to ω_r.

Equation (2.9) indicates that the nonlinear polarization $\vec{\mathcal{P}}^{(2)}(\vec{x},t)$ oscillates at frequencies ω_r, which are in general not present in the incoming electric fields. This is in strong contrast compared to linear optics and gives rise to numerous interesting effects, which are discussed in Section 2.1.2.

Note that in the following the space-dependence of the complex time domain amplitudes is often omitted for the sake of readability.

Symmetry properties of the second-order nonlinear susceptibility

The second-order susceptibility $\chi^{(2)}(\omega_\Sigma : \omega_{s_1}, \omega_{s_2})$ is a tensor of rank 3 resulting in $3^3 = 27$ tensor elements. However, for a given material, the number of independent and non-vanishing elements may be significantly reduced due to symmetry properties of the underlying crystal class, which dictates the symmetry properties of the $\chi^{(2)}$-tensor, following Neumann's principle [24]. In fact, for materials which are centrosymmetric, all elements of the $\chi^{(2)}$-tensor vanish [6]. As a result, bulk silicon with its centrosymmetric diamond lattice lacks a $\chi^{(2)}$ nonlinearity. This absence is the main motivation for hybrid integration of second-order nonlinear materials on the silicon-photonic platform. The specific form of the $\chi^{(2)}$-tensor for crystal classes without center of inversion is found in standard textbooks such as in Ref. [25].

Amorphous materials such as silica glass do not feature a periodic atomic lattice, such that Neumann's principle cannot be strictly applied. Nonetheless, this class of materials does not possess a second-order nonlinearity either. The reason for that is the random atomic arrangement in amorphous materials: While these materials may, *e.g.*, have a non-vanishing $\chi^{(2)}$ nonlinearity on the

microscopic scale, these contributions average to zero on the macroscopic scale due to their random orientation, which implies the lack of a preferential direction and hence the invariance of the macroscopic properties with respect to an inversion operation.

The finding that centrosymmetric crystals do not possess second-order nonlinearity holds true only for bulk materials. At material boundaries, however, the inversion symmetry is clearly broken, resulting in a sheet nonlinearity at the interface. Similarly, also amorphous materials possess a surface nonlinearity at the interface. In both cases, the nonlinear sheet extends only over the first few atomic layers in the vicinity of the interface [6]. Therefore, the effect of a single interface is quite weak. If many interfaces are densely packed, however, an appreciable nonlinearity is achieved. This effect is exploited in thin-film nanolaminate materials [21,22,26], which are also investigated in Chapter 6.

2.1.2 Second-order nonlinear effects

In this part, the second-order nonlinear effects, which are relevant for the remainder of this thesis, are briefly discussed.

Second-harmonic generation

Second-harmonic generation (SHG) describes the effect of optical frequency doubling, which was first observed in 1961 by Franken *et al.* [27]. The effect is, *e.g.*, exploited to realize laser sources in frequency ranges, which are technologically challenging to address by ordinary sources. For example, green and blue high-power laser sources can be realized by frequency doubling of readily available infrared lasers [28,29]. For SHG, Eq. (2.10) reads

$$\underline{\mathcal{P}}_i^{(2)}(2\omega) = \frac{1}{2}\epsilon_0 \chi_{ijk}^{(2)}(2\omega : \omega, \omega)\underline{E}_j(\omega)\underline{E}_k(\omega), \tag{2.11}$$

where the space-dependence of the field quantities was omitted for the sake of readability.

Pockels effect

The Pockels effect, which is also known as the linear EO effect describes the modulation of the refractive index by an applied electric field. Most notably, the Pockels effect is used to realize EO modulators for optical communications systems [30], where a change in refractive index is used to modulate the phase of an optical carrier at frequency ω_c, see Section 2.3. The applied electric field may be static or slowly varying with a modulation frequency $\omega_m \ll \omega_c$ such that we can assume $\omega_m = 0$ in this quasi-static case [31].

For the Pockels effect, Eq. (2.10) simplifies to

$$\underline{\mathcal{P}}_i^{(2)}(\omega_c) = 2\epsilon_0 \chi_{ijk}^{(2)}(\omega_c : \omega_c, 0)\underline{E}_j(\omega_c)\underline{E}_k(0), \tag{2.12}$$

where again the space-dependence was omitted for better readability.

Similar to the electric field and the polarization, the electric displacement field $\vec{D}(\vec{x},t) = \epsilon_0 \vec{E}(\vec{x},t) + \vec{\mathcal{P}}(\vec{x},t)$ can be also described as a superposition of monochromatic waves with complex amplitudes. Using Eq. (2.12) for the second-order nonlinear contribution to the polarization, we find for the complex amplitude of the displacement field at frequency ω_c

$$\underline{D}_i(\omega_c) = \epsilon_0 \left(\delta_{ij}\underline{E}_j(\omega_c) + \chi_{ij}^{(1)}(\omega_c)\underline{E}_j(\omega_c) + 2\chi_{ijk}^{(2)}(\omega_c : \omega_c, 0)\underline{E}_j(\omega_c)\underline{E}_k(0) \right), \tag{2.13}$$

where δ_{ij} denotes a Kronecker delta as defined in Eq. (2.6). In Eq. (2.13), we can identify an effective permittivity, which depends on the applied electric field [23]

$$\epsilon_{ij}(\omega_c) = \delta_{ij} + \chi_{ij}^{(1)}(\omega_c) + 2\chi_{ijk}^{(2)}(\omega_c : \omega_c, \omega_m)\underline{E}_k(\omega_m). \tag{2.14}$$

It becomes thus apparent that also the refractive index of the medium depends on the applied electric field, giving rise to the Pockels effect. Historically, the Pockels effect is described in terms of the impermeability tensor η_{ij}, which is defined as the inverse of the permittivity $\eta_{ij} = \epsilon_{ij}^{-1}$. We assume in the following that ϵ_{ij} is real and symmetric, which is valid if ω_c is far away from any material resonance [6]. The change of η_{ij} for an applied electric field with respect to the field-free case η_{ij}^0 is given by [31]

$$\Delta\eta_{ij}(\omega_{\mathrm{c}}) = r_{ijk}(\omega_{\mathrm{c}})\underline{E}_k(0), \tag{2.15}$$

where r_{ijk} is the EO tensor, which is used to quantify the strength of the nonlinearity of a Pockels-type material. The connection between r_{ijk} and the second-order susceptibility tensor $\chi_{ijk}^{(2)}$ is given by [31,32]

$$\chi_{ijk}^{(2)}(\omega_{\mathrm{c}}:\omega_{\mathrm{c}},0) = -\frac{1}{2}n_i^2(\omega_{\mathrm{c}})n_j^2(\omega_{\mathrm{c}})r_{ijk}(\omega_{\mathrm{c}}), \tag{2.16}$$

where n_i and n_j denote the refractive indices along the principal axes of the indicatrix in the field-free case.

Note that if ϵ_{ij} is real and symmetric also $\eta_{ij} = \eta_{ij}^0 + \Delta\eta_{ij} = \epsilon_{ij}^{-1}$ is real and symmetric. According to Eq. (2.15), r_{ijk} is thus symmetric in its first two indices. As a consequence, the EO tensor is often expressed using a contracted notation r_{hk} where the index h is chosen according to the following rule [6]

$$h = \begin{cases} 1 \text{ for } ij = 11 \\ 2 \text{ for } ij = 22 \\ 3 \text{ for } ij = 33 \\ 4 \text{ for } ij = 23 \text{ or } 32 \\ 5 \text{ for } ij = 13 \text{ or } 31 \\ 6 \text{ for } ij = 12 \text{ or } 21 \end{cases}. \tag{2.17}$$

This results in general in 18 tensor components. However, the number of independent and non-vanishing components of r_{hk} is typically significantly reduced due to symmetry properties of the medium [6], see Section 2.1.1.

In general, the application of an electric field induces off-diagonal elements in η_{ij}, such that a cumbersome diagonalization may be required to obtain the new principal refractive indices of the medium [32]. Organic EO materials are a special case in this regard. The EO tensor of these materials is defined by a so-called poling field along which the EO molecules align, see Section 2.2.2. In this case only a single element of the EO tensor dominates. Without loss of generality this direction can be chosen to be along the 3 axis, such that the component r_{33} of the EO tensor dominates. In this case η_{ij} remains diagonal

and the induced change in refractive index along the main principal axis of the optical indicatrix is found to be [31]

$$\Delta n_3(\omega_c) = -\frac{1}{2} n_3^3 r_{33}(\omega_c) \underline{E}_3(0).$$

(2.18)

2.1.3 Nonlinear wave equation

The nonlinear wave equation governs the propagation of electro-magnetic fields, which are driven by a nonlinear polarization. Solving this equation is essential, *e.g.*, for predicting and modelling the optical power of waves with newly generated frequencies in frequency mixing applications. For a nonmagnetic material, which does not contain free charges, nor free currents, the nonlinear wave equation in time domain reads [6]

$$\nabla \times \nabla \times \vec{E}(\vec{x},t) + \frac{n^2}{c^2}\frac{\partial^2}{\partial t^2}\vec{E}(\vec{x},t) = -\frac{1}{\epsilon_0 c^2}\frac{\partial^2}{\partial t^2}\vec{\mathcal{P}}_{\mathrm{NL}}(\vec{x},t).$$

(2.19)

The nonlinear polarization $\vec{\mathcal{P}}_{\mathrm{NL}}(\vec{x},t)$ on the right-hand side acts as a source term, which may drive electric fields at frequencies that are obtained by mixing the respective frequencies of the incoming electric fields. To solve the equation, it is again practical to represent the electric field and the nonlinear polarization as a superposition of monochromatic waves with complex amplitudes, according to Eq. (2.5) and Eq. (2.9). We assume here a stationary case, in which the complex time domain amplitudes are time-independent. The wave equation can then be sorted in separate differential equations in which the complex time domain amplitudes with distinct frequencies ω_s are considered individually,

$$\nabla \times \nabla \times \underline{\vec{E}}(\vec{x},\omega_s) - \frac{n^2(\omega_s)\omega_s^2}{c^2}\underline{\vec{E}}(\vec{x},\omega_s) = \frac{\omega_s^2}{\epsilon_0 c^2}\underline{\vec{\mathcal{P}}}(\vec{x},\omega_s).$$

(2.20)

If the involved optical beams propagate in different media, special care is required when solving Eq. (2.20) since the boundary conditions for the electric fields need to be fulfilled at each material interface. Such a situation arises often in frequency mixing experiments, where, *e.g.*, a nonlinear material is deposited on an optically linear substrate which is surrounded by air. For this experimental

scenario, Herman and Hayden [33] solved Eq. (2.20) for the nonlinear process of second harmonic generation, where a pump beam with distinct frequency ω is frequency-doubled, resulting in an outgoing wave at frequency 2ω. The authors considered the special case in which the involved media are isotropic and both the incoming electric fields as well as the second-harmonic (SH) fields are p-polarized, *i.e.*, polarized in the plane of incidence. The solution to this problem was generalized to arbitrary polarizations of the incoming electric field more recently. The p- and s-polarized SH powers $P_{2\omega}^{(\mathrm{p/s})}$ in transmission are then given by [21]

$$
P_{2\omega}^{(\mathrm{p/s})} = \frac{2\left(\left(\sin(\varphi)t_{\mathrm{a\text{-}f},\omega}^{(\mathrm{p})}\right)^2 + \left(\cos(\varphi)t_{\mathrm{a\text{-}f},\omega}^{(\mathrm{s})}\right)^2\right)^2 (t_{\mathrm{f\text{-}s},2\omega}^{(\mathrm{p/s})} t_{\mathrm{s\text{-}a},2\omega}^{(\mathrm{p/s})})^2}{c A^{(\mathrm{spot})} \varepsilon_0 (n_{\mathrm{f},2\omega}\cos(\theta_{\mathrm{f},2\omega}))^2}
$$
$$
\times \left(\chi_{\mathrm{eff}}^{(\mathrm{p/s})} d \frac{2\pi}{\lambda} P_\omega \frac{\sin(\Psi)}{\Psi}\right)^2 . \tag{2.21}
$$

Here, the superscripts (p/s) indicate quantities at polarizations of the electric field parallel/perpendicular to the plane of incidence. Frequency-dependent quantities at the fundamental/SH frequency are indicated by the subscript $\omega/2\omega$. For example, $t_{\mathrm{u\text{-}v},2\omega}^{(\mathrm{p/s})}$ denotes the standard Fresnel coefficient for transmission of the electric field amplitude from medium u to medium v for p/s polarization at the SH frequency. The indices $u,v \in \{\mathrm{a,f,s}\}$ stand for **a**ir, nonlinear **f**ilm, and **s**ubstrate. The quantity n_u denotes the refractive index of medium $u \in \{\mathrm{a,f,s}\}$, d is the thickness of the nonlinear material, λ, $A^{(\mathrm{spot})}$, and P_ω are the vacuum wavelength, the focal spot size of the laser and the power of the fundamental pump beam, respectively. The angle φ describes the polarization of the fundamental beam where $\varphi = 0°$ and $\varphi = 90°$ corresponds to s- and p-polarization, respectively. The effective second-order nonlinear susceptibility $\chi_{\mathrm{eff}}^{\mathrm{p/s}}$ depends on the symmetry properties of the investigated nonlinear medium as well as on the polarization of the fundamental electric field as well as on the angle of incidence ϑ of the fundamental beam. The quantity

$$
\Psi = \frac{2\pi d}{\lambda}\left(n_{\mathrm{f},\omega}\cos(\theta_{\mathrm{f},\omega}) - n_{\mathrm{f},2\omega}\cos(\theta_{\mathrm{f},2\omega})\right) \tag{2.22}
$$

takes into account phase mismatch between the SH and the fundamental fields, which is pronounced for thick or very dispersive nonlinear materials. The angles of propagation $\theta_{\mathrm{f},\omega}$ and $\theta_{\mathrm{f},2\omega}$ of the fundamental and the SH fields in the nonlinear film are obtained by Snell's law

$$\sin(\theta_{\mathrm{f},\omega}) = \sin(\vartheta) / n_{\mathrm{f},\omega} \tag{2.23}$$
$$\sin(\theta_{\mathrm{f},2\omega}) = \sin(\vartheta) / n_{\mathrm{f},2\omega}.$$

In this work, we measure the generated SH power from several nonlinear materials, and we use Eq. (2.21) to determine the tensor elements of the second-order nonlinear susceptibility, see Chapters 6 and 7.

2.2   Second-order nonlinear materials

In this section, three classes of second-order nonlinear materials for potential hybrid integration on the SiP platform are briefly discussed. These classes range from traditionally used crystalline materials over highly nonlinear organic materials to novel nanolaminate metamaterials grown by atomic layer deposition.

2.2.1   Crystalline materials

In the field of nonlinear optics, crystalline materials are traditionally used as nonlinear media. For example, in Franken's ground-breaking experiments, a pump laser was focused on a quartz crystal to achieve optical frequency doubling [27]. Various other crystals such as potassium dihydrogen phosphate (KDP), beta-barium borate (BBO), or lithium triborate (LBO) have become standard materials in frequency-mixing applications [34–36]. In the 1990s, the ferroelectric material lithium niobate ($LiNbO_3$) became very popular in frequency conversion applications due to the possibility to realize quasi-phase matched crystals by domain inversion using electric-field poling [37]. In addition, $LiNbO_3$ is arguably the most commonly used material in discrete EO modulators. The material shows good transparency in the wavelength bands traditionally used for optical communications [38]. Furthermore, the dominant component of the EO tensor of $LiNbO_3$ is $r_{33} = 31$ pm/V [6], which allows

technologically simple modulator implementations in which optical and electric fields are polarized in parallel. Another noteworthy second-order nonlinear crystal is barium titanate ($BaTiO_3$). This material attracted significant attention in recent years due to its ultra-high EO coefficient of $r_{42} = 923$ pm/V [39], which potentially allows realizing very efficient EO modulators.

Besides their excellent EO properties, $LiNbO_3$ and $BaTiO_3$ are also thermally and chemically stable, which makes them attractive for a hybrid combination with SiP circuits. However, technological challenges concerning the bonding or growth of these materials on SiP chips limit the performance and thus hinder widespread application of such devices, see Section 2.4.2.2.

2.2.2 Organic materials

Organic EO (OEO) materials have attracted considerable attention since the late 1980s for several reasons. On the one hand, OEO materials offer fast response times to externally applied electric fields in the order of ten femtoseconds [40]. On the other hand, these materials feature ultra-high second-order nonlinearities resulting in a Pockels effect which can be orders of magnitude stronger than in $LiNbO_3$ [41]. Furthermore, many OEO materials are not naturally occurring, but created by theory-based design and targeted chemical synthesis, offering vast potential to synthesize for further improvements in terms of EO activity and resilience against harsh environmental conditions [31]. An additional advantage is the ease of processing and combining OEO materials with other material platforms. For instance, the materials can be spin-coated, dispensed, or printed in a back-end-of-line post-processing step, and are thus compatible with virtually any platform for integrated photonic circuits. OEO materials are thus attractive candidates for realizing highly efficient and broadband Pockels-type EO modulators on the SiP platform.

The macroscopic properties of OEO materials and in particular their EO activity are defined by properties of the underlying molecular units, the so-called EO chromophores. These units contain a chain-like conjugated electron system, also referred to as π-bridge, in which single and double bonds alternate, resulting in π-electrons that are delocalized along the entire atomic chain [31]. The distribution of these loosely bound electrons is strongly perturbed when an

external electric field is applied, resulting in a large induced molecular polarization [31]. However, a second-order nonlinear polarization arises only if the conjugated system is asymmetrically perturbed, leading to a pronounce molecular hyperpolarizability. This asymmetry can be induced by attaching different moieties with either high electron affinity, so-called electron acceptors, or low electron affinity, so-called electron donors, at the ends of the π-bridge [31]. As an example, Figure 2.1 depicts the chemical structure of JRD1, which is the chromophore used in the experimental demonstrations presented in Chapters 3 and 4. The donor is highlighted in blue, the π-bridge in black, and the acceptor in red. The four phenyl side groups at the donor are quite bulky. This results in an increased inter-chromophore distance, which hinders detrimental centrosymmetric pairing of chromophores due to dipole-dipole interactions [42].

Similar to Eq. (2.2), the molecular dipole moment $\vec{p}(\vec{x},t)$ of a single chromophore can be written as

$$
\begin{aligned}
p_i(\vec{x},t) = \mu_i &+ \epsilon_0 \int\limits_{-\infty}^{\infty} d\tau_1 \, \hat{\alpha}_{ij}^{(1)}(\tau) E_j(\vec{x},t-\tau_1) \\
&+ \epsilon_0 \int\limits_{-\infty}^{\infty} d\tau_1 \int\limits_{-\infty}^{\infty} d\tau_2 \, \hat{\beta}_{ijk}(\tau_1,\tau_2) E_j(\vec{x},t-\tau_1) E_k(\vec{x},t-\tau_2) + \dots
\end{aligned}
\tag{2.24}
$$

where μ_i is the permanent dipole moment, $\hat{\alpha}_{ij}$ the linear polarizability, and $\hat{\beta}_{ijk}$ the first hyperpolarizability. All higher-order contributions to the dipole moment are neglected within the scope of this work. The indices $i,j,k \in \{x,y,z\}$ correspond to a local coordinate system of the molecule with the z axis pointing along the main chromophore axis. Second-order nonlinear effects in OEO materials arise due to the third term in which the field components enter quadratically. The hyperpolarizability tensor $\hat{\beta}_{ijk}$ is an important parameter for determining the strength of these effects. For typical chromophores, the dominant tensor component is $\hat{\beta}_{zzz}$ for which the interacting electric fields as well as the induced polarization point along the z-axis of the chromophore. It is now interesting to consider the relation between this quantity and the macroscopic second-order nonlinear susceptibility $\chi_{333}^{(2)}$ for the Pockels effect. Note that in this case the orientation of the global coordinate system is chosen
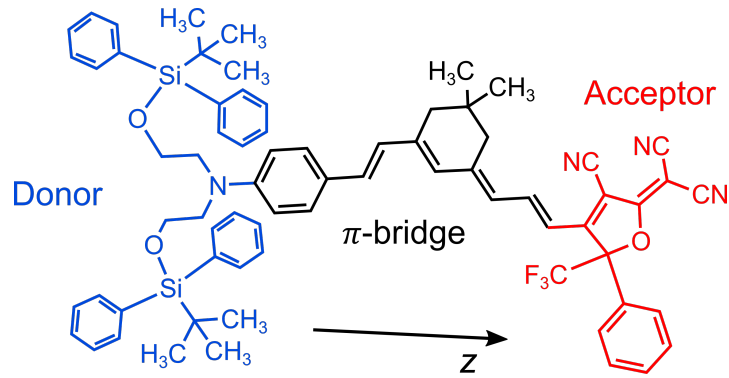
Figure 2.1: Chemical structure of the chromophore JRD1. The π-bridge (black) with highly delocalized π-electrons leads to a large polarizability of the molecule. Different electron affinities of the donor group (blue) and the acceptor group (red) at either end of the π-bridge result in a non-centrosymmetric electron density distribution along the chromophore axis. This leads to a nonlinear contribution to the molecular polarization when the chromophore is exposed to electric fields, quantified by a strong molecular hyperpolarizability. The arrow indicates the main chromophore axis z.

such that the 3-axis coincides with the direction of the poling field, see next paragraph. In the frequency domain the relation between $\hat{\beta}_{zzz}$ and $\chi^{(2)}_{333}$ is given by [31]

$$\chi^{(2)}_{333}(\omega_c : \omega_c, 0) = N \hat{\beta}_{zzz}(\omega_c : \omega_c, 0) \hat{g}(\omega_c, \epsilon) \left\langle \cos^3(\Theta) \right\rangle, \qquad (2.25)$$

where N denotes the number density, *i.e.*, the number of chromophores per unit volume, $\hat{g}(\omega_c, \epsilon)$ is the Lorentz–Onsager local field factor, which takes into account partial screening of the applied electric field in the direct surrounding of the chromophore, and $\langle \cos^3(\Theta) \rangle$ is the average acentric order parameter, where Θ denotes the angle between the 3-axis of the global coordinate system defined by the poling direction and the chromophore z-axis.

Electric field poling of OEO materials

In an ideal case, *i.e.*, for maximum $\chi^{(2)}_{333}$, all chromophores have to be aligned along the 3-axis of the global coordinate system, such that $\langle \cos^3(\Theta) \rangle$ in Eq. (2.25) is unity. However, after deposition of the OEO material from solution, the chromophores are typically randomly oriented leading to a random distribution of Θ and thus to a vanishing order parameter, see Figure 2.2(a), where chromophores are indicated as ellipses while the local molecular z-axes are indicated by arrows. A nonzero order parameter is, *e.g.*, achieved by
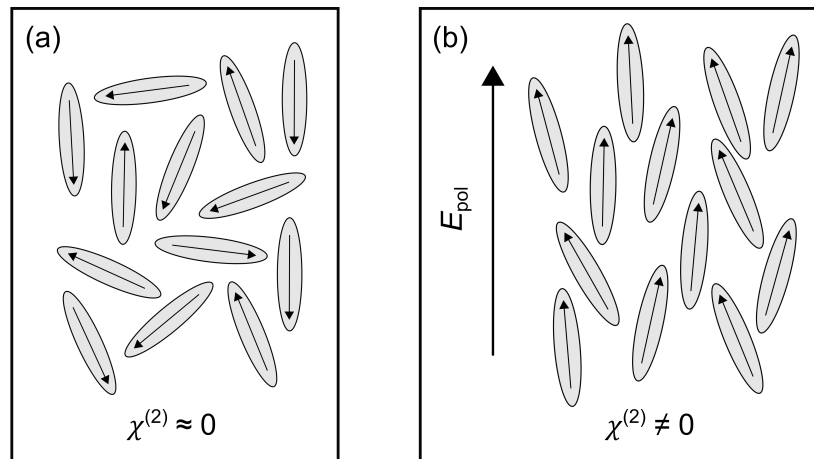
Figure 2.2: Molecular alignment of chromophores by electric-field poling. **(a)** After deposition from solution, the EO chromophores, which are schematically illustrated as ellipses, are randomly oriented. The respective molecular z-axes are indicated by arrows. Due to the random orientation, the molecular nonlinearity of the various chromophores cancels, *i.e.*, the average acentric order parameter and thus the macroscopic $\chi^{(2)}$ vanish. **(b)** A non-vanishing $\chi^{(2)}$ is achieved by electric-field poling. The material is heated to the glass-transition temperature, and a static poling field E_{pol} is applied to align the dipolar chromophores. The poling field is removed only after the material is cooled down to room temperature such that the induced average acentric orientation is maintained.

electric-field poling. An illustration of this process is schematically depicted in Figure 2.2(b). The OEO material is first heated close to its glass-transition temperature (T_g), where it undergoes a transition from a solid glassy state to a liquid-like state in which the chromophores become highly mobile. A static electric poling field E_{pol} is then applied to the material, which aligns the dipolar chromophores. In a next step, the material is cooled down while keeping the poling field applied. This reduces the chromophore mobility, while the average acentric orientation is preserved. At room temperature, the acentric chromophore orientation is essentially frozen, and the poling field can be removed.

Classes of OEO materials

Chromophores can be either used in pure form, as so-called neat or monolithic materials [42], in guest-host systems, where the chromophores are doped as guests into a polymer host matrix [43,44], or in so-called side-chain polymers [45], where chromophore side groups are covalently bound to a polymer backbone. In this work, both neat systems, see Chapters 3 and 4, and

side-chain polymers, see Chapter 5, were used. Neat chromophore materials have the advantage of large number density, resulting in record-high second-order nonlinearity. However, for neat systems, T_g is typically below 100 °C, such that thermal relaxation of the poling-induced order at elevated temperatures can become an issue. For a low fraction of dispersed or bound chromophores, guest-host systems or side-chain polymers feature much higher T_g, which comes at the price of a reduced EO activity. This trade-off between high thermal stability and high EO activity may be overcome by recently introduced highly nonlinear cross-linkable chromophore systems [46]. For these materials, glass-transition temperatures as high as 160 °C along with high EO coefficients of 300 pm/V were realized.

Thermal relaxation of OEO materials

The poling-induced average acentric chromophore orientation increases the potential energy of the OEO material due to dipole-dipole interactions between neighboring chromophores. The chromophore state after poling is thus energetically unfavorable, and the chromophores tend to relax back towards a random orientation with minimum potential energy. The extent of thermal relaxation is strongly influenced by the difference between the temperature at which the material is stored and T_g of the material [47]. The relaxation effect is weak if the storage temperature is far below T_g. In this case, the chromophore mobility is negligible and the acentric orientation is preserved. For storage temperatures close to T_g, however, the molecular mobility is increased such that the acentric order of chromophores is reduced, resulting in a reduction or even in a complete loss of the macroscopic EO activity [19,48,49]. If the storage temperature is well below the decomposition temperature [50], the relaxation process is in principle reversible by simply repeating the poling procedure. For many industrial applications, however, this approach would not be viable. Materials with high values of T_g are thus of paramount importance for commercial application of SOH devices, *e.g.*, in the field of optical communications, where operation at elevated temperatures is usually unavoidable.

To obtain a better understanding of the involved relaxation mechanisms, the thermal relaxation can be modelled. In literature there exists a variety of different models, which describe the relaxation dynamics of different OEO

materials. These models range from bi-exponential decay models [51,52] to so-called stretched exponential models, in which a continuous range of decay times is considered [53,54].

In this work, the thermal relaxation of a high-T_g side-chain polymer in an silicon-organic hybrid (SOH) modulator is investigated, see Chapter 5. The devices are stored for more than 2700 h at 85 °C according to Telcordia testing protocols [55]. During the first few hundreds hours we find a decrease of the EO activity, which we model by an exponential decay with a single decay time. After this initial burn-in the EO activity remains stable for the remainder of the high-temperature storage test.

Photo-chemical degradation of OEO materials

Besides thermal relaxation, photo-chemical degradation is another challenge when working with OEO materials: If an EO chromophore is exposed to intense laser light, the molecule may be irreversibly damaged by a photochemical reaction. The main degradation process is photo-oxidation [56], which can be explained using a typical energy diagram of a chromophore [57], see Figure 2.3. The chromophore is excited from the singlet ground state S_0 to the singlet excited state S_1 by absorption of a photon. The excited system may now either relax back to the ground state by emission of a fluorescence photon, or undergo an intersystem crossing (ISC) to the excited triplet state T_1. The latter process is unlikely, but can be mediated by the presence of triplet ground-state oxygen $^3O_2$, which then undergoes a transition to singlet oxygen $^1O_2$, indicated in blue. The second ISC from the T_1 to the S_0 level is also mediated by triplet oxygen, which again produces singlet oxygen, indicated in red. The generated highly aggressive singlet oxygen can then attack the chromophore in ground state S_0, which leads to formation of a compound without EO activity.

Photo-chemical stability of the chromophores can be either achieved by protecting the molecules from the generated singlet oxygen or by reducing the generation of singlet oxygen in the first place. The latter is, *e.g.*, achieved by lowering the concentration of available ground state oxygen $^3O_2$. This requires processing of the OEO material under exclusion of oxygen, *e.g.*, in an inert nitrogen atmosphere. In addition, the OEO material should feature a low oxygen diffusivity, such that only little oxygen can diffuse into the material after
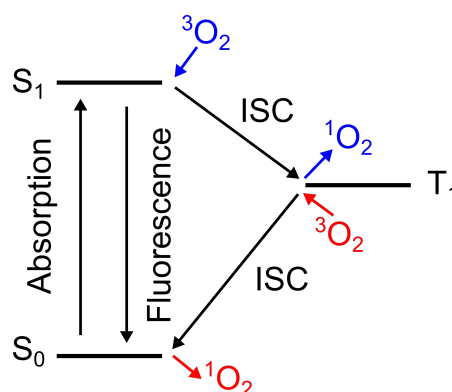
Figure 2.3: Energy diagram of a chromophore for the description of photo-oxidation. Photo oxidation damage is caused by the reaction of singlet oxygen $^1O_2$ with the chromophore singlet ground state S_0. Singlet oxygen is produced either during the intersystem crossing (ISC) from the excited singlet state S_1 to the excited triplet state T_1 (indicated in blue), or by the ISC from T_1 to S_0 (indicated in red).

processing. This is, *e.g.*, achieved in high-T_g cross-linked materials [31,58]. An even improved performance is achieved if the OEO material is placed in a hermetically encapsulated package, which entirely prevents the penetration of oxygen [19,20]. If singlet oxygen is still present in the material despite these measures, the chemical structure of the molecule can in principle be adapted such that the reactive chromophore sites are protected [31]. A more practical approach is adding efficient singlet oxygen quenchers to the material [59–61]. In this case, singlet oxygen either directly oxidizes the quencher instead of the chromophore or relaxes back to its triplet ground state by energy transfer to the quencher [61,62].

2.2.3 Nanolaminate materials grown by atomic layer deposition

A relatively novel class of second-order nonlinear materials are nanolaminates consisting of alternating thin layers of different inorganic materials [21,22]. Due to their inorganic nature, these nanolaminates are inherently resilient against photo-degradation and are also expected to be long-term thermally stable even at elevated temperatures. Furthermore, these nanolaminates can be grown by conformal atomic layer deposition (ALD) [63], which is a standard technique used in semiconductor processing [64]. ALD growth does not require sophisticated substrate preparation as compared to, *e.g.*, molecular beam
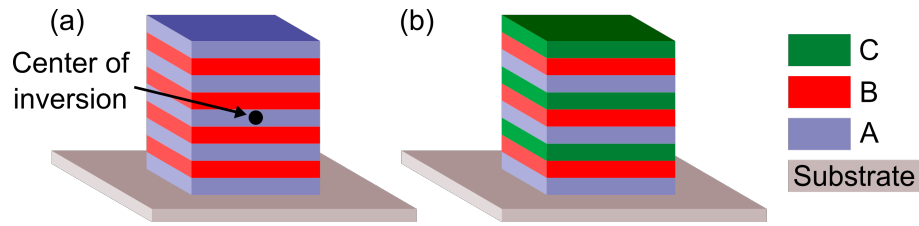
Figure 2.4: Structure of nanolaminates. **(a)** Binary nanolaminate consisting of two centrosymmetric constituents A and B. Globally, the inversion symmetry is maintained, indicated by the center of inversion (black dot). Such binary nanolaminates thus feature no macroscopic second-order nonlinearity. **(b)** Ternary nanolaminate consisting of three centrosymmetric constituents A, B, and C. No center of inversion is found for this class of nanolaminates, such that a macroscopic nonlinearity can be expected. All nanolaminates are grown on a substrate.

epitaxy [39]. Instead, simple hydroxyl-(OH-)groups as found on, *e.g.*, the native oxide of silicon are sufficient to initialize the growth process [65]. Nanolaminates grown by ALD are thus well suited to realize second-order nonlinearities on the SiP platform.

Recently, ABC-type nanolaminates consisting of three centrosymmetric metal-oxides A, B, and C grown on glass substrates were demonstrated [21,22]. In these demonstrations, the constituents are aluminum oxide (Al_2O_3), titanium dioxide (TiO_2), and indium oxide (In_2O_3) [22] or Al_2O_3, TiO_2 and hafnium dioxide (HfO_2) [21]. While none of these constituents feature any bulk nonlinearity, each inner interface gives rise to a surface nonlinearity, see the discussion of symmetry properties of the second-order nonlinear susceptibility in Section 2.1.1. However, the nonlinearity of a single interface is weak, and an appreciable effective nonlinearity is achieved only if the individual layers are atomically thin, thereby resulting in densely stacked interfaces. To achieve macroscopic second-order nonlinearity, this class of nanolaminate should at least have three different constituents. A binary nanolaminate with centrosymmetric constituents A and B is schematically depicted in Figure 2.4(a). The inversion symmetry is still broken locally at each inner interface. However, the surface nonlinearity at the interface AB cancels out with the nonlinearity of the adjacent interface BA [21], such that no macroscopic second-order nonlinearity is found. In fact, for such AB-type nanolaminates the inversion symmetry is maintained on a macroscopic level. This is illustrated in Figure 2.4(a), where the center of inversion is depicted as a black dot. In

Figure 2.4(b), we show a ternary ABC-type nanolaminate with an additional centrosymmetric material C. This structure has no center of inversion, resulting in a non-vanishing macroscopic nonlinearity.

Ternary nanolaminates based on centrosymmetric constituents currently feature second-order nonlinearities in the range of $\chi^{(2)} = 1\,\text{pm}/\text{V}$ [26]. While this value is already of the same order of magnitude as $\chi^{(2)}$ of established crystals such as KDP [66], further improvements are required to make the technology attractive for actual applications. A first step in this direction is presented in Chapter 7: We show binary nanolaminates based on the second-order nonlinear material zinc oxide (ZnO), having a nonlinearity of roughly $\chi^{(2)} = 4\,\text{pm}/\text{V}$.

2.3 Principle of Mach-Zehnder modulators

In this section, the working principle of a Mach-Zehnder modulator (MZM) is introduced and typical performance metrics of MZM are defined. Other types of EO modulators such as electro-absorption modulators [67] or resonant devices based on micro-rings [68] are not considered within the scope of this work. Figure 2.5 shows schematically a waveguide-based MZM in top view. The input field $E_{\text{in}}(t)$ of the optical carrier is split equally in the two arms of the MZM using a 2×2 multi-mode interference (MMI) coupler [69] with a 50:50 power splitting ratio. Each arm comprises a phase-shifter section with length L (yellow), which contains electrodes with spacing w across which modulating voltages $U_1(t)$ and $U_2(t)$ can be applied. These voltages can be used to independently modulate the phases $\phi_1(t)$ and $\phi_2(t)$ of the optical fields by varying the effective refractive indices by Δn_1 and Δn_2

$$\phi_1(t) = -\Delta n_1 k_0 L,$$
$$\phi_2(t) = -\Delta n_2 k_0 L. \tag{2.26}$$

In these relations, the free-space wavenumber is given by $k_0 = 2\pi / \lambda_0$. Another MMI at the output of the phase-shifter sections recombines the optical fields. Assuming lossless components, we find for the output fields $E_{\text{out,1}}(t)$ and $E_{\text{out,2}}(t)$ of the optical carrier [70]
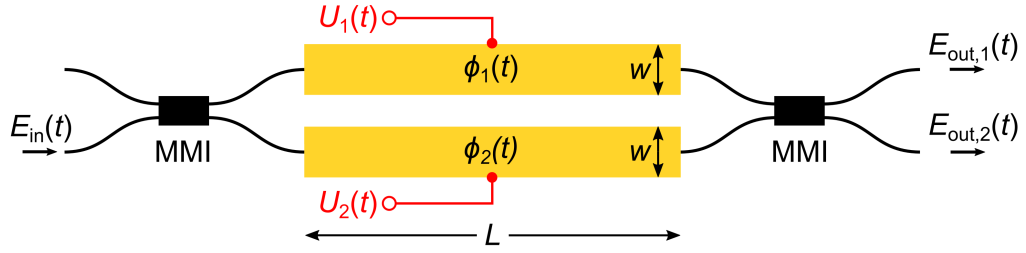
Figure 2.5: Schematic of an Mach-Zehnder modulator (MZM) in top view. The input field $E_{in}(t)$ is split equally in the two arms of the MZM by a multi-mode interference (MMI) coupler. The phase shifter sections of length L are indicated in yellow. They contain electrodes with spacing w across which modulating voltages $U_1(t)$ and $U_2(t)$ can be applied. This induces phase shifts of $\phi_1(t)$ and $\phi_2(t)$ in the upper and lower MZM arm , respectively. The modulated optical fields interfere in another MMI at the output of the phase shifters forming the output fields $E_{out,1}(t)$ and $E_{out,2}(t)$.

$$
\begin{aligned}
E_{out,1}(t) &= j E_{in}(t) \exp\left(j \frac{\phi_1(t) + \phi_2(t)}{2} \right) \cos\left(\frac{\Delta\phi(t)}{2} \right) \\
E_{out,2}(t) &= j E_{in}(t) \exp\left(j \frac{\phi_1(t) + \phi_2(t)}{2} \right) \sin\left(\frac{\Delta\phi(t)}{2} \right)
\end{aligned} , \tag{2.27}
$$

where we introduced the phase difference $\Delta\phi(t) = \phi_2(t) - \phi_1(t)$. We can see that in general both the amplitude and the phase of the output fields are modulated. Pure phase modulation is achieved by choosing $\phi_1(t) = \phi_2(t)$. In this so-called push-push configuration, $E_{out,2}(t)$ vanishes and the cosine term, which modulates the amplitude of $E_{out,1}(t)$, becomes unity. Conversely, pure amplitude modulation is realized by choosing $\phi_1(t) = -\phi_2(t)$. In this so-called push-pull configuration, the complex exponentials, which cause phase modulation, are unity. This avoids undesired chirp of the modulated optical signal. In practical implementations, only a single output of the MMI is connected. The following discussion is thus restricted to the upper output with optical field $E_{out,1}(t)$ for the case of push-pull operation. The transmitted optical power is proportional to the square of the output field, which leads to

$$
P_{out}(\Delta\phi(t)) = P_{in} \cos^2\left(\frac{\Delta\phi(t)}{2} \right). \tag{2.28}
$$

The power transfer function P_{out}/P_{in} of the MZM is depicted in Figure 2.6. For an induced phase shift of $\Delta\phi = \pi/2$ the power is reduced by a factor of 2. In

this so-called quadrature-, or 3-dB point, the transfer function can be linearized. This operation point is thus ideally suited for intensity modulation.

In Pockels-type MZM which are based on a material with dominant EO coefficient r_{33}, the induced change in refractive index in Eq. (2.26) can be substituted by Eq. (2.18). We then obtain a new expression for the induced phase changes

$$\phi_1(t) = \frac{1}{2} n_{EO}^3 r_{33} E_1(t) k_0 L \Gamma$$
$$\phi_2(t) = \frac{1}{2} n_{EO}^3 r_{33} E_2(t) k_0 L \Gamma$$
. (2.29)

The quantity Γ is the field interaction factor [15], which takes into account the reduced overlap of the optical and electrical mode in the Pockels-type material. A detailed discussion on how Γ is calculated for SOH MZM is presented in Appendix A.3. Assuming push-pull operation with $E_1 = -E_2 = U/w$ we obtain for the induced phase difference at the MZM output

$$\Delta\phi(t) = n_{EO}^3 r_{33} \frac{U(t)}{w} k_0 L \Gamma .$$
(2.30)

An important metric of an MZM is the so-called π-voltage U_π associated with an induced phase shift $\Delta\phi(t) = \pi$, which drives the MZM from maximum to minimum transmission. Using Eq. (2.30), the π-voltage of a Pockels-type MZM in push-pull configuration can be written as

$$U_\pi = \frac{1}{2} \frac{\lambda_0 w}{n_{EO}^3 r_{33} L \Gamma} .$$
(2.31)

An additional important metric is the so-called $U_\pi L$ product of the π-voltage of a MZM and the length L of the associated phase-shifter sections. The metric indicates the modulation efficiency of a MZM and reflects that there is a trade-off between small π-voltages and short phase shifters. For a Pockels-type MZM in push-pull operation the $U_\pi L$- product reads

$$U_\pi L = \frac{1}{2} \frac{\lambda_0 w}{n_{EO}^3 r_{33} \Gamma} .$$
(2.32)
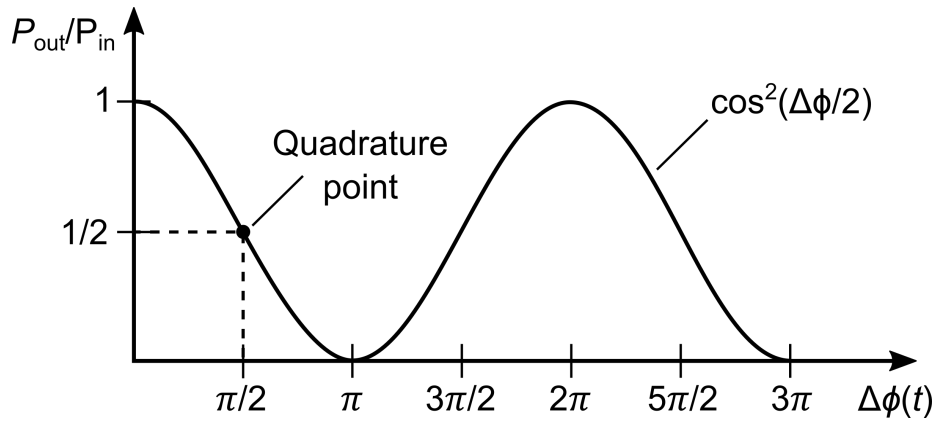
Figure 2.6: MZM power transfer function. At the quadrature point $\Delta\phi = \pi/2$ the transfer function features best linearity, ideally suited for intensity modulation. For a phase difference of $\Delta\phi = \pi$ the MZM is driven from its maximum its minimum power transmission point.

Considering a fixed wavelength λ_0, a low $U_\pi L$ product and therefore efficient modulation is achieved by a tight electrode spacing w, by using a Pockels-type material with a large value of $n_{\text{EO}}^3 r_{33}$, or by exploiting a phase shifter structure with a large interaction factor Γ.

Another essential metric is the optical power attenuation a_{PS} of the phase shifter specified in dB,

$$a_{\text{PS}} = -10\log\left(\frac{P_{\text{PS,out}}}{P_{\text{PS,in}}}\right), \tag{2.33}$$

where $P_{\text{PS,in}}$ and $P_{\text{PS,out}}$ denote the optical power at the input and output of the phase shifter section, respectively. This attenuation can be calculated as the product of the phase shifter propagation loss a in dB per length and the phase shifter length L

$$a_{\text{PS}} = aL. \tag{2.34}$$

A relation between a and the optical attenuation coefficient $\tilde{\alpha}$ defined by $P_{\text{PS,out}} = P_{\text{PS,out}}\exp(-\tilde{\alpha}L)$ is given by

$$\frac{a}{\text{dB}} = \tilde{\alpha} \times 4.34. \tag{2.35}$$

For a given phase shifter implementation with fixed propagation loss a, the phase shifter attenuation a_{PS} can be reduced by simply shortening the phase shifter, see Eq. (2.34). However, according to Eq. (2.32), shortening the phase shifter increases the π-voltage. Thus, we find a trade-off between phase shifter attenuation and π-voltage, which is typically expressed by the so-called loss-efficiency product $aU_\pi L$ measured in units of V dB. This quantity corresponds to the π-voltage (in V) of a device with a phase-shifter attenuation of $a_{PS} = 1$ dB or, equivalently, the attenuation of a phase shifter (in dB) having a π-voltage of $U_\pi = 1$ V.

Optical signal generation using MZM

Using Eq. (2.30) in combination with Eq.(2.31) we can express the power transfer function of the MZM in Eq. (2.28) as a function of an applied signal voltage $U(t)$

$$\frac{P_{out}(U(t))}{P_{in}} = \cos^2\left(\frac{\pi U(t)}{2U_\pi}\right). \tag{2.36}$$

The MZM can be thus used to generate intensity-modulated optical signals. For simple on-off keying (OOK), see Figure 2.7(a), the device is biased in the so-called quadrature point at $U_{bias} = U_\pi/2$, where the transmitted optical power is reduced by 3 dB with respect to the point of maximum transmission. For operation, a binary sequence with voltage levels of $U = U_{bias} \pm U_\pi/2$ may be fed to the device, such that the MZM is switched between maximum and minimum optical transmission. Since the signal voltage is binary, only a single bit per symbol is transmitted. More information per symbol can be transmitted using non-binary input signals. For example, Figure 2.7(b) shows four-level pulse-amplitude modulation (PAM4) with four equidistant voltage levels such that 2 bit/symbol are transmitted. The device is again biased at the quadrature point, but, in contrast to OOK, the peak-to-peak voltage swing is usually smaller than U_π to remain in the linear range of the power transfer function. Alternatively, a voltage swing of U_π can be used in combination with non-equidistant voltage levels of the drive signal.
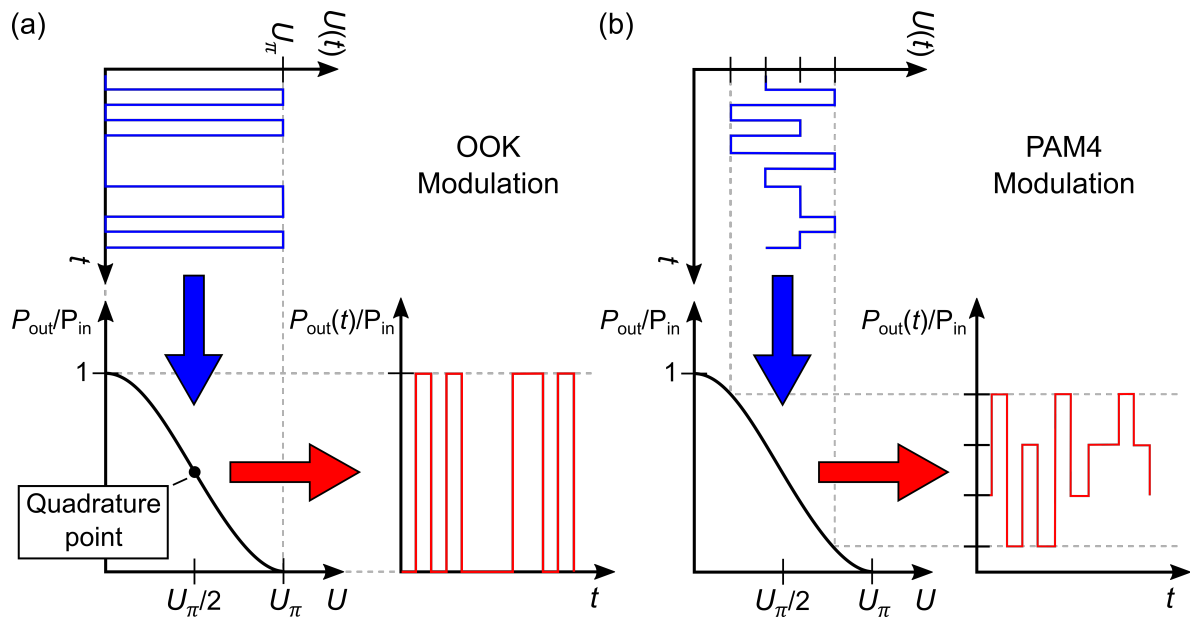
Figure 2.7: Intensity modulation (IM) using an MZM. **(a)** IM using simple on-off-keying (OOK) as a modulation format. The device is biased in the quadrature point $U_{bias} = U_\pi/2$ and operated at a peak-to-peak drive voltage of $U_{pp} = U_\pi$. This leads to two distinct voltage levels at which the optical power is either switched on or off. **(b)** IM using four-level pulse amplitude modulation (PAM4). The device is biased in the quadrature point $U = U_\pi/2$ and a sequence of four equidistant voltage levels is fed to the MZM. To remain in the linear regime of the transfer function the peak-to-peak drive voltage must be smaller than U_π. Alternatively, a voltage swing of U_π can be used in combination with non-equidistant voltage levels of the drive signal.

2.4 Silicon photonic electro-optic modulators

In this section, the state-of-the-art of silicon photonic (SiP) modulators is reviewed. This includes standard all-Si devices based on *pn*-junctions, which rely on charge depletion, so-called silicon-insulator-silicon capacitors (SISCAP) operated in charge accumulation mode, but also SiP modulators based on hybrid integration of materials which may feature second-order nonlinearities.

2.4.1 All-silicon modulators

Due to the lack of second-order nonlinearities in bulk silicon, SiP EO modulators typically have to rely on the free-carrier dispersion effect [7]. The effect causes a change in refractive index when the concentration of free carriers

is modulated. All-Si modulators can be thus categorized in devices which either deplete or accumulate free carriers to realize EO modulation. Depletion-type devices are typically realized as reverse-biased *pn*-junctions, which are embedded in the waveguide, see Figure 2.8(a). For efficient modulation, these devices should have a large capacitance such that a small modulation voltage induces large variations of the free carrier concentration. However, a large device capacitance C leads to large RC time constants, leading to a fundamental trade-off between modulation efficiency and EO bandwidth of the device [8]. For efficient devices, the capacitance is often increased by high doping concentrations, which reduces the depletion region of the *pn*-junction. However, higher doping also increases the optical loss due to free-carrier absorption, which leads to an additional trade-off between modulation efficiency and optical insertion loss [8]. As a consequence, high-speed and low-loss modulators with high efficiency are hard to realize in all-Si EO modulators. Best-in-class devices in terms of modulation efficiency achieve $U_\pi L$ products of 4.6 Vmm and loss-efficiency products $aU_\pi L$ of 5.8 VdB. However, the 3 dB-bandwidth amounts then to only 13 GHz [71]. Conversely, high-speed devices with 3 dB-bandwidths around 40 GHz have been realized, but the $U_\pi L$ and $aU_\pi L$-products increase to 16 Vmm and 28 VdB, respectively. These fundamental limitations can be partially relaxed in accumulation-type devices based on silicon-insulator-silicon capacitors (SISCAP). These devices are typically realized as a vertical stack consisting of a p-doped Si bottom layer, an insulating intermediate layer and an n-doped Si top layer, see Figure 2.8(b). The junction is typically operated under "forward" bias such that majority carriers accumulate at the respective interface of the insulator. For these devices, the capacitance can be increased independently from the doping concentration by reducing the thickness of the insulator. Therefore, there is no inherent trade-off between modulation efficiency and optical insertion loss. As a result, SISCAP-devices can feature $U_\pi L$ products down to 1.6 Vmm and loss-efficiency products of $aU_\pi L = 7$ VdB [72]. However, the trade-off between modulation efficiency and bandwidth also holds for SISCAP devices, leading to a low 3 dB-bandwidth of, *e.g.*, 15 GHz [72].
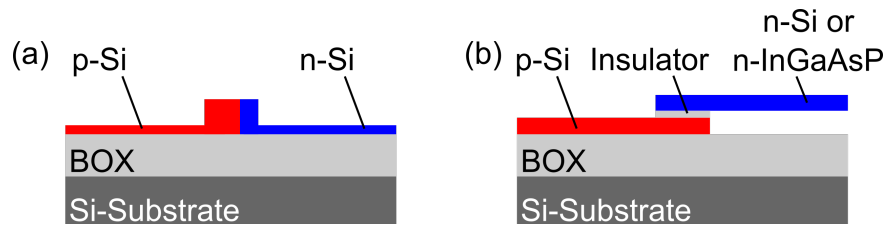
Figure 2.8: Schematic cross section of typical SiP phase shifters based on the free-carrier plasma effect. **(a)** All-Si depletion-type phase shifter implemented as a *pn*-junction embedded in a rib waveguide. Reverse-biasing of the junction leads to a depletion of free carriers in the waveguide. **(b)** Accumulation-type phase shifter realized as a vertical semiconductor-insulator-semiconductor-junction. For all-Si devices, the top and bottom semiconductor layers consist of p- and n-doped Si, respectively. "Forward" biasing of the junction results in an accumulation of free carriers at the two interfaces of the insulator. The performance can be enhanced by replacing the top n-doped Si layer by n-doped IIIV-materials such as InGaAsP.

2.4.2 SiP modulators with heterogeneously integrated materials

The performance of all-Si modulators can be enhanced by heterogeneous integration of other material systems. These material systems are typically categorized in two groups. The first group includes semiconductors, which, when compared to Si, have a stronger free-carrier plasma effect. The second group includes materials with a second-order nonlinearity.

2.4.2.1 Hybrid integration of III-V semiconductors

The free-carrier dispersion effect has the unwanted side effect to change also the optical absorption coefficient $\tilde{\alpha}$ of the material when its carrier concentration is modulated. In silicon the ratio $\Delta n / \Delta \tilde{\alpha}$ of the change in refractive index Δn and the change in absorption $\Delta \tilde{\alpha}$ is roughly 3.5 times larger for holes than for electrons [7]. The performance of all-Si SISCAP-type devices can be thus significantly improved by replacing the top *n*-doped Si layer by, *e.g.* *n*-doped indium-gallium-arsenide-phosphide (InGaAsP), for which the ratio of $\Delta n / \Delta \tilde{\alpha}$ is considerably improved as compared to electrons in silicon [8,73]. The integration of InGaAsP is achieved using direct wafer bonding on standard SiP waveguides. These hybrid Si-insulator-InGaAsP capacitors show low π-voltage length products of $U_\pi L = 0.47$ Vmm and loss efficiency products down to $aU_\pi L = 0.9$ VdB [73]. However, a fabrication related issue in the proof-of-concept experiments shown in [73] resulted in a large *RC* time constant, which

limited the demonstrated bandwidth to only 100 MHz. This problem does not seem to be of fundamental nature, such that these devices remain promising for high-performance SiP modulators.

2.4.2.2 Hybrid integration of Pockels-type materials

The free-carrier plasma effect in Si does not only lead to a modulation of the refractive index but also to a modulation of the optical absorption [7]. The resulting amplitude-phase coupling leads to chirp of the modulated optical signal [74]. This can be avoided by integrating Pockels-type materials, which provide pure amplitude modulation when implemented in a MZM, see Section 2.3.

In recent years, a significant effort was made to integrate the Pockels-type material lithium niobate (LiNbO$_3$) on the SiP platform. The integration process is typically based on single-crystal thin-film LiNbO$_3$ (TFLN), which is bonded on various substrates. However, in many publications, the involved fabrication processes deviate entirely from typical SiP process flows. For instance, in some approaches, Si waveguides and electrodes are fabricated on top TFLN bonded to Si or LiNbO$_3$ substrates [9,10]. Other approaches do rely on standard SiP waveguides fabricated on silicon-on-insulator (SOI) chips, the MZM electrodes, however, are still patterned on top of the TFLN layer [11,12]. For these devices, moderate π-voltage length products of $U_\pi L = 22$ Vmm and loss-efficiency products of 2.2 VdB are achieved [12]. The approach, which is currently the most compatible with standard SiP process flows, relies on Sandia National Laboratories' SiP process [13]. In this concept, hybrid EO modulators are realized in a back-end-of-line post-processing step by bonding TFLN to the SiP chip without any further need for processing. However, the performance of these hybrid SiP devices is still suboptimal with $U_\pi L$ products as high as 67 Vmm and loss-efficiency products of around $a U_\pi L = 130$ VdB [13].

Another promising Pockels-type material for hybrid integration in SiP circuits is barium titanate (BaTiO$_3$). The material can be grown epitaxially on top of the Si device layer of planar SOI wafers with a diameter of up to 200 mm. These BaTiO$_3$ wafers are then flipped and bonded to an inter-layer dielectric (ILD) of a standard SiP process [75]. Subsequently, the Si substrate and the buried oxide is removed from the bonded BaTiO$_3$ wafer. The exposed Si device layer is then
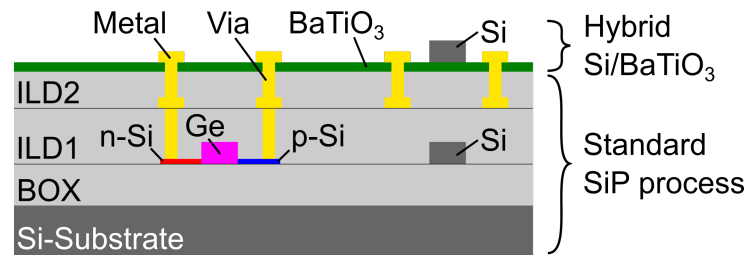
Figure 2.9: Schematic cross section of a hybrid SiP chip with an integrated BaTiO$_3$ layer. The BaTiO$_3$ is bonded to an inter-layer dielectric (ILD) in a wafer-scale process, which does not affect the performance of other standard components such as germanium (Ge) photodiodes. Hybrid Si/BaTiO$_3$ phase shifters are realized by patterning Si strip waveguides and metal electrodes on top of the BaTiO$_3$ layer.

patterned to realize strip waveguides on top of the BaTiO$_3$ layer. To complete the Si/BaTiO$_3$ EO modulators, electrodes are structured next to the Si waveguides and connected to metal layers underneath by vias. A cross section of the hybrid SiP layer stack is depicted in Figure 2.9. The BaTiO$_3$ wafer bonding process does not deteriorate the performance of standard germanium (Ge) photo diodes, which are implemented in the same SiP process flow [75]. Furthermore, low-loss optical coupling between standard Si waveguides in the lower layer and hybrid Si/BaTiO$_3$ waveguides in the upper layer was demonstrated recently [76], which underlines the potential of this approach. The hybrid Si/BaTiO$_3$ EO modulators feature $U_\pi L$ products down to 2.3 Vmm and loss-efficiency products of $aU_\pi L = 1.3$ VdB [14], which already surpasses the performance of typical SiP modulators. Even more efficient modulation may be achieved by implementing BaTiO$_3$ in more efficient phase shifter structures such as slot waveguides [15]. This is currently challenging, however, due to the epitaxial growth of BaTiO$_3$.

Yet another approach relies on the integration of organic EO (OEO) materials. The OEO material can be either applied on top ultra-thin Si strip waveguides resulting in so-called silicon-polymer hybrid modulators [77–79], or it can be filled into standard Si slot waveguides [15], resulting in so-called silicon-organic hybrid (SOH) devices. The latter approach is followed and investigated in this work. For the SOH technology, the organic materials can be applied to standard SiP chips or wafers in a back-end-of-line processing step, such that a good compatibility with standard SiP process flows is given. The efficent phase shifter structures based on slot waveguides in combination with the high

nonlinearity of OEO materials lead to ultra-efficient SOH modulators which clearly outperform standard SiP devices. A detailed description of the SOH integration technology is given in Section 2.4.3.

2.4.3   Silicon-organic hybrid (SOH) modulators

In this section, the SOH device principle as well as the bandwidth limitations of SOH modulators are discussed.

2.4.3.1   SOH Mach-Zehnder modulator concept

Silicon-organic hybrid (SOH) MZM are realized by combining standard SiP chips with highly efficient organic EO materials. The chips used in this work are fabricated by 248 nm deep-UV lithography on 200 mm silicon-on-insulator wafers in the commercial foundry A*Star IME in Singapore. A top view of an SOH MZM is depicted schematically in Figure 2.10(a). Light is coupled to and from the SiP chip using grating couplers (GC). Si strip waveguides connect the GC with multi-mode interference (MMI) couplers, which split and recombine the light in the two arms of the MZM. Each MZM arm features an SOH phase shifter of length L. For the devices investigated in this work, the phase-shifter length is in the range of $L = 0.28\ldots1.5$ mm. The aluminum (Al) electrodes (orange) are realized as a coplanar transmission line (TL) in ground-signal-ground (GSG) configuration. The dash-dotted line labeled AA' indicates the location of the cross section of the MZM, which is schematically depicted in Figure 2.10(b). Each MZM arm contains a Si slot waveguide, which is formed by two Si rails with a width of $w_{rail} = 240$ nm and a height of $h_{rail} = 220$ nm. The two rails are separated by a narrow slot whose width is in the range of $w_{slot} = 130\ldots190$ nm for the devices investigated in this work. The rails are electrically connected to the GSG TL by 70 nm-high n-doped Si slabs and Al vias. The oxide above the slot waveguides is opened such that the OEO material can be applied to the waveguides in a back-end-of-line processing step. In this work, we use a micro-dispensing tool to locally apply the OEO material on the slot waveguides. In particular, we leave the metal contact pads uncovered to ensure a reliable electrical contacting of the SOH MZM. The dominant x-component of the optical mode experiences a strong enhancement in the low-index slot region, see Figure 2.10(c). Similarly, the dominant x-component of the electrical mode is tightly confined to the slot, see Figure 2.10(d). The
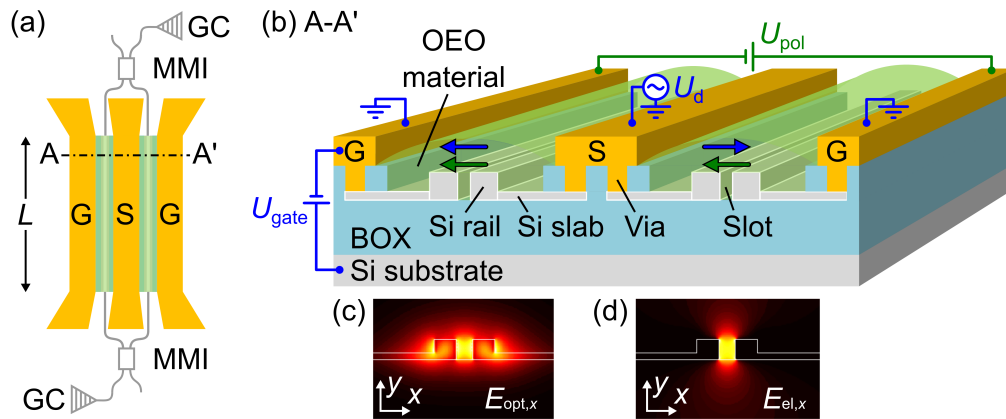
Figure 2.10: Silicon-organic hybrid (SOH) MZM. **(a)** Schematic top view of an SOH MZM with phase shifter length L. Light is coupled to and from the SiP chip by grating couplers (GC). A pair of multi-mode interference (MMI) couplers splits and recombines the light in the two arms of the MZM. The coplanar transmission line in ground signal ground (GSG) configuration is depicted in orange. The location of the cross section depicted in (b) is indicated by the dash-dotted line labeled AA'. **(b)** Schematic cross section of the two MZM arms. Each arm contains a SOH phase shifter, which consists of a Si slot waveguide. Each slot waveguide is formed by a pair of Si rails, which are separated by a narrow slot and which are electrically connected to the GSG transmission line by thin n-doped Si slabs. The waveguides are clad by an organic EO (OEO) material. For poling, the OEO material is heated to its glass-transition temperature and a poling voltage U_{pol} is applied across the floating ground electrodes, which aligns the dipolar chromophores in this region (green arrows). After cooling the device to room temperature, the acentric chromophore orientation is frozen and the poling voltage is removed. A drive voltage U_d applied to the center signal electrode (blue arrows) leads to an efficient push-pull operation of the MZM. To emulate a higher doping concentration in the Si slabs, we apply a gate voltage U_{gate} between the Si substrate and the Si device layer. This induces an electron accumulation layer in the Si slabs and thus reduces the RC time constants. The gate voltage becomes obsolete for optimized doping profiles [80] **(c)** Dominant E_x-component of the optical mode field. **(d)** Dominant E_x-component of the modulating RF mode. Figures adapted from [J3].

resulting strong modal overlap leads to a large value of the interaction factor Γ. In combination with the small slot widths w_{slot} across which the modulating voltage drops and the large EO coefficients of OEO materials, this leads to highly efficient electro-optic interaction, see Eq. (2.32). As discussed in Section 2.2.2, a poling process is required to achieve macroscopic EO activity in an OEO material. For poling of the SOH devices, we heat the entire chip by a Peltier element, and we apply the poling voltage U_{pol} (green arrows) across the floating ground electrodes of the MZM. When operating the poled device with a signal drive voltage U_d, the vector of the modulating electric field (blue arrows) points in the poling direction in one arm and in the opposite direction

in the other arm. This results in chirp-free efficient push-pull operation of the device.

Note that the slot waveguides act as capacitors, which need to be charged and discharged via the doped Si slabs when the modulating voltage changes. For the devices used in this work, the doping concentration in the slabs is insufficient due to insufficient doping, resulting in large RC time constants, which limit the device bandwidth [80]. We therefore emulate a higher doping concentration by applying a gate voltage U_{gate} between the Si substrate and the Si device layer. This results in an electron accumulation layer in the Silicon slabs [81], which improves the slab conductance and hence relaxes the RC bandwidth limitation. Properly designed doping profiles will render the gate voltage obsolete.

2.4.3.2 Bandwidth of SOH modulators

The subsequent discussion of the EO bandwidth of SOH MZM follows the formalism introduced in reference [80].

The frequency response of SOH MZM can be described using a distributed-element model of the associated radio-frequency (RF) transmission line (TL) [80]. An infinitesimally short TL element of length Δz can be modelled by the equivalent-circuit depicted in Figure 2.11(a). The yellow circuit and the associated distributed elements describe the metal GSG TL. The elements include a series resistance $R_{\text{TL}} = R'_{\text{TL}}\Delta z$, a series inductance $L_{\text{TL}} = L'_{\text{TL}}\Delta z$, and a shunt capacitance $C_{\text{TL}} = C'_{\text{TL}}\Delta z$, where the primed quantities describe resistance, inductance, and capacitance per unit length, respectively. The Si slot waveguides form an additional capacitance, which is charged and discharged via the doped Si slabs, see Figure 2.10. The slot waveguides can thus be included in the equivalent-circuit model by adding an RC shunt, which is depicted in blue in Figure 2.11(a). This RC shunt includes the slot capacitance $C_{\text{S}} = C'_{\text{S}}\Delta z$, the conductance of the Si slabs $G_{\text{S,bulk}} = G'_{\text{S,bulk}}\Delta z$, and the gate voltage-induced conductance $G_{\text{S,acc}} = G'_{\text{S,acc}}\Delta z$ of the electron accumulation layer in the slabs. The accumulation layer is induced to increase the total slab conductance $G_{\text{S}} = G_{\text{S,bulk}} + G_{\text{S,acc}}$, and hence to improve the device bandwidth, see Section 2.4.3.1. Note that the capacitance between the signal electrode and a single ground electrode amounts to only $C_{\text{TL}}/2$ due to the GSG configuration of the TL. Similarly, the capacitance of a single slot amounts to only $C_{\text{S}}/2$. The
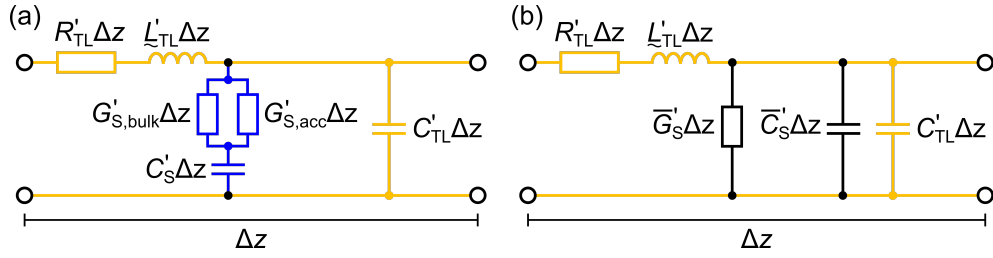
Figure 2.11: Equivalent-circuit model of an infinitesimally short transmission line describing the SOH MZM. **(a)** The distributed elements of the metal electrodes and the Si slot waveguide are depicted in yellow and blue, respectively. R'_{TL}, L'_{TL}, and C'_{TL} denote the series resistance, the series inductance and the shunt capacitance per unit length of the electrodes. $G'_{S,bulk}$ and $G'_{S,acc}$ denote the conductance per unit length of the resistive Si slabs and the gate-induced electron accumulation layer. C'_S denotes the capacitance per unit length of the slot waveguides. **(b)** Transformed equivalent circuit of the SOH MZM by introducing a frequency dependent conductance $\overline{G}'_S$ and a frequency dependent capacitance $\overline{C}'_S$. Figure adapted from Fig. 1 in reference [80].

equivalent circuit can be transformed in a Telegrapher-type equivalent circuit, see Figure 2.11(b). This is achieved by introducing the frequency-dependent capacitance [82]

$$\overline{C}'_S = \frac{C'_S}{1 + C'^2_S \omega^2 / G'^2_S} \tag{2.37}$$

and the frequency-dependent conductance [82]

$$\overline{G}'_S = \frac{C'^2_S \omega^2}{G'_S \left(1 + C'^2_S \omega^2 / G'^2_S\right)}. \tag{2.38}$$

Exploiting the similarity to a standard TL, we can now characterize the MZM TL by the complex propagation constant $\underline{\gamma} = \alpha + j\beta$ and the complex characteristic impedance $\underline{Z}_0$ [80]

$$\underline{\gamma} = \alpha + j\beta = \sqrt{\left(R'_{TL} + j\omega_{RF}L'_{TL}\right)\left(\overline{G}'_S + j\omega_{RF}\left(\overline{C}'_S + C'_{TL}\right)\right)}, \tag{2.39}$$

$$\underline{Z}_0 = \sqrt{\frac{R'_{TL} + j\omega_{RF}L'_{TL}}{\overline{G}'_S + j\omega_{RF}\left(\overline{C}'_S + C'_{TL}\right)}}, \tag{2.40}$$
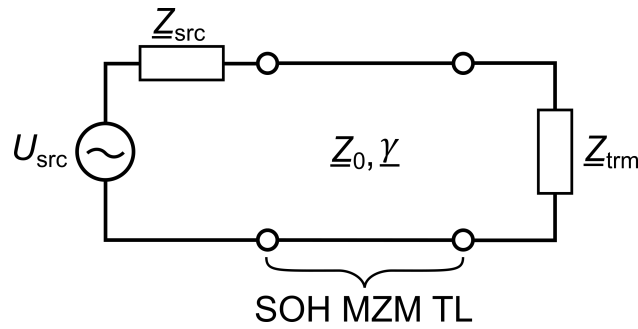
Figure 2.12: The SOH MZM is driven by an RF source with impedance $\underline{Z}_{\mathrm{src}}$ and terminated by a resistor with impedance $\underline{Z}_{\mathrm{trm}}$. The SOH MZM transmission line (TL) is characterized by a complex characteristic impedance $\underline{Z}_0$ and a complex propagation constant $\underline{\gamma}$.

where ω_{RF} denotes the angular frequency of the electrical signal travelling along the TL. The modulator is operated by connecting the SOH MZM TL to an RF source with source impedance $\underline{Z}_{\mathrm{src}}$ and to a termination with impedance $\underline{Z}_{\mathrm{trm}}$, see Figure 2.12.

The bandwidth of the modulator is determined by the frequency dependence of the induced phase shift of the optical carrier that is accumulated along the TL. The induced phase shift at a specific location of the TL is proportional to the modulation voltage at this point. If the modulator is driven by a sinusoidal voltage with frequency ω_{RF}, the accumulated phase shift $\varphi(t) = \Re\left(\hat{\underline{\varphi}}(\omega_{\mathrm{RF}})\exp(\mathrm{j}\omega_{\mathrm{RF}}t)\right)$ is thus calculated by integrating the modulation voltage seen by the optical carrier along the length L of the TL [80,83]. For this calculation we need to take into account that the optical signal and the RF voltage do in general not travel at the same velocity along the TL. Furthermore, we need to include reflections of the modulation voltage at both ends of the TL if the impedance of the signal source $\underline{Z}_{\mathrm{src}}$ or the impedance of the termination $\underline{Z}_{\mathrm{trm}}$ are not matched to the characteristic impedance $\underline{Z}_0$ of the TL.

The frequency response $\underline{m}(\omega_{\mathrm{RF}})$ of the modulator is obtained by normalizing the complex phase amplitude $\hat{\underline{\varphi}}(\omega_{\mathrm{RF}})$ by its zero-frequency counterpart $\hat{\underline{\varphi}}(0)_{\underline{Z}_{\mathrm{src}}=\underline{Z}_{\mathrm{trm}}=\underline{Z}_0}$ for a perfectly matched impedance of the source and the termination [83]. This results in [80]

$$m(\omega_{RF}) = \frac{\hat{\varphi}(\omega_{RF})}{\hat{\varphi}(0)}\bigg|_{\underline{Z}_{src}=\underline{Z}_{trm}=\underline{Z}_0} = \underline{A}\underline{H}_{RC}\left(\frac{\exp(\underline{q}^-L)-1}{\underline{q}^-} + \underline{B}\frac{\exp(\underline{q}^+L)-1}{\underline{q}^+}\right), \quad (2.41)$$

where

$$\underline{A} = \frac{2}{L}\frac{\underline{Z}_0}{\underline{Z}_0+\underline{Z}_{src}}\frac{1}{1-\tilde{\underline{\Gamma}}_{src}\tilde{\underline{\Gamma}}_{trm}\exp(-2\underline{\gamma}L)}, \quad (2.42)$$

$$\underline{B} = \exp(-2\underline{\gamma}L)\tilde{\underline{\Gamma}}_{trm}, \quad (2.43)$$

$$\underline{q}^{\pm} = \pm\underline{\gamma} + jn_{g,opt}\omega_{RF}/c. \quad (2.44)$$

Here, $n_{g,opt}$ denotes the optical group refractive index in the slot waveguide, c is the vacuum speed of light and the quantities $\tilde{\underline{\Gamma}}_{src}$ and $\tilde{\underline{\Gamma}}_{trm}$ are voltage reflection factors at the source and the termination, respectively, given by

$$\tilde{\underline{\Gamma}}_{src} = \frac{\underline{Z}_{src}-\underline{Z}_0}{\underline{Z}_{src}+\underline{Z}_0} \quad \text{and} \quad \tilde{\underline{\Gamma}}_{trm} = \frac{\underline{Z}_{trm}-\underline{Z}_0}{\underline{Z}_{trm}+\underline{Z}_0}. \quad (2.45)$$

The term $\underline{H}_{RC}$ in Eq. (2.41) takes into account that only the fraction of the voltage, which drops across the slot waveguide contributes to the phase shift. The expression $\underline{H}_{RC}$ takes thus the form of a voltage divider between the slab conductance and the slot capacitance

$$\underline{H}_{RC} = \frac{1}{1+j\omega_{RF}C_S'/G_S'}. \quad (2.46)$$

In summary, the described model of the frequency response of SOH MZM takes into account the effects of velocity mismatch between optical and RF field, impedance mismatch, microwave-loss, and the *RC*-limitation of the silicon slot waveguide. Reference [80] gives an in-depth overview about the impact of these individual contributions and discusses the associated implications for design guidelines to realize ultra-broadband SOH modulators.

3   Efficient SOH modulators with ultra-high in-device EO activity

The following section reports on SOH modulators with ultra-high in-device EO activity, resulting in highly efficient EO modulation and low power consumption. It is taken from a publication in *Optica* [J1]. To fit the structure and layout of this document, it was adapted accordingly. The associated supplementary information is found in Appendix A.

For this publication Clemens Kieninger (Cl.K.) and Yasar Kutuvantavida (Y.K.) formulated the EO material and coated the SOH modulators. Cl.K. and Y.K. developed the poling recipe for the coated SOH modulators. Cl.K. optimized the poling conditions for the SOH devices and performed the π-voltage characterization as well as the electro-magnetic simulations required to calculate the in-device EO coefficient. Cl.K., Stefan Wolf, Heiner Zwickel, Matthias Blaicher, and Juned. N. Kemal performed and evaluated the high-speed data transmission experiments. Delwin L. Elder (D.L.E.) and Larry R. Dalton developed the EO material. D.L.E. performed ellipsometry measurements on thin-film samples of the EO material. The work was supervised by Sebastian Randel, Wolfgang Freude and Christian Koos (Ch.K.). The paper was written by Cl.K., and Ch.K. All authors revised the paper.

[start of paper [J1]]

Clemens Kieninger[1,2], Yasar Kutuvantavida[1,2], Delwin L. Elder[3], Stefan Wolf[1], Heiner Zwickel[1], Matthias Blaicher[1], Juned N. Kemal[1], Matthias Lauermann[1], Sebastian Randel[1], Wolfgang Freude[1], Larry R. Dalton[3] and Christian Koos[1,2]

[1] Karlsruhe Institute of Technology (KIT), Institute of Photonics and Quantum Electronics (IPQ), 76131 Karlsruhe, Germany

[2] Karlsruhe Institute of Technology (KIT), Institute of Microstructure Technology (IMT), 76344 Eggenstein-Leopoldshafen, Germany

[3] University of Washington, Department of Chemistry, Seattle, Washington 98195, USA

Efficient electro-optic (EO) modulators crucially rely on advanced materials that exhibit strong electro-optic activity and that can be integrated into high-speed and efficient phase shifter structures. In this paper, we demonstrate ultrahigh in-device EO figures of merit of up to $n^3 r_{33} = 2300$ pm/V achieved in a silicon-organic hybrid (SOH) Mach-Zehnder modulator (MZM) using the EO chromophore JRD1. This is the highest material-related in-device EO figure of merit hitherto achieved in a high-speed modulator at any operating wavelength. The π-voltage of the 1.5-mm-long device amounts to 210 mV, leading to a voltage-length product of $U_\pi L = 320$ Vμm – the lowest value reported for MZM that are based on low-loss dielectric waveguides. The viability of the devices is demonstrated by generating high-quality on-off-keying signals at 40 Gbit/s with Q factors in excess of 8 at a peak-to-peak drive voltage as low as 140 mV$_{pp}$. We expect that efficient high-speed EO modulators will not only have a major impact in the field of optical communications, but will also open new avenues towards ultrafast photonic-electronic signal processing.

3.1　Introduction

Electro-optic (EO) phase modulators are key for many applications such as optical communications [84], optical signal processing [85], or high-precision metrology [86]. Among the various concepts, devices based on the linear electro-optic effect (Pockels effect) are particularly powerful, providing pure phase modulation at high speed, thereby enabling the generation of high-quality optical data signals based on advanced modulation formats [16,87,88]. Pockels-effect modulators can be broadly subdivided in two categories: The first one comprises conventional devices, where optical waveguides are directly fabricated in crystalline or amorphous EO materials. This approach is used for, *e.g.*, LiNbO$_3$ devices [38], all-polymer modulators [89], or devices based on III-V compound semiconductors [90,91], which often exploit a combination of the Pockels effect and other phase modulation mechanisms such as the quantum-

confined Stark effect (QCSE) or the Franz Keldysh effect. More recently, a second category of devices has emerged, relying on hybrid integration approaches that combine Pockels-type EO materials with dielectric or plasmonic waveguide structures that do not feature any EO activity. This approach is often used to overcome the intrinsic lack of second-order nonlinearities in otherwise highly attractive material systems such as the silicon photonics platform. Examples of this category comprise the concepts of silicon-organic hybrid (SOH) [15,92,93] and plasmonic-organic hybrid (POH) [94–96] devices, that combine organic EO (OEO) materials with silicon photonic or plasmonic waveguide structures or other approaches that exploit hybrid combinations of lithium-niobate (LiNbO$_3$) thin films [97] or barium-titanate (BaTiO$_3$) layers [98] with silicon-on-insulator (SOI) waveguides.

In all of these cases, one of the most important design goals is to achieve high modulation efficiency, *i.e.*, large phase shifts for low operating voltages and small device lengths, along with low optical insertion loss. For Mach-Zehnder modulators (MZM), the modulation efficiency can be quantified by the product $U_\pi L$ of the phase shifter length L and the voltage U_π that is required to achieve a phase shift of π between the optical signals at the output of the MZM arms [15]. For Pockels-effect modulators based on dielectric waveguides, the lowest demonstrated $U_\pi L$-product amounts to 0.5 Vmm, achieved in an SOH device that combines a silicon photonic slot waveguide with the OEO chromophore DLD164 [99]. For plasmonic waveguides, even lower values down to $U_\pi L = 0.05$ Vmm can be achieved [100]. However, while these devices feature large electro-optic bandwidths [101], they suffer from intrinsic propagation losses, which limit the range of practical device lengths to a few tens of micrometers [15,100]. This effect can be quantified by the product $a U_\pi L$ which combines the π-voltage U_π, the phase shifter length L, and the waveguide propagation loss a measured in dB/mm. Previously demonstrated values of $a U_\pi L$ amount to 2.8 VdB for SOH devices [99], indicating that a phase shifter section with length L and insertion loss $aL = 1$ dB requires an operating voltage of 2.8 V for a phase shift of π. For the previously mentioned POH devices [100], this number amounts to 25 VdB.

In principle, all these performance parameters can be improved by using Pockels-type materials that feature strong electro-optic activity, quantified by

large EO figures of merit n^3r, where n is the refractive index and r the EO coefficient. However, it is equally important that the materials offer good processing properties and allow easy application to efficient and high-speed phase shifter structures such as slot waveguides. The importance of fulfilling both requirements may be illustrated by the example of silicon-based $BaTiO_3$ modulators: These devices exhibit record-high in-device EO figures of merit of up to $n^3r = 3200$ pm/V [98,102], but feature rather high voltage-length products in excess of $U_\pi L = 13.5$ Vmm. Moreover, $BaTiO_3$ modulators still suffer from low modulation speeds, with highest data rates below 1 Gbit/s [102]. The limited performance of these devices is directly linked to the complexity of the growth process of crystalline $BaTiO_3$, which can only be used in combination with rather simple phase shifter structures based on conventional strip waveguides.

In contrast to that, OEO materials are widely applicable and compatible to a wide variety of integration platforms and device structures, enabling high-speed modulators with record performance parameters [18,81,103,104] and data rates of up to 400 Gbit/s [16]. The materials can be easily spin-coated, micro-dispensed or printed in high-throughput processes. For devices based on OEO materials, the largest in-device EO figure of merit reported so far amounts to $n^3r_{33} = 1220$ pm/V $(n^3r_{33} = 2040$ pm/V$)$ at a wavelength of $\lambda_0 = 1.55$ µm $(\lambda_0 = 1.25$ µm$)$, achieved for an organic binary-chromophore compound in a POH modulator [105].

Here we demonstrate that even higher EO figures of merit of up to $n^3r_{33} = 2300$ pm/V at $\lambda_0 = 1.55$ µm can be achieved. The results were obtained in an SOH modulator that uses the organic EO material JRD1 [41] as a cladding. To the best of our knowledge, this is the highest in-device EO figure of merit ever achieved in a high-speed Pockels-type modulator at any operation wavelength. The devices feature $U_\pi L$-products down to 0.32 Vmm – the lowest value ever achieved for a modulator based on low-loss dielectric waveguides. We measure a $aU_\pi L$-product of 1.2 VdB, which is on par with the lowest values reported so far [91]. The viability of the device is demonstrated by generation of on-off-keying (OOK) signals at a data rate of 40 Gbit/s. For a peak-to-peak operation voltage as low as $U_{pp} = 140$ mV$_{pp}$, we obtain high-quality signals with measured Q factors in excess of 8.

3.2   SOH modulator concept and material design

The concept of an SOH phase shifter is depicted in Figure 3.1(a). The device comprises a silicon (Si) slot waveguide formed by two 240 nm wide and 220 nm high Si rails that are separated by a narrow slot, which is filled by the OEO material. An electrical connection between the Si rails and the aluminum (Al) transmission lines is achieved by 70 nm high doped Si slabs and Al vias. Both optical and RF field are tightly confined in the slot region, leading to a strong modal overlap in the OEO material and hence to highly efficient phase modulation. The waveguide structures are fabricated on standard silicon-on-insulator (SOI) wafers in a commercial silicon photonic foundry process using standard 248 nm deep-UV (DUV) lithography. As an OEO cladding, we use the

neat chromophore material JRD1 [41], which is locally deposited on the slot waveguides in a dedicated post-processing step. The molecular structure of JRD1 is displayed in Figure 3.1(b). The material is the result of theory-guided optimization of the previously used OEO chromophore YLD124 [104]. Both materials share common donor and acceptor groups that are separated by a π-conjugated bridge. Due to this common chromophore core, both materials show a very similar molecular hyperpolarizability [106]. However, JRD1 features bulky phenyl side groups denoted as R_1 in Figure 3.1(b), rather than methyl groups as used in YLD124. The bulkier side groups significantly increase the intermolecular distance of neighboring chromophores, which reduces the strength of detrimental dipole-dipole interactions that promote centrosymmetric pairing of chromophores [107]. As a result, JRD1 chromophores can be used in high number densities without a polymer host [107], while still maintaining high molecular mobility during electric-field poling and avoiding unwanted centrosymmetric pairing of chromophores. This leads to large EO figures of merit of $n^3 r_{33} = 3850$ pm/V in bulk samples of JRD1 [41] – more than a 2-fold increase compared to YLD124 [41]. Note that the glass-transition temperatures of JRD1 ($T_g = 82°C$) and YLD124 ($T_g = 81°C$) are comparable [42]. For the JRD1-coated SOH modulator presented in this work, thermally induced relaxation of the chromophore orientation at room temperature does not impair the device performance significantly: A π-voltage increase of about 5% was recorded one week after the poling of the device. Thermal relaxation is most

Figure 3.1: Concept of a silicon-organic hybrid (SOH) phase shifter. **(a)** Device principle. The phase shifter comprises a Si slot waveguide formed by a pair of Si rails. The slot is filled with an organic electro-optic (OEO) material. The rails are electrically connected to an aluminum (Al) transmission line via doped Si slabs and Al vias, such that an externally applied voltage U_d drops entirely across the narrow slot. At the same time, the optical mode is tightly confined to the OEO material in the slot, resulting in highly efficient phase modulation. **(b)** Molecular structure of the employed OEO material JRD1 and of the previously used material YLD124 [104]. Compared to YLD124, JRD1 features bulky phenyl side groups denoted as R_1, which decrease inter-molecular interactions and thus increase molecular mobility during electric-field poling. This is instrumental for achieving ultra-high in-device EO activity.

pronounced during the first few hundred hours [20,108], and a much weaker growth of U_π is expected for longer storing times. Thermal stability at elevated temperatures without significant impairment of the EO activity can be achieved by modifying the material JRD1 with crosslinking agents which enable post-poling lattice hardening. This approach has led to similar classes of OEO materials with a T_g of up to 250°C [109].

Note that the field enhancement of the optical mode in the silicon photonic slot waveguide leads to high intensities, which may damage the electro-optic chromophores. However, this effect is directly linked to the presence of oxygen in the material. It was previously reported that photo degradation can be

prevented operating the device in an oxygen-free atmosphere [19,20]. This can be achieved by appropriate sealing techniques.

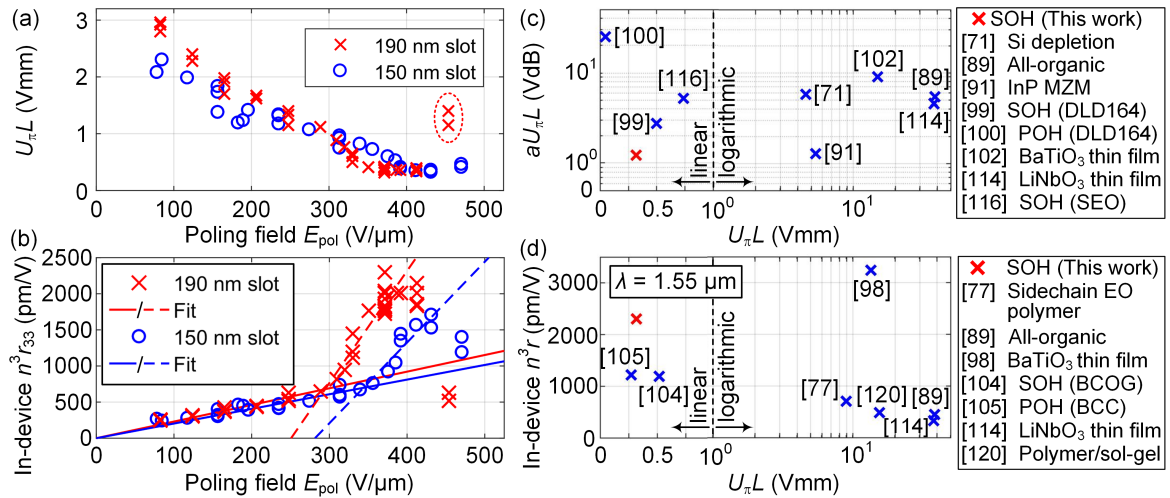## 3.3   Device preparation and characterization

For our experimental demonstration, we use Mach-Zehnder type SOH modulators rather than the phase modulator shown in Figure 3.1(a). The concept of an SOH Mach-Zehnder modulator (MZM) is schematically depicted in Figure 3.2(a). The coplanar transmission line is realized in a ground-signal-ground (GSG) configuration. Light is coupled to and from the chip via grating couplers (GC), and a multi- mode interference coupler (MMI) is used to split and combine the light of the two arms of the MZM. Figure 3.2(b) shows a cross-section of the two MZM arms at the position indicated by the dash-dotted line A-A' in Figure 3.2(a). Each MZM arm comprises an SOH phase shifter with a JRD1 cladding. The material is deposited in solution, thus the EO chromophores are randomly oriented after deposition. An average acentric orientation and thus a macroscopic EO effect is obtained by a one-time electric-field poling process [56]. To this end, the chip is heated close to the glass-transition temperature of JRD1 ($T_g = 82°C$), and a DC poling voltage U_{pol} is then applied across the floating ground electrodes, inducing an electric poling field E_{pol} (green arrows) in the EO material which aligns the dipolar chromophores. This order is frozen by cooling the device to room temperature while maintaining the poling field. The device enables simple push-pull-operation: An RF voltage applied to the GSG transmission line of the MZM induces electric fields in the slots (red arrows) that are parallel to the orientation of the EO chromophores (green arrows) in the right arm and antiparallel in the left arm of the MZM.

The modulation speed of SOH devices may be limited by various aspects such as walk-off between the microwave drive signal and the optical wave, frequency-dependent RF transmission line loss, or *RC* limitations. Based on previous investigations of very similar devices [70], we expect resistance-capacitance (RC) limitations as the dominant effects, originating from the fact that the slot acts as a capacitor which has to be charged and de-charged via the thin doped silicon slabs. To increase the bandwidth of the device, the resistivity of the doped silicon slabs can be decreased by generating an electron
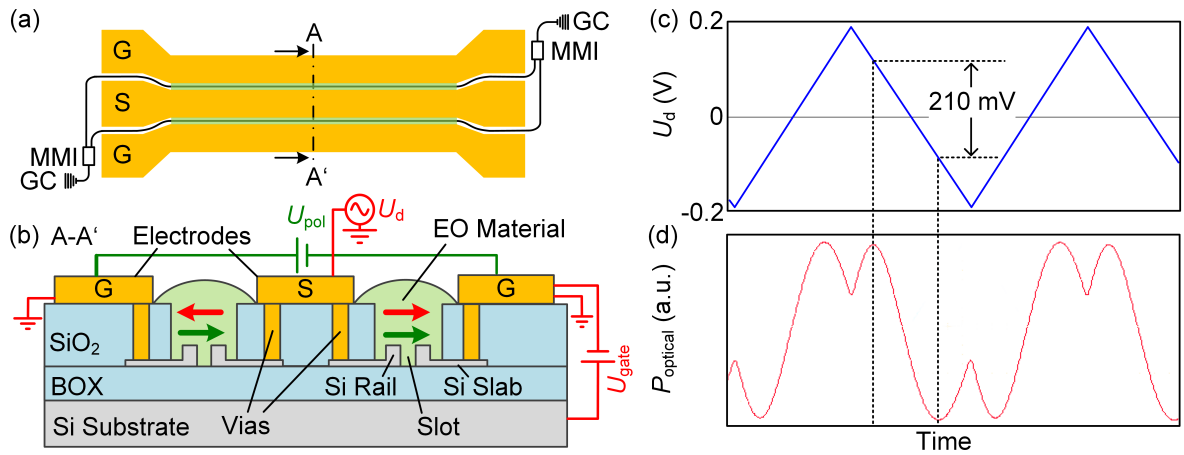
Figure 3.2: Schematic of an SOH MZM and measurement of U_π. **(a)** Top view. Light is coupled to and from the device via grating couplers (GC). The coplanar transmission line is arranged in a ground-signal-ground (GSG) configuration. A pair of multi-mode interference (MMI) couplers is used to split and recombine the light of the two MZM arms. **(b)** Cross section of the two arms of the SOH MZM at the position defined by the dash-dotted line A-A' in (a). Each arm comprises an SOH phase shifter. A one-time poling process is required to achieve a macroscopic in-device r_{33} after deposition of the EO chromophores from solution. To this end, a poling voltage U_{pol} is applied across the floating ground electrodes at elevated temperature close to $T_g = 82°C$, thereby inducing an electric poling field (green arrows) in the slot regions. The dipoles of the EO material align along the poling field in acentric order. After cooling the device down to room temperature, U_{pol} is removed and the acentric order of the chromophores is conserved. For modulation, a radio-frequency (RF) signal voltage U_d induces electric fields in the slots (red arrows) that are antiparallel (parallel) to the aligned chromophores in the left (right) arm of the MZM, thereby realizing push-pull operation. The bandwidth of the modulator can be increased by decreasing the resistance of the silicon slab. This is achieved by applying a gate voltage U_{gate} between the silicon substrate and the ground electrodes. **(c)** Low-speed triangular drive signal for the static U_π measurement as a function of time. **(d)** Over-modulated optical signal as a function of time when the modulator is fed by the waveform depicted in (c). The MZM is biased in its quadrature point and the π-voltage U_π can be directly read from the voltage increment needed to drive the device from minimum to maximum transmission. For the depicted measurements, we extract a π-voltage of 210 mV, corresponding to a π-voltage-length product of $U_\pi L = 0.32$ Vmm.

accumulation layer [81]. In the experiment, this is realized by applying a gate voltage U_{gate} between the Si substrate and the ground electrode. For the 1.5 mm-long devices used in our experiments, we have measured the electro-optic bandwidth at an externally applied gate field of 0.09 V/nm, leading to a 6 dB bandwidth of approximately 43 GHz. This bandwidth can be improved by further increasing the conductivity of the thin silicon slabs, which can, *e.g.*, be achieved by increasing the doping concentration in these regions. To quantify the modulation efficiency, we measure the static π-voltage of the device, see

Figure 3.3: Electro-optic characterization and benchmarking of the SOH MZM. **(a)** Measured $U_\pi L$-product as a function of the poling field E_{pol}. Two sets of devices are investigated: Red crosses correspond to samples with slot widths of 190 nm, and blue circles indicate slot widths of 150 nm. The $U_\pi L$-product decreases for an increasing poling field, levels off, and rises again. The rise is attributed to the onset of conductance, possibly in combination with dielectric breakdown, which may cause permanent damage of the affected chromophores. This is confirmed by the fact that the samples indicated by the large red ellipse do not recover typical EO activity when re-poling at moderate fields of 200 V/µm is attempted. The minimum $U_\pi L$ product amounts to 0.32 Vmm for both sample geometries. **(b)** Calculated $n^3 r_{33}$ as a function of E_{pol}. Red crosses (blue circles) indicate samples with slot widths of 190 nm (150 nm). For both data sets, $n^3 r_{33}$ increases linearly with the poling field and features a steep increase in slope once a certain threshold poling field is exceeded. The behavior below (above) the threshold poling field is visualized by the red and blue solid (dashed) lines obtained from least square fits to linear functions. The drop of $n^3 r_{33}$ at even higher poling fields is attributed to the onset of conductance in the OEO material, possibly in combination with dielectric breakdown. The threshold effect may be explained by surface-chromophore interactions leading to alignment of chromophores along the slot sidewalls – this aspect is subject to theoretical investigations. The maximum $n^3 r_{33}$ amounts to 2300 pm/V and is obtained for a slot width of 190 nm. Devices with 150 nm wide slots feature systematically lower values of $n^3 r_{33}$, which is attributed to a stronger influence of surface effects in narrower slots. **(c)** Measured $a U_\pi L$-product as a function of the $U_\pi L$-product for various modulator concepts. The abscissa exhibits a linear scale for $U_\pi L < 1$ Vmm and a logarithmic scale for $U_\pi L \geq 1$ Vmm. Indicated by the proximity to the origin of the figure, SOH MZMs combine low voltage-length products with low losses, and hence compare favorably with competing modulator concepts. The device presented in this work shows a $U_\pi L$ of 0.32 Vmm and an $a U_\pi L$ of 1.2 VdB. Only POH modulators offer a lower $U_\pi L$-product of 0.05 Vmm, which comes, however, at the price of an increased $a U_\pi L$-product of 25 VdB **(d)** In-device EO figure of merit $n^3 r$ as a function of $U_\pi L$ for competing material platforms for integrated EO modulators. The abscissa exhibits a linear scale for $U_\pi L < 1$ Vmm and a logarithmic scale for $U_\pi L \geq 1$ Vmm. It can be seen that slot waveguide modulators based on organic EO materials offer highest efficiency: Although the in-device EO figures of merit achieved in SOH and POH devices are lower compared to BaTiO$_3$ modulators, the achieved $U_\pi L$-products are almost two orders of magnitude smaller. Note that for all depicted devices except the BaTiO$_3$ modulator, the coefficient r in $n^3 r$ refers to the r_{33} element of the corresponding EO tensor. For the BaTiO$_3$ device an effective EO coefficient which neglects the tensor nature is used since individual tensor components could not be measured. All values given in (d) refer to an operating wavelength of 1550 nm.

Appendix A for details on the experimental setup. A low-frequency triangular waveform obtained from a function generator (FG) is applied to the signal electrode of the SOH MZM, which is fed by an optical CW signal at a wavelength of 1550 nm through an on-chip grating coupler. The modulated optical signal is detected by a low-speed photodiode (PD). Both, the output of the FG (blue curve) and the output of the PD (red curve) are recorded simultaneously by an oscilloscope, see Figure 3.2(c) and (d). The modulator is biased in its quadrature point, and the peak-to-peak drive voltage amplitude is chosen larger than the π-voltage such that the MZM is over-modulated. The π-voltage then corresponds to the voltage difference needed to drive the MZM from its minimum to its maximum transmission point.

For achieving high electro-optic activity, one of the essential parameters is the applied electric poling field E_{pol}. In our experiments, we systematically varied this parameter and measured the resulting $U_\pi L$-product for two different sets of devices having slot widths of 190 nm and 150 nm. The experimental results are summarized in Figure 3.3(a), where red crosses (blue circles) correspond to slot widths of 190 nm (150 nm). For both sets of devices, the measured $U_\pi L$-products first decrease with increasing E_{pol}, then level off, and finally rise again. The rise is attributed to the onset of conductance, possibly in combination with dielectric breakdown. This can inflict permanent damage of the material, which is found by attempting to re-pole the two devices indicated by the red ellipse. In the re-poling experiment, we use moderate poling fields of 200 V/µm, leading to measured $U_\pi L$-products of 3.5 Vmm and 4.0 Vmm. This is much worse than the values of approximately 1.7 Vmm that are typically achieved for this poling field. For both sets of devices, the lowest measured $U_\pi L$-product amounts to 0.32 Vmm, which was achieved at poling fields of 370 V/µm (430 V/µm) for the 190 nm (150 nm) slots. To the best of our knowledge this is the lowest value of $U_\pi L$ hitherto demonstrated for a non-resonant device based on low-loss dielectric waveguides. The propagation loss of the phase-shifter section amounts to about 3.9 dB/mm, see Appendix A.2, leading to an $aU_\pi L$ value of 1.2 VdB. This is on par with ultra-low $aU_\pi L$ values of 1.3 VdB achieved for advanced InP-based phase modulators, which combine a rather large $U_\pi L$-product of 5.4 Vmm with a very low on-chip propagation loss of 2.4 dB/cm [91].

Using the simulated fields of the optical and the radio frequency (RF) mode of the device, the measured $U_\pi L$-product in Figure 3.3(a) can be linked to the in-device EO figure of merit $n^3 r_{33}$, see Appendix A.3 for a derivation of the corresponding mathematical relations. The results are shown in Figure 3.3(b), where the calculated $n^3 r_{33}$ is plotted versus the applied poling field. The red crosses and blue circles correspond again to devices having slot widths of 190 nm and 150 nm, respectively. Remarkably, when increasing the poling field, $n^3 r_{33}$ does not exhibit a linear increase with a single slope, as typically observed [110]. Instead, both data sets show a steep increase in slope once a certain threshold poling field is exceeded. To illustrate the two distinctively different poling regimes, we fit a linear function to the measured $n^3 r_{33}$ values below (solid line) and above (dashed line) the threshold poling field. At very high poling fields, we observe a roll-off and finally a drop of $n^3 r_{33}$, which is attributed to the onset of conductance, possibly in combination with dielectric breakdown. These data points are omitted for the linear fit. The unusual dependency of $n^3 r_{33}$ on E_{pol} is still under investigation. It may be explained by chromophore interactions at surfaces - recent simulations have shown that chromophores at the sidewalls of POH slot waveguides align in parallel to these sidewalls and do not contribute to the EO activity [100]. As a consequence, poling is only effective at a sufficient distance from the surface, *i.e.*, in the center of the slot region, where the chromophores are initially randomly oriented and become aligned during poling. Most likely, similar effects are present in SOH slot waveguides. It is conceivable that for sufficiently large poling fields, a threshold is reached that triggers the reorientation of chromophores at the sidewalls, leading to a steeper slope of $n^3 r_{33}$. For a better understanding of the underlying mechanisms, further investigations are required and will be subject to a joint theoretical and experimental effort in the near future. To the best of our knowledge the effect has never been reported so far. We attribute this to the fact that in typical sample geometries the maximum applicable poling field is restricted to 100-200 V/µm before dielectric breakdown occurs [109,111,112]. This is well below the threshold poling field observed in our study. The outstanding stability against dielectric breakdown in SOH devices was already observed in previous experiments where fields above 300 V/µm could be applied without dielectric breakdown [104]. This was attributed to the low number of defects in the EO material filling the nano-scale slot. The maximum

calculated n^3r_{33} is achieved for a sample with slot width of 190 nm and amounts to (2300 ± 170) pm/V. This result represents not only the highest material-related in-device EO figure of merit for organic EO materials at any operating wavelength but also the highest in-device EO figure of merit ever achieved in a high-speed Pockels-type modulator. Devices with slot widths of 150 nm show systematically smaller values of n^3r_{33}. The largest value achieved amounts to only (1700 ± 170) pm/V. We attribute this to an even higher fraction of chromophores near the surface than in the center of the slot, which limits the EO activity. The specified error bounds are dominated by the uncertainties of the slot width measurement and the refractive index of JRD1 in the nanoscopic slot waveguide, see Figure A.5 and the corresponding discussion in Appendix A.5. In principle, if the refractive index of the EO material is known, the in-device EO coefficient r_{33} can be calculated from the in-device EO figure of merit n^3r_{33}. If we assume the estimated in-device refractive index of JRD1 of $n = 1.81$ we obtain an EO coefficient $r_{33} = 390$ pm/V for the device with 190 nm wide slot, see Appendix A.4. However, this value has to be taken with caution, since the refractive index is subject to large uncertainties which are related to birefringence caused by poling-induced chromophore alignment and surface interaction with the sidewalls of the slot waveguide, see Appendix A.5.

Note that, for a slot width of 190 nm, the reported value of the in-device n^3r_{33} is close to the value reported on bulk JRD1 [41] when taking into account the wavelength dependency of n^3r_{33}. It is hence unlikely that increasing the slot width further will lead to a significant increase of the in-device n^3r_{33}. Additionally, larger slot widths would lead to decreased optical-electrical interaction, see Figure A.4 in Appendix A, and a smaller RF drive field strength for a given drive voltage. Accordingly, despite the reduced n^3r_{33}, the MZMs with 150 nm slots exhibit the same value for $U_\pi L$ as the devices with 190 nm slots, see Figure 3.3(a): The devices with narrow slot width exhibit higher drive field strengths as well as a larger overlap of the optical and RF mode, which results in a more efficient modulation and compensates the reduced n^3r_{33}. Note that the threshold effect is less visible in the measurement of the $U_\pi L$-product in Figure 3.3(a) due to the inverse relation of n^3r_{33} and $U_\pi L$.

For a benchmarking of the presented performance parameters of the SOH MZM, we plot the loss-efficiency product $aU_\pi L$ as a function of the voltage-

length product $U_\pi L$ for competing state-of-the-art EO modulators, which are based on various concepts and technologies. The results are shown in Figure 3.3(c) for an operating wavelength of 1.55 µm, unless stated otherwise. Note that the abscissa features a linear scale for $U_\pi L < 1$ Vmm and a logarithmic scale for $U_\pi L \geq 1$ Vmm. Ideal devices combine low values of $U_\pi L$ with low losses and hence low $aU_\pi L$-products, to be found in the lower left-hand corner of the plot, close to the origin. Besides Pockels-effect modulators, the comparison in Figure 3.3(c) also includes selected high-speed InP and silicon-based depletion-type devices. In the future, this group might be complemented by highly efficient accumulation-type devices [73,113], which are currently still subject to limited EO modulation bandwidth of a few gigahertz.

The comparison in Figure 3.3(c) shows that modulators fabricated on the thin-film LiNbO₃ platform [114] as well as all-organic modulators [89] feature comparatively high $U_\pi L$-products in excess of 38 Vmm, but show also low propagation losses. Hence, despite their large footprint, these devices exhibit moderate $aU_\pi L$-products of around 5 VdB. For the novel BaTiO₃-on-Si platform, MZMs with lower $U_\pi L$-product of 15 Vmm have been demonstrated [102]. While previous device generations suffered from pronounced propagation losses in excess of 4.5 dB/mm, passive waveguides with losses of only 0.6 dB/mm were demonstrated recently [115], potentially leading to loss-efficiency products of $aU_\pi L = 9$ VdB. State-of-the-art depletion-type Si MZM with U-shaped pn junctions operated at 1310 nm show more efficient modulation with $U_\pi L$-products of 4.6 Vmm and reduced $aU_\pi L$-products down to 5.8 VdB [71]. Similar π-voltage-length products of $U_\pi L = 5.4$ Vmm are achieved in indium phosphide (InP) based MZM [91]. At the same time, these devices show significantly reduced propagation losses as compared to silicon-based depletion-type modulators, leading to very low $aU_\pi L$ values of only 1.3 VdB. SOH MZM stand out due to their low $U_\pi L$-products of 0.74 Vmm [116] and 0.5 Vmm [99], obtained by the commercial OEO material SEO100 and by the even more efficient neat chromophore DLD164, respectively. However, the propagation losses of SOH slot waveguides are also higher than the losses of advanced InP waveguides, leading to $aU_\pi L$-products of 5 VdB and 2.8 VdB for the two EO materials. The SOH modulators presented in this work outperform these devices by exhibiting $U_\pi L$-products as low as 0.32 Vmm and a propagation loss of about 3.9 dB/mm, which results in a $aU_\pi L$-product of

1.2 VdB. This is on par with the $aU_\pi L$-product of advanced InP modulators, which feature significantly higher $U_\pi L$-products. The $U_\pi L$-products of POH modulators are even smaller than those of SOH devices, with published values down to 0.05 Vmm [100] when the OEO material DLD164 is employed. However, the small $U_\pi L$-products come at the price of increased propagation losses in the plasmonic slot waveguides, which is reflected in the increased loss-efficiency product of typically $aU_\pi L = 25$ VdB. Hence, in comparison to all other devices, the SOH modulator presented in this work comes closest to the origin, indicating an ideal combination of high modulation efficiency and low propagation loss of the dielectric waveguide structure. We hence expect that the SOH concept will have major impact on future implementations of optical communication systems and may also open new opportunities in ultra-fast photonic-electronic signal processing, where highly efficient low-loss devices can, *e.g.*, enable advanced electro-optic sampling. SOH devices have previously been demonstrated to enable high-speed coherent [117,118] and non-coherent [17,18] transmission with single-polarization line rates of up to 400 Gbit/s (100 GBd 16QAM) [16].

In Figure 3.3(d) we plot the in-device EO figure of merit n^3r versus $U_\pi L$ for state-of-the-art Pockels-effect EO modulators. For all depicted devices except the BaTiO$_3$ modulator, the EO coefficient r refers to the r_{33} element of the corresponding EO tensor. For the BaTiO$_3$ device, the tensor components could not be measured individually due to the poly-domain structure of the thin film. Instead, r was estimated as an effective EO coefficient by neglecting the tensor nature [98]. Note that the in-device EO figures of merit n^3r depicted in Figure 3.3(d) are purely material-related and do not comprise additional enhancements that can, *e.g.*, be achieved through slow-light structures [119]. For a better comparison between different EO materials, we examine only the values obtained at the standard telecommunication wavelength of 1550 nm. Note that n^3r is in general wavelength-dependent and usually increases towards smaller wavelengths.

Due to the inverse relation of $U_\pi L$ and n^3r, the lowest value for $U_\pi L$ is expected for the largest n^3r. However, $U_\pi L$ additionally depends on the efficiency of the phase shifter geometry, the limits of which are determined also by the EO material processing technology.

The first class of EO modulators is based on crystalline materials, for which the implementation on well-established photonic platforms such as Si photonics was considered challenging and cumbersome. Recently, however, thin films of $LiNbO_3$ were fabricated and bonded to various substrates such as SOI wafers [97]. In this approach, the EO properties of bulk $LiNbO_3$ can be maintained, leading to devices with EO figures of merit of $n^3 r_{33} = 330$ pm/V [114] and with moderate π-voltage-length products of $U_\pi L = 38$ Vmm. The so far highest in-device EO figure of merit of $n^3 r = 3200$ pm/V is realized on the hybrid $BaTiO_3$-on-SOI platform [98]. Here, the crystalline $BaTiO_3$ is grown by a sophisticated molecular beam epitaxy process, which requires simple phase shifter structures and results in moderate π-voltage-length products of $U_\pi L = 13.5$ Vmm. Much simpler processing is achieved with OEO materials, which additionally open the possibility of theory-guided molecular design for tailoring the optical properties. All-polymer modulators reach $n^3 r_{33} = 450$ pm/V [89] when implemented in rather inefficient low index-contrast EO waveguides featuring $U_\pi L = 38$ Vmm. More efficient modulation with $U_\pi L$-products down to 15.6 Vmm is realized in hybrid polymer/sol-gel modulators [120]. This is on par with $BaTiO_3$ modulators, while the EO figure of merit $n^3 r_{33} = 490$ pm/V is almost an order of magnitude smaller. This again indicates the advantages of OEO modulator concepts. Modulators based on ultra-thin silicon waveguides clad in thermally stable side-chain EO polymers reach $n^3 r_{33} = 710$ pm/V [77], which decreases the π-voltage-length product to 9 Vmm. The highest $n^3 r_{33}$ for an SOH modulator so far was achieved with the binary chromophore organic glass (BCOG) PSLD41/YLD124 and amounts to $n^3 r_{33} = 1200$ pm/V [104], resulting in a $U_\pi L$-product down to 0.52 Vmm. The largest in-device EO figure of merit for a POH modulator amounts to $n^3 r_{33} = 1220$ pm/V, and is achieved for a binary chromophore composite (BCC) [105]. The π-voltage-length product amounts to $U_\pi L = 0.28$ Vmm and is significantly higher than the one reported in [100] since a wider slot width of 200 nm was used. Note that the efficiency of the POH phase shifter concept comes at the price of an increased propagation loss, see Figure 3.3(c). The SOH modulator presented in this work features an in-device EO figure of merit of $n^3 r_{33} = 2300$ pm/V and an $U_\pi L$-product of only 0.32 Vmm.

In general, due to the strongly dispersive nature of both the EO coefficient and the refractive index, the EO figure of merit can be further increased when the

operating wavelength shifts closer to the absorption maximum of the EO material. As an example, for the POH modulator discussed in [105] the in-device $n^3 r_{33}$ increased by roughly 50 % when the device was operated closer to the absorption maximum of the EO material. Similarly, a significantly higher in-device $n^3 r_{33}$ can be obtained if we operate the presented SOH modulator closer to the absorption maximum of JRD1. For example, for an operation wavelength in the O-band, we expect an in-device EO figure of merit of approximately 4000 pm/V, which even exceeds the EO figure of merit achieved in bulk JRD1 samples at 1310 nm [41].

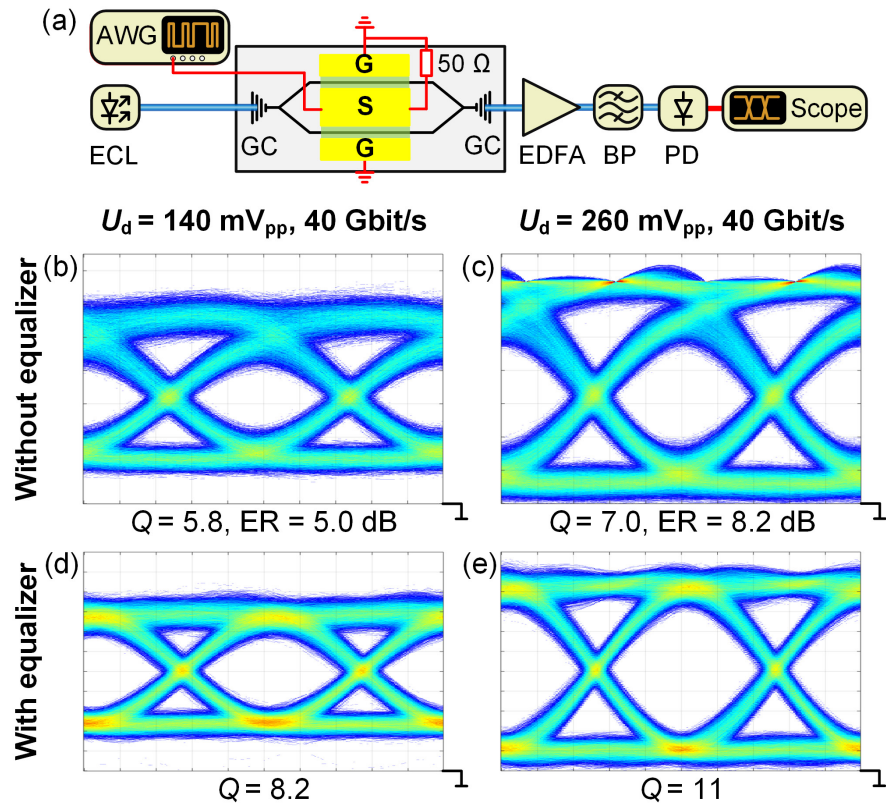## 3.4   Data transmission experiment

To demonstrate the viability of the SOH MZM for high-speed data transmission, we generate on-off-keying (OOK) signals at data rates of 40 Gbit/s. The experimental setup is shown in Figure 3.4(a). A pseudo random bit sequence of length 2^{15}-1 at 40 Gbit/s is obtained from an arbitrary waveform generator (AWG) and applied to the device by a microwave probe without further amplification. The MZM is biased at its quadrature point and terminated by an external 50 Ω impedance in order to reduce reflections of the RF field.

An erbium-doped fiber amplifier (EDFA) after the MZM amplifies the optical signal to a constant power of 8 dBm. A 0.6 nm bandpass filter (BP) is used to suppress the amplified spontaneous emission noise of the EDFA. The optical signal is then detected by a high-speed photodiode and a real-time oscilloscope. The oscilloscope features a memory size of 2 Gpts and a sampling rate of 80 GSa/s, which results in a maximum recording time of 25 ms. For a data rate of 40 Gbit/s, this corresponds to a maximum number of 1×10^9 recorded bits. We are hence limited to measuring a bit error ratio (BER) of BER $\geq 10^{-8}$ [121]. In contrast to that, the Q factors of the recorded eye diagrams indicate BER values below this limit. Therefore we use the Q factor to characterize and compare the signal quality across the various signaling experiments.

The total fiber coupling losses amount to 8.9 dB, and the optical on-chip insertion loss of the MZM adds another 8.2 dB. The on-chip losses are caused by non-ideal MMI-couplers, lossy Si strip waveguides and strip-to-slot converters. The Si slot waveguide propagation losses amount to about

3.9 dB/mm and are mainly attributed to the sidewall roughness of the slot. It can hence be assumed that more advanced lithography processes will allow to further reduce these losses in the future. In fact, it has been already shown that asymmetric strip-loaded Si slot waveguides with propagation losses as low as 0.2 dB/mm can be realized [122].

The device used for the data transmission experiment features a U_π of 270 mV. In the following experiments we use 130 µs-long recordings, containing roughly 5×10^6 symbols. Without any equalization and for a peak-to-peak drive voltage of 140 mV$_{pp}$, we obtain a measured Q factor of 5.8, see Figure 3.4(b). The energy consumption amounts to 2.5 fJ/bit and is dominated by the power dissipation in the 50 Ω terminating resistor. Operating the device without the terminating resistor, i. e., as a purely capacitive load as in [99], would further reduce the energy consumption. In this case, bandwidth is traded for energy consumption. Note that, since the drive voltage is below the actual U_π of the device (270 mV), the extinction ratio of 5 dB (ER = 3.2) as measured from the eye diagram is moderately high, leading to a power penalty of $10 \log_{10}((ER+1)/(ER-1)) = 2.8$ dB These numbers can be improved by increasing the drive voltage, which increases the extinction ratio and the modulation amplitude at the output, but not the modulation loss. The eye diagram without equalization and for a peak-to-peak drive voltage of 260 mV$_{pp}$ is depicted in Figure 3.4(c). It shows a wider opening with a measured Q factor of 7.0. The energy consumption amounts to 8.5 fJ/bit. The extinction ratio increases to 8.2 dB with a reduced power penalty of only 1.3 dB. This is on par with silicon pn modulators operating at the same symbol rate, where extinction ratios in the range of (7…10) dB are achieved [123–125]. However, the $U_\pi L$-product for the SOH modulator is at least an order of magnitude smaller than for pn modulators with a comparable extinction ratio. Note that the static extinction ratio is typically 20 dB to 25 dB higher than the measured one for 40 Gbit/s OOK. This is due to inter-symbol interference caused by the limited modulator bandwidth, and by detected optical noise. The high static extinction ratios in excess of 30 dB are also key to ensure low-chirp operation of push-pull MZM [126]. In general, static extinction ratios of better than 30 dB lead to a chirp parameter $\alpha^{(c)} \leq 0.1$, assuming perfect push-pull operation. This estimation is in good accordance with direct chirp measurements of similar

Figure 3.4: Data transmission experiments. **(a)** Schematic of the experimental setup. Signals obtained from an arbitrary waveform generator (AWG) are fed to the MZM via microwave probes. The optical carrier provided by an external-cavity laser (ECL) is coupled to and from the chip by grating couplers (GC). The modulated light is amplified by an erbium doped fiber amplifier (EDFA), filtered using a band pass filter (BP), and detected by a high-speed photodiode (PD) connected to a real-time oscilloscope for recording eye diagrams. **(b)** Measured eye diagram at 40 Gbit/s for a peak-to-peak drive voltage of 140 mV_{pp} without equalization. The measured Q factor amounts to 5.8 and the extinction ratio (ER) amounts to 5.0 dB. **(c)** Measured eye diagram at 40 Gbit/s for a peak-to-peak drive voltage of 260 mV_{pp} without equalization. Both the Q factor and the ER are increased and amount to 7.0 and 8.2 dB, respectively. **(d)** Measured eye diagram at 40 Gbit/s for a peak-to-peak drive voltage of 140 mV_{pp} after equalization. From the measured Q factor of 8.2 we estimate a bit error ratio (BER) of 1×10^{-16}. **(e)** Measured eye diagram at 40 Gbit/s for a peak-to-peak drive voltage of 260 mV_{pp} after equalization. We measure a high Q factor of 11.

SOH devices [18] and compares favorably with typical pn modulators featuring chirp parameters in the range of 0.8 [74].

The signal quality of the recordings shown in Figure 3.4(b) and (c) can be improved by an adaptive filter at the receiver to equalize the detected signals. The filter takes into account the frequency response of the whole signal path

including the AWG, the RF cables, the microwave probes, the SOH modulator, the photodiode, and the oscilloscope. The resulting eye diagrams are shown in Figure 3.4(d) and Figure 3.4(e) for peak-to-peak drive voltages of 140 mV_{pp} and 260 mV_{pp}, respectively. For the 140 mV_{pp} recording, we obtain a measured Q factor of 8.2. Assuming that after equalization the inter-symbol interference is negligible and that the signal is impaired by additive white Gaussian noise only, this Q factor would lead to a calculated BER of 1×10^{-16}, which is well below the 10^{-9} limit for error-free transmission. To the best of our knowledge, 140 mV_{pp} is the smallest peak-to-peak drive voltage ever reported for a system demonstration that achieves comparable Q factors at 40 Gbit/s. For the peak-to-peak drive voltage of 260 mV_{pp} we achieve an even better signal quality with a measured Q factor of 11.

3.5   Summary and Outlook

We demonstrate a silicon-organic hybrid (SOH) Mach-Zehnder modulator (MZM) featuring an ultra-high in-device electro-optic (EO) figure of merit of $n^3 r_{33} = 2300$ pm/V by employing the highly efficient EO chromophore JRD1. This is the highest material-related value ever achieved in a high-speed Pockels-type modulator at any operating wavelength. The reported $n^3 r_{33}$ is a factor of two larger compared to previously published values for SOH or plasmonic-organic hybrid (POH) modulators operating at the same wavelength of 1550 nm [104,105]. The devices feature ultra-small voltage-length products down to $U_\pi L = 0.32$ Vmm along with loss-efficiency products of $a U_\pi L = 1.2$ VdB. Devices as short as 320 µm may hence be directly driven from binary outputs of energy-efficient CMOS electronics [116], providing voltage swings of the order of 1 V. For these devices, optical propagation losses in the phase shifter sections would amount to less than 1.5 dB, leading to total insertion losses of less than 2 dB when assuming existing implementations of strip-to-slot mode converters [127] and MMI couplers [128] without any further optimization. This compares favorably to competing device concepts such as silicon-based depletion-type pn modulators [129,130] or POH devices [100]. The viability of the presented modulator is demonstrated by generating OOK signals at a data rate of 40 Gbit/s. We obtain high-quality signals with a

measured Q factor of 8.2 for an ultra-low peak-to-peak drive voltage of only 140 mV$_{pp}$.

[end of paper [J1]]

4   Low-loss, small footprint SOH modulators for high-speed signaling

The following section demonstrates compact SOH Mach-Zehnder modulators with sub-1 dB phase-shifter insertion loss and achieved line rates up to 200 Gbit/s. It is taken from a publication in *Optics Express* [J2]. To fit the structure and layout of this document, it was adapted accordingly. The associated supplementary information is found in Appendix B.

For this publication Clemens Kieninger (Cl.K.) and Yasar Kutuvantavida formulated the EO material and coated the SOH modulators. Cl.K. optimized the poling efficiency of the devices and performed the π-voltage characterization of the poled devices. Cl.K. further simulated the optical and electric fields in the SOH modulator for the calculation of the in-device EO coefficient and performed and evaluated the optical loss measurements. Cl.K., Christoph Füllner, Heiner Zwickel and Juned N. Kemal performed and evaluated the high-speed data transmission experiments. Delwin L. Elder and Larry R. Dalton developed the EO material. The work was supervised by Wolfgang Freude (W.F.), Sebastian Randel and Christian Koos (Ch.K.). The paper was written by Cl.K., W.F. and Ch.K. All authors revised the paper.

[start of paper [J2]]

Silicon-organic hybrid (SOH) Mach-Zehnder modulators for 100 GBd PAM4 signaling with sub-1 dB phase-shifter loss

Clemens Kieninger,[1] Christoph Füllner,[1] Heiner Zwickel,[1] Yasar Kutuvantavida,[1] Juned N. Kemal,[1] Carsten Eschenbaum,[1] Delwin L. Elder,[2] Larry R. Dalton,[2] Wolfgang Freude,[1] Sebastian Randel,[1] and Christian Koos,[1,3]

[1] Karlsruhe Institute of Technology (KIT), Institute of Photonics and Quantum Electronics (IPQ), 76131 Karlsruhe, Germany
[2] University of Washington, Department of Chemistry, Seattle, WA 98195, USA
[3] Karlsruhe Institute of Technology (KIT), Institute of Microstructure Technology (IMT), 76344 Eggenstein-Leopoldshafen, Germany

We report on compact and efficient silicon-organic hybrid (SOH) Mach-Zehnder modulators (MZM) with low phase-shifter insertion loss of 0.7 dB. The 280 µm-long phase shifters feature a π-voltage-length product of 0.41 Vmm and a loss-efficiency product as small as $aU_\pi L = 1.0$ VdB. The device performance is demonstrated in a data transmission experiment, where we generate on-off-keying (OOK) and four-level pulse-amplitude modulation (PAM4) signals at symbol rates of 100 GBd, resulting in line rates of up to 200 Gbit/s. Bit error ratios are below the threshold for hard-decision forward error correction (HD-FEC) with 7 % coding overhead, leading to net data rates of 187 Gbit/s. This is the highest PAM4 data rate ever achieved for a sub-1 mm silicon photonic MZM.

4.1   Introduction

Electro-optic (EO) Mach-Zehnder modulators (MZM) are key building blocks of optical communication systems. Ideal devices should combine small π-voltages U_π with small device lengths L while offering low optical loss in the underlying phase shifters. These quantities are subject to various trade-offs, which can be described by two figures of merit: The π-voltage-length product $U_\pi L$ and the loss-efficiency product $aU_\pi L$, where a is the phase-shifter propagation loss measured in dB/mm [15,131]. In practical devices, it is challenging to simultaneously minimize both quantities. For example, ultra-low loss-efficiency products of 0.5 VdB were recently achieved in thin-film lithium-niobate (LiNbO$_3$) MZM [132]. However, while these devices offer bandwidths up to 100 GHz and lend themselves to high-speed signaling [132], the efficiency is fundamentally limited by the comparatively low EO coefficient of LiNbO$_3$. This results in rather high $U_\pi L$ products of more than 20 Vmm such that low drive voltages can only be achieved in cm-long devices. Much shorter device lengths can be realized by using semiconductor-based MZM. For example, 4 mm-long indium-phosphide-(InP-)based MZM with bandwidths of 80 GHz

were demonstrated [133]. The devices have low $aU_\pi L$ products down to 0.9 VdB, but the $U_\pi L$ products still amount to 6 Vmm, making sub-millimeter InP modulators with low drive voltages hard to realize. In addition, InP-based photonic integrated circuits (PIC) rely on rather expensive fabrication processes on small wafers. Silicon photonic (SiP) devices can overcome this deficiency, exploiting sophisticated high-yield fabrication processes on large-area substrates. However, silicon does not exhibit any Pockels-type second-order nonlinearity due to its inversion-symmetric crystal lattice and the associated symmetry properties of the second-order nonlinear susceptibility tensor $\chi^{(2)}$ [6,134]. Thus, SiP MZM have to rely on phase shifters that exploit the plasma dispersion effect, *e.g.*, by means of reverse-biased pn-junctions that are integrated into the optical waveguides. To increase the efficiency of these phase shifters, high doping concentrations are needed, which increases the optical loss [8]. This trade-off leads to rather high loss-efficiency products, which amount to, *e.g.*, $aU_\pi L = 5.8$ VdB for best-in-class depletion-type phase shifters, which still feature substantial $U_\pi L$ products of 4.6 Vmm [71]. Photonic devices made from dielectric waveguides can be supplemented by metallic structures to exploit surface plasmon polaritons for enhanced light-matter interaction. This effect was, *e.g.*, used for high-resolution fluorescence microscopy [135], for high-speed and compact photo detectors [136] and may also open a route towards efficient extraction of light from quantum-dot emitters [137]. For EO modulators, this approach is exploited in plasmonic-organic hybrid (POH) MZM, which combine plasmonic slot waveguides with highly efficient organic EO materials. These devices offer ultra-efficient modulation with small $U_\pi L$ products down to 0.05 Vmm [100] and bandwidths of hundreds of GHz [138,139]. However, the plasmonic phase-shifter structure is intrinsically linked to strong optical absorption loss, which leads to $aU_\pi L$ products of more than 20 VdB [100]. A modulator technology which simultaneously minimizes both the π-voltage-length product and the loss-efficiency product is hence still lacking.

In this paper, we expand on our recent research [140] and show silicon-organic hybrid (SOH) MZM that combine low $U_\pi L$ products of 0.41 Vmm with $aU_\pi L$ products of 1.0 VdB. The MZM rely on 280 μm-long phase shifters and thus offer a small footprint, while the optical insertion loss of the phase shifters amounts to only 0.7 dB. To the best of our knowledge, this is the lowest phase-

shifter loss reported so far for a high-speed MZM on the SiP platform. The high-speed performance of the modulator is demonstrated by generating OOK and PAM4 signals at symbol rates of 100 GBd, resulting in a line rate (net data rate) of up to 200 Gbit/s (187 Gbit/s) with a bit error ratio (BER) below the 7% HD-FEC limit. To the best of our knowledge, this is the highest PAM4 data rate so far achieved with a sub-1 mm SiP modulator [141,142]. The low insertion loss and the ability to co-integrate SOH phase shifters with the full portfolio of standard SiP devices makes the concept not only attractive for conventional optical communications, but also for emerging applications in the fields of quantum optics [143,144] or solid-state LiDAR [145].

4.2   SOH modulator principle

The waveguide structure of SOH modulators is fully compatible with standard fabrication processes of commercial SiP foundries. Specifically, the modulators used in this work were fabricated by UV lithography on 200 mm silicon-on-insulator wafers at A*Star Institute of Microelectronics (IME) in Singapore. Figure 4.1(a) shows a false-colored top-view micrograph of an SOH MZM. The aluminum (Al) contact pads (yellow) in the top metal layer are connected by Al vias to a coplanar transmission line in ground-signal-ground (GSG) configuration. The optical path is highlighted in blue: We use grating couplers (GC) to the left and the right of the device to couple light to and from the SiP chip. Strip waveguides connect the GC with the SOH MZM where 2×2 multimode interference couplers (MMI, not visible, approximately 30 μm long) equally split and combine the incoming and outgoing light to and from the two arms of the MZM. The MZM arms contain 280 μm-long phase-shifter sections, which are realized as slot waveguides that are clad with an organic EO (OEO) material (green) in a back-end-of-line post-processing step. Strip-to-slot and slot-to-strip waveguide mode converters (not visible in Figure 4.1(a), approximately 30 μm long) are used for an efficient transition between the standard silicon strip waveguides and the slot waveguide at the input and the output of the phase-shifter sections [127]. For our current devices, the width of the MZM is dictated by the Al contact pads, having a 100 μm pitch, which leads to an overall footprint of approximately 600 μm × 300 μm per MZM. Note, however, that the contact pads are currently oversized to facilitate contacting by

microwave probes and that their size could be considerably reduced in a packaged device. The pads could be even removed entirely if the device is directly co-integrated with CMOS electronics, leading to footprints of 400 µm × 60 µm or less for the MZM including the phase shifters, the MMI, and the mode converters.

Figure 4.1(b) shows a schematic cross section of the phase-shifter section. The position of the cross section is indicated by the black dashed-dotted line labelled A−A' in Figure 4.1(a). The optical slot waveguide is formed by two Si rails with width $w_{\text{rail}} \approx 240$ nm and height $h_{\text{rail}} \approx 220$ nm separated by the slot with a width of $w_{\text{slot}} \approx 130$ nm. The rails are electrically connected to the GSG transmission line in the bottom metal layer by n-doped Si slabs with height $h_{\text{slab}} \approx 70$ nm. A 2 µm-thick buried silicon-dioxide layer (BOX) separates the waveguides from the silicon substrate. The 3 µm-thick SiO_2 top cladding covers the whole chip and is selectively opened above the phase-shifter sections for deposition of the highly efficient OEO material JRD1 [41]. The contact pads remain uncovered to ensure reliable contacting with microwave probes. In our experiments, the OEO material is dissolved in trichloroethene and applied to the SiP chips using a manual micro-dispensing tool. The remaining solvent is removed from the deposited material by baking the SiP chip for 20 min at 60 °C. After deposition, the OEO chromophores are randomly oriented, and no macroscopic EO activity can be observed. An average acentric orientation of the molecules and thus a macroscopic EO activity can be induced in a one-time poling process. To this end, we heat the material to the glass-transition temperature to increase the molecular mobility. We then apply a DC poling voltage U_{p} across the floating ground electrodes. In our experiments, the poling voltage amounts to 140 V and drops in equal parts across the two 130 nm-wide slots. This leads to electric poling fields of around 530 V/µm in each slot, thereby aligning the dipolar chromophores (green arrows). This results in an average acentric orientation, which is maintained when cooling down the material while keeping the poling field applied. At room temperature, the chromophores have lost their mobility, and the poling voltage can be removed. For the devices presented here, the entire poling procedure takes roughly 35 min including heating and cooling of the chip. For mass production of SOH devices, the throughput could be increased by poling many SOH devices in parallel during a single poling process. When an RF drive voltage U_{d} is applied to the GSG transmission line,
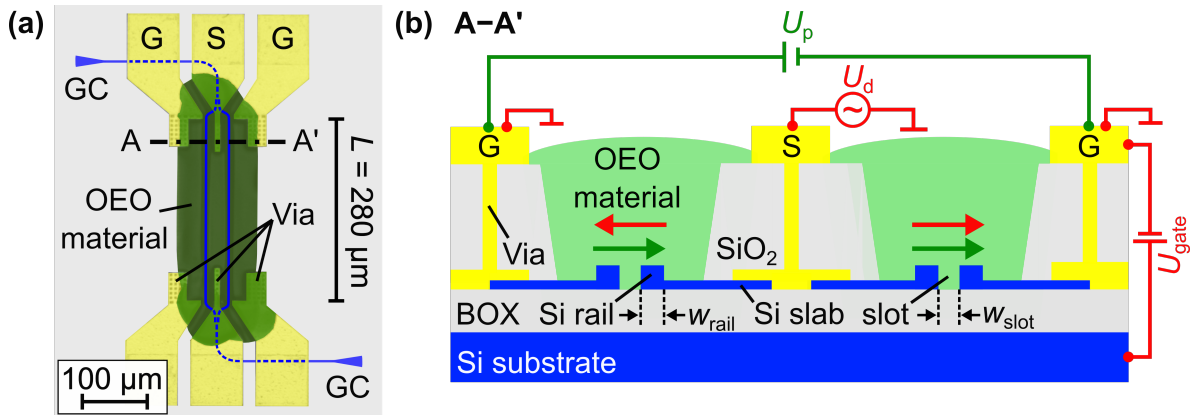
Figure 4.1: Silicon-organic hybrid (SOH) modulator concept and structure. **(a)** False-color top-view micrograph of an SOH Mach-Zehnder modulator (MZM). Grating couplers (GC) and optical waveguides to the MZM are drawn in blue. To split and recombine the light in the two arms of the MZM we use multi-mode interference (MMI) couplers, which are hidden below the contact pads (yellow). The electrical signal is applied via a coplanar transmission line in ground-signal-ground (GSG) configuration, from which only the top-layer contact pads are visible. The OEO material (green) is deposited by a micro-dispensing tool and serves as the cladding for the SOH slot waveguide. The black dashed-dotted line labeled A-A' indicates the position of the cross section shown in (b). **(b)** Cross section A-A'. In each arm, two Si rails (width $w_{rail} \approx 240$ nm, height $h_{rail} \approx 220$ nm) define an optical slot waveguide (slot width $w_{slot} \approx 130$ nm), which is filled with the OEO material JRD1 [41]. The rails are electrically connected to the GSG transmission line by doped Si slabs (slab height $h_{slab} \approx 70$ nm). Aluminum vias connect the bottom-layer transmission line to the top-layer contact pads. For poling, the OEO material is heated and a voltage U_p is applied across the floating ground electrodes, thereby aligning the dipolar molecules (green arrows). By cooling the chip, the EO chromophores are frozen in the aligned orientation, and the poling voltage can be removed. After poling, a modulating drive voltage U_d induces electric fields in the slots (red arrows) which are parallel to the poling direction in one arm and anti-parallel in the other arm, thus resulting in efficient push-pull operation of the MZM. To compensate for an insufficient doping concentration in the Si slabs, a gate voltage U_{gate} is applied to induce an electron accumulation layer in the silicon slabs. For properly adjusted doping profiles, the gate voltage becomes obsolete [80].

the electric fields in both arms point in opposite directions (red arrows). This results in a push-pull operation of the MZM, which reduces undesired phase modulation (chirp) of the modulated optical signal [17,18].

In general, SOH modulators stand out due to ultra-low $U_\pi L$ products, which results from a combined effect of the phase-shifter structure and the high EO activity of the organic material. Specifically, both the electrical and the optical mode fields are tightly confined to the OEO material in the slot, which leads to a high field interaction factor [15]. The optical confinement to the slot results

from the field enhancement in the low-index OEO material at the interface to the high-index Si rails [146]. The electrical mode is also strongly confined to the slot, because a signal voltage U_d applied to the GSG transmission line drops essentially across the slot. For a given signal voltage, this results in large electric driving fields of about U_d/w_{slot} experienced by the OEO material, leading to a strong Pockels-type phase shift.

The currently used MZM still suffer from a low doping level in the silicon slabs, which leads to high RC time constants and hence limits the bandwidth of the phase shifters. In the 100 GBd signaling experiments presented in this work, we emulate higher doping concentrations by applying a gate voltage U_{gate} between the Si base wafer and the silicon-on-insulator (SOI) device layer. The gate voltage induces an electron accumulation in the device layer and thereby increases the slab conductivity [81]. For our signaling experiments, we use a gate field of 0.1 V/nm, which we generate by applying a rather high gate voltage of $U_{gate} = 200$ V across the 2 μm-thick BOX layer. Note that this gate voltage can be reduced to CMOS-compatible levels of the order of 1 V by using a top gate with a nanometer-thin oxide on the Si slabs [147]. Alternatively, the gate voltage can be omitted entirely once the doping profiles are optimized [80].

Note that the employed OEO material JRD1 is primarily optimized for high efficiency and still has a relatively low glass-transition temperature of $T_g = 82$ °C [42], which renders the material susceptible to thermal relaxation at temperatures close to T_g. We still chose JRD1 as a readily available material to demonstrate efficient low-loss SOH devices in our current experiments. When used in cryogenic applications [148–150], thermal relaxation should not represent a problem. At room temperature, poled JRD1 in SOH devices is still reasonably stable. For testing our devices, we performed the data transmission experiment on the day after poling, but this is actually not crucial. Specifically, in a previous investigation [140], we measured a small increase of the π-voltage of only 5 % after storing an SOH device functionalized with JRD1 for one week at room temperature. Taking into account that thermal relaxation is usually most pronounced during the first few hundred hours after poling [20,108,151], we expect a slower increase of U_π which might eventually stall for longer storing times. Still, for long-term stable devices operated at elevated temperatures, a higher T_g is required. We have recently used a side-chain polymer with

(a)

(b)
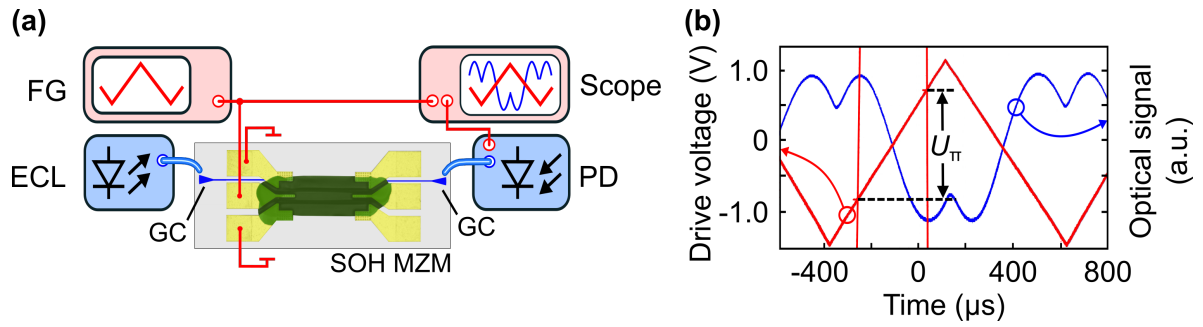
Figure 4.2: Characterization of the SOH MZM. **(a)** Setup for measuring the π-voltage U_π. A 1 kHz triangular waveform from a function generator (FG) is used to drive the modulator in push-pull mode. Light from an external-cavity laser (ECL) is coupled to the SOH MZM. A photodiode (PD) detects the modulated light. An oscilloscope (Scope) monitors both the drive voltage (red) and the photocurrent (blue). **(b)** Recorded time traces of the applied drive voltage (red) and the output signal of the photodetector (blue). The π-voltage is determined from the voltage increment required to drive the modulator between minimum and maximum transmission.

$T_\mathrm{g} = 172\,°\mathrm{C}$ and demonstrated SOH devices, which showed thermal stability at 85 °C for more than 2000 h [151]. However, high-T_g materials are typically less efficient. A way out of the tradeoff between thermal stability and modulation efficiency is cross-linking of the EO chromophores. For this procedure, the core of an efficient chromophore is modified by crosslinking agents, which enables lattice hardening after the poling step [109]. For an OEO material similar to JRD1, this approach has recently been shown to lead to a high glass-transition temperature of 160 °C while maintaining a large EO coefficient of 300 pm/V [46]. An additional challenge is photochemical degradation if the material is exposed to high optical intensities. However, the effect is related to the presence of oxygen such that the OEO material may be protected from degradation by hermetically sealing the modulator by an oxygen blocking sealant [19,20].

4.3   Determination of π-voltage

To determine the π-voltage of the devices, we use the setup shown in Figure 4.2(a). The SOH MZM is fed by an optical carrier at 1550 nm from an external-cavity laser (ECL), which is coupled to the device via a grating coupler (GC). The device is driven by a triangular waveform at a frequency of 1 kHz that is provided by a function generator (FG) and coupled to the chip via DC

probes. The modulated light is coupled to a fiber and detected by a photodiode (PD), which is connected to an oscilloscope (Scope) to simultaneously monitor the MZM output power (blue line) and the drive voltage (red line). If the peak-to-peak amplitude of the drive voltage exceeds the π-voltage U_π, the latter can be directly measured from the drive voltage difference between the minimum and the maximum power transmission of the MZM, see Figure 4.2(b). We repeatedly poled and tested three MZM, leading to π-voltages of 1.48 V, 1.50 V, and 1.54 V. For the 1.48 V-device, the $U_\pi L$ product amounts 0.41 Vmm, from which we deduce an EO coefficient of 190 pm/V. Note that, in a previous study [140] using also the OEO material JRD1, we achieved slightly better $U_\pi L$ products of 0.32 Vmm and EO coefficients of 290 pm/V and 390 pm/V for devices with larger slot widths of 150 nm and 190 nm, respectively. The reduced modulation efficiency and the smaller EO coefficient for the current devices is attributed to the smaller slot width of 130 nm. In general, EO chromophores near the slot walls are mostly oriented parallel to the sidewalls due to surface interactions [100]. As a consequence, the volume fraction of perpendicularly aligned chromophores becomes smaller the narrower the slot is. Increasing the slot width in future devices beyond the current value of 130 nm may thus lead to further improvements of the modulation efficiency and to lower drive voltages.

## 4.4 Determination of insertion loss of SOH phase shifters

To determine the phase-shifter insertion loss, the wavelength of the ECL is swept and the wavelength-dependent total transmitted optical power $P_{tot}(\lambda)$ at the modulator output is measured. In the following, the fiber-to-fiber attenuation of the device is specified in dB and can be calculated by $a_{tot}(\lambda) = -10\log(P_{tot}(\lambda)/P_0)$, where P_0 corresponds to the optical launch power. To de-embed the attenuation of the phase-shifter sections, we subtract the dB-values of the attenuation of the two grating couplers $(2a_{GC}(\lambda))$, of the feeding strip waveguides (a_{Strip}), of the two MMI couplers $(2a_{MMI}(\lambda))$, and of the strip-to-slot and slot-to-strip mode converters $(2a_{Conv})$ from the overall attenuation $(a_{tot}(\lambda))$ of the device. The attenuation of the strip waveguides is calculated

according to the specification of the foundry. For all other components, we use suitable test structures on the fabricated wafer, see Appendix B for more details.

The on-chip MZM attenuation $a_{\mathrm{MZM}}(\lambda) = a_{\mathrm{tot}}(\lambda) - 2a_{\mathrm{GC}}(\lambda) - a_{\mathrm{Strip}}$ of the bare MZM shows a strong wavelength dependence, see Figure 4.3(a). This is caused by the fact that the passive waveguide sections of the MZM arms were designed to have different lengths such that the operating point of the device can be set by the laser wavelength. This leads to a transmission characteristic in which constructive and destructive interference alternates. We choose wavelengths λ_i of constructive interference to determine the phase-shifter insertion loss $a_{\mathrm{PS}}(\lambda_i)$ by

$$a_{\mathrm{PS}}(\lambda_i) = a_{\mathrm{MZM}}(\lambda_i) - 2a_{\mathrm{MMI}}(\lambda_i) - 2a_{\mathrm{Conv}}. \tag{4.1}$$

The calculated insertion loss $a_{\mathrm{PS}}(\lambda_i)$ varies slightly in the investigated wavelength range between 1510 nm and 1580 nm. We therefore specify a mean phase-shifter insertion loss $\overline{a}_{\mathrm{PS}}$ obtained by averaging over all considered wavelengths λ_i. The procedure is illustrated in Figure 4.3(a), where the top panel shows the MZM attenuation $a_{\mathrm{MZM}}(\lambda) = a_{\mathrm{tot}}(\lambda) - 2a_{\mathrm{GC}}(\lambda) - a_{\mathrm{Strip}}$ of a typical imbalanced SOH MZM with 280 µm-long phase shifters(red line). We find an extinction ratio of around 30 dB, which is consistent for all investigated devices. The blue solid line indicates the losses $2a_{\mathrm{MMI}}(\lambda) + 2a_{\mathrm{Conv}}$ of the MMI and the strip-to-slot converters in the MZM as obtained from separate test structures on the same wafer. The center panel shows a zoom-in of the low-attenuation region, in which the blue dashed line additionally indicates the converter attenuation $2a_{\mathrm{Conv}}$. The envelope of $a_{\mathrm{MZM}}(\lambda)$ follows $2a_{\mathrm{MMI}}(\lambda) + 2a_{\mathrm{Conv}}$, which indicates that the phase-shifter section itself does not show a strong wavelength dependence. The bottom panel displays the phase-shifter insertion loss $a_{\mathrm{PS}}(\lambda_i)$ (blue crosses) according to Eq. (4.1) for one single device. The error bars reflect the overall measurement uncertainty σ_{meas} in dB arising from the uncertainties of all contributing attenuations, see Appendix A for details. The insertion loss of the grating couplers increases towards smaller wavelengths, leading to larger error bars due to smaller absolute power levels obtained in the measurement. The red dashed horizontal line corresponds to the wavelength average $\overline{a}_{\mathrm{PS}} = 0.55\,\mathrm{dB}$, and the associated standard deviation amounts to $\sigma_{a_{\mathrm{PS}}} = 0.08\,\mathrm{dB}$.
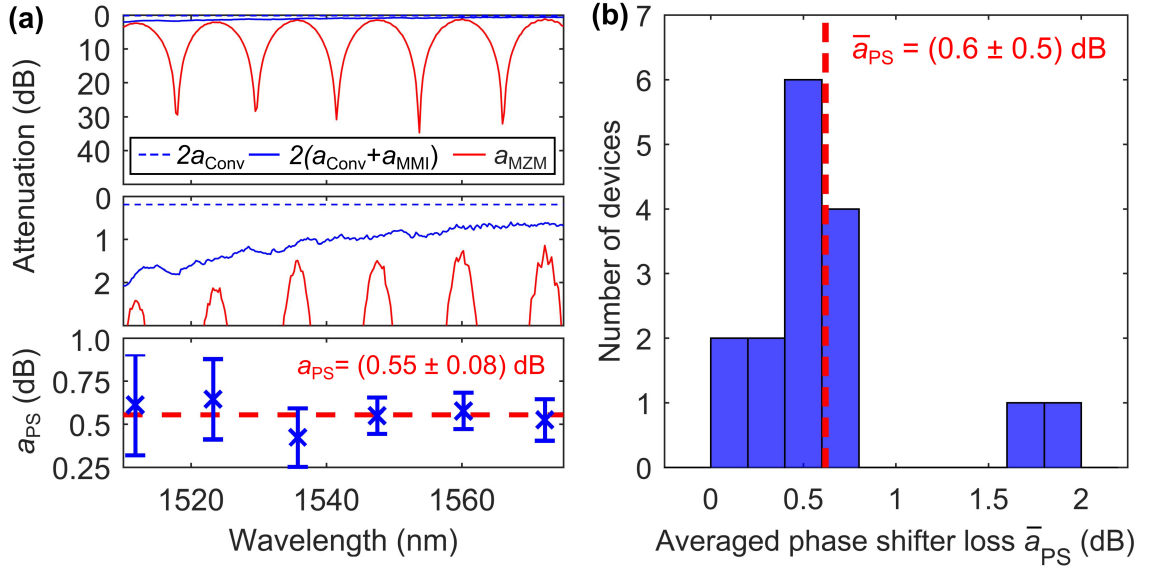
Figure 4.3: Measurement of phase-shifter insertion loss. **(a)** Top panel: On-chip attenuation $a_{\mathrm{MZM}}(\lambda)$ of an imbalanced SOH MZM with 280 μm-long phase shifters (red line) as a function of wavelength. The blue solid line represents the attenuation $2a_{\mathrm{MMI}}(\lambda) + 2a_{\mathrm{Conv}}$ of the two MMI couplers and of the two strip-to-slot mode converters. Center panel: Zoom-in of the low-attenuation region seen in the top panel. The blue dashed line indicates the attenuation $2a_{\mathrm{Conv}}$. The envelope of $a_{\mathrm{MZM}}(\lambda)$ follows $2a_{\mathrm{MMI}}(\lambda) + 2a_{\mathrm{Conv}}$. Bottom panel: Calculated phase-shifter loss $a_{\mathrm{PS}}(\lambda_i)$ (blue crosses) for one device for various wavelengths λ_i where constructive interference occurs. The red dashed line corresponds to an average over the insertion losses $a_{\mathrm{PS}}(\lambda_i)$ and amounts to $\overline{a}_{\mathrm{PS}} = 0.55\,\mathrm{dB}$ with a standard deviation of $\sigma_{a_{\mathrm{PS}}} = 0.08\,\mathrm{dB}$. **(b)** Histogram of wavelength-averaged phase-shifter losses $\overline{a}_{\mathrm{PS}}$ of 16 nominally identical devices from four different locations of the wafer. The histogram mean amounts to $\overline{\overline{a}}_{\mathrm{PS}} = 0.6\,\mathrm{dB}$ (red dashed line) and the standard deviation is $\sigma_{\overline{a}_{\mathrm{PS}}} = 0.5\,\mathrm{dB}$. The two outliers are attributed to the fact that the OEO material is filled into the slots by a manual process, and we expect that an automated dispensing of the OEO material will further improve the uniformity and reduce the losses.

To account for statistical variations, we investigate nominally identical dies from four different positions on the wafer, each die containing four nominally identical SOH MZM with 280 μm-long phase shifters. A histogram of the wavelength-averaged phase-shifter losses $\overline{a}_{\mathrm{PS}}$ of all 16 devices is shown in Figure 4.3(b). By averaging over the 16 devices of the histogram, we estimate a mean phase-shifter loss of $\overline{\overline{a}}_{\mathrm{PS}} = 0.6\,\mathrm{dB}$ and a standard deviation of $\sigma_{\overline{a}_{\mathrm{PS}}} = 0.5\,\mathrm{dB}$. Note that the rather high standard deviation is dominated by two outliers, which we attribute to the fact that the OEO material is filled into the slots by a manual process. We expect that an automated dispensing of the OEO material will improve these figures. This is subject to future research.

In the subsequent signaling experiments, we improve the device bandwidth by applying a gate voltage U_{gate}, see Section 4.2. The gate-induced electron accumulation in the Si device layer improves the slab conductivity, but also increases the total optical insertion loss by 0.8 dB for an applied gate field of 0.1 V/nm. Note, however, that this increase in insertion loss comprises the contributions of both the 280 µm-long phase shifter and the 1.3 mm-long access waveguides. Assuming approximately equal carrier-induced propagation losses in both sections, we estimate an increase of the phase-shifter loss of approximately 0.14 dB, leading to a still acceptable phase-shifter insertion loss of around (0.7 ± 0.5) dB. To the best of our knowledge, this is the lowest phase-shifter insertion loss so far demonstrated for a high-speed MZM on the SiP platform, see Appendix B for a more detailed overview and a comparison to other state-of-the-art modulator technologies. Note also that the gate voltage and the associated loss can be avoided by using optimized doping profiles, which rely on high doping concentrations in the slabs outside the core region of the slot waveguide, and which lead to negligible extra insertion losses of below 0.1 dB [80].

There are two reasons why the phase-shifter attenuation of 0.7 dB compares favorably to losses of SOH devices used in previous demonstrations [17,18,140,151,152]. First, as compared to previous fabrication runs [17,18], the propagation loss of the slot waveguides has significantly improved: Previous devices showed propagation losses of the order of 6 dB/mm [17,18], whereas the devices in this work feature values down to $a = \overline{a}_{\text{PS}} / L = 2.5 \,\text{dB} / \text{mm}$. We attribute this loss reduction to improved fabrication processes leading to lower scattering losses in the underlying slot waveguides. Second, when compared to previous devices from the same fabrication run [140,151,152], the devices presented in this work have much shorter phase-shifter lengths of only 280 µm and therefore much smaller insertion losses. For example, previous devices from the same fabrication run had phase-shifter lengths in the range of 600…1500 µm, resulting in much higher phase-shifter losses in the range of 1.6…5.9 dB [140,151,152]. The straightforward approach to shorten the phase-shifter section is practical only for modulators with a small $U_{\pi}L$ product. Because in our case we have $U_{\pi}L = 0.41$ Vmm, our 280 µm-long phase shifters can still be operated at CMOS compatible voltage levels, even when signaling with 100 GBd PAM4.

With the determined phase-shifter propagation loss coefficient of $a = 2.5$ dB/mm, together with the measured $U_\pi L$ product of 0.41 Vmm, we calculate an excellent loss-efficiency product of $aU_\pi L = 1.0$ VdB, which is competitive with state-of-the-art EO modulators, see Table B.2 in Appendix B. To identify the source of the phase-shifter propagation loss, we consider three possible contributions: Gate-induced or doping-induced free-carrier absorption (FCA), scattering loss due to surface roughness of the high-index-contrast SiP waveguides, and absorption of photons in the organic cladding material itself. At a wavelength of 1550 nm, the latter can be neglected for the OEO material JRD1 [100]. Regarding the estimation of FCA, we exploit the fact that the optical loss in bulk Si is proportional to its conductivity [153], which, in our waveguide structures, is dominated by the effect of the gate-induced electron accumulation layer [80]. In our experiments, we measure 0.14 dB of gate-voltage-dependent contribution to the optical insertion loss, while the overall phase-shifter loss amounts to 0.7 dB. The remaining loss of 0.56 dB is hence attributed to optical scattering at the rough sidewalls of the slot waveguides, which may be significantly reduced by further improved fabrication processes. In fact, slot waveguides with propagation losses down to 0.2 dB/mm were already shown [122]. Together with the measured $U_\pi L$ product of 0.41 Vmm, this would potentially lead to an outstanding loss-efficiency product of only $aU_\pi L = 0.08$ VdB.

4.5 Data transmission experiment

We demonstrate the high-speed performance of the SOH MZM by generating on-off-keying (OOK) and four-level pulse-amplitude modulation (PAM4) signals at symbol rates of 100 GBd. The experimental setup is shown in Figure 4.4(a). An arbitrary-waveform generator (AWG) with a bandwidth of 45 GHz delivers the electrical drive signal, which is boosted by an RF amplifier (RF amp) with a bandwidth of 55 GHz. The drive signal is coupled to the open-ended SOH MZM by a microwave probe. The MZM is optically fed by an external-cavity laser (ECL), which is set to an emission wavelength of 1560 nm and an output power of 11.5 dBm. To compensate for the relatively high insertion losses of the grating couplers at the input and the output of the SOH MZM, we use an erbium-doped fiber amplifier (EDFA), which is followed by

a band-pass filter (BP, bandwidth 2 nm) to suppress amplified spontaneous emission (ASE) noise. A variable optical attenuator (VOA) is used to adjust the optical power before coupling the modulated signal to a 70 GHz photodiode (PD). The PD output is recorded by a real-time oscilloscope (RTO) having an analog bandwidth of 63 GHz and a sampling rate of 160 GSa/s. The digitized waveforms are post-processed offline. The digital signal processing (DSP) chain includes resampling, timing recovery, blind adaptive time-domain equalization using the Sato algorithm [154] with a filter length of 58 taps, and finally error counting. The signal is a pseudo random binary sequence of length 2^{11}-1, which is mapped to OOK or PAM4 symbols and encoded onto pulses with a raised-cosine spectrum (roll-off factor $\beta = 0.1$).

For a gate field of 0.1 V/nm the SOH MZM has a 3 dB EO bandwidth of 40 GHz when terminating the electrodes with a 50 Ω resistor. The data transmission experiment, however, is done without device termination. This reduces the bandwidth of the device, but leads to an inherent doubling of the drive voltage through reflection at the open end of the transmission line [99] and thus allows us to use a drive signal with a comparatively small peak-to-peak voltage swing of only 0.72 V_{pp}. Such signals can be generated with standard CMOS circuits, thereby enabling highly efficient operation of the devices without any dedicated driver amplifiers [116]. In our experiment, a linear digital pre-equalization of the drive signals is used to flatten the frequency response of the AWG and the RF amplifier. For a 100 GBd PAM4 signal, the peak-to-peak voltage swing at the amplifier output measured at a 50 Ω impedance amounts to 0.78 V_{pp}. This reduces to the above-mentioned 0.72 V_{pp} when taking into account the insertion loss of the microwave probe, which amounts to 0.7 dB at the Nyquist frequency of 50 GHz. For the open-ended device, this results in an effective peak-to-peak drive voltage of 1.44 V_{pp}, which is close to the modulator's DC π-voltage of 1.50 V. However, due to the modulator's frequency roll-off, the MZM is still operated in the linear regime of its transfer function such that nonlinearities do not play a role. The total fiber-to-fiber attenuation of the MZM amounts to 13.6 dB, measured without a gate voltage, and the gate-induced extra loss amounts to 0.8 dB. The wavelength-averaged phase-shifter loss amounts to $\bar{a}_{PS} = 0.74\,\mathrm{dB}$ without gate voltage, which increases by an estimated 0.14 dB once the gate is applied.
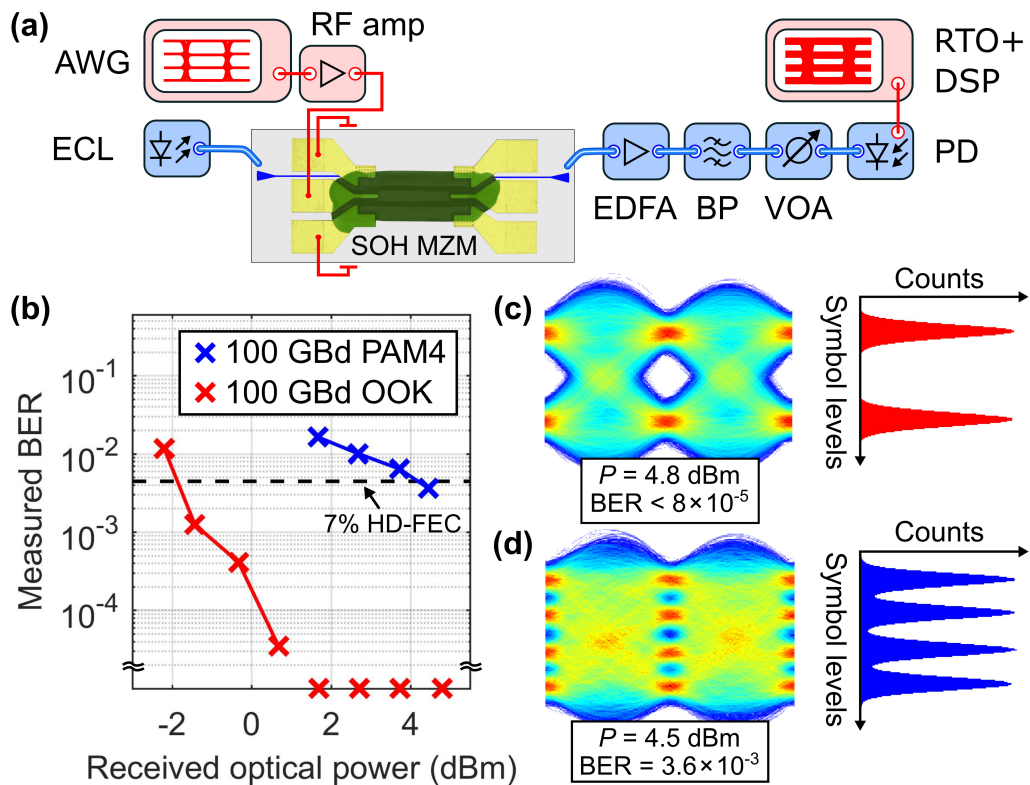
Figure 4.4: Data transmission experiments. **(a)** Experimental setup. An external-cavity laser (ECL) provides the optical carrier, which is coupled to the SOH MZM via a grating coupler. An erbium-doped fiber amplifier (EDFA) compensates the optical insertion loss of the grating couplers, and a band pass filter (BP) is used to suppress out-of-band amplified spontaneous emission (ASE) noise. An arbitrary-waveform generator (AWG) is used to drive the open-ended modulator via an RF amplifier (RF amp). A variable optical attenuator (VOA) sets the power level at the receiver, which consists of a high-speed photodiode (PD) connected to a real-time oscilloscope (RTO). Offline digital signal processing (DSP) provides post-equalization and error counting. **(b)** Measured bit error ratio (BER) as a function of the received optical power for OOK and PAM4 at 100 GBd. For OOK (red crosses) and received powers > 1 dBm, we do not detect any errors in our 12.5 µs-long recordings. The BER value remains below the threshold for hard-decision forward error correction (HD-FEC) down to power levels of −1.4 dBm. For PAM4 (blue crosses), we see a power penalty of about 6 dB compared to OOK. At a received power of 4.45 dBm, the BER is $3.6 \cdot 10^{-3}$ and stays just below the threshold for HD-FEC. **(c)**, **(d)** Eye diagrams, corresponding BER, and histograms for 100 GBd OOK and PAM4 signals at the highest measured received power.

Figure 4.4(b) shows the measured bit-error ratio (BER) as a function of the received power. The dashed horizontal line indicates the BER threshold 4.45×10^{-3} [155] for hard-decision forward error correction (HD-FEC) with a 7 % overhead. For OOK and received optical powers > 1 dBm, we cannot detect any errors in our 12.5 µs long recordings, which contain 1.25×10^6 bit. We thus

plot the corresponding data points at the lower edge of the diagram. For a received power of -1.4 dBm, the BER amounts to 1.2×10^{-3}, which is still well below the threshold for HD-FEC. Figure 4.4(c) depicts the eye-diagram for 100 GBd OOK at a received optical power of 4.8 dBm along with the corresponding histogram of the signal levels measured at the sampling point in the center of the eye.

PAM4 is less robust against inter-symbol interference (ISI) and noise such that our recordings show systematically higher BER values compared to OOK with a power penalty of approximately 6 dB measured at the BER threshold for 7% HD-FEC. For a received optical power of 4.5 dBm, the BER amounts to 3.6×10^{-3}, which is just below the 7% HD-FEC threshold. In Figure 4.4(d), we depict the eye diagram for a received optical power of 4.5 dBm along with the histogram, which was again obtained at the temporal sampling point in the center of the eye diagram. The eyes are not fully open, resulting in histogram counts between the symbol power levels. The achieved line rate amounts to 200 Gbit/s, corresponding to a net data rate of 187 Gbit/s. To the best of our knowledge, this is the highest PAM4 data rate so far demonstrated using a sub-1 mm SiP modulator.

4.6   Summary

We show SOH MZM with $U_\pi L$ products of 0.41 Vmm and $aU_\pi L$ products of 1.0 VdB. The compact devices have 280 µm-long phase shifters with optical insertion losses of only 0.7 dB, which corresponds to the lowest phase-shifter insertion loss reported so far for a high-speed MZM on the SiP platform. We demonstrate high-speed optical signaling by generating OOK and PAM4 signals at symbol rates of 100 GBd, resulting in line rates of up to 200 Gbit/s. The measured BER values are below the 7 % hard-decision FEC limit. We believe that compact low-loss MZM with small $U_\pi L$ products are not only interesting for optical communications but may be also useful for applications requiring dense photonic integration of energy-efficient phase shifters such as in optical phased arrays or in the field of quantum optics. The presented device concept can easily be extended to in-phase/quadrature (IQ) modulators [16,118]. In the future, low-loss SOH devices could be also

embedded in even more advanced photonic circuits in which two-dimensional semiconductors, such as monolayers of MoS_2, provide additional functionality [156,157].

[end of paper [J2]]

5   Long-term thermally stable SOH modulators

This section reports on long-term thermally stable SOH modulators in accordance with Telcordia standards for high-temperature storage. It is taken from a publication in *Optics Express* [J3]. To fit the structure and layout of this document, it was adapted accordingly.

For this publication Clemens Kieninger (Cl.K.) and Yasar Kutuvantavida formulated the EO material and coated the SOH modulators. Cl.K. optimized the poling efficiency in the coated devices and performed the π-voltage characterization as well as the electro-magnetic simulations required to calculate the in-device EO coefficient. Cl.K. performed the long-term thermal stability measurements of the SOH modulators and evaluated the associated data. Cl.K., Juned N. Kemal and Heiner Zwickel performed and evaluated the high-speed data transmission experiments. Hiroki Miura, Feng Qiu and Shiyoshi Yokoyama (S.Y.) developed the EO material. The work was supervised by Wolfgang Freude (W.F.), Sebastian Randel, S.Y. and Christian Koos (Ch.K.). The paper was written by Cl.K., W.F. and Ch.K. All authors revised the paper.

[start of paper [J3]]

Demonstration of long-term thermally stable silicon-organic hybrid modulators at 85 °C

Clemens Kieninger,[1,2] Yasar Kutuvantavida,[1] Hiroki Miura,[3] Juned N. Kemal,[1] Heiner Zwickel,[1] Feng Qiu,[4] Matthias Lauermann,[1] Wolfgang Freude,[1] Sebastian Randel,[1] Shiyoshi Yokoyama,[3,4] and Christian Koos[1,2]

[1] Karlsruhe Institute of Technology (KIT), Institute of Photonics and Quantum Electronics (IPQ), 76131 Karlsruhe, Germany
[2] Karlsruhe Institute of Technology (KIT), Institute of Microstructure Technology (IMT), 76344 Eggenstein-Leopoldshafen, Germany
[3] Department of Molecular and Material Sciences, Kyushu University, 6-1 Kasuga-koen Kasuga-city, Fukuoka 816-8580, Japan
[4] Institute for Materials Chemistry and Engineering, Kyushu University, 6-1 Kasuga-koen Kasuga-city, Fukuoka 816-8580, Japan

We report on the first demonstration of long-term thermally stable silicon-organic hybrid (SOH) modulators in accordance with Telcordia standards for high-temperature storage. The devices rely on an organic electro-optic side-chain polymer with a high glass-transition temperature of 172 °C. In our high-temperature storage experiments at 85 °C, we find that the electro-optic activity converges to a constant long-term stable level after an initial decay. If we consider a burn-in time of 300 h, the π-voltage of the modulators increases on average by less than 15 % if we store the devices for additional 2400 h. The performance of the devices is demonstrated by generating high-quality 40 Gbit/s OOK signals both after the burn-in period and after extended high-temperature storage.

5.1   Introduction

Silicon photonics is a promising integration platform for photonic devices, exploiting mature CMOS processes for low-cost high-yield mass fabrication of densely integrated photonic circuits that are ideally suited for high-volume applications such as optical communications [68]. However, due to the centrosymmetric crystal lattice of silicon (Si), the material does not exhibit a linear electro-optic (EO) effect [6]. For that reason, high-speed Si EO modulators are typically realized with reverse-biased pn junctions, exploiting the plasma dispersion effect [158]. Since the associated change in the refractive index is small, the π-voltage-length product $U_\pi L$ is typically as large as 10 Vmm [159–161]. This shortcoming of the Si platform can be overcome by combining silicon photonic or plasmonic waveguides with highly efficient organic EO (OEO) materials, leading to the so-called silicon-organic hybrid (SOH) [15,107] or plasmonic-organic hybrid (POH) [95,96] approach.

SOH devices have been demonstrated to show excellent performance. This includes, *e.g.*, ultra-low voltage-length products down to $U_\pi L = 320$ Vμm [140] in combination with small efficiency-loss products down to $aU_\pi L = 1.2$ VdB [140] and high-speed modulation at line rates of up to 100 Gbit/s for on-off keying (OOK) [17], up to 120 Gbit/s for PAM4 [18], and 400 Gbit/s for 100 GBd 16QAM [16,118]. In addition, low chirp with an α- parameter of 0.1 [18] and a high extinction ratio in excess of 30 dB [104] have been shown. However, while these demonstrations outperform many competing device concepts in terms of efficiency, footprint, and speed, the reliability and long-term stability of SOH devices was less extensively investigated and still represents a weakness of the technology.

In this paper, we report on the first demonstration of long-term thermally stable SOH modulators that fulfill high-temperature storage requirements according to Telcordia standards GR-468-CORE [55]. The devices exploit a side-chain EO polymer with bulky adamantyl units that lead to a high glass-transition temperature of $T_g = 172$ °C [77,162]. We investigate SOH devices stored at 85 °C in ambient atmosphere and show that the electro-optic activity reaches a constant long-term stable level after an initial decay. When allowing for a burn-in time of approximately 300 h, the average in-device EO activity decreases by less than 15 % for an additional 2400 h of high-temperature storage. At the end of the test period, the modulators exhibit a $U_\pi L$-product of 3.3 Vmm, which represents a four-fold improvement compared to previously demonstrated long-term stable OEO modulators [19,163]. To confirm that the high-temperature storage does not impair the high-speed performance of the modulator, we demonstrate the generation of high-quality 40 Gbit/s On-Off -Keying (OOK) signals both after the burn-in period and after extended high-temperature storage. We believe that our demonstration represents an important milestone towards industrial adoption of the SOH technology.

5.2   Silicon-organic hybrid device concept

The concept of a silicon-organic hybrid (SOH) Mach-Zehnder modulator (MZM) is schematically depicted in Figure 5.1, and Figure 5.1(a) shows a top view of the device [18]. We use two multi-mode interference (MMI) couplers
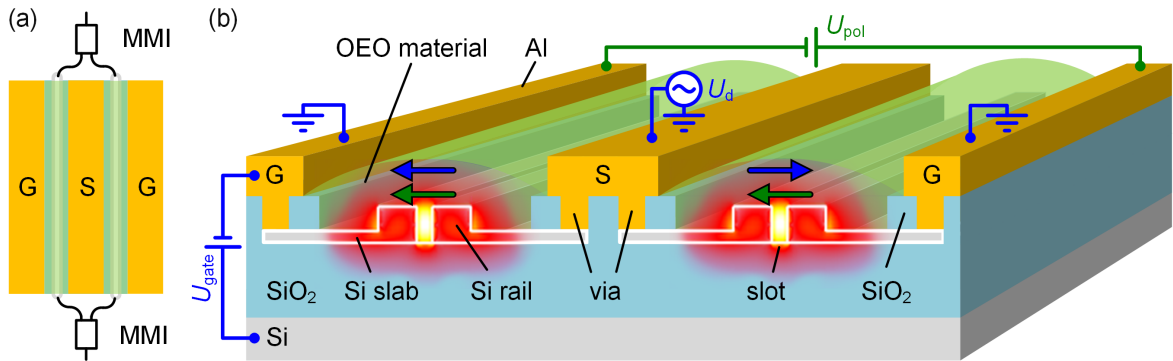
Figure 5.1: Silicon-organic hybrid (SOH) device concept. **(a)** Top view of an SOH Mach-Zehnder modulator (MZM). The MZM features a ground-signal-ground (GSG) transmission line and two multi-mode interference (MMI) couplers for splitting and recombining the light in the two MZM arms. **(b)** Perspective view of an SOH MZM. Each MZM arm comprises a silicon (Si) slot waveguide consisting of two closely spaced Si rails that form a slot which is filled by the EO material. Electrical vias and thin n-doped Si slabs connect the GSG transmission line to the optical waveguide. Both the optical mode (red/yellow shading) and the radio frequency (RF) mode are highly localized in the slot region, which leads to efficient EO modulation. In order to establish macroscopic EO activity, the chip is heated to the glass-transition temperature (T_g) of the OEO material, and a poling voltage U_{pol} is applied across the ground electrodes. The corresponding poling fields (green arrows) induce an average acentric orientation of the dipolar EO molecules. This orientation is conserved by cooling the device and removing the poling field only when room temperature is reached. An applied signal voltage U_d induces electric fields (blue arrows) which are parallel (antiparallel) to the poling direction in the left (right) arm of the MZM, enabling push-pull operation.

at the input and output of the MZM to split and recombine the light. The modulator electrodes form a coplanar transmission line in ground-signal-ground (GSG) configuration. Figure 5.1(b) shows a perspective view of the SOH MZM. Each MZM arm comprises an SOH phase shifter consisting of a Si slot waveguide. The slot waveguide is formed by two parallel 240 nm wide and 220 nm high Si rails separated by a 190 nm wide slot, which is filled by the OEO material. Electrical vias and thin n-doped Si slabs connect the aluminum (Al) GSG transmission line and the optical waveguides. An applied radio frequency (RF) drive voltage U_d drops entirely across the narrow slots with a width w_{slot}, inducing electric fields of approximately U_d / w_{slot} in the the OEO material. These fields are significantly larger than those obtained in competing organic EO modulators, in which the spacing between the RF electrodes typically amounts to several micrometers [19,163]. The optical mode, illustrated by a red and yellow shading in Figure 5.1(b), is strongly confined

to the slot region, resulting in a large overlap with the RF field in the OEO material. This leads to the excellent modulation efficiency of SOH devices. The silicon photonic chips are fabricated on standard 8-inch silicon-on-insulator (SOI) wafers in a commercial foundry using 248 nm optical lithography. The OEO cladding is applied to the chips by a post-processing step. To this end, the synthesized OEO material is dissolved in cyclopentanone and deposited on the Si slot waveguides using a microdispenser. This technique is well suited for highly localized deposition of the OEO material with a typical resolution of approximately 20 µm, thereby allowing to cover the SOH phase shifters while leaving the Al RF contact pads free. Note that local microdispensing of OEO material does not impair the device performance as compared to globally covering the entire chip by a simple spin-coating process which was used in previous demonstrations of SOH devices [17,118]. After depositing the OEO material, the coated chips are heated to remove remaining solvent from the OEO material. At that point, the molecules are randomly oriented in the slot, and a one-time poling process is required to establish average acentric molecular orientation leading to macroscopic EO activity. To this end, we heat up the chip close to T_g of the OEO cladding material and apply a poling voltage U_{pol} across the floating ground electrodes of the MZM. The voltage induces poling fields, indicated as green arrows in Figure 5.1(b), in the slot regions of the MZM, which align the dipolar molecules in the OEO cladding. After cooling the device down to room temperature, the molecular orientation is frozen and the poling voltage can be removed. A drive voltage U_d applied to the GSG transmission line induces electric fields in the two slot regions (blue arrows) that are parallel to the poling orientation in one arm and antiparallel to the poling orientation in the other arm of the MZM. This leads to phase shifts of equal magnitude but opposite sign in the two MZM arms, which results in an efficient and low-chirp push-pull operation of the modulator [18].

Regarding the high-speed performance of the devices, the main limitation is caused by the fact that the slot waveguide acts as a capacitor which has to be charged and discharged via the resistive doped Si slabs. The corresponding resistance-capacitance RC cut-off frequency can be increased by decreasing the Si slab resistance. This can be achieved by applying a gate voltage U_{gate} between the Si substrate and the Si device layer which induces a highly

conductive charge accumulation layer in the Si slabs [81]. For the high-speed experiments discussed in Section 5.4, we apply a gate field of about 0.07 V/nm, which results in a measured 3 dB EO bandwidth of about 20 GHz for both investigated devices. The bandwidth can be increased by using optimized doping profiles, which reduce the resistance of the Si slabs without compromising the low optical attenuation.

5.3 EO material and thermal stability tests of SOH modulators

For testing the stability and reliability of the SOH modulators, we adhere to Telcordia standards which specify generic test protocols for telecommunication equipment [55]. For modulators that are based on OEO materials, high-temperature storage tests over 2000 h at 85°C according Telcordia GR-468-CORE (paragraph 3.3.2.1) are particularly challenging. This is due to the fact that the macroscopic EO activity of organic materials is externally induced in a poling process at elevated temperatures [56], which leads to an acentric orientation of the dipolar OEO molecules and hence to an increased potential energy of the system. This state is conserved by cooling the device to room temperature, thus reducing molecular mobility and preventing relaxation of the molecules towards an energetically favored random orientation. When exposing a poled OEO device to an elevated temperature, however, the molecular mobility is again increased, thus giving rise to a relaxation of molecular orientation and to partial or complete loss of the electro-optic activity [19,48,49,163]. A critical parameter regarding thermal relaxation of acentric molecular order is the glass-transition temperature T_g: Thermal relaxation is negligible as long as the storage temperature is well below T_g and only becomes relevant for temperatures close to or above T_g. High-T_g materials are hence instrumental for long-term thermal stability of modulators using OEO materials.

In our devices, we use a recently introduced side-chain EO material [162]. The molecular structure of the OEO material is depicted in Figure 5.2(a). The material is based on a methyl methacrylate (MMA) polymer backbone with four different units. The first unit contains an adamantyl side group (magenta).

Due to its bulky character, this side group makes the polymer chain less mobile and thus increases T_g. Additionally, the side group is nonpolar such that no detrimental interaction with the chromophore group arises. The second unit is a non-functionalized MMA group, and the third unit contains a phenyl vinylene thiophene (PVT) chromophore (blue), which provides the EO activity of the polymer and which is connected to the MMA backbone via a linker (red). The last unit is an unintentional residual, which contains only a linker side group where no PVT chromophore was attached. The sequence of the four units along a polymer chain is random, and the relative proportions amount to $l = 0.4$, $l = 0.4$, m and o, for the first, second, third and fourth unit, respectively, where $m + o = 0.2$ and $m \gg o$. For this composition, the material exhibits a high T_g of 172 °C, measured by differential scanning calorimetry. The material thus promises excellent thermal stability even at elevated storage temperatures. During material synthesis, the proportion of all units can be adjusted by the concentration of the associated educts which allows to design both T_g and the EO activity. For example, a very similar EO polymer with a higher adamantyl proportion of 54 % was recently synthesized and featured an increased T_g of 194 °C but a slightly reduced EO activity [163].

To pole our specific EO polymer Figure 5.2(a), its temperature is set to $T_g = 172$ °C while we apply an electric field of 140 V/µm. To quantify the modulation efficiency of the poled devices, we measure the π-voltages U_π by using the experimental setup depicted in Figure 5.2(b). An external-cavity laser provides the optical carrier that we couple to and out of the device via grating couplers (GC). Using a function generator (FG), we feed the modulator with a triangular electrical voltage having a peak-to-peak amplitude $U_{d,pp} > U_\pi$. The modulated out-coupled light is detected with a photodiode (PD), and an oscilloscope records both the modulated optical signal (red line, left axis) and the triangular drive voltage (blue line, right axis), see Figure 5.2(c) for typical curves. Since the modulating voltage is chosen slightly larger than U_π, we can directly measure U_π as the drive voltage difference, which switches the MZM between maximum and minimum transmission. The lowest measured π-voltage amounts to 1.48 V for a 1.5 mm long device resulting in a π-voltage-length product of 2.22 Vmm. From this
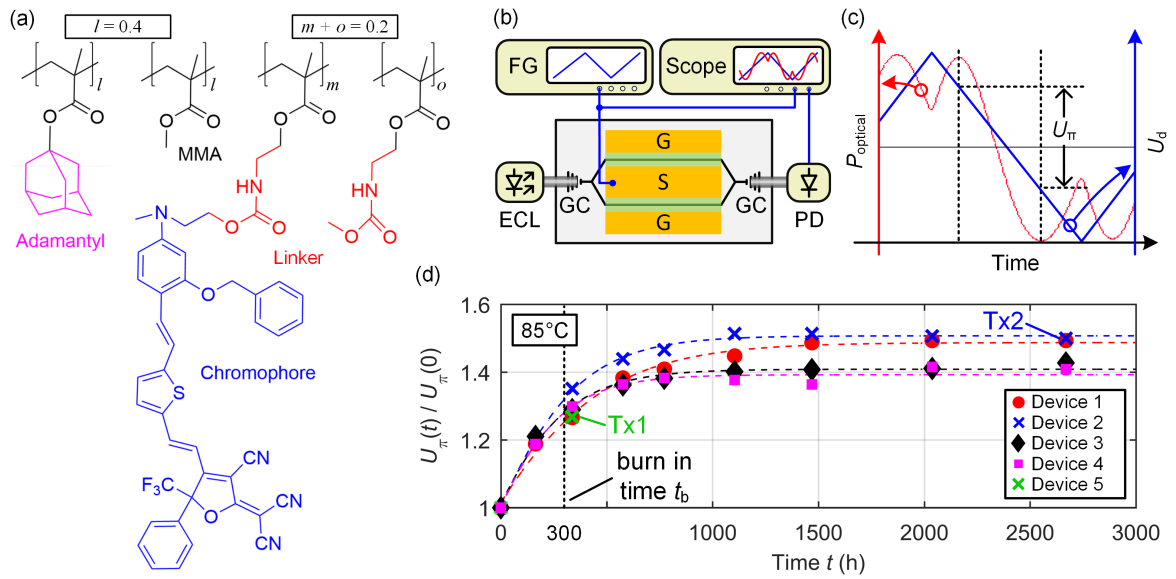
Figure 5.2: EO material characterization. **(a)** Molecular structure of the EO polymer. The polymer chain consists of a random concatenation of many methyl-methacrylate-(MMA-)based units, marked by square brackets [unit]$_{l,m,o}$. The first unit contains a bulky *adamantyl* side group (magenta), which increases T_g of the polymer, while the second unit is an MMA unit *without* a side group. The third unit contains a phenyl vinylene thiophene *chromophore* side group (blue), which induces the EO activity and which is connected to the MMA backbone via a *linker* group (red). The fourth unit contains only the *linker* side group and corresponds to unintentionally unoccupied chromophore binding sites. The relative proportions of the four types of units (*adamantyl*, *without*, *chromophore*, *linker*) amount to $l = 0.4$, $l = 0.4$, m, o, respectively, with $m + o = 0.2$ and $m \gg o$. With this composition, T_g amounts to 172 °C, measured by differential scanning calorimetry. **(b)** Experimental setup for static π-voltage measurement. Light of an external-cavity laser (ECL) is coupled to and out of the modulator by grating couplers (GC). A triangular waveform from a function generator (FG) is fed to the GSG transmission line. The modulated light is detected by a photodiode (PD). The signals of the PD and the FG are monitored by an oscilloscope. **(c)** Modulated optical power (red line, left axis) and triangular drive voltage (blue line, right axis) as a function of time. The device is operated at its 3 dB point. The voltage increment required for a transition from maximum to minimum transmission corresponds to the π-voltage U_π. **(d)** Long-term thermal stability testing of four SOH modulators at 85 °C according to Telcordia protocols GR-468-CORE (paragraph 3.3.2.1) for high-temperature storage. We depict the normalized π-voltage as a function of time. In all experiments, the π-voltage reaches a constant long-term stable level after an initial increase. When allowing for a burn-in time of $t_b \approx 300$ h, the π-voltage of the devices increases on average by less than 15 % for an additional high-temperature storage period of at least 2400 h, *i.e.*, $U_\pi(t_b + 2400\,\text{h}) < 1.15\,U_\pi(t_b)$. Tx1 and Tx2 indicate devices that are used for data transmission experiments to prove that high-temperature storage does not impair the high-speed functionality of the devices, see Section 5.4. Device 1 … 4 were simultaneously tested in a first storage run, whereas Device 5 (Tx1), indicated by a green cross, was measured during a second run and removed from the oven shortly after the burn-in time t_b to serve as a benchmark to Device 2 (Tx2) in the transmission experiments.

value we calculate a maximum in-device EO coefficient of 80 pm/V assuming

a refractive index $n = 1.67$ of the OEO material and a computed field interaction factor $\Gamma = 0.18$ [140], Supplementary information, Eq. (S6).

For a systematic investigation of thermally induced relaxation in SOH modulators, we pole four nominally identical devices and store them in an oven at a temperature of 85 °C in accordance with pertinent Telcordia standards GR-468-CORE (paragraph 3.3.2.1) for high-temperature storage [55]. Note that the devices were not hermetically sealed and thus not protected from oxygen or humidity. During the storage, the devices are neither optically nor electrically connected. Since thermal relaxation reduces the in-device EO activity of the modulators, the π-voltage of the devices increases. To monitor this process, the modulators are removed from the oven from time to time to measure the change in U_π. The experimental results for the four devices are summarized in Figure 5.2(d) where $U_\pi(t)$ normalized to its respective initial value $U_\pi(0)$ is plotted as a function of time t. All devices show qualitatively the same trend where $U_\pi(t)$ converges towards a constant long-term stable level after an initial increase during the first few hundred hours.

For a better understanding of the relaxation processes, we model the decay of the EO activity by a theoretical model. There exists a multitude of published models to describe the thermally induced decrease in EO activity in poled organic EO materials. These models range from theory-based Debye models [164], which describe a simple exponential decay, to semi-empirical models describing a bi-exponential decay [51,52], or purely empirical models, e. g., stretched exponential models [165–167]. In this work, we choose a modified Debye model due to its simplicity and its good fit to the measured data. Taking into account that the π-voltage U_π is inversely proportional to the EO activity and that it converges towards a stable value, the relaxation can be modelled by

$$\frac{U_\pi(t)}{U_\pi(0)} = \frac{1}{\mathcal{A} + \mathcal{B}e^{-t/\tau}} \, . \tag{5.1}$$

In this relation, the quantities $\mathcal{A}$, $\mathcal{B}$ and τ are used as fit parameters to adapt the model to the experimental findings. The quantity $1/\mathcal{A}$ is the limit of $U_\pi(t)/U_\pi(0)$ for large times t, $\mathcal{B}$ is a weighting parameter for the exponential decay of the EO activity, and τ is the corresponding characteristic decay time.

The experimental data in Figure 5.2(d) show good agreement with this model as indicated by the dashed lines, which are obtained from least-squares fits. The increase of U_π may be attributed to a thermally induced relaxation process in the EO polymer, which releases mechanical stress that was previously induced during the cooling step of the poling process. We believe that this effect can be further reduced by using optimized poling and cooling protocols. The fact that U_π reaches a long-term stable level can be attributed to the large difference between $T_g = 172$ °C and the storing temperature of 85 °C, at which the molecular mobility of the polymer chain is negligible. Quantitatively, we deduce from Figure 5.2(d) that after an initial burn-in time t_b of approximately 300 h, the π-voltages of the devices increase on average by less than 15 % for at least an additional 2400 h.

In a potential application scenario, the poled SOH MZM would undergo the burn-in process after poling and prior to shipping the devices. It is therefore particularly interesting to compare the high-speed performance of a device right after the burn-in process with a device that has undergone the full 2700 h of high-temperature storage. To that end, we performed a second high-temperature storage run with a single device (Device 5) indicated by a green cross in Figure 5.2(d), which we removed from the oven at $t = 330$ h, *i.e.*, shortly after the burn-in time t_b. This device serves as a benchmark to Device 2 in the transmission experiments described in Section 5.4. The relative increase of U_π of Device 5 is in good agreement with the other data sets, confirming the reproducibility of the experiments.

To the best of our knowledge, these experiments represent the first demonstration of SOH MZM that are long-term thermally stable in accordance with Telcordia standards for high-temperature storage. The measured values for $U_\pi(0\text{ h})$ and $U_\pi(2700\text{ h})$ as well as the fitting parameters for all four devices are summarized in Table 5.1 and indicate consistent performance. After 2700 h at 85 °C, the devices with a length of $L = 1.5$ mm exhibit an average π-voltage-length product $U_\pi L$ as low as 3.3 Vmm. This is roughly four times lower than the values obtained from other long-term stable organic-based EO modulators [19,163]. The improvement can be mainly attributed to the slot waveguide used in the SOH phase shifter: The narrow slot width w_{slot} leads to much larger modulating field strengths of approximately U_d / w_{slot} for a given

modulating drive voltage U_d as compared to competing device geometries where the electrodes are spaced several micrometers apart [19,163]. In addition, the SOH devices exhibit a large overlap of the optical and the modulating RF electric field [15], which is instrumental to achieve good modulation efficiency, see also Section 5.2.

5.4   Data transmission experiment

To demonstrate the full functionality of our devices even after high-temperature storage, we validate the high-speed performance of the SOH MZM by generating 40 Gbit/s on-off keying (OOK) signals. To this end, we use a device shortly after its burn-in (Device 5), labeled by Tx1 in Figure 5.2(d), as well as a device that was stored for the full 2700 h (Device 2), labeled as Tx2 in Figure 5.2(d). The experimental setup is shown in Figure 5.3(a). We use an arbitrary-waveform generator (AWG) as a signal source to obtain a pseudo random bit sequence of length 2^{15}-1. The signal is amplified by a broadband RF amplifier and applied to the SOH MZM using a microwave probe. To avoid back-reflections of the RF signal, we terminate the modulator with an external 50 Ω impedance via another microwave probe. An external-cavity laser (ECL) provides the optical carrier, which we couple to and from the chip via grating couplers (GC). For both, Tx1 and Tx2, we measure an extinction ratio in excess of 30 dB. The total insertion loss of each of the devices amounts to 14 dB and consists of fiber coupling losses, which are 4.5 dB per GC interface, and on-chip losses of 5 dB. The on-chip losses are caused by excess losses in passive structures such as strip waveguides, power splitters and strip-to-slot mode converters [127], which add up to about 2.5 dB, and losses in the phase shifter

Table 5.1. Summary of measurement and fitting results for thermal relaxation in SOH modulators

Device #	Experiment		Fit		
	$U_\pi(0\ \mathrm{h})$ [V]	$U_\pi(2700\ \mathrm{h})$ [V]	$\mathcal{A}$	$\mathcal{B}$	τ [h]
1	1.54	2.30	0.672	0.313	329
2	1.48	2.22	0.662	0.336	236
3	1.52	2.17	0.710	0.281	217
4	1.54	2.17	0.718	0.281	199
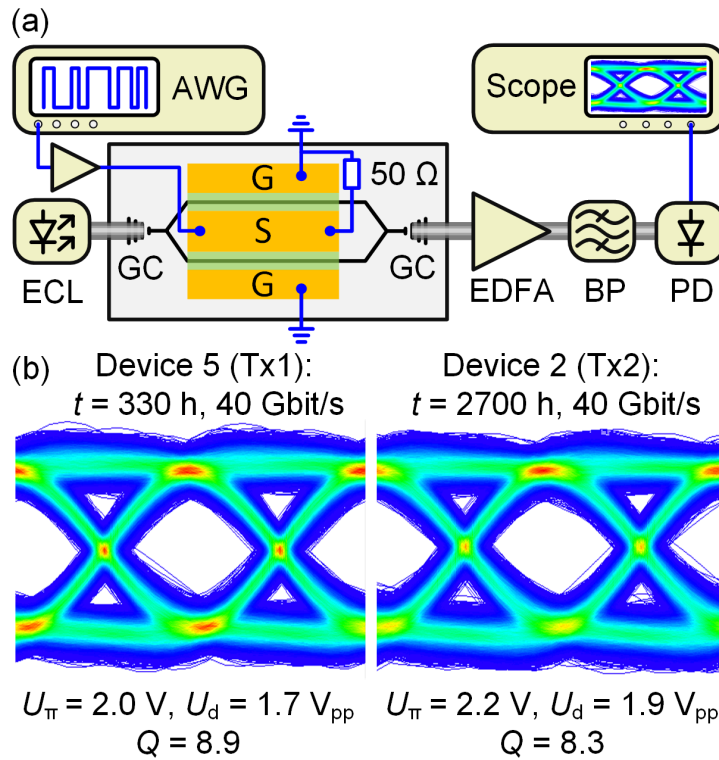
Figure 5.3: Data transmission experiment. **(a)** Experimental setup. The electrical 40 Gbit/s signal is obtained from an arbitrary-waveform generator (AWG). The drive signal is amplified and coupled to the chip by a microwave probe. A 50 Ω termination avoids back-reflection of the RF signal. An external-cavity laser (ECL) provides the optical carrier, which is coupled to and from the chip via grating couplers (GC). The modulated light is amplified in an erbium-doped fiber amplifier (EDFA), filtered by a bandpass filter (BP), and detected by a high-speed photodiode (PD) connected to a real-time oscilloscope. An adaptive digital filter at the receiver flattens the end-to-end frequency response of the system. **(b)** Measured 40 Gbit/s eye diagrams for Device 5 (left) after 330 h high-temperature storage and Device 2 (right) after 2700 h of high-temperature storage, see data points labeled as Tx1 and Tx2, respectively, in Figure 5.2(d). For a similar signal quality, the drive voltage for Device 2 needs to be increased by approximately 10%. This increase corresponds to the 10% higher π-voltage of Device 2 at 2700 h as compared to Device 5 at 330 h.

arms of the 1.5 mm long MZMs, which amount to another 2.5 dB. The relatively small propagation losses of the slot waveguides of 1.7 dB/mm in combination with the high extinction ratios of the MZM give us confidence that the slots are homogeneously filled with the OEO material. In addition, from previous experiments we know that PMMA, which is very similar to the MMA-based OEO material used in our present work, fills the slot entirely without forming any voids, as was confirmed by opening a cross-section by a focused ion beam

(FIB) cut [168]. Note that the on-chip losses can be reduced on the one hand by an optimized design of the passive components and on the other hand, by lithography processes featuring a higher resolution that may result in lower sidewall roughness of the strip and slot waveguides. The high coupling losses can be significantly reduced by optically packaging the devices, *e.g.*, by following the approach of photonic wire bonding [169]. Using this technique, indium phosphide lasers were connected to silicon photonic chips with coupling losses down to 0.4 dB [170]. The high insertion loss of the present devices requires compensation, and we amplify the optical signal after the chip using an erbium doped fiber amplifier (EDFA). To suppress amplified spontaneous emission noise we use a bandpass filter (BP). For signal detection, we use a high-speed photodiode (PD) connected to a real-time sampling oscilloscope. We rely on a commercial vector signal analysis software provided by Keysight to flatten the end-to-end frequency response in a post-processing step [171]. To this end, we use an adaptive filter with a length of only six taps according to an application-oriented scenario where latency should be minimized. Because the transfer characteristics of the modulators used in Tx1 and Tx2 are virtually identical with a deviation of less than 0.5 dB, the equalizing filters are practically the same in both cases.

Figure 5.3(b) shows the recorded OOK eye diagrams at a data rate of 40 Gbit/s for Device 5 (left), which was tested after 330 h of high-temperature storage and Device 2 (right), which was tested at the end of the full 2700 h. After the respective storage times, the π-voltages amount to 2.0 V and 2.2 V for Device 5 and Device 2, respectively. The peak-to-peak drive voltages are chosen such that roughly the same signal quality is achieved for both modulators. For Device 5, the measured Q factor amounts to 8.9 for a peak-to-peak drive voltage of 1.7 V_{pp}. For Device 2, we measure a Q factor of 8.3 for a slightly higher peak-to-peak drive voltage of 1.9 V_{pp}. Thus, to achieve roughly the same signal quality for both modulators, we have to increase the drive voltage of Device 2 by about 10 % compared to the drive voltage of Device 5. This increase in drive voltage can be directly linked to the 10 % larger π-voltage of Device 2 after 2700 h high-temperature storage as compared to Device 5 after 330 h. These results indicate that high-temperature storage primarily results in the slightly increased π-voltage while high-speed performance remains unchanged.

5.5　　Summary and outlook

We report on the first demonstration of long-term thermally stable silicon-organic hybrid (SOH) modulators in accordance with Telcordia standards of high-temperature storage. We find that after an initial burn-in time of 300 hours the SOH modulators retain more than 85 % of their modulation efficiency for at least an additional 2400 h. These demonstrations represent an important milestone towards industrial adoption of SOH technology outside a controlled laboratory environment. For future applications, the burn-in time can be significantly decreased by using higher burn-in temperatures, which accelerates the initial relaxation process [19]. The average π-voltage-length product of the four investigated 1.5 mm long modulators amounts to 3.3 Vmm after 2700 h at 85 °C. This corresponds to a four-fold improvement compared to previously reported long-term stable modulators based on organic EO materials [19,163]. Given the vast potential of theory-guided material optimization, we expect that even more efficient long-term stable SOH devices with $U_\pi L$-products below 1 Vmm will come into reach in the near future. We have also shown that the devices are suitable for applications in high-speed optical communication systems by demonstrating the generation of 40 Gbit/s OOK signals using devices shortly after the 300 h burn-in as well as devices that have undergone the full 2700 h of high-temperature storage at 85 °C. The results show that the long-term storage at 85 °C does not impair the general high-speed performance of the devices.

One of the last remaining challenges for an industrial adoption of SOH modulators is a potential photo-induced degradation of the organic EO chromophores due to the high optical intensities in the nanoscopic slot waveguide. Studies have shown that the degradation process is caused by an oxidation of the EO chromophores, and that it can be prevented by operating the modulators in an oxygen-free environment [19,20]. This can be achieved by, *e.g.*, applying an oxygen-blocking encapsulation on the devices. We are thus confident that in the near future SOH modulators will be not only resistant against thermal relaxation but also against photo-induced damages.

[end of paper [J3]]

6   Measurement techniques for $\chi^{(2)}$ of thin-film materials based on second-harmonic generation

This section compares two second-harmonic generation measurement methodologies, which are well suited for thin film nonlinear films. The respective advantages and disadvantages are investigated and a thorough discussion of the involved measurement inaccuracies is included. The section is taken from a publication in *Scientific Reports* [J4]. To fit the structure and layout of this document, it was adapted accordingly. The associated supplementary information is found in Appendix C.

For this publication Artur Hermans (A.H.) conducted and analyzed the experiments performed with the setup at Ghent University. Clemens Kieninger (Cl.K.) conducted and analyzed the experiments performed with the setup at Karlsruhe Institute of Technology (KIT). Kalle Koskinen conducted the ITA reference measurement on a blank glass substrate. Cl.K. conducted the HTA reference measurement on a quartz crystal. Andreas Wickberg fabricated the HTA sample. Eduardo Solano and Jolien Dendooven contributed to the fabrication of the ITA sample. All authors contributed to writing the manuscript. The work was supervised by Martin Wegener, Christian Koos and Roel Baets.

[start of paper [J4]]

Artur Hermans,[1,2]* **Clemens Kieninger**,[3,4]* Kalle Koskinen,[5] Andreas Wickberg,[6] Eduardo Solano,[7] Jolien Dendooven,[7] Martti Kauranen,[5] Stéphane Clemmen,[1,2] Martin Wegener,[6,8] Christian Koos,[3,4] and Roel Baets[1,2]

*These authors contributed equally to this work.

[1] Ghent University (UGent) - imec, Department of Information Technology (INTEC), Photonics Research Group, Ghent 9052, Belgium
[2] Ghent University (UGent) - imec, Center for Nano- and Biophotonics (NB-Photonics), Ghent 9052, Belgium
[3] Karlsruhe Institute of Technology (KIT), Institute of Photonics and Quantum Electronics (IPQ), 76131 Karlsruhe, Germany
[4] Karlsruhe Institute of Technology (KIT), Institute of Microstructure Technology (IMT), 76344 Eggenstein-Leopoldshafen, Germany
[5] Tampere University of Technology, Optics Laboratory, Tampere 33101, Finland
[6] Karlsruhe Institute of Technology (KIT), Institute of Applied Physics, 76128 Karlsruhe, Germany
[7] Ghent University, Department of Solid State Sciences, Ghent 9000, Belgium
[8] Karlsruhe Institute of Technology (KIT), Institute of Nanotechnology, 76021 Karlsruhe, Germany

The determination of the second-order susceptibility ($\chi^{(2)}$) of thin film samples can be a delicate matter since well-established $\chi^{(2)}$ measurement methodologies such as the Maker fringe technique are best suited for nonlinear materials with large thicknesses typically ranging from tens of microns to several millimeters. Here we compare two different second-harmonic generation setups and the corresponding measurement methodologies that are especially advantageous for thin film $\chi^{(2)}$ characterization. This exercise allows for cross-checking the $\chi^{(2)}$ obtained for identical samples and identifying the main sources of error for the respective techniques. The development of photonic integrated circuits makes nonlinear thin films of particular interest, since they can be processed into long waveguides to create efficient nonlinear devices. The investigated samples are ABC-type nanolaminates, which were reported recently by two different research groups. However, the subsequent analysis can be useful for all researchers active in the field of thin film $\chi^{(2)}$ characterization.

6.1 Introduction

Second-order nonlinear optical processes enable a whole range of applications used in a variety of areas, ranging from research oriented tools to widespread commercially available devices [172]. One major field of application are the

light sources based on second-order nonlinear effects, such as frequency doubled lasers [173] (*e.g.,* most green laser pointers), optical parametric oscillators (OPO's, sold by plenty of laser manufacturers [174,175]), THz generators5 and quantum light sources [176,177]. Another application domain is optical signal processing. Electro-optic modulators [178], widely used in fiber-optic communication, and optical correlators [179,180] are two prominent examples of such signal processing devices. Also various characterization methods utilized in research are based on second-order nonlinear processes, like second-harmonic imaging microscopy [181,182] and surface second-harmonic generation to probe material interfaces [183,184].

Exploiting the advancements made in integrated optics, the aforementioned devices can be implemented in photonic integrated circuits (PIC's) to decrease cost and footprint, increase the device efficiency and add functionality to existing PIC's. In integrated optics, materials that are deposited or grown in thin films are of vital importance, as they very often serve as a starting point in the fabrication of waveguide circuits through lithography techniques [185]. The integration of nonlinear functions and the search for second-order nonlinear thin film materials are both active fields of research. This makes the existence of easy and reliable methods for the characterization of the second-order nonlinearity in thin films undoubtedly an asset.

The strength of any second-order nonlinear process is characterized by the second-order susceptibility tensor $\chi^{(2)}$. As a tensor of rank 3, $\chi^{(2)}$ consists of $3^3 = 27$ elements. Typically, the number of independent, non-zero elements is much lower because of symmetry properties [6]. Nonetheless, determining the $\chi^{(2)}$ tensor elements of a nonlinear material remains a delicate task.

There are several different approaches to determine $\chi^{(2)}$ of a material. Often, electro-optic modulation via the Pockels effect is exploited for that purpose [15,186]. However, this technique requires electrodes and typically uses waveguiding structures, which means additional design and fabrication effort is needed. A more straightforward way to determine $\chi^{(2)}$ is to exploit the effect of second-harmonic generation (SHG). In this well-known second-order nonlinear process, light at the fundamental frequency ω interacts with a nonlinear material to generate light at the double frequency 2ω. SHG in waveguiding structures can be very efficient if the phase matching condition is

satisfied and the modal overlap is large [187]. But as these requirements demand a substantial amount of engineering, the use of waveguiding structures is not very suitable for material characterization. Hence simple free-space transmission experiments are usually preferred.

Shortly after the first demonstration of second-harmonic generation [27], a standard technique, called the Maker fringe method, was developed to determine $\chi^{(2)}$ of nonlinear crystals [188]. Over the years various alterations of the formalism have been suggested to include effects such as anisotropy, absorption and reflections in multilayer media [33,189–191]. The technique is based on Maker's finding that the pattern of the transmitted second-harmonic (SH) power generated in a bulk nonlinear crystal reveals the so-called Maker fringes when the crystal is rotated [192]. These fringes occur since the SHG process is not phase matched and the SH waves generated at different locations in the crystal can interfere constructively or destructively depending on the effective length of the crystal that is changed by the rotation. The Maker fringes serve as characteristic features that allow for a reliable extraction of $\chi^{(2)}$ when the experimental data is fitted with theoretical expressions. The downside of this approach is that distinct Maker fringes are only visible if the thickness of the nonlinear material is significantly larger than the coherent build-up length [6]. This is not the case for submicron thin films which have attracted attention in recent years due to their application perspectives in integrated optics [193–197]. Therefore, there is a demand for alternative measurement methodologies that are better suited for thin film $\chi^{(2)}$ characterization.

In parallel to the early research on bulk effects in nonlinear crystals, the field of surface second-harmonic generation emerged. In media with inversion symmetry second-order effects are forbidden in the electric dipole approximation, *i.e.*, $\chi^{(2)} = 0$. However, at the interface between two centrosymmetric media, the inversion symmetry is naturally broken and second-order effects are allowed again [6,183]. The effect was first reported in calcite by Terhune and co-workers [198]. Since then, it has been used as a research tool for investigating the interface structure of various centrosymmetric materials, for studying the adsorption of molecular monolayers and monitoring surface chemistry [199–203]. In a typical experiment the strength of the transmitted or reflected SHG is measured as a

function of the angle of incidence and/or the polarization state [204]. This allows determination of the surface $\chi^{(2)}$ tensor elements, which on its turn provides information about the atomic structure of the interface, the concentration and orientation of adsorbed molecules, etc. As in surface SHG the $\chi^{(2)}$ layer is only a few atoms thick, no Maker fringes are observed.

In this work we use elements from both the worlds of SHG in bulk media and surface SHG to determine $\chi^{(2)}$ of ultrathin films deposited on a centrosymmetric substrate. More specifically, the samples characterized are second-order nonlinear ABC-type nanolaminate optical metamaterials on glass substrates. These materials were recently introduced to the community by two independent research groups at Karlsruhe Institute of Technology (KIT) [21] and Ghent University (UGent) [22]. The UGent and KIT group utilize different $\chi^{(2)}$ measurement techniques. In the present work, the two measurement methodologies with their corresponding calibration methods and theoretical models will be analyzed and the main sources of error will be identified. Both groups use a one-beam second-harmonic generation characterization technique. It has been shown that accurate determination of $\chi^{(2)}$ for thin films is possible with a sophisticated two-beam geometry, that is, an arrangement with two fundamental beams incident on the sample [205]. However, the alignment of the two fundamental beams is challenging and can introduce additional errors.

The approach of the UGent group is similar to the Maker fringe technique where for a fixed polarization of the fundamental beam the SH power is recorded while rotating the sample. Also in the UGent measurements fringes appear and they are used in the data fitting to obtain $\chi^{(2)}$. However, the source of these fringes is not the same as in a traditional Maker fringe experiment. It is exploited that the SH signal generated in the thin film interferes with SH radiation generated at the glass-air interface (backside of the sample). For very thin films that do not have a very high nonlinearity (films in this work are thinner than 100 nm and have $\chi^{(2)} \sim 1$ pm/V) a fringe pattern shows up in the recorded SH powers. To implement the glass-air surface nonlinearity in the UGent model, a formalism from the field of surface SHG is utilized. Because a femtosecond laser is used in the measurements, also temporal walk-off effects occurring in the substrate need to be taken into account for a correct $\chi^{(2)}$ characterization. The KIT group uses a different approach where the angle of incidence is fixed and the s- and p-

polarized SH power is recorded as a function of the polarization of the incident fundamental beam. An adapted form of a standard Maker fringe model is used to accommodate for the varying polarization state rather than a change in angle of incidence.

In summary, we present a comparison between two measurement techniques with their corresponding calibration methods and theoretical models for determination of the $\chi^{(2)}$ tensor elements of ABC-type metamaterials. For both techniques, the major advantages but also the shortcomings and most important sources of error will be identified. In order to compare the reliability of the absolute values of the determined $\chi^{(2)}$ tensor elements for the two different techniques, both research teams exchanged their nanolaminates. That is, identical samples are measured by both teams with their respective measurement technique and the results are compared to identify potential sources of uncertainty. Note that these findings are not restricted to ABC-type nanolaminate metamaterials but hold for thin nonlinear films in general. Therefore this paper can be used as a guideline for researchers wanting to characterize their own $\chi^{(2)}$ thin films.

6.2   Materials and Setups

The ABC-type nanolaminates analyzed in this article consist of very thin layers (on the order of 1 nm) of three amorphous (and thus centrosymmetric) materials A, B and C that are deposited alternately through atomic layer deposition (ALD). At each of the interfaces the inversion symmetry is broken locally and consequently second-harmonic (SH) waves can be generated. The layers are combined to an ABCABC… stack that also breaks the inversion symmetry globally. In this way destructive interference between the generated SH waves is avoided, as would happen in an ABAB… stack. The nanolaminate of Ghent University consists of the three materials TiO_2, Al_2O_3 and In_2O_3. It is deposited on a 500 μm BOROFLOAT$^®$ 33 substrate and has a total thickness of 66 nm obtained from ellipsometry and transmission electron microscopy. The nanolaminate of Karlsruhe Institute of Technology is composed of the three materials Al_2O_3, HfO_2 and TiO_2. It has a thickness of 75 nm obtained from ellipsometry and the substrate is borosilicate glass of the first hydrolytic class
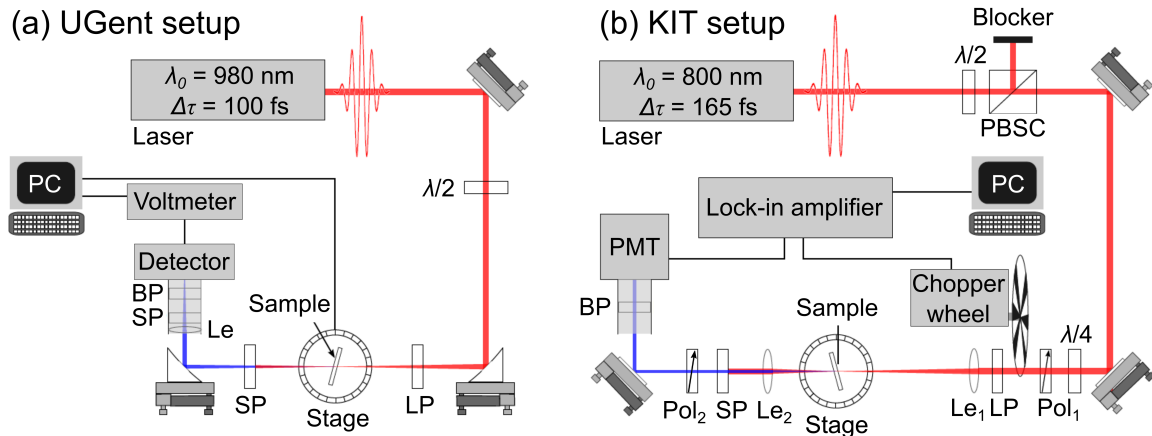
Figure 6.1: Schematic representation of the experimental setups at **(a)** UGent and **(b)** KIT for characterizing the second-order nonlinearity of the nanolaminates by means of second-harmonic generation (SHG). PBSC: polarizing beam-splitter cube, Pol_1, Pol_2: wire-grid polarizers, $\lambda/2$, $\lambda/4$: half- and quarter-wave plate, LP: longpass filter, Le: lenses, SP: shortpass filter, BP: bandpass filter, PMT: photomultiplier tube.

with a thickness of 170 μm. More information about the fabrication of these ABC-type thin films can be found in the Methods section 6.6. In the remainder of this paper the nanolaminates of UGent and KIT will be referred to as ITA ($In_2O_3/TiO_2/Al_2O_3$) and HTA ($HfO_2/TiO_2/Al_2O_3$) respectively.

Due to the limited thickness of these nanolaminates, the generated SH power is quite small, which means a powerful laser combined with sufficiently sensitive detection is necessary for generating and detecting the SH power. The UGent and KIT setups are shown in Figure 6.1(a,b), respectively. In the UGent setup the light source is a commercial Ti:Sapphire laser (Mai Tai HP from Spectra-Physics) emitting 100 fs pulses at a wavelength of 980 nm, a repetition rate of 80 MHz and an average power close to 1 W. A half-wave plate ($\lambda/2$) is used to rotate the polarization direction of the linearly polarized laser light to p-polarization. Two parabolic mirrors of 5 cm focal length are used to focus the laser beam on the sample and to collimate it again after passing through the sample. The focusing brings the beam diameter ($1/e^2$) down from 1.2 mm to 52 μm. This leaves us with a depth of focus, *i.e.,* $2 \times$ Rayleigh length, of 4.5 mm, giving enough tolerance for the alignment of the sample in the focal plane. Surrounding the sample there is a longpass (LP) and shortpass (SP) filter. The former filters out any spurious light at wavelengths below 800 nm, while the latter suppresses the laser light at the fundamental wavelength and lets the SH

light through. It is important to place these filters right before and after the sample to eliminate parasitic SHG originating in the beam path. The sample is placed on a motorized rotation stage (Thorlabs CR1-Z7) and allows for measurement automation. A lens (Le) is placed in front of the femtowatt detector (Thorlabs PDF10A) which compensates for beam displacements induced by the rotation of the sample. There is also a bandpass (BP) filter that removes part of the stray light. Moreover it allows to check that the detected light is truly SHG: by tuning the fundamental wavelength until the SH wavelength falls out of the passband of the filter and checking that the detected signal vanishes. During a measurement the sample is rotated and the SH power is measured as a function of the incidence angle.

In the KIT setup, the nonlinear samples are excited using laser pulses from a Ti:Sapphire mode-locked oscillator (Tsunami from Spectra-Physics) operating at a repetition rate of 80.5 MHz, a pulse duration of 165 fs FWHM (full width at half maximum), a center wavelength of 800 nm and an average power of around 2 W. The excitation power can be set by rotating a half-wave plate ($\lambda/2$) which is followed by a polarizing beam-splitter cube (PBSC). A quarter-wave plate ($\lambda/4$) is used to get a circularly polarized beam. Subsequently, a wire-grid polarizer (Pol_1) sets the beam at a constant power to a linear polarization at an angle tunable between 0° (s-polarized) and 90° (p-polarized). The laser beam is chopped to allow for lock-in detection and passes a longpass filter (LP) that removes potential parasitic SHG prior to the sample. The fundamental pump beam is then loosely focused onto the sample to a spot diameter ($1/e^2$) of about 50 μm using a lens (Le_1) with a focal length of 200 mm. The diverging light is collimated by a lens (Le_2) with a focal length of 100 mm and filtered by a shortpass (SP) (cut-off wavelength 700 nm) and a bandpass (BP) filter (center wavelength 400 nm, spectral width 40 nm). Finally, the SH power is detected using a Hamamatsu R4332 photomultiplier tube (PMT). To distinguish between s- and p-polarized SH light, a wire-grid polarizer (Pol_2) is placed in the beam path between the sample and the photomultiplier tube. The sample is mounted on a rotation stage which allows to set the angle of incidence. In addition, the sample mount features two goniometers that can be used to correct for tilt of the sample relative to the fundamental beam and relative to the rotation axis of the rotation stage.
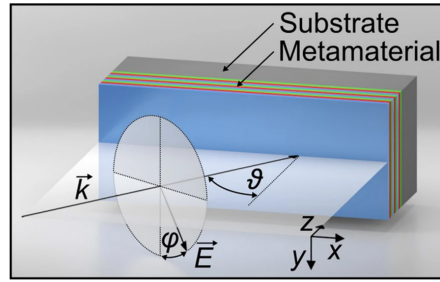
Figure 6.2: Illustration of the excitation geometry including the angle of incidence ϑ and the polarization angle φ. Incident s-polarization corresponds to $\varphi = 0°$, p-polarization to $\varphi = 90°$. Figure taken from Ref. [21].

6.3 Models and calibration

The individual nanoscale A, B and C layers of the nanolaminate are not considered in the analysis, instead an effective medium approach is used. Since these ABC-type materials show a $C_{\infty v}$ symmetry with respect to the film normal, the non-vanishing second-order susceptibility tensor components for SHG are $\chi^{(2)}_{xxz} = \chi^{(2)}_{yyz} = \chi^{(2)}_{xzx} = \chi^{(2)}_{yzy}$, $\chi^{(2)}_{zxx} = \chi^{(2)}_{zyy}$ and $\chi^{(2)}_{zzz}$, where z is the film normal and x and y are two orthogonal in-plane directions, see Figure 6.2 [202]. We assume that these tensor elements are real as we are working at wavelengths far from resonance. Note that the presented theoretical models are readily applicable to thin nonlinear films that possess the same symmetry properties, *e.g.*, ZnO thin films [195]. After adapting the non-zero tensor elements, the models can be used for films with a different symmetry as well.

In general the SH electric field components generated in an achiral thin film with in-plane isotropy ($C_{\infty v}$ symmetry) can be expressed as $E_{2\omega,p} = fE^2_{\omega,p} + gE^2_{\omega,s}$ and $E_{2\omega,s} = hE_{\omega,s}E_{\omega,p}$, where p and s stand for the p- and s-polarized components and E_ω refers to the electric field amplitude of the incident fundamental beam [206]. The quantities f, g and h are functions that depend on the nonlinear susceptibility tensor components, the incidence angle, the linear optical properties, the frequency and the thickness.

In the UGent model, two contributions to the total SH signal are considered: SH waves generated at the front interface of the sample, where the thin film is deposited, and SH waves generated at the back glass-air interface. Furthermore,

the thin film is assumed to have zero thickness. This translates into a physical model where polarized sheets are located at the front and back interface of the sample. The nonlinearities are described by surface second-order susceptibility tensors χ_s^i for the air-thin film ($i = \text{ABC}$) and the glass-air interface ($i = \text{glass}$) [204]. In our definition of χ_s^i we use internal electric fields, meaning that the nonlinearities are defined with respect to the electric fields inside the thin film (for the front interface) and inside the glass (for the back interface). The surface susceptibility of the thin film is converted to a bulk susceptibility by dividing χ_s^{ABC} by the thin film thickness. We neglect multiple reflections (inside the thin film and the glass substrate) and we also do not take into account the birefringent character of the thin films. Instead we use an average refractive index. Note that the degree of anisotropy is only a few percent for the ITA sample [22] and negligible for the HTA sample according to ellipsometry measurements. To justify these simplifications, we compared our model to a more advanced model taking into account reflections, anisotropy and finite film thickness, see Figure C.4, showing the limited impact of these factors. When including these effects the involved equations become cumbersome and less straightforward to interpret physically. Intuitively, one can understand that the zero film thickness is a good approximation for films much thinner than the wavelength and the coherence length. As we are dealing with small refractive index contrasts ($n_{\text{glass}} \approx 1.5$ and $n_{\text{ABC}} \approx 2$), reflections will also be small as long as the incidence angle is not too large. For p-polarized light, the reflection only rises significantly once Brewster's angle is passed. Our analysis shows that we can safely neglect reflections if we keep the incidence angle below 70°. Since the incident fundamental beam is p-polarized in the UGent setup, the generated SH waves will also be p-polarized. For a monochromatic p-polarized plane wave at the fundamental frequency with electric field amplitude $E_{\omega,\text{in}}$ incident on the sample, we can find the following expression for the transmitted electric field at the SH frequency [207,208]

$$E_{2\omega,\text{total}} = E_{2\omega,\text{front}} + E_{2\omega,\text{back}}$$

$$= -j\frac{\omega}{2c}(t_{\text{a-f},\omega}^{\text{p}})^2 E_{\omega,\text{in}}^2 \left[\frac{t_{\text{f-s},2\omega}^{\text{p}} t_{\text{s-a},2\omega}^{\text{p}}}{n_{\text{f},2\omega}\cos(\theta_{\text{f},2\omega})} \chi_{\text{s,eff}}^{\text{ABC}} \exp\left(-j\frac{2\omega n_{\text{s},2\omega}\cos(\theta_{\text{s},2\omega})}{c}d_{\text{s}} \right) \right. \quad (6.1)$$

$$\left. - \frac{(t_{\text{f-s},\omega}^{\text{p}})^2 t_{\text{s-a},2\omega}^{\text{p}}}{n_{\text{f},2\omega}\cos(\theta_{\text{f},2\omega})} \chi_{\text{s,eff}}^{\text{glass}} \exp\left(-2j\frac{\omega n_{\text{s},\omega}\cos(\theta_{\text{s},\omega})}{c}d_{\text{s}} \right) \right]$$

,

with $\chi_{\text{s,eff}}^{i=\{\text{ABC,glass}\}}$ the effective surface second-order susceptibility defined as

$$\chi_{\text{s,eff}}^{i} = \chi_{\text{s,xxz}}^{i}\sin(2\theta_{f,\omega})\cos(\theta_{f,2\omega}) + \chi_{\text{s,zxx}}^{i}\sin(\theta_{f,2\omega})\cos^2(\theta_{f,\omega})$$

$$+ \chi_{\text{s,zzz}}^{i}\sin^2(\theta_{f,\omega})\sin(\theta_{f,2\omega})$$

$$\approx (\chi_{\text{s,zxx}}^{i} + 2\chi_{\text{s,xxz}}^{i})\sin(\theta_{f,2\omega})\cos^2(\theta_{f,\omega}) \qquad (6.2)$$

$$+ \chi_{\text{s,zzz}}^{i}\sin^2(\theta_{f,\omega})\sin(\theta_{f,2\omega})$$

.

In these relations, the index ω (2ω) indicates parameters specified at the fundamental frequency ω (SH frequency 2ω). The quantities $t_{i\text{-}j}^{\text{p}}$ are the Fresnel transmission coefficients (for p-polarized light) propagating from medium i to j, with $i,j = \{\text{a,f,s}\}$ for **a**ir, **f**ilm, **s**ubstrate. The parameter n_i is the refractive index of medium i, θ_i is the propagation angle with respect to the surface normal z in medium i, d_{s} is the thickness of the glass substrate and c is the speed of light. The refractive indices of the samples are: $n_{\text{f},\omega} = 1.9556$, $n_{\text{f},2\omega} = 2.0975$, $n_{\text{s},\omega} = 1.4633$ and $n_{\text{s},2\omega} = 1.4766$ for the ITA sample, and $n_{\text{f},\omega} = 1.901$, $n_{\text{f},2\omega} = 1.996$, $n_{\text{s},\omega} = 1.513$ and $n_{\text{s},2\omega} = 1.5297$ for the HTA sample. The refractive indices for the nanolaminates are determined through ellipsometry; for the glass substrate they are found in the datasheet supplied by the manufacturer. The approximation in Eq. (6.2) can be done because $\theta_{f,\omega} \approx \theta_{f,2\omega}$ for samples with low dispersion. This also means that $\chi_{s,zxx}^{\text{ABC}}$ and $\chi_{s,xxz}^{\text{ABC}}$ cannot be determined separately in the UGent measurement. Instead we use the combined value $\chi_{s,\text{sum}}^{\text{ABC}} = \chi_{s,zxx}^{\text{ABC}} + 2\chi_{s,xxz}^{\text{ABC}}$ as a fitting parameter. Using the non-approximated version of Eq. (6.2) in the regression analysis of the data leads to diverging results. In principle, $\chi_{s,zxx}^{\text{ABC}}$ and $\chi_{s,xxz}^{\text{ABC}}$ can be determined separately even for low-dispersion materials by studying the polarization signature of carefully chosen polarization combinations for the input and/or output beams. For example, if an

s-polarized fundamental beam is used only $\chi_{s,zxx}^{\mathrm{ABC}}$ will be probed. But in practice it is difficult to obtain reliable information from this type of measurements in the UGent setup, as the SH powers are close to the detection limit for the considered samples.

As we rotate the sample and detect the SH power, the front and back contributions will interfere resulting in an angle-dependent fringe pattern. These interference fringes form the basis of the UGent calibration method and can be used for $\chi^{(2)}$ extraction. A reference measurement needs to be done on a blank glass substrate to determine its surface second-order susceptibility $\chi_s^{(2)}$. For BOROFLOAT® 33, this measurement and the obtained $\chi_s^{(2)}$ values are shown in Figure C.1. For several other types of glass, the surface nonlinear susceptibility can be found in ref. [209]. The average detected power is given by $P_{2\omega} = K_1 \left| E_{2\omega,\mathrm{total}} \right|^2$, where K_1 is a function of the pulse duration, the repetition rate of the laser, the spot size and the transmission of the optics. As it can be difficult to know all these properties accurately, it is often preferred to determine K_1 from a calibration measurement. In the UGent calibration method we use the known nonlinear susceptibility of the back glass-air interface, to fit K_1 and the unknown susceptibility tensor elements of the thin film simultaneously. However, this calibration method cannot be used for films with a very strong nonlinear response, since the interference fringes will no longer be discernible.

Equation (6.1) is only strictly valid for monochromatic waves. When working with short laser pulses, there will be a temporal walk-off between the SH pulse generated at the front and back surface of the sample which Eq. (6.1) does not account for. The pulse at the fundamental wavelength will travel at a different group velocity through the substrate than the SH pulse generated at the front and thus there will be a small delay between both generated SH pulses. This reduces the depth of the interference fringes. If this effect is not taken into account, it will result in an overestimation of $\chi^{(2)}$ of the thin film. The temporal walk-off effect is implemented in the model by introducing sech^2 pulses [210]

$$P_{2\omega} = K_2 \int\limits_{-\infty}^{\infty} \left| E_{2\omega,\mathrm{front}} \operatorname{sech}^2 \left(\frac{t}{\frac{\Delta\tau}{2\ln(1+\sqrt{2})}} \right) + E_{2\omega,\mathrm{back}} \operatorname{sech}^2 \left(\frac{(t+t_{\mathrm{walk\text{-}off}})}{\frac{\Delta\tau}{2\ln(1+\sqrt{2})}} \right) \right|^2 dt, \quad (6.3)$$

with $\Delta\tau$ the FWHM pulse duration, $t_{\mathrm{walk-off}}$ the walk-off time and K_2 again a calibration constant. The walk-off time increases for increasing incidence angles and can be expressed as $t_{\mathrm{walk-off}} = t_{\mathrm{walk-off,0}}/\cos(\theta_{\mathrm{glass}})$, with $t_{\mathrm{walk-off,0}}$ the walk-off time for normal incidence.

The KIT model is based on the approach of Herman and Hayden [33] which solves the nonlinear wave equation and satisfies the boundary conditions for the SH wave at all interfaces of the sample: at the air-film, the film-substrate, and the substrate-air interface. The approach has been generalized for arbitrary polarization of the fundamental pump beam [21]. The model takes into account the thickness of the nanolaminate and therefore also the phase mismatch between fundamental and SH wave which becomes of importance for thick or very dispersive nonlinear films. However, the effect of multiple reflections inside the nanolaminate as well as inside the glass substrate at both the fundamental and SH frequency are neglected due to the small index difference. In addition, the small birefringence of the nanolaminate is neglected. Also, the formalism does not take into account the SH wave that is generated by the second-order nonlinearity of the substrate-air interface. For the p/s-polarized peak SH power which is generated in the sample the following expression is derived

$$P_{2\omega}^{\mathrm{p/s,peak}} = \underbrace{\frac{1}{A^{(\mathrm{spot})}\Delta\tau^2 f_{\mathrm{rep}}^2}}_{\alpha}$$

$$(6.4)$$

$$\times \frac{2\left(\left(\sin(\varphi)t_{\mathrm{a\text{-}f},\omega}^{\mathrm{p}}\right)^2 + \left(\cos(\varphi)t_{\mathrm{a\text{-}f},\omega}^{\mathrm{s}}\right)^2\right)^2 (t_{\mathrm{f\text{-}s},2\omega}^{\mathrm{p/s}} t_{\mathrm{s\text{-}a},2\omega}^{\mathrm{p/s}})^2}{c\varepsilon_0 (n_{\mathrm{f},2\omega}\cos(\theta_{\mathrm{f},2\omega}))^2} \left(\chi_{\mathrm{eff}}^{\mathrm{p/s}} \frac{2\pi}{\lambda} d_{\mathrm{f}} P_\omega \frac{\sin(\Psi)}{\Psi} \right)^2.$$

Parameters specified at the fundamental frequency (SH frequency) are indicated with a subscript ω (2ω). The quantity $t_{i-j}^{\mathrm{p/s}}$ denotes the Fresnel transmission coefficient (for p/s-polarized light) propagating from medium i to j, and n_i is the

refractive index of medium i. The constant c is the vacuum speed of light, $A^{(\text{spot})}$ is the spot size of the laser at the focus, $\Delta\tau$ is the FWHM of the temporal pulse and f_{rep} is the repetition rate of the laser. The quantity P_ω corresponds to the average incident laser power outside the nonlinear film, d_{f} is the thickness of the nonlinear film, λ_0 is the vacuum wavelength of the fundamental beam and φ is the pump polarization angle in air with $\varphi = 0°, 90°$ for s- and p-polarization, respectively. Possible phase mismatch between fundamental and SH waves is accounted for by the quantity $\Psi = 2\pi d_{\text{f}} / \lambda_0 \left(n_{\text{f},\omega} \cos(\theta_{\text{f},\omega}) - n_{\text{f},2\omega} \cos(\theta_{\text{f},2\omega}) \right)$, where $\theta_{\text{f},\omega}$ and $\theta_{\text{f},2\omega}$ are given by Snell's law $\sin(\theta_{f,\omega}) = 1 / n_{\text{f},\omega} \sin(\vartheta)$ and $\sin(\theta_{f,2\omega}) = 1 / n_{\text{f},2\omega} \sin(\vartheta)$ with the angle of incidence ϑ. The quantity α is independently determined by a reference measurement. This is advantageous because of the potentially inaccurately determined spot size $A^{(\text{spot})}$ and pulse width $\Delta\tau$ of the fundamental beam. The parameter $\chi_{\text{eff}}^{\text{p/s}}$ is the effective second-order susceptibility for p/s-polarized SHG, which takes the following form for $C_{\infty v}$ symmetry

$$
\begin{aligned}
\chi_{\text{eff}}^{\text{p}} = -\frac{1}{2}\Big[& \chi_{xxz} \cos(\theta_{\text{f},2\omega})\sin(2\theta_{\text{f},\omega})\sin^2(\varphi') \\
& + \chi_{zxx} \sin(\theta_{\text{f},2\omega})\left(\cos^2(\theta_{\text{f},\omega})\sin^2(\varphi') + \cos^2(\varphi')\right) \\
& + \chi_{zzz} \sin(\theta_{\text{f},2\omega})\sin^2(\theta_{\text{f},\omega})\sin^2(\varphi') \Big] \\
\chi_{\text{eff}}^{\text{s}} = -\frac{1}{2} & \sin(\theta_{\text{f},\omega})\sin(2\varphi')
\end{aligned}
\tag{6.5}
$$

In this relation, the quantity φ' is the polarization angle of the fundamental beam inside the nonlinear material which is defined by $\tan(\varphi') = t_{\text{a-f},\omega}^{p} / t_{\text{a-f},\omega}^{s} \tan(\varphi)$. The excitation geometry is depicted in Figure 6.2 where also φ and ϑ are indicated. The refractive indices of the samples are: $n_{\text{f},\omega} = 1.979$, $n_{\text{f},2\omega} = 2.1935$, $n_{\text{s},\omega} = 1.4661$ and $n_{\text{s},2\omega} = 1.4839$ for the ITA sample, and $n_{\text{f},\omega} = 1.9242$, $n_{\text{f},2\omega} = 2.0194$, $n_{\text{s},\omega} = 1.5163$ and $n_{\text{s},2\omega} = 1.5405$ for the HTA sample.

To determine the second-order nonlinearity of a sample the s- and p-polarized SH power is recorded as a function of the polarization of the fundamental beam φ for a fixed angle of incidence. The detected s- and p-polarized SH power are fitted simultaneously with the theoretical expressions presented in Eq. (6.4), where the three independent tensor elements of $\chi^{(2)}$ are the corresponding fitting parameters. The parameter α is determined in an independent Maker fringe

measurement of a Y-cut quartz crystal with known second-order nonlinearity of $\chi_{xxx}^{\mathrm{SiO_2}} = 0.6\,\mathrm{pm/\,V}$ [211]. This is done immediately after the $\chi^{(2)}$ measurement on the nanolaminate in order to avoid the influence of possible laser fluctuations.

6.4 Results and discussion

In this section the weaknesses and strengths of the two measurement techniques will be discussed and the most important sources of errors for the deduction of $\chi^{(2)}$ will be identified. Since the measurement methodologies are different, the relevant sources of errors will be also different for the KIT and UGent approach. The fitting of the measurement data in the following section is carried out using a nonlinear least-squares algorithm. The nonlinear regression is done assuming a constant error, *i.e.*, equal weights for all data points.

6.4.1 UGent measurement and fitting

The reference measurement to determine the nonlinear surface susceptibility of a blank glass substrate was performed at Tampere University of Technology using a picosecond laser, see Figure C.1. From this reference measurement, which was calibrated against a Y-cut quartz crystal, we get: $\chi_{S,zzz}^{\mathrm{glass}} = 43 \times 10^{-22}\,\mathrm{m^2/\,V}$ and $2\chi_{S,xxz}^{\mathrm{glass}} + \chi_{S,zxx}^{\mathrm{glass}} = 18 \times 10^{-22}\,\mathrm{m^2/\,V}$. To find the walk-off time $t_{\mathrm{walk-off},0}$, the measurement of a blank substrate needs to be repeated with the UGent setup, see Figure 6.3. The data is fitted using the model with and without walk-off (see Eq. (6.1) and Eq. (6.3), except the ABC-type coating on the front surface needs to be replaced with glass). The fitting parameters are the substrate thickness d_s, the constants K_1 and K_2 and the walk-off time $t_{\mathrm{walk-off},0}$. The fitting of the substrate thickness is necessary to ensure that the extrema of the fringes in the fitted curve are positioned at the right incidence angles. Incidence angles greater than 70° are not considered, since the theoretical model does not hold any more due to the unaccounted reflections. Figure C.3 illustrates the consequences for the fitting when larger incidence angles are included. In Figure 6.3, we see that the visibility of the fringes is lower for the measurement data than it is for the fitted curve when walk−off is
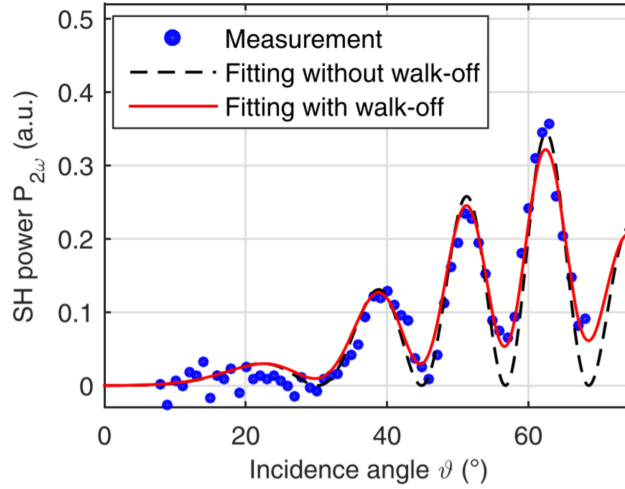
Figure 6.3: Fitting the measurement data for a blank BOROFLOAT® 33 substrate without temporal walk-off (black dashed line) and with walk-off (red full line). Negative SH powers for the measurement data are obtained due to subtraction of background noise. The regression analysis gives us a walk-off of 45.3 fs and a substrate thickness of 485 μm. The thickness agrees well with the specified thickness of (500±20) μm.

not included in the model. Including the temporal walk−off effect clearly improves the agreement between the measurement and the fitted curve. The regression analysis gives a walk-off time of $t_{\text{walk−off,0}} = 45.3$ fs. This result will be used later in the fitting of the data of the ABC-type thin films. From the refractive index versus wavelength graph in the datasheet [212] we get 37 fs as a very rough estimate (estimating $dn/d\lambda$ graphically), which agrees well with the fitted value.

The measured SH powers and corresponding fitted curves for both the ITA and HTA sample are shown in Figure 6.4. The theoretical model is described by Eq. (6.3) where K_2, d_s, $\chi_{s,\text{sum}}^{\text{ABC}}$ and $\chi_{s,zzz}^{\text{ABC}}$ are the fitting parameters. The corresponding bulk nonlinearities are calculated by dividing the surface nonlinearities χ_s^{ABC} by the thin film thickness d_s. The results for the ITA sample are: $\chi_{\text{sum}}^{\text{ITA}} = (0.211 \pm 0.011)\,\text{pm/ V}$, $\chi_{zzz}^{\text{ITA}} = (0.974 \pm 0.054)\,\text{pm/ V}$ and $d_s^{\text{ITA}} = (498.26 \pm 0.16)\,\mu\text{m}$. For the HTA sample we get: $\chi_{\text{sum}}^{\text{HTA}} = (0.605 \pm 0.008)\,\text{pm/ V}$, $\chi_{zzz}^{\text{HTA}} = (0.697 \pm 0.010)\,\text{pm/ V}$ and $d_s^{\text{HTA}} = (170.31 \pm 0.04)\,\mu\text{m}$. The quoted uncertainties are the standard deviations following from nonlinear regression analysis; these only reflect the uncertainty due to statistical intensity fluctuations. The standard deviations are kept low by averaging over many read-outs for a single angle of incidence.
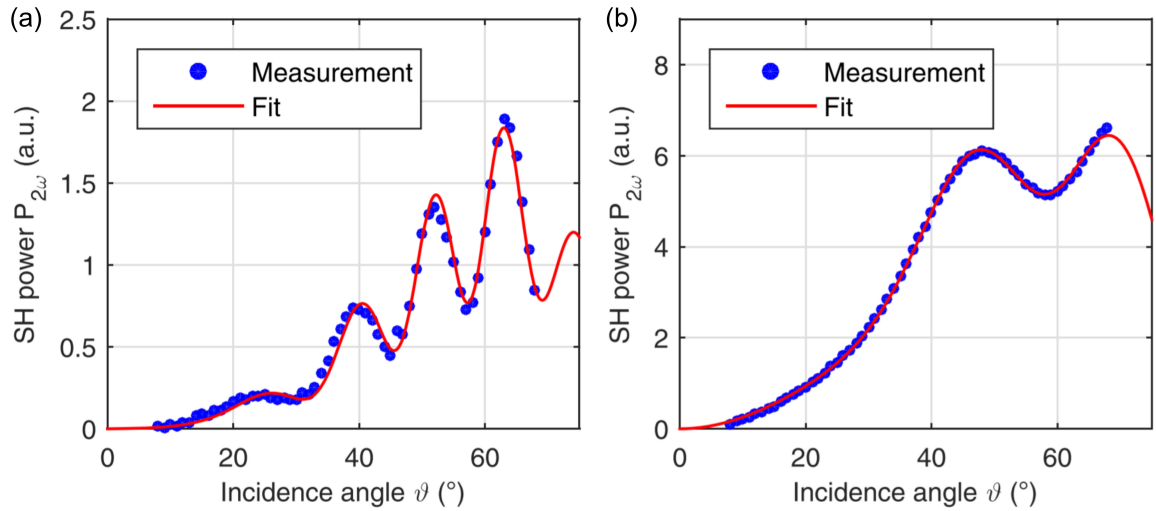
Figure 6.4: Measured and fitted SH power vs incidence angle for **(a)** ITA sample and **(b)** HTA sample in the UGent setup (laser wavelength of 980nm). As the substrate is thinner for the HTA sample, there are fewer interference fringes.

There is also an uncertainty on the incidence angle which can impact the final results. Since we are working with a motorized rotation stage, the relative angle setting is very precise (repeatability $< 1'$ according to specifications). The main uncertainty originates in the setting of the reference angle: after we have placed the sample, we need to manually set the angle corresponding to normal incidence. We estimate that this results in a maximum systematic error of 2°. Table 6.1 illustrates how this systematic error will influence the retrieved $\chi^{(2)}$ values. The uncertainties are several times larger than the standard deviations following from the nonlinear regression, and currently they are the main source of uncertainty in the UGent measurements.

Table 6.1. Error margins on the bulk susceptibilities and substrate thicknesses as a consequence of the systematic error on the incidence angle (±2°) for the UGent measurement technique. Results are shown both for the ITA and the HTA sample.

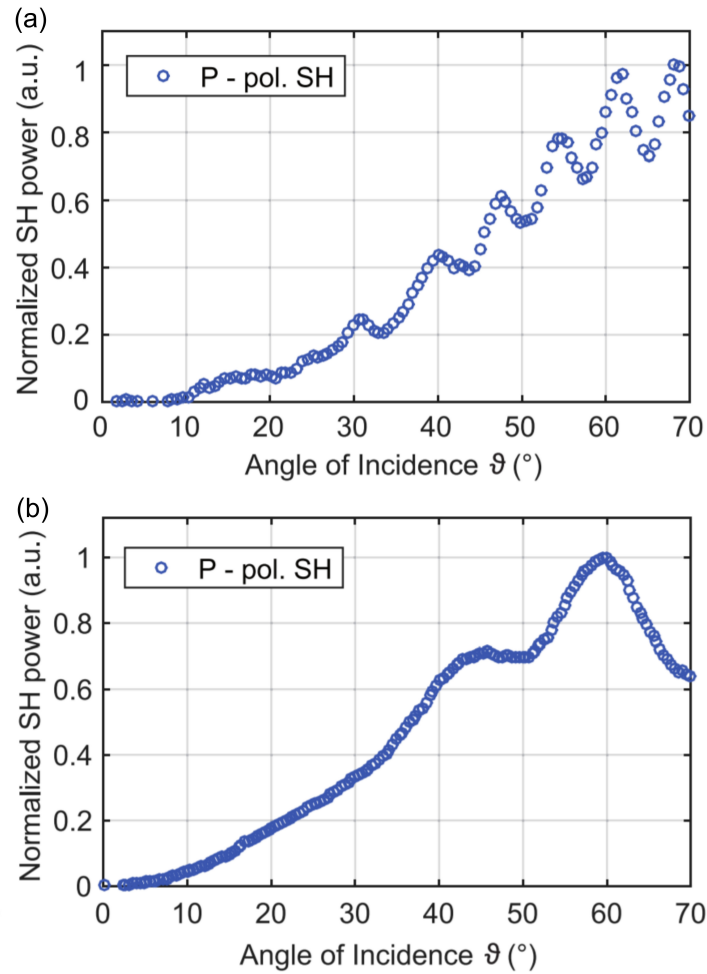|	ITA sample	HTA sample
χ_{sum}^{ABC} (pm/V)	0.21 ± 0.04	0.6 ± 0.07
χ_{zzz}^{ABC} (pm/V)	1.0 ± 0.2	0.7 ± 0.3
L_s (µm)	498 ± 5	170 ± 1

Another aspect that needs to be stressed is the importance of proper alignment in this type of measurements. The depth of focus is only 4.5 mm, so care must be taken to avoid the sample from moving out of the laser focus while rotating it. We achieve this by aligning at two widely spaced incidence angles: we maximize the signal for both angles by iteratively adjusting the mirrors in our setup. When the rotation axis of the sample is not positioned in the laser focus, it will cause an apparent shift in the weights of the fitted nonlinear tensor elements, *i.e.*, certain elements will become smaller, others larger. From simulations we estimated that displacements of the rotation axis with respect to the focus on the order of 1 mm can cause the tensor elements to change by several 10's of percent, which would make the induced error of similar magnitude to the error due to uncertainty on the incidence angle. To avoid possible alignment issues one can choose to focus the laser beam less tightly, but again this requires a more sensitive detection mechanism.

The reproducibility of the measurements was tested by doing multiple measurements on the same sample. In between measurements the sample was removed from the sample holder and put back into place. The setup was also intentionally misaligned and realigned. Including error boundaries, these measurements gave identical results.

## 6.4.2 KIT measurements and fitting

An advantage of the KIT approach is the simplicity in sample alignment. Since ϑ is constant during a measurement there is no risk of rotating the sample out of focus. Moreover, the influence of the slightly inhomogeneous sensitivity of the active region of the PMT is eliminated since the SH light spot on the PMT does not move during the measurement.

The most important source of error for the KIT technique is the fact that the KIT model does not take into account interference effects between SH wave emanated from the nanolaminate and the glass back surface. In fact, these interference fringes are also visible in the KIT setup as depicted in Figure 6.5 where the p-polarized SH power is plotted as a function of the angle of incidence ϑ for a p-polarized fundamental beam for the HTA and ITA sample. Note that in the KIT setup, a fundamental wavelength of 800 nm instead of 980 nm in the

Figure 6.5: p-polarized SH power as a function of the angle of incidence ϑ for p-polarized fundamental beam obtained from **(a)** the ITA sample and **(b)** the HTA sample. These measurements are done using the KIT setup (laser wavelength of 800nm). Both measurements show oscillations in the SH power which can be attributed to interference effects between SH waves generated in the nanolaminate and SH waves generated at the back surface of the glass substrate.

UGent setup is used. This is why the interference patterns are different from the ones measured with the UGent setup. In order to estimate the error that is introduced by neglecting the influence of interference, several measurements at different angles of incidence are performed for both the HTA and ITA sample. These angles are chosen such that constructive interference ($\vartheta_{\text{constr.}}$) or destructive interference ($\vartheta_{\text{destr.}}$) occurs. For these two extreme cases the determined value for $\chi^{(2)}$ will be overestimated or underestimated, respectively.
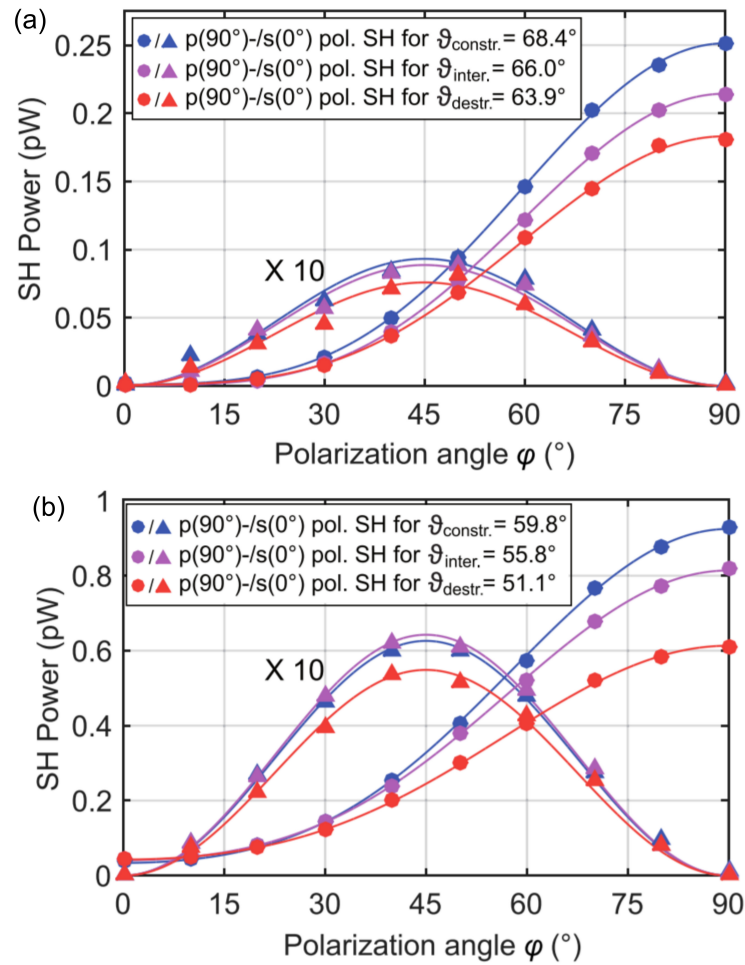
Figure 6.6: s- (triangles) and p-polarized SH power (circles) and corresponding fitting curves (lines) as a function of the polarization angle φ for an average excitation power of $P_\omega = 200$ mW obtained from **(a)** the ITA sample at $(\vartheta^{\mathrm{ITA}}_{\mathrm{constr.}}, \vartheta^{\mathrm{ITA}}_{\mathrm{inter.}}, \vartheta^{\mathrm{ITA}}_{\mathrm{destr.}}) = (68.4°, 66.0°, 63.9°)$ and **(b)** the HTA sample at $(\vartheta^{\mathrm{HTA}}_{\mathrm{constr.}}, \vartheta^{\mathrm{HTA}}_{\mathrm{inter.}}, \vartheta^{\mathrm{HTA}}_{\mathrm{destr.}}) = (59.8°, 55.8°, 51.1°)$. Here, $\varphi = 0°$, 90° corresponds to incident s- and p-polarization, respectively. To quantify the impact of interference we perform three measurements at different angles of incidence where $\vartheta_{\mathrm{constr.}}$ and $\vartheta_{\mathrm{destr.}}$ denote the angles of incidence under which constructive and destructive interference occurs, respectively and $\vartheta_{\mathrm{inter.}}$ denotes an intermediate angle of incidence. Note that data and fit of the s-polarized SH power is multiplied by a factor 10 for better visibility.

An additional measurement at an intermediate angle ($\vartheta_{\mathrm{inter.}}$) between those two specified angles will give a good indicator of the true value of $\chi^{(2)}$.

Figure 6.6 shows three separate measurements of the s- (triangles) and p-polarized (circles) SH power and the corresponding fitted theoretical expressions (lines) as a function of φ obtained for the ITA and the HTA sample. The measurements are performed for three different angles of incidence where

the blue, magenta and red markers and lines correspond respectively to $\vartheta_{\text{constr.}}^{\text{ITA}} = 68.4°$, $\vartheta_{\text{inter.}}^{\text{ITA}} = 66.0°$ and $\vartheta_{\text{destr.}}^{\text{ITA}} = 63.9°$ for the ITA sample and $\vartheta_{\text{constr.}}^{\text{HTA}} = 59.8°$, $\vartheta_{\text{inter.}}^{\text{HTA}} = 55.8°$ and $\vartheta_{\text{destr.}}^{\text{HTA}} = 51.1°$ for the HTA sample. For better visibility of the s-polarized SH power the data sets and corresponding fitting curves are multiplied by a factor of 10. The determined values of the $\chi^{(2)}$ tensor components depend significantly on the angle of incidence ϑ, as summarized in Table 6.2 where the last column contains the average value of the determined tensor elements and the corresponding standard deviation. Note that for all deduced tensor elements the error following from curve fitting is well below 10%. It is interesting to observe that for the HTA sample the decrease of the determined value of χ_{zzz}^{HTA} is very pronounced when going from constructive to destructive interference. On the other hand, the determined off-diagonal tensor elements vary only little for the three different angles. This finding suggests that the off-diagonal tensor elements of the HTA nanolaminate are much larger than the off-diagonal tensor elements of the glass surface, which would result in ϑ-independent values of these tensor components. Indeed, only minor interference occurs for s-polarized SH power when the fundamental beam polarization is defined by $\varphi = 45°$, in this case only χ_{xxz}^{HTA} is addressed, see Figure C.5. Furthermore, no interference effects are visible for p-polarized SH power when the fundamental beam is s-polarized, in this case only χ_{zxx}^{HTA} is addressed, see Figure C.6. For the ITA sample the deduced value for χ_{zzz}^{ITA} decreases more moderately when changing the angle of incidence from $\vartheta_{\text{constr.}}$ to $\vartheta_{\text{destr.}}$.

Table 6.2. Deduced $\chi^{(2)}$ tensor elements for different angles of incidence $\vartheta_{\text{constr.}}$, $\vartheta_{\text{destr.}}$ and $\vartheta_{\text{inter.}}$ corresponding to constructive interference, destructive interference and an intermediate case respectively. Results are shown for the HTA and ITA sample.

HTA sample	$\vartheta_{\text{constr.}}^{\text{HTA}} = 59.8°$	$\vartheta_{\text{inter.}}^{\text{HTA}} = 55.8°$	$\vartheta_{\text{destr.}}^{\text{HTA}} = 51.1°$	Average
χ_{zzz}^{HTA} (pm/V)	0.86	0.69	0.45	0.67 ± 0.21
χ_{xxz}^{HTA} (pm/V)	0.26	0.26	0.24	0.25 ± 0.02
χ_{zxx}^{HTA} (pm/V)	0.22	0.23	0.23	0.23 ± 0.01
ITA sample	$\vartheta_{\text{constr.}}^{\text{ITA}} = 68.4°$	$\vartheta_{\text{inter.}}^{\text{ITA}} = 66.0°$	$\vartheta_{\text{destr.}}^{\text{ITA}} = 63.9°$	Average
χ_{zzz}^{ITA} (pm/V)	1.25	1.15	1.09	1.17 ± 0.09
χ_{xxz}^{ITA} (pm/V)	0.17	0.14	0.13	0.15 ± 0.01
χ_{zxx}^{ITA} (pm/V)	0.06	0.03	0.05	0.05 ± 0.01

Additionally, also the calculated value of the off-diagonal tensor element χ_{xxz}^{ITA} decreases with decreasing ϑ. In fact, s-polarized SH power for a fundamental beam polarization of $\varphi = 45°$ exhibits major interference effects, which can explain this decrease in χ_{xxz}^{ITA}, see Figure C.5(a). The large variation of χ_{zxx}^{ITA} is attributed to the fact that the low level of p-polarized generated SH power for s-polarized fundamental beam is close to the detection limit. Note that the visibility of the fringes and therefore this source of error is eliminated for thicker or more strongly nonlinear films as it was shown for 290 nm thick, strongly nonlinear ZnO/Al$_2$O$_3$ nanolaminates [213].

As an additional source of error, an imprecisely calibrated angle of incidence is investigated. The angle calibration is done by studying the back reflected fundamental beam close to normal incidence and trying to make it overlap with the incident beam by rotating the sample. In order to illustrate the effect on the deduction of $\chi^{(2)}$, an error of $\Delta\vartheta = \pm 1.0°$ will be assumed. Note that using the same technique in the UGent setup gives larger errors, as a focusing element with a smaller focal length is used. The effect is quantified by performing $\chi^{(2)}$ measurements on the ITA and HTA sample at angles of incidence of $\vartheta_0^{\text{ITA}} = 68.4°$ and $\vartheta_0^{\text{HTA}} = 59.8°$ (blue data in Figure 6.6) while the data is evaluated at angles of incidence of ϑ_0 and $\vartheta_0 \pm \Delta\vartheta$. The fitting results for $\Delta\vartheta = \pm 1.0°$ are $\chi_{zzz}^{\text{HTA}} = (0.86 \mp 0.05)\,\text{pm/V}$, $\chi_{xxz}^{\text{HTA}} = (0.264 \pm 0.004)\,\text{pm/V}$ and $\chi_{zxx}^{\text{HTA}} = (0.216 \pm 0.004)\,\text{pm/V}$ for the HTA sample and $\chi_{zzz}^{\text{ITA}} = (1.25 \mp 0.02)\,\text{pm/V}$, $\chi_{xxz}^{\text{ITA}} = (0.169 \pm 0.008)\,\text{pm/V}$ and $\chi_{zxx}^{\text{ITA}} = (0.063 \pm 0.003)\,\text{pm/V}$ for the ITA sample. It can be seen that the values for the tensor elements change by roughly 5%. This can be understood as an upper error bound since the error in the angle of incidence of $\Delta\vartheta = \pm 1.0°$ is chosen pessimistically.

The reproducibility of the measurements was also checked by doing multiple measurements on the same sample. The setup was deliberately misaligned and realigned before each measurement. The results of these measurements were in very good agreement with one another.

Lastly, the Maker fringe reference measurement on a Y-cut quartz plate that is necessary for the determination of the quantity α in (6.4) is briefly discussed. To validate the stability of the calibration measurement and the corresponding fit, a set of Maker fringe measurements is performed, see Figure C.2. The fitting

results vary by less than 1% for consecutive measurements. Therefore it can be assumed that the calibration technique does not introduce any significant error.

6.5   Conclusions

In conclusion, two different thin film $\chi^{(2)}$ measurement methodologies, their corresponding calibration techniques and underlying theoretical models are described and the most important sources of errors are identified. The techniques are tested with two similar ABC-type nanolaminates grown by ALD on glass substrates, fabricated by two independent groups from UGent and KIT.

The UGent methodology takes into account the interference from the backside of the substrate and it even exploits this for calibration purposes. During a measurement, the sample needs to be rotated, and thus care must be taken when aligning the sample such that it stays in the laser focus. Currently, the main source of error in the UGent method is related to the setup rather than the theoretical model, namely the systematic error on the incidence angle. The obtained $\chi^{(2)}$ values and associated overall error margins are $\chi_{zzz}^{\mathrm{ITA}} = (1.0 \pm 0.2)\,\mathrm{pm/V}$ and $\chi_{\mathrm{sum}}^{\mathrm{ITA}} = (0.21 \pm 0.05)\,\mathrm{pm/V}$ for the ITA sample. For the HTA sample we have $\chi_{zzz}^{\mathrm{HTA}} = (0.7 \pm 0.3)\,\mathrm{pm/V}$ and $\chi_{\mathrm{sum}}^{\mathrm{HTA}} = (0.60 \pm 0.08)\,\mathrm{pm/V}$. These overall error margins include the error listed in Table 6.1 and the error introduced by curve fitting. By improving the sensitivity of the current setup, the off-diagonal tensor elements could be identified separately. This could also allow to focus the beam more loosely, which eases the alignment and leads to a reduced error on the angle.

The KIT technique for $\chi^{(2)}$ determination is very robust against misalignment between the sample and the fundamental beam, since the sample is not moved during the measurement. Additionally, the high detection sensitivity allows to determine the three tensor components individually. The main source of error is due to the fact that the KIT formalism used for the evaluation does not take into account interference effects of the SH waves generated in the nonlinear film and at the glass back surface. The deduced values and corresponding overall error bounds for the tensor elements are $\chi_{zzz}^{\mathrm{HTA}} = (0.7 \pm 0.2)\,\mathrm{pm/V}$, $\chi_{\mathrm{sum}}^{\mathrm{HTA}} = (0.73 \pm 0.04)\,\mathrm{pm/V}$ and $\chi_{zzz}^{\mathrm{ITA}} = (1.2 \pm 0.1)\,\mathrm{pm/V}$, $\chi_{\mathrm{sum}}^{\mathrm{HTA}} = (0.34 \pm 0.06)\,\mathrm{pm/V}$ for the HTA and the ITA sample, respectively. The
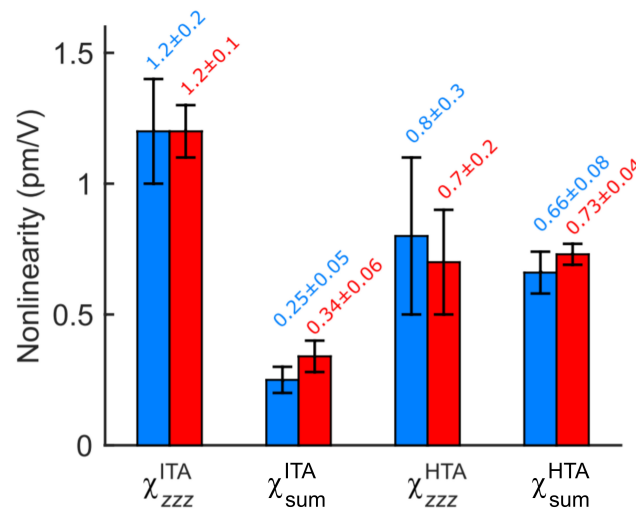
Figure 6.7: Overview of the obtained $\chi^{(2)}$ tensor elements for the 2 samples under investigation via the UGent measurement (blue) and the KIT measurement (red). The tensor elements determined in the UGent measurement are scaled according to Miller's rule in order to fairly compare the values at a reference wavelength of 400nm.

specified error bounds include the error due to interference effects, the errors introduced by curve fitting and the errors due to an imprecise setting of the angle of incidence. The interference effect, the main source of error, is reduced significantly if thicker samples are examined or if samples with higher nonlinearity are introduced.

Finally, we compare the $\chi^{(2)}$ values determined with the two different techniques. Since, the two presented setups use lasers at different wavelengths, we compensate for the dispersion of $\chi^{(2)}$ by considering Miller's rule [214]. As a reference wavelength we choose the second harmonic wavelength in the KIT setup, *i.e.*, 400 nm. Therefore we need to scale the tensor elements determined in the UGent setup by using the relation

$$\chi_i^{(2)}(400\,\text{nm}) = \frac{(n_f^2(400\,\text{nm})-1)(n_f^2(800\,\text{nm})-1)^2}{(n_f^2(490\,\text{nm})-1)(n_f^2(980\,\text{nm})-1)^2}\,\chi_i^{(2)}(490\,\text{nm})\,, \tag{6.6}$$

where $\chi_i^{(2)}$ can be χ_{zzz} or χ_{sum}. The $\chi^{(2)}$ values at the reference wavelength of 800 nm are summarized graphically in Figure 6.7. The values for the relevant tensor element χ_{zzz} determined with the different techniques match very well for both the ITA and HTA sample and also for the off-diagonal elements the error bounds overlap. It is also interesting to compare these values with previously

reported values [21,22]. For the ITA sample, ref. [22] reported a value of $\chi_{zzz}^{\mathrm{ITA}}=\left(5\pm2\right)\mathrm{pm/\,V}$, compared to a value of $\chi_{zzz}^{\mathrm{ITA}}=\left(1.0\pm0.2\right)\mathrm{pm/\,V}$ presented in this paper. On the one hand, this is caused by the use of a larger reference surface nonlinearity for the glass substrate in ref. [22] (the surface nonlinearity of BK7 calibrated against $\chi_{xyz}^{(2)}$ of quartz was used). Additionally, the thin film thickness was underestimated. Indeed, we now have measurements performed via electron microscopy and ellipsometry that give a thickness of 66 nm while the previous estimate of 50 nm was done solely by summing up the ALD calibrated thickness of each layer ($0.7\,\mathrm{nm}\times24\times3=50\,\mathrm{nm}$). The remaining discrepancy can be explained by all the factors discussed above with a dominant impact of the temporal walk-off. The HTA sample reported here is nominally identical to the ACB sample with inverted order of growth and adapted thicknesses of the individual layers reported in the main text of ref. [21] for which a dominant $\chi^{(2)}$ tensor element of $\chi_{zzz}=0.43$ pm/V can be estimated. This is in fair agreement with the value of $\chi_{zzz}^{\mathrm{HTA}}=\left(0.7\pm0.2\right)\mathrm{pm/\,V}$ reported here. The discrepancy is due to the fact that the effect of SHG from the back surface was not accounted for in ref. [21]. Additionally, in ref. [21] the $\chi^{(2)}$ deduction was done without the reference measurement on quartz which led to an underestimation of $\chi^{(2)}$.

In summary, both $\chi^{(2)}$ measurement techniques represent attractive alternatives to the traditional Maker fringe technique if thin film samples are investigated. For thin films generating high levels of SH power with negligible interference from the substrate, the KIT technique is very well suited. On the other hand, the UGent technique is the technique of choice when very thin and weakly nonlinear films are investigated, provided that a reliable measurement of the backside nonlinearity is available. Because of the interesting application perspectives of nonlinear thin films in photonic integrated circuits, the use of reliable $\chi^{(2)}$ measurement techniques is of considerable importance to the research community.

6.6 Methods

UGent sample fabrication

The UGent ABC-type thin film is deposited through plasma-enhanced atomic layer deposition. The materials A, B and C are TiO_2, Al_2O_3 and In_2O_3. After cleaning the glass substrate in O_2 plasma, the deposition is done by alternating 10 s pulses of the corresponding metal-organic precursor at a pressure of 6.0×10^{-5} bar and O_2 plasma pulses at 1.2×10^{-5} bar. The substrate temperature is 120 °C throughout the full deposition process. The plasma is generated at an RF power of 200 W and a frequency of 13.56 MHz. The precursors used for Ti, Al and In are tetrakis(dimethylamino)titanium 99% (Strem Chemicals P.Nr. 93-2240), trimethyaluminium 97% (Strem Chemicals P.Nr. 93-1360) and tris(2,2,6,6-tetramethyl-3,5-heptanedionato)indium 99% (Strem Chemicals P.Nr. 49-2200). The number of cycles for each TiO2, Al2O3 and In2O3 layer are 12, 7 and 70. This gives individual layer thicknesses of about 0.7 nm. The ABC period is repeated 24 times which gives a total of $24 \times (12 + 7 + 70) = 2136$ ALD cycles.

KIT sample fabrication

The substrates for the KIT sample are borosilicate glass of the first hydrolytic class with a thickness of 170 μm for SHG measurements and silicon wafers for ellipsometry measurements. Before deposition, the substrates are cleaned with acetone and dry-blown by N_2. In order to limit deposition on the substrate front side, the back surface is covered with high temperature resistant masking tape. The film is fabricated by ALD using a Savannah 100 system by Cambridge Nanotech at a deposition temperature of 150 °C. The precursors for Al, Hf and Ti and O are trimethyaluminium 97% (Sigma-Aldrich P.Nr. 257222), tetrakis(dimethylamido)hafnium(IV) ≥99.99% (Sigma-Aldrich P.Nr. 455199), titanium(IV) isopropoxide 99.999% (Sigma-Aldrich P.Nr. 377996) and hydrogen peroxide 30% (Merck P.Nr. 107209), respectively. The reaction chamber is constantly flushed with 20 sccm of Ar, unless differently specified. Further parameters are given in Table C.1. The sample consists of 32 ABC macrocycles. The numbers of growth cycles for the individual layers in each macrocycle are 8, 8 and 12 for Al_2O_3, HfO_2 and TiO_2 corresponding to estimated layer thicknesses of 0.9 nm, 0.9 nm and 0.3 nm, respectively. *[end of paper [J4]]*

7 Second-order optical nonlinear ZnO/Al₂O₃ nanolaminates

This section demonstrates a novel binary nanolaminate grown by atomic layer deposition using the two constituents zinc oxide (ZnO) and aluminum oxide (Al₂O₃). The Al₂O₃ layers serve as seed layers to tailor the ZnO crystallite growth, which results in best in class second-order nonlinearity for nanolaminates. The section is taken from a publication in *Advanced Optical Materials [J5]*. To fit the structure and layout of this thesis, it was adapted accordingly. Appendix D shows the associated supplementary information.

The conceptual idea for the binary ZnO/Al₂O₃ nanolaminates was developed by Andreas Wickberg (A.W.) and Clemens Kieninger (Cl.K.). A.W. optimized the ALD growth parameters and fabricated the nanolaminates. A.W. and Cl.K. conducted the SHG experiments. Christoph Sürgers performed the XRD measurement. Sabine Schlabach and Xiaoke Mu conducted the STEM measurements. Cl.K. supported A.W. in writing the paper. All authors revised the paper. Christian Koos and Martin Wegener supervised the work.

[start of paper [J5]]

Second-Harmonic Generation from ZnO/Al₂O₃ Nanolaminate Optical Metamaterials Grown by Atomic-Layer Deposition

Andreas Wickberg,[1]* **Clemens Kieninger**,[2,3]* Christoph Sürgers,[4] Sabine Schlabach,[5] Xiaoke Mu,[6,7] Christian Koos,[2,3] and Martin Wegener[1]

*These authors contributed equally to this work.

[1] Karlsruhe Institute of Technology (KIT), Institute of Applied Physics (APH), 76131 Karlsruhe, Germany
[2] Karlsruhe Institute of Technology (KIT), Institute of Photonics and Quantum Electronics (IPQ), 76131 Karlsruhe, Germany

[3] Karlsruhe Institute of Technology (KIT), Institute of Microstructure Technology (IMT), 76344 Eggenstein-Leopoldshafen, Germany
[4] Karlsruhe Institute of Technology (KIT), Physikalisches Institut (PHI), 76131 Karlsruhe, Germany
[5] Karlsruhe Institute of Technology (KIT), Institute of Applied Materials (IAM), 76344 Eggenstein-Leopoldshafen, Germany
[6] Karlsruhe Institute of Technology (KIT), Institute of Nanotechnology (INT) 76344 Eggenstein-Leopoldshafen, Germany
[7] Helmholtz-Institute Ulm for Electrochemical Energy Storage (HIU), 89081 Ulm, Germany

Nanolaminates composed of alternating layers of ZnO and Al_2O_3 are grown by conformal atomic-layer deposition. Their structural and nonlinear optical properties are correlated. Optimized nano-laminates exhibit an effective bulk second-order nonlinear optical susceptibility that is independent of the substrate and that is five times larger than that of potassium dihydrogen phosphate.

7.1   Introduction

Nonlinear optical interactions are crucial for a variety of applications ranging from optical frequency conversion via optical signal processing in telecommunications to sensing. Often, bulk crystals like lithium niobate ($LiNbO_3$) or lithium triborate (LBO) can be used to achieve a large second-order nonlinear optical response. Unfortunately, these crystals cannot easily be integrated into compact optical systems or chips. A straightforward alternative is thin films that can be grown using conventional deposition techniques. Among the suitable materials, ZnO is a promising candidate and has consequently received considerable attention [215]. ZnO lacks centrosymmetry and crystallizes in the hexagonal wurtzite structure, giving rise to a second-order susceptibility tensor element of $\chi_{zzz}^{(2)} = -14.31 \mathrm{pmV}^{-1}$ in bulk crystals [216]. Additionally, it is transparent throughout the visible spectrum and shows a high thermal stability [217]. Thin films of ZnO have been fabricated by various deposition techniques ranging from dual-ion-beam sputtering to laser-assisted molecular-beam epitaxy. The resulting $\chi^{(2)}$ values have partly been even larger than for bulk ZnO crystals [195,197,218–226]. These publications have also highlighted some of the important links between the structural properties of the thin films and their nonlinear optical susceptibility. In the work by Cao et al.,

thin films of ZnO were fabricated on sapphire substrates by pulsed laser ablation [195]. The second-order susceptibility was determined to be $\chi^{(2)}_{zzz} = -13.40\,\mathrm{pmV}^{-1}$. Furthermore, it was shown that the second-order susceptibility decreases with increasing crystalline quality and with increasing film thickness. This finding was attributed to a strong contribution of grain boundaries and interfaces to the second-order susceptibility. Another group highlighted the strong dependence of the structural and second-order nonlinear properties on the deposition conditions and the choice of the substrate [197]. Clearly, different deposition techniques lead to different growth behavior, hence different structural properties and thus different nonlinear optical properties. Atomic-layer deposition (ALD) is a fabrication technique that is particularly well-suited for the needs of optical integration. ALD is CMOS-compatible and allows for an inexpensive and conformal deposition on a large variety of substrates with a precision down to a monolayer [63]. Unfortunately, ZnO crystallites grown by ALD seem to have properties unfavorable for a strong second-order nonlinear response as there is not a single publication covering this topic. As we will show in this publication, the weak second-order response can be ascribed to the random orientation of the ZnO crystallites in pure ALD-grown ZnO thin films. In general, there are only few publications showing the realization of ALD-grown second-order nonlinear thin films and these are solely based on the idea of a strong interface-connected response [21,22]. In this Communication, we use the concept of nanolaminates to tune the second-order nonlinear properties as it has previously been demonstrated for the mechanical, linear optical, and also the third-order nonlinear optical properties of ALD-grown thin films [227–229]. Using this approach, we are able to control the ZnO crystallite growth and thus, for the first time, achieve a strong bulk second-order nonlinear susceptibility in ALD-grown thin films.

7.2   ZnO/Al₂O₃ nanolaminates

The literature on ZnO thin films suggests that two key factors have to be controlled to maximize the second-order susceptibility in ALD-grown ZnO films. The first key factor is a well-defined ZnO crystallite orientation to avoid mutual cancellation of the contributions of neighboring misaligned crystallites. Without a preferential direction within a plane parallel to the substrate, the

substrate normal is the only extraordinary direction. Indeed, ZnO films with a strong nonlinear response consist of crystallites oriented with their optical axes (crystallographic c-axis) perpendicular to the substrate. In practice, the crystallite orientation is strongly influenced by the choice of the deposition conditions as well as by the substrate. For ALD-grown ZnO, it was shown that the growth of crystallites with their c-axis perpendicular to the substrate is greatly suppressed for deposition temperatures in the range from 155 to 220 °C [230]. In contrast, the c-axes of the crystallites are oriented perpendicular to the substrate for growth temperatures in the range 220–300 °C. Furthermore, it was shown that a layer of amorphous Al_2O_3 underneath the ZnO layer enhances the growth of crystallites with their optical axis perpendicular to the substrate, while at the same time suppressing other growth directions [227]. The second key factor for a large second-order nonlinearity is an optimal crystallite size, which is also responsible for the thickness dependent secondorder susceptibility observed in ZnO thin films [226]. Hausmann and Gordon demonstrated the control of surfacee morphology and crystallite growth in ALD films through amorphous intermediate layers [231]. Especially, they showed that an Al_2O_3 layer with a thickness of 0.5 nm is sufficient to disrupt the crystallite growth between two zirconium or hafnium oxide layers. Based on these results, we design a nanolaminate in which a seed layer of Al_2O_3 is used underneath the ZnO film to seed a well-defined orientation of the ZnO crystallites. In addition, we introduce intermediate Al_2O_3 layers subdividing the ZnO film to improve the crystallite orientation throughout the entire film. At the same time, the intermediate layers allow us to tune the crystallite size within each ZnO sublayer. By systematically comparing three different sets of samples, we illustrate the influence that the added Al_2O_3 layers have on the structural film properties as well as on the second-order nonlinear response.

All samples are fabricated at a deposition temperature of 250 °C. The recipes for the individual structures are given in terms of ALD cycle sequences. The ZnO crystallite orientation and size are investigated by means of θ–2θ X-ray diffraction (XRD). Ellipsometry measurements are used to determine the sample thicknesses and refractive indices. Further details on the sample fabrication and structural characterization are given in the Experimental Section 7.6. The nonlinear optical characterization is based on the measurement of the second-harmonic (SH) power, $P_{2\omega}$, generated from the samples. The films

are excited by a Ti:Sa femtosecond laser oscillator at a center wavelength of 800 nm, an average power of 100 mW, a repetition rate of 80 MHz, and an incidence angle of 45° with respect to the surface normal. $P_{2\omega}$ is measured with a photomultiplier tube after filtering out the fundamental beam. To compare samples with different thicknesses, we use the fact that $P_{2\omega}$ is proportional to the square of the thickness d, provided that film thicknesses below the coherent buildup length are considered [6]. Therefore, we use $P_{2\omega}/d^2$ as a figure of merit for the bulk second-order nonlinearity in our samples.

Sample A is a pure ZnO film consisting of 700 ZnO growth cycles with an ellipsometrically determined thickness of 95.1 nm. In sample B, a seed layer of approximately 6 nm Al_2O_3 is grown on the glass substrate before deposition of ZnO. The cycle sequence is $50 \times Al_2O_3 + 350 \times$ ZnO, leading to a total thickness of 73.3 nm. Sample C is a 79.7 nm thick nanolaminate, which uses the basic sequence of sample B, interrupted by additional intermediate Al_2O_3 layers. The sample consists of $M_{ALD} = 7$ ZnO/ Al_2O_3 macrocycles on top of the seed layer, resulting in the overall sequence $50 \times Al_2O_3 + 7 \times (50 \times$ ZnO $+ 10 \times Al_2O_3)$ or in terms of estimated layer thicknesses 6 nm $Al_2O_3 + 7 \times (9.3$ nm ZnO $+ 1.2$ nm $Al_2O_3)$. The cycling sequences and sample parameters are summarized in Table 7.1. Note that the ZnO growth per ALD cycle is much lower for the pure film (sample A) as compared to the growth of ZnO on a thin Al_2O_3 seed layer (sample B). We ascribe this finding to a nucleation delay of ZnO when deposited on a plain substrate. In contrast, ALD-deposited Al_2O_3 is known to adhere well to all kinds of substrates and grow in a stable amorphous phase. Furthermore, ZnO grows well on Al_2O_3. Therefore, the Al_2O_3 seed layer allows us to eliminate the strong influence of the substrate usually encountered in the

Table 7.1. Summary of the sample parameters used to demonstrate the influence of additional Al2O3 layers on the ZnO crystallite orientation. The growth per cycle in the nanolaminates is estimated to be 1.9 and 1.2 Å cycle^{-1} for ZnO and Al2O3, respectively.

	Sample A	Sample B	Sample C
Cycle Sequence	700×ZnO	50×Al2O3+350×ZnO	50×Al2O3+7×(50×ZnO+10×Al2O3)
Measured total thickness	95.1 nm	73.3 nm	79.7 nm
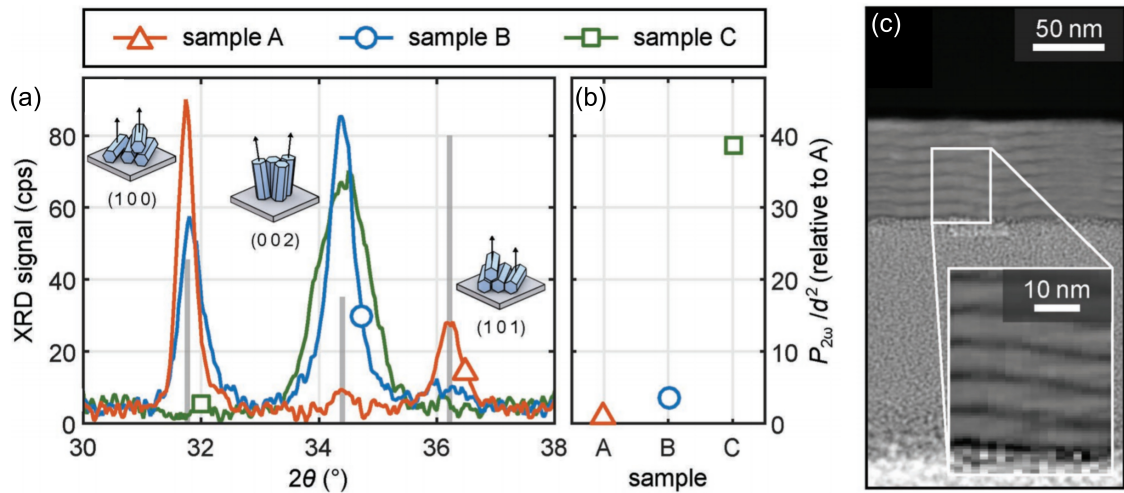
Figure 7.1: (a) XRD measurement showing the effect of seed and intermediate Al_2O_3 layers on the ZnO crystallite orientation and size. Sample A is a pure ALD ZnO film with $700 \times$ ZnO cycles; sample B consists of a 50 cycles thick Al_2O_3 seed layer underneath 350 cycles of ZnO. Sample C is a nanolaminate structure where the sequence of sample B is complemented by intermediate layers, which subdivide the ZnO film, resulting in a layer stack of the form $50 \times Al_2O_3 + 7 \times (50 \times ZnO + 10 \times Al_2O_3)$. The three dominant peaks in the measurement curves are ascribed to ZnO crystallites with (100), (002), and (101) orientation (see the three different insets). The seed and intermediate Al_2O_3 layers have a huge impact enhancing the growth of crystallites with (002) orientation and the optical axis perpendicular to the substrate. At the same time, the intermediate layers limit the crystallite size perpendicular to the substrate, leading to a broadening of the (002) peak. For comparison, the gray bars indicate relative intensities obtained from ZnO-powder diffraction measurements [232]. **(b)** $P_{2\omega}/d^2$ is normalized to the value obtained for sample A. This quantity is used as an indicator for the second-order bulk susceptibility of the three samples. The nanolaminate structure with intermediate Al_2O_3 layers (sample C) shows an increase by nearly 40 times as compared to the pure ZnO (sample A). **(c)** Scanning transmission electron image of a sample with a cycle sequence corresponding to sample C. The nanolaminate structure of the sample is clearly visible and shows seven macrocycles on top of the substrate

growth of ZnO thin films and thereby ensures substrate-independent effective properties.

The XRD measurements for the three samples are depicted in Figure 7.1(a). For comparison, the gray bars indicate relative intensities obtained from ZnO-powder diffraction measurements [232]. The curve for sample A exhibits a strong peak at a Bragg angle of 31.8° and a smaller peak at 36.2° corresponding to (100) and (101) ZnO crystallite planes, respectively. These peaks show that the ZnO crystallites in sample A are predominantly oriented with their optical c-axis parallel to the substrate, leading to randomly distributed optical axis

directions in the substrate plane. The weak peak at a Bragg angle of 34.4° indicates a very small amount of ZnO crystallites with (002) lattice planes parallel to the substrate. The picture changes completely for sample B, for which an Al_2O_3 seed layer is introduced underneath the ZnO. The XRD measurement shows a considerable increase of ZnO crystallites with (002) lattice planes parallel to substrate surface. These crystallites have their optical axes oriented perpendicularly to the substrate and are responsible for nonzero second-order susceptibility. At the same time, the intensity of the (100) Bragg reflection, corresponding to crystallites oriented parallel to the substrate, decreases by roughly one third. This structural change also manifests itself in the nonlinear measurements shown in Figure 7.1(b). $P_{2\omega}/d^2$ increases more than threefold from sample A to sample B. The nonlinear performance can be further increased by introducing additional intermediate Al_2O_3 layers in sample C. The XRD measurement of sample C indicates that the ZnO crystallite growth with orientations of the optical axis other than perpendicular to the substrate is nearly completely suppressed. Additionally, the broadening of the (002) Bragg peak from sample B to sample C indicates a decrease in crystallite size. We estimate the lower limit for the crystallite size using the Scherrer equation

$$\underset{\sim}{\tau} = \frac{0.9\lambda_0}{\Delta(2\theta)\cos(\theta)}, \tag{7.1}$$

where $\underset{\sim}{\tau}$ denotes the mean size of the crystalline domains, λ_0 the X-ray wavelength, $\Delta(2\theta)$ the full width at half maximum of the XRD peak, and θ the Bragg angle [233]. We deduce a change in the crystallite size from 15.1 nm in sample B to 8.4 nm in sample C. The calculated size of the crystallites in sample C is in good agreement with the actual ZnO layer thickness of 9.3 nm as estimated from the ALD growth per cycle. It is known that the ZnO layer thickness correlates with its roughness [228]. The structural changes indicated by the XRD measurements are correlated with the nonlinear optical measurements, where $P_{2\omega}/d^2$ for sample C is 11 times larger than for sample B and nearly 40 times larger than sample A. These measurements demonstrate the anticipated structural change in the ZnO films introduced by additional seed and intermediate layers of Al_2O_3 as well as the impact of the improved ZnO crystallite orientation and size on the second-order nonlinear optical response. We further study our ZnO/Al_2O_3 nanolaminates in cross section using scanning

transmission electron microscopy (STEM). The cycle sequence of the sample investigated by STEM is identical to that of sample C with 10 intermediate layer cycles. However, it was grown on silicon rather than a glass substrate (see the Experimental Section 7.6). Even for these extremely thin Al_2O_3 intermediate layers, corresponding to a nominal thickness of approximately 1.2 nm, a clear separation of the individual ZnO layers is visible, resulting in the nanolaminate structure shown in Figure 7.1(c). Additional, energy-dispersive X-ray (EDX) maps are shown in Figure D.1, see Appendix D. The Al and Zn maps exhibit a modulation corresponding to the layers visible in Figure 7.1(c). As expected, the O signal is nearly constant within the nanolaminate.

7.3   Optimization of growth parameters

Furthermore, a systematic parameter variation is performed to get a deeper understanding of the influence of the Al_2O_3 layers on the generated SH power. Taking sample C as a starting point, we vary the thickness of the seed and intermediate layers as well as the thickness of the ZnO layers. As before, the SH power $P_{2\omega}$ is measured and the different sample thicknesses d, estimated from the material growth per cycle, are taken into account by using $P_{2\omega}/d^2$ as a measure for the effective second-order nonlinearity. In the first parameter sweep, the number of Al_2O_3 seed layer cycles, S_{ALD}, is varied over six samples with the layer sequence $S_{ALD} \times Al_2O_3 + 7 \times (50 \times ZnO + 10 \times Al_2O_3)$. The experiments show an increase of $P_{2\omega}$ for small S_{ALD} and a saturation at around $S_{ALD} = 100$ seed layer cycles, Figure 7.2(a). Again, the Al_2O_3 seed layer reduces the influence of the substrate on the ZnO and enforces an optimized crystallite orientation. The substrate is completely "screened" once a certain number of seed layer cycles is reached, leading to a saturation of $P_{2\omega}$. The optimal number of seed layer cycles $S_{ALD} = 50$ is determined from the maximum of $P_{2\omega}/d^2$ versus S_{ALD}. In the second parameter sweep, the number I_{ALD} of intermediate Al_2O_3 layer cycles is optimized by investigating samples with sequence $50 \times Al_2O_3 + 7 \times (50 \times ZnO + I_{ALD} \times Al_2O_3)$. Figure 7.2(b) shows that $P_{2\omega}$ increases rapidly up to $I_{ALD} = 7$ cycles (≈ 0.8 nm) and continues increasing more slowly for larger values. This indicates that a minimum number of intermediate layer cycles between adjacent layers is required to restart ZnO crystallite growth. This finding is in very good agreement with results obtained for the crystallite growth
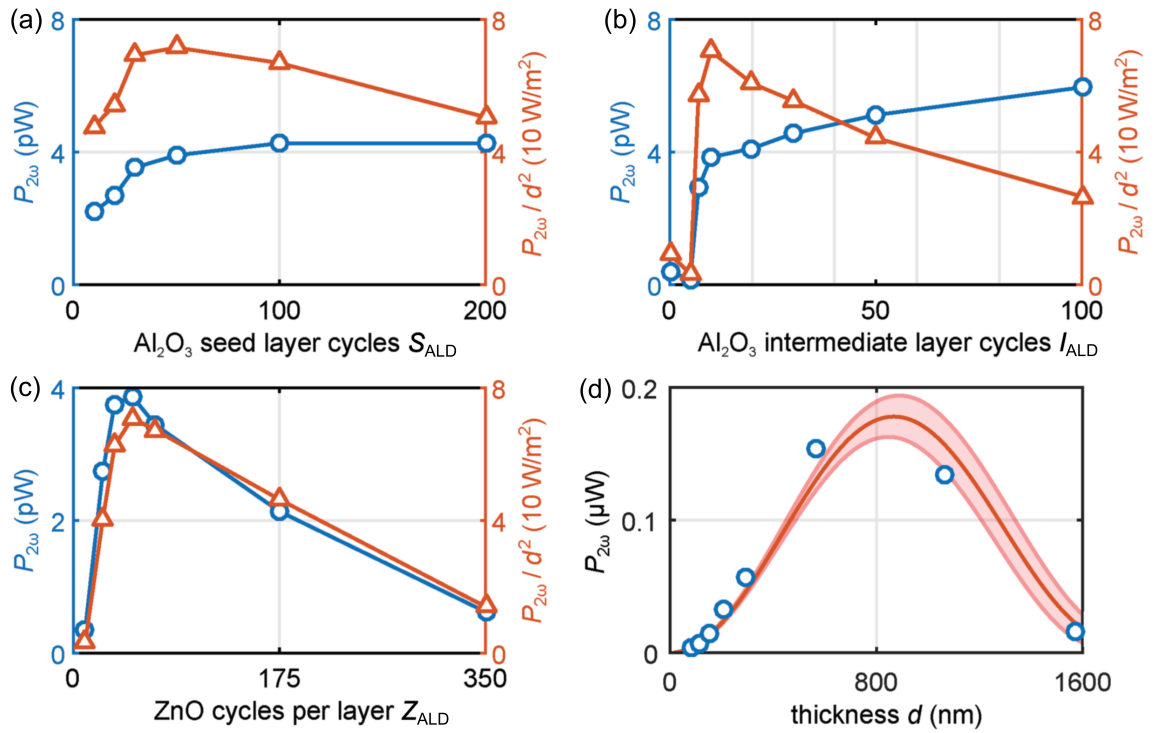
Figure 7.2: (a) Parameter sweeps for nanolaminates based on sample C. All measurements are performed with a p-polarized fundamental beam with a power of 100 mW and an incidence angle of 45°. **(a)–(c)** $P_{2\omega}$ (blue line, circles) and $P_{2\omega}/d^2$ (red line, triangles) are measured for different cycle sequences. Starting from sample C, (a) the number of seed layer cycles S_{ALD}, (b) the number of intermediate layer cycles I_{ALD}, and (c) the number of ZnO cycles per layer Z_{ALD} in a structure with a fixed overall number of 350 ZnO cycles are varied to get a deeper understanding of the individual influence factors on the second-order susceptibility. The optimal configuration is determined by finding the maximum of $P_{2\omega}/d^2$ versus Z_{ALD}. **(d)** $P_{2\omega}$ for samples with the optimized sequence $50 \times Al_2O_3 + M \times (50 \times ZnO + 10 \times Al_2O_3)$. M_{ALD} is varied from 7 to 168 macrocycles to fabricate samples with increasing thickness d. The experimental data (blue circles) are in excellent agreement with the theoretical calculations (red line) validating the effective material hypothesis. The red area is the error introduced through the different sets of refractive indices measured for the individual samples.

in zirconium and hafnium oxide films [231]. When taking into account the sample thickness, we obtain an optimum bulk second-order nonlinearity for $I_{ALD} = 10$ intermediate layer cycles. Finally, we investigate the influence of the ZnO layer thickness and, hence, of the ZnO crystallite size, on the nonlinear properties. We use samples with a fixed number of 350 ZnO cycles on top of a seed layer of 50 Al$_2$O$_3$ cycles. The 350 ZnO cycles are further subdivided into thinner layers by inserting Al$_2$O$_3$ intermediate layers, forming a total number of $350/Z_{ALD}$ macrocycles M_{ALD}, each built from Z_{ALD} ZnO and 10 Al$_2$O$_3$ cycles.

The samples are described by the cycle sequence $50 \times Al_2O_3 + 350/Z_{ALD} \times (Z_{ALD} \times ZnO + 10 \times Al_2O_3)$. The measurement results depicted in Figure 7.2(c) show an interesting behavior: $P_{2\omega}$ is quite small for a sample that consists of $M_{ALD} = 35$ macrocycles and thin ZnO layers, each composed of only $Z_{ALD} = 10$ cycles. At the same time, this is also true for a sample with $M_{ALD} = 1$ and a single thick ZnO layer made of $Z_{ALD} = 350$ cycles. On the one hand, the second-order response requires that the ZnO crystallites have a certain minimum size. The crystallites cannot grow properly if their growth is hindered after only a few cycles by an intermediate Al_2O_3 layer. On the other hand, the size of the ZnO crystallites and the probability for stacking faults increases if the individual ZnO layers become thicker [224]. Furthermore, the crystallite alignment and the number of interfaces and grain boundaries decrease [226]. Each of these aspects leads to a decreased second-order response. The trade-off between a sufficient crystallite size and the advantageous contributions of grain boundaries in combination with a good crystallite orientation leads to an optimum number of 50 ZnO cycles per layer.

The repeated cycling of ZnO and Al_2O_3 layers on top of the seed layer should, in principle, ensure a fixed crystallite orientation and size throughout the entire material, leading to nonlinear properties that are independent of the number of macrocycles and the film thickness. To verify this effective-material hypothesis, samples with the cycle sequence $50 \times Al_2O_3 + M_{ALD} \times (50 \times ZnO + 10 \times Al_2O_3)$ and $M_{ALD} = 7$ to 168 macrocycles are fabricated. For small thicknesses, $P_{2\omega}$ is expected to grow proportional to d^2. As usual, films with a thickness approaching the coherent buildup length deviate from this behavior due to a phase-mismatch between the fundamental and SH wave. We use the refractive indices and sample thicknesses derived from ellipsometry measurements and calculate the theoretical thickness dependence of $P_{2\omega}$ [33]. For each sample the set of measured refractive indices is used for the calculations, resulting in a total of eight curves. Afterwards, the curves are averaged and scaled with one global parameter to best fit the measured data. The error region is calculated from the deviations of the individual curves. The excellent overall agreement between experimental data and theoretical calculations in Figure 7.2(d) validates our effective-material hypothesis and, therefore, allows for an arbitrary up-scaling of the nanolaminate metamaterial thickness without the drawbacks usually encountered in other nonlinear thin films.
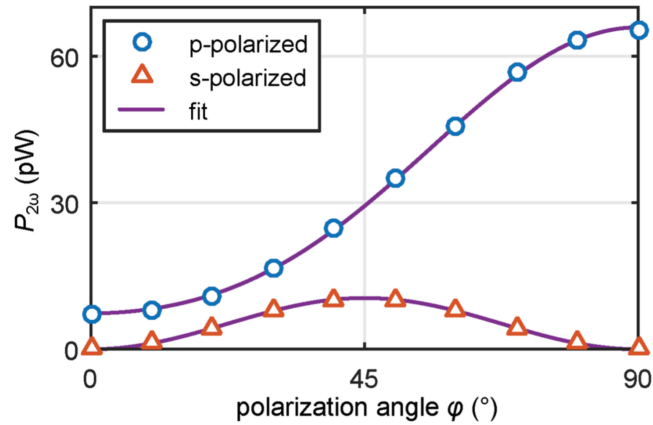
Figure 7.3: Typical measured s- and p-polarized SH power $P_{2\omega}$ from a sample with $M = 28$ macrocycles for varying polarization angle φ of the incident beam. Power and incidence angle of the fundamental beam are fixed to 200 mW and 45°, respectively. The second-order susceptibility tensor elements $\chi_{zzz}^{(2)} = -4.0\,\mathrm{pm V^{-1}}$, $\chi_{yyz}^{(2)} = 1.6\,\mathrm{pm V^{-1}}$, and $\chi_{zyy}^{(2)} = 1.5\,\mathrm{pm V^{-1}}$ are derived by fitting to theory and by calibration with respect to a quartz reference crystal.

7.4   Measurement of $\chi^{(2)}$ tensor elements

Finally, the second-order susceptibility tensor for a nanolaminate with $M_{\mathrm{ALD}} = 28$ macrocycles is determined following ref. [21]. The basic idea is to measure the s- or p-polarized SH power generated at a fixed incidence angle while the polarization angle of the fundamental beam is varied (for details, see the Experimental Section 7.6). The second-order susceptibility tensor can then be determined by fitting the theoretical model used in ref. [21] to the experimental data. To determine the reproducibility of the technique, we perform a total of 23 such measurements on different spots of two nominally identical samples. Each measurement is fitted and provides as a result a set of three independent tensor components. The mean values are $\chi_{zzz}^{(2)} = -4.0\,\mathrm{pm V^{-1}}$, $\chi_{yyz}^{(2)} = 1.6\,\mathrm{pm V^{-1}}$, and $\chi_{zyy}^{(2)} = 1.5\,\mathrm{pm V^{-1}}$, each with a relative standard deviation of at most 10%. A typical measurement is depicted in Figure 7.3, where the solid lines indicate the fitted theoretical model. It is, of course, interesting to compare these values to previous work on second-order nonlinear optical nanolaminates [21,22]. However, measured absolute values of these coefficients are prone to errors and should thereby be taken with a grain of salt. To arrive at a fair comparison, we have repeated the experiments on the optimum samples used in refs. [21,22], using the same experimental setup and
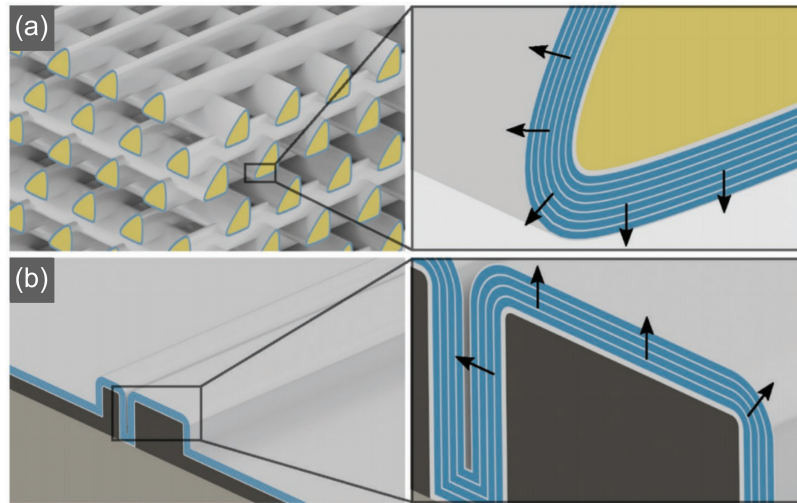
Figure 7.4: The efficient second-order nonlinear optical nanolaminates demonstrated in this work together with conformal coating by atomiclayer deposition (ALD) allows for the realization of 3D architectures that are fundamentally inaccessible via other thin-film deposition techniques like evaporation or molecular-beam epitaxy. **(a)** Scheme of a nanolaminate deposited on a 3D microlattice using ALD. **(b)** Scheme of a nanolaminate deposited on a silicon-on-insulator slot waveguide using ALD. The two insets on the right-hand side show magnified views of the nanolaminate with the optical axis of the ZnO crystallites indicated by arrows.

the same fitting procedure as for the ZnO/Al$_2$O$_3$ nanolaminates. The sample of ref. [22] has kindly been provided to us by the authors. We again perform several measurements on each sample and obtain mean values of $\chi^{(2)}_{zzz} = 1.3 \, \mathrm{pmV}^{-1}$ for the optimum sample in ref. [22], and $\chi^{(2)}_{zzz} = 0.8 \, \mathrm{pmV}^{-1}$ for the best sample of ref. [21], each with a relative standard deviation of less than 15%. Hence, despite potential inaccuracies of the absolute values of the second-order nonlinear-optical tensor coefficients, we may conclude that binary ZnO nanolaminates as presented in this communication can exhibit second-order susceptibilities that exceed those of the ABC-type nanolaminates studied in refs. [21,22]. In conclusion, we have shown that nanolaminates grown with ALD allow us to control both ZnO crystallite size and orientation, leading to a strongly enhanced second-order nonlinear response. The crystallite properties are tuned by means of seed and intermediate Al$_2$O$_3$ layers. At the same time, these additional layers ensure effective material properties independent of the actual film thickness and of the substrate properties. To the best of our knowledge, this is the first time an ALD-grown material shows such a strong second-order susceptibility with $\chi^{(2)}_{zzz} = -4.0 \, \mathrm{pmV}^{-1}$.

7.5   Outlook

Finally, we believe that our approach and the highly nonlinear metamaterial demonstrated in this work combined with the CMOS-compatible and conformal deposition via ALD potentially enables novel devices, for example in the context of silicon photonics. Figure 7.4 illustrates the well-known fact that ALD enables 3D architectures that are not accessible via other deposition techniques.

7.6   Experimental Section

Sample Fabrication: 170 μm thick borosilicate glass and silicon wafers as substrates were used in this study. Prior to deposition, the substrates were cleaned with acetone and dry-blown with nitrogen. To avoid errors in the nonlinear characterization, the film growth was limited to the front side of the substrates by covering the back side with high temperature resistant masking tape. The films were deposited with a Cambridge NanoTech Savannah 100 ALD system. Diethylzinc (Sigma-Aldrich) and deionized water were used as precursors for ZnO, and Al_2O_3 was grown from Trimethylaluminium (Sigma-Aldrich) and deionized water. The materials were deposited at a constant Argon flow of 20 sccm and a deposition temperature of 250 °C. All precursors were kept at room temperature and opened successively for a pulse time of 15 ms. After each pulse, the chamber was flushed for a period of 5 s before the next precursor was injected.

Ellipsometry: The nanolaminates deposited on silicon wafers substrates were used for ellipsometric measurements with a Sentech SE 850. The film thickness and the isotropic refractive index dispersion were derived using Cauchy's equation to fit the data.

X-Ray Diffraction: A D8-Discover diffractometer (Bruker AXS GmbH) with Cu-K_α radiation was used for the θ–2θ measurement. In the Bragg– Brentano θ–2θ configuration, only reciprocal-lattice vectors parallel to the surface normal gave rise to a signal. A quadratic baseline was subtracted from the actual data. The full width at half maximum of the Bragg peaks, as it was used in the Scherrer equation, was determined by fitting a Gaussian curve.

Transmission Electron Microscopy: For the STEM measurements, a sample deposited on a silicon wafer was prepared by cutting a cross-sectional lamella from the film using a Focused-Ion-Beam (FIB) system (FEI Strata 400 S). The initial cutting was performed with 30 kV gallium ions. The final polishing was done at 5 and 2 kV. A Philips Tecnai F20 ST operated at 200 kV in STEM mode using spot size 6, gun lens 6, an extraction voltage of 4.5 kV and a 70 μm C2 aperture (nominal beam diameter ≈ 1 nm) was used for high-angle annular dark-field (HAADF) STEM data acquisition. The EDX maps were acquired using an EDAX s-UTW EDX detector.

$\chi^{(2)}$ *Measurement:* The samples were excited using laser pulses derived from a Ti:Sa mode-locked oscillator operating at a repetition rate of 80.5 MHz, a full width at half maximum of 165 fs, and a center wavelength of 800 nm. The excitation power could be set by rotating a half-wave plate, followed by a polarizing beam-splitter cube. A wire-grid polarizer preceded by a quarter-wave plate was used to set the polarization of the fundamental beam impinging onto the sample. The laser beam was chopped to allow for lock-in detection and was loosely focused onto the sample to a spot radius of about 24.5 μm using a lens with a focal length of 200 mm. The diverging light was collimated by a lens with a focal length of 100 mm and filtered with a short-pass (cutoff wavelength 700 nm) and a band-pass filter (center wavelength 400 nm, spectral width 40 nm). Finally, the SH power was detected using a Hamamatsu R4332 photomultiplier tube. To distinguish between s- and p-polarized SH light, a wire-grid polarizer was placed in the beam path between sample and photomultiplier.

For determination of the $\chi^{(2)}$ tensor components, the SH power was recorded as a function of the input polarization φ while the sample was excited under a constant angle of incidence of 45° with respect to the substrate normal and a mean power of 200 mW. The measured SH power could be fitted by a theoretical expression as described in the supplementary material of the publication by Alloatti et al. [21]. The measurements presented there relied on absolute values for the fundamental power, pulse duration, focal spot size, photomultiplier sensitivity, etc. These quantities could not be easily determined with high precision. To eliminate the associated uncertainties, this study switched to using a reference sample, namely a 100 μm-thick *y*-cut quartz plate

with the well-known tensor element $\chi_{xxx}^{(2)} = 0.6\,\mathrm{pmV}^{-1}$ [211]. In a Maker-fringe measurement, the quartz plate was excited using p-polarized light with a mean input power of 100 mW while detecting emerging p-polarized SH light [198]. The data were fitted to theoretical expressions given by Herman and Hayden to determine the specified unknown quantities [33]. In this fashion, in sharp contrast to a previous work [21], no absolute values were needed. In all calculations performed in this work, the suggestion given by Herman and Hayden was followed to set the Fresnel coefficient for the SH beam between air and nonlinear material to zero.

[end of paper [J5]]

8   Summary and outlook

8.1   Summary

Photonic integrated circuits based on the silicon photonic (SiP) platform stand out due to high integration density and highly reproducible mass production based on sophisticated CMOS-based fabrication processes. However, silicon lacks second-order nonlinearities such that devices like optical frequency converters, ultra-fast optical gates, or Pockels-type EO modulators are not available in all-silicon integrated circuits. This distinct deficiency of SiP can be overcome by heterogeneous integration of silicon waveguide structures with materials that offer second-order nonlinearities.

In this work, two material classes for heterogeneous integration were investigated. The first class are organic EO materials with tailored EO properties, geared towards ultra-high Pockels coefficients. These materials were combined with SiP slot waveguides to realize silicon-organic hybrid (SOH) modulators for optical communications. In several experimental demonstrations with SOH devices, new record performance parameters for EO modulators in terms of energy efficiency, footprint, optical insertion loss, and data rates were achieved. In a first set of experiments, the highly efficient organic material JRD1 was integrated in SOH devices. These modulators showed a record-high in-device EO figure of merit of $n^3 r_{33} = 2300$ pm/V, leading to an estimated Pockels coefficient of 390 pm/V and a π-voltage-length product of only $U_\pi L = 0.32$ Vmm. In a next step, we shortened the phase-shifter sections of these devices from 1.5 mm to 0.28 mm to reduce the optical insertion loss without unduly increasing the π-voltage. The resulting low-footprint SOH devices featured a phase-shifter insertion loss of only 0.7 dB and were used to generate PAM4 signals at a symbol rate of 100 GBd using CMOS compatible drive voltages of roughly 0.7 V_{pp}. Another SOH device demonstration addressed the arguably biggest challenge towards industrial adoption of SOH modulators: Thermally induced relaxation of the poling-induced order of the EO chromophores. To realize long-term thermally stable SOH devices, a side-chain EO polymer with high glass-transition temperature was used. The

resulting modulators were tested according to Telcordia standards for high temperature storage, exhibiting stable performance at 85 °C for thousands of hours, which marks a crucial breakthrough for SOH integration technology.

The second class of second-order nonlinear materials investigated in this work are novel nanolaminate thin-films fabricated using CMOS-compatible atomic layer deposition (ALD). For simplicity, the thin films in this work were grown and characterized on planar glass slides. However, ALD is also suited to conformally coat optical waveguides. In addition, due to their inorganic nature, these materials are expected to offer excellent stability against elevated temperatures and high optical intensities, thus opening promising options for hybrid integration in future SiP circuits. A reliable measurement of the second-order nonlinearity of these nanolaminates is a challenging task. For that reason, two different characterization techniques, which both rely on second-harmonic generation, were investigated in this work. The individual strengths and weaknesses of the two techniques were determined and a detailed analysis of error sources was conducted such that a reliable extraction of the second-order nonlinearity is ensured. In addition, a novel binary nanolaminate consisting of alternating layers of Al_2O_3 and ZnO was introduced. The second-order nonlinearity was optimized by systematic variations of the growth parameters, leading to a value of $\chi^{(2)}$ = -4.0 pm/V at a wavelength of 400 nm. This already exceeds the value of traditional nonlinear crystals such as KDP.

8.2   Outlook and future work

SOH modulators

The achieved performance parameters of the SOH modulators presented in this work mark important milestones towards deployment of these devices in practical applications outside well-controlled laboratory environments. However, there are still various technological obstacles which have to be overcome to achieve this final goal. First, the thermal stability of the organic EO materials needs to be improved. While long-term thermal stability at 85 °C was shown in this work, short-term stability at temperatures of 250 °C for tens of seconds are required to ensure compatibility of SOH devices with standard reflow soldering processes for electrical packaging. This might be achieved

using materials with even higher glass-transition temperatures. In addition, the photochemical stability of SOH modulators requires improvement. A straightforward approach to achieve this goal could be a hermetic encapsulation of the devices, which would prevent oxygen from penetrating and degrading the organic materials. The photochemical stability could be further improved by using cross linkable materials, which are less susceptible to photo-oxidation. These materials could additionally overcome the trade-off between high glass-transition temperatures and ultra-large EO coefficients, thus offering great potential for future SOH modulators. Another area for improvement is the EO bandwidth of the devices. A recently developed model of the RF properties of the devices predicts that optimized modulator designs will result in 3 dB EO bandwidths in excess of 100 GHz, entirely avoiding the currently used gate voltage and targeting an application space that was so far only accessible by plasmonic devices [136], which suffer from high optical loss.

In the near future, the SOH integration technology could also penetrate new applications, *e.g.*, in the field of microwave photonics, where SOH devices could be employed in ultra-broadband photonic-aided RF-amplifiers. In these devices, a weak input electrical signal modulates an optical carrier in an Mach-Zehnder modulator. The optical signal is amplified using an EDFA and detected by a broadband photodiode with large RF output power. For a large RF-gain and a low noise figure this system should employ an EO modulator featuring a small π-voltage and low optical insertion loss, which makes SOH devices promising candidates.

Nanolaminates

An important next step for the nonlinear nanolaminates investigated in this work would be a proof of concept of the combination with SiP circuits. For example, hybrid EO modulators could be realized by growing nanolaminates on a SiP base structure similar to the one of SOH modulators. However, in contrast to SOH devices, the slot waveguides should feature Si rails with different widths. This is required since ALD growth is conformal, resulting in simultaneous growth of the nanolaminate from both interfaces of the slot waveguide. A non-vanishing Pockels effect is thus only achieved for an optical mode, which is asymmetric with respect to the center of the slot – this is achieved in an asymmetric slot waveguide.

Another crucial aspect for future work is the further improvement of the nonlinearity of the nanolaminates. Presumably an increase by up to two orders of magnitude is required for the technology to become attractive for practical applications in the field of optical communications. This is a challenging task, which requires systematic material screening and a thorough optimization of the ALD growth parameters. Considering the fairly early research stage of this technology in combination with the vast portfolio of materials that can be potentially implemented in ALD-grown nanolaminates, it is still conceivable that this goal can be ultimately met in a dedicated effort with material scientists.

Appendices

A. Efficient SOH modulators with ultra-high in-device EO activity

[start of supplementary information of paper [J1]]

A.1 Experimental Setup for the π-voltage measurement

The experimental setup for the measurement of the π-voltage U_π of the silicon-organic hybrid (SOH) modulator is depicted in Figure A.1. The optical carrier obtained from an external cavity laser (ECL) is coupled to and from the silicon photonics chip via grating couplers (GC) while a triangular waveform obtained from a function generator (FG) is fed to the SOH Mach-Zehnder Modulator (MZM) via microwave probes. The modulated light is detected with a photodiode that is connected to an oscilloscope. The oscilloscope additionally monitors the drive voltage applied to the MZM. The modulator is biased in its 3 dB point and the amplitude of the triangular waveform is chosen such that the modulator is over-modulated. That is, the peak-to-peak drive voltage is larger than the U_π of the device under test. In this case, U_π can be directly read out on the oscilloscope as the voltage increment needed to drive the modulator from
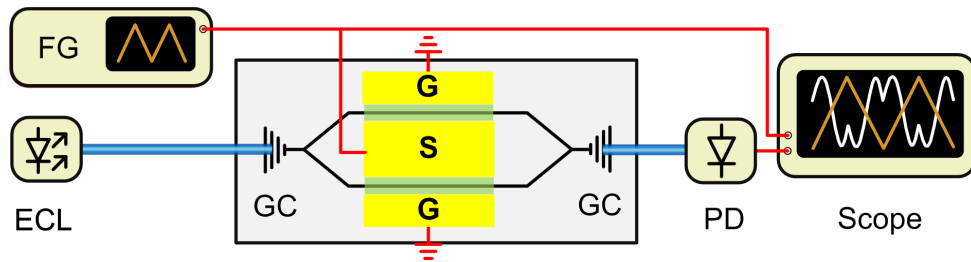
Figure A.1: Experimental setup for the π-voltage measurement. A triangular waveform obtained from a function generator (FG) is fed to the SOH modulator while an optical carrier obtained from an external cavity laser (ECL) is coupled to and from the chip via grating couplers (GC). The over-modulated optical signal is detected with a photodiode and an oscilloscope which also monitors the output of the FG. U_π can be read out as the voltage increment needed to drive the modulator from minimum to maximum transmission.

its minimum to its maximum transmission point, see Figure 3.2(c) and (d) of Chapter 3.

A.2 Optical loss of the SOH modulator

The total fiber–to-chip coupling losses amount to 8.9 dB caused by the non-ideal grating couplers. The on-chip loss of the MZM amounts to 8.2 dB. These on-chip losses can be decomposed into passive components and the loss in the SOH slot waveguide. The passive components include two multi-mode interference (MMI) couplers with losses of 0.37 dB per coupler, two optical mode converters at the strip-slot waveguide interfaces with losses of 0.20 dB per converter, and strip-waveguide insertion losses of 1.3 dB. The remaining 5.8 dB are attributed to the SOH slot waveguide insertion losses of the 1.5 mm long MZM which results in a propagation loss of 3.9 dB/mm. This includes both scattering loss from the slot waveguide sidewalls and free-carrier absorption loss in the doped silicon waveguide structures. Note that dedicated test structures were used to determine the grating coupler losses and the losses of the MMI couplers and the mode converter structures. The propagation losses of the strip waveguide amount to 2.5 dB/cm, specified by the chip manufacturer.
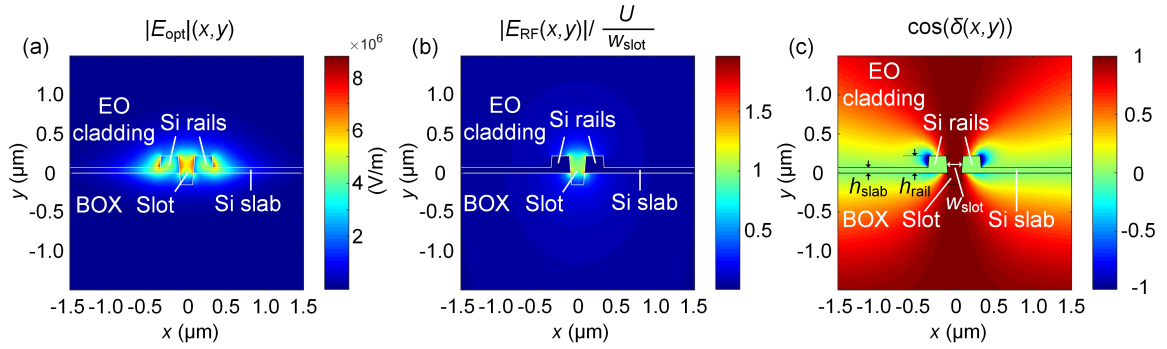
Figure A.2: Simulation results. **(a)** Magnitude of the optical field $\left|E_{\text{opt}}(x,y)\right|$ for a launched optical power of 20 mW. **(b)** Normalized magnitude of the RF field, $\left|E_{\text{RF}}(x,y)\right|/\left(U/w_{\text{slot}}\right)$ which amounts to about unity in the center of the slot, due to the normalization. Both optical and RF mode are tightly confined to the EO-material-filled slot region which results in efficient modulation. **(c)** $\cos(\delta(x,y))$, where $\delta(x,y)$ is the angle between field lines of the optical and the RF mode. Inside, as well as above and below the slot region, field lines of optical and RF field are parallel resulting in $\cos(\delta(x,y)) = 1$. Directly above the slabs $\cos(\delta(x,y))$ amounts to zero since the field lines are perpendicular. For all simulations we take into account that the slot is over-etched by 150 nm and we assume that the slot sidewalls are inclined by 5° with respect to the sample normal. We use two sets of devices in our work. They share the same slab height h_{slab} of 70 nm and silicon rail height h_{rail} of 220 nm but are different with respect to the slot width w_{slot} which is measured at half the silicon rail height and amounts to 190 nm and 150 nm, respectively.

A.3 Mathematical relations for calculating the in-device EO figure of merit $n^3 r_{33}$ of the SOH MZM

The phase change $\Delta\phi$ of the optical carrier in the silicon-organic hybrid (SOH) modulator can be written as [234]

$$\Delta\phi = n^4 \frac{\epsilon_0 c \pi L}{2\lambda_0 P} \int\limits_{-\infty}^{\infty} \int\limits_{-\infty}^{\infty} r_{33}(x,y) E_{\text{RF,EO}}(x,y)\,|\,E_{\text{opt,EO}}(x,y)\,|^2 \mathrm{dxdy}, \tag{A.1}$$

where n is the refractive index of the organic electro-optic (EO) material, ε_0 is the vacuum permittivity, c is the vacuum speed of light, L is the length of the phase shifter, λ_0 is the wavelength of the optical carrier, $r_{33}(x,y)$ is the non-uniform EO coefficient. $E_{\text{RF,EO}}(x,y)$ is the component of the vectorial mode field of the applied radio frequency (RF) field pointing in the direction of the local chromophore orientation, which is defined by the axis of the molecular dipole. Similarly, $E_{\text{opt,EO}}(x,y)$ is the corresponding component of the vectorial mode

139

field of the optical carrier. The parameter P is the power of the optical mode, which is defined as

$$P = \frac{1}{2} \int_{-\infty}^{\infty} \int_{-\infty}^{\infty} \mathrm{Re}\{\vec{E}_{\mathrm{opt}}(x,y) \times \vec{H}_{\mathrm{opt}}^{*}(x,y)\} \cdot \hat{e}_z \,\mathrm{dxdy}. \tag{A.2}$$

The non-uniformity of $r_{33}(x,y)$ is caused by the inhomogeneity of the electric poling field that dictates the local orientation of the chromophore dipoles. Due to this non-uniformity we consider here the mean value of the EO coefficient $\overline{r}_{33\,\mathrm{slot}}$ in the slot region of the SOH modulator, $i.e.$, the region between the Si rails. We furthermore assume a linear dependence of r_{33} on the poling field E_{pol} and approximate the (x,y)-dependency of the static poling field by the (x,y)-dependency of the RF mode field. This leads to

$$r_{33}(x,y) = \overline{r}_{33\,\mathrm{slot}} \frac{\left|E_{\mathrm{pol}}(x,y)\right|}{\overline{\left|E_{\mathrm{pol}}\right|}_{\mathrm{slot}}} \rho(x,y) \approx \overline{r}_{33\,\mathrm{slot}} \frac{\left|E_{\mathrm{RF}}(x,y)\right|}{\overline{\left|E_{\mathrm{RF}}\right|}_{\mathrm{slot}}} \rho(x,y), \tag{A.3}$$

where $\overline{\left|E_{\mathrm{pol}}\right|}_{\mathrm{slot}}$ and $\overline{\left|E_{\mathrm{RF}}\right|}_{\mathrm{slot}}$ are the mean values of the magnitude of the static poling field and the RF field in the slot region, respectively and $\rho(x,y)$ is unity for (x,y)-values in the EO material and zero otherwise. By using Eq. (A.3) we can rewrite Eq. (A.1) as

$$\Delta\phi = n^4 \frac{\epsilon_0 c \pi L}{2\lambda P} \overline{r}_{33\,\mathrm{slot}} \int_{-\infty}^{\infty} \int_{-\infty}^{\infty} \frac{\left|E_{\mathrm{RF}}(x,y)\right|}{\overline{\left|E_{\mathrm{RF}}\right|}_{\mathrm{slot}}} \rho(x,y) E_{\mathrm{RF,EO}}(x,y) \,|\, E_{\mathrm{opt,EO}}(x,y)|^2 \mathrm{dxdy}.$$

$$\tag{A.4}$$

Since the chromophore dipole moments align along the poling field (which is approximated by the RF field), the component $E_{\mathrm{RF,EO}}(x,y)$ is simply given by the magnitude of the RF field $\left|E_{\mathrm{RF}}(x,y)\right|$. For the corresponding component of the optical mode we can deduce $\left|E_{\mathrm{opt,EO}}(x,y)\right| = \left|E_{\mathrm{opt}}(x,y)\right| \cos(\delta(x,y))$, where $\delta(x,y)$ is the angle between field lines of the optical and the RF mode. Finally, we normalize the RF field by U/w_{slot}, where U is the RF voltage which is applied across the SOH slot waveguide and w_{slot} is the slot width measured at half the height of the silicon rails. Using these simplifications the induced phase change writes

$$\Delta\phi = n^4 \frac{\epsilon_0 c\pi L}{2\lambda P} \overline{r_{33\,\mathrm{slot}}} \frac{U}{w_{\mathrm{slot}}} \int\limits_{-\infty}^{\infty}\int\limits_{-\infty}^{\infty} \frac{|E_{\mathrm{RF}}(x,y)|^2 \, \rho(x,y)}{|E_{\mathrm{RF}}|_{\mathrm{slot}} U / w_{\mathrm{slot}}} \, | E_{\mathrm{opt}}(x,y)|^2 \cos^2(\delta(x,y))\mathrm{dxdy}.$$

(A.5)

The SOH modulator is implemented as a Mach-Zehnder modulator (MZM) with a ground-signal-ground (GSG) transmission line configuration realizing push-pull operation. Therefore, for a total phase shift of π, the phase is shifted by only ±π/2 in the two arms of the MZM, respectively. As a consequence, the mean value of the EO figure of merit in the slot region $n^3 \overline{r_{33\,\mathrm{slot}}}$ is linked to the π -voltage U_π by

$$n^3 \overline{r_{33\,\mathrm{slot}}} = \frac{\lambda w_{\mathrm{slot}}}{2U_\pi L}\left(\frac{\epsilon_0 cn}{2P} \int\limits_{-\infty}^{\infty}\int\limits_{-\infty}^{\infty} \frac{|E_{\mathrm{RF}}(x,y)|^2 \, \rho(x,y)}{|E_{\mathrm{RF}}|_{\mathrm{slot}} U / w_{\mathrm{slot}}} \, | E_{\mathrm{opt}}(x,y)|^2 \cos^2(\delta(x,y))\mathrm{dxdy} \right)^{-1}$$

$$= \frac{\lambda w_{\mathrm{slot}}}{2U_\pi L} \times \frac{1}{\Gamma},$$

(A.6)

where we introduced the interaction factor Γ. The mode fields are simulated with the commercial software CST MICROWAVE STUDIO by using a finite integration method. The magnitude of the optical field for a launched power of 20 mW is depicted in Figure A.2(a). Figure A.2(b) shows the magnitude of the RF field at a frequency of 20 GHz normalized by U/w_{slot}. Since the electrical conductivity of the Si rails and slabs are much higher compared to the EO material and the lower SiO_2 cladding, these components are modeled as perfect electric conductors. Due to the normalization, the plotted field amounts to approximately unity in the slot region. In close proximity to the corners of the rails, values of about 2 are reached, which is hardly visible in the figure. It can be seen that both the RF and the optical mode are tightly confined in the slot region, which results in highly efficient modulation. Simulation results for $\cos(\delta(x,y))$ are shown in Figure A.2(c). In the slot region as well as above and below the slot, field lines of RF and optical field are parallel resulting in $\cos(\delta(x,y)) \approx 1$ whereas further left and right of the slot $\cos(\delta(x,y))$ decreases and becomes zero directly above and below the silicon slabs. Near the outer sidewalls of the rails, values of $\cos(\delta(x,y)) \approx$ -1 are found, since field lines of the optical and RF field are antiparallel in this region. With the simulated mode fields we can calculate the interaction factor Γ. Note that the slot dimensions, in
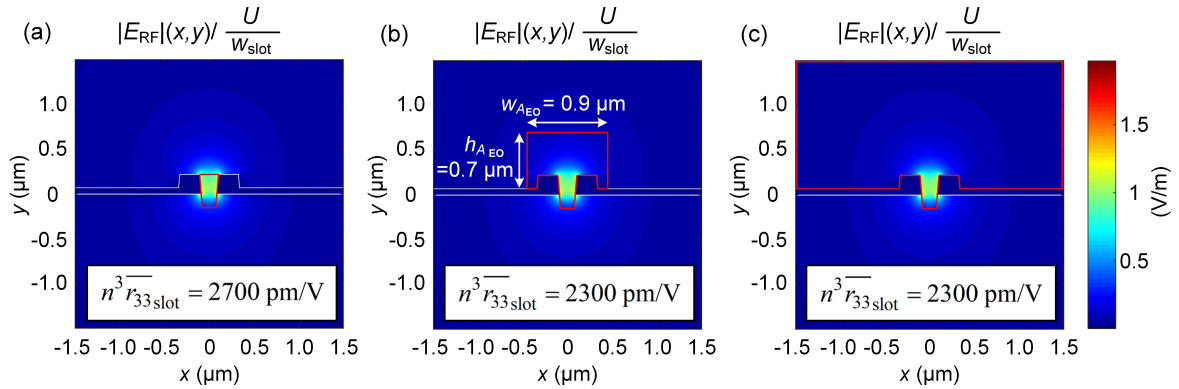
Figure A.3: Influence of choice of finite integration area A_{EO} on calculated $n^3\overline{r_{33\,slot}}$. Depicted is the normalized magnitude of the RF field $\left|E_{RF}(x,y)\right|/(U/w_{slot})$ and different integration areas A_{EO} are indicated by red lines. **(a)** The integration area A_{EO} includes only the slot region and the over-etched volume. The corresponding $n^3\overline{r_{33\,slot}}$ would amount to $2700\,\mathrm{pm/V}$, which overestimates the actual value. **(b)** $n^3\overline{r_{33\,slot}}$ decreases and converges to a constant value for growing A_{EO}. For an integration area of width and height of $w_{A_{EO}} = 0.9\,\mu\mathrm{m}$ and $h_{A_{EO}} = 0.7\,\mu\mathrm{m}$, respectively, the limit of $n^3\overline{r_{33\,slot}} = 2300\,\mathrm{pm/V}$ is reached. **(c)** Increasing the integration area over the whole displayed range doesn't influence the calculated $n^3\overline{r_{33\,slot}}$ any further.

particular the slot width w_{slot}, slightly influence the interaction factor. In Figure A.4 we plot the interaction factor Γ as a function of the slot width w_{slot}. It can be seen that Γ slightly decreases with increasing w_{slot}, due to the decreasing modal overlap of optical and RF mode.

Note that the slot of the presented SOH modulators is slightly over-etched, generating a free volume underneath the slot, as indicated in Figure A.2. This was confirmed by cutting a trench perpendicular to the direction of propagation of the slot waveguide by using focused ion beam (FIB) milling and by subsequently investigating the cross section of the waveguide. We extracted an over-etch depth of $130 \pm 20\,\mathrm{nm}$. For our simulations, we assume that the volume caused by the over-etching is entirely filled with the organic EO material, and for all simulations we use an over-etch depth of $150\,\mathrm{nm}$ in order to not overestimate the calculated $n^3\overline{r_{33\,slot}}$. Additionally, we consider in our model a silicon rail sidewall angle of $5°$ with respect to the wafer-normal direction. This value was obtained from transmission electron microscope (TEM) investigations of the cross section of similar SOH devices. In our simulations, we further use an increased density of mesh cells near the angled

sidewall interfaces in order to better describe the inhomogeneity of the poling field in these regions.

The numerical evaluation of the integral in Eq. (S6), in praxis, requires the limitation to a finite integration area A_{EO} rather than an integration over the entire XY-plane. However, A_{EO} has to be carefully selected as $n^3 \overline{r_{33\,\mathrm{slot}}}$ is overestimated if A_{EO} is chosen too small.

In Figure A.3, the normalized magnitude of the RF field $\left|E_{\mathrm{RF}}(x,y)\right| / \left(U / w_{\mathrm{slot}}\right)$ is depicted and three different integration areas A_{EO} are indicated by the red lines. In Figure A.3(a) A_{EO} extends only over the slot region and the over-etched region underneath the slot. Here, the calculated $n^3 \overline{r_{33\,\mathrm{slot}}}$ would amount to 2700 pm/V, which overestimates the actual value. This is due to the fact, that a considerable part of the RF and the optical mode are excluded from the chosen integration area A_{EO}. For growing integration area A_{EO}, $n^3 \overline{r_{33\,\mathrm{slot}}}$ decreases and converges to a constant value of 2300 pm/V. This value can be reached by only moderately extending A_{EO} with respect to the case shown in Figure A.3(a), as illustrated in Figure A.3(b). Here, the integration area width and height amounts to $w_{\mathrm{AEO}} = 0.9\ \mu\mathrm{m}$ and $h_{\mathrm{AEO}} = 0.7\ \mu\mathrm{m}$, respectively. In Figure A.3(c) the integration area is extended over the whole displayed range. However, the corresponding $n^3 \overline{r_{33\,\mathrm{slot}}} = 2300\,\mathrm{pm/V}$ does not change compared to the smaller integration area depicted in Figure A.3(b) since the contribution of the additionally included parts of the RF field and of the optical mode field is negligible.

For the remainder of the document as well as in the manuscript (Chapter 3) we avoid the inconvenient notation $\overline{r_{33\,\mathrm{slot}}}$ for the mean in-device EO coefficient in the slot region. Instead, for the sake of readability, we simply refer to the in-device EO coefficient r_{33}. Note, however, that all reported values for $n^3 r_{33}$ and r_{33} for JRD1 in Chapter 3 actually refer to $n^3 \overline{r_{33\,\mathrm{slot}}}$ and $\overline{r_{33\,\mathrm{slot}}}$, respectively.

A.4 Estimation of refractive index and in-device r_{33}

In principle, if the in-device refractive index n of the OEO material is known, the EO coefficient r_{33} can be calculated from the measured in-device EO figure of merit $n^3 r_{33}$. Quantifying the refractive index n, however, is a challenging task

due to the inherent optical anisotropy of the OEO chromophores and the associated birefringence. The birefringence is caused by a local alignment of the chromophores, which may result from externally applied poling fields or from interactions of chromophores with adjacent surfaces. To estimate the refractive index of JRD1, we prepared unpoled and poled thin-film samples and directly measured the birefringence using variable-angle spectroscopic ellipsometry (VASE) [235]. The unpoled reference sample was fabricated by spin coating a roughly 1 μm thick JRD1 film on an ITO-coated glass slide. Samples for poling are fabricated by additionally sputtering a thin film of gold on the JRD1 layer such that JRD1 is sandwiched between layers of ITO and gold, which serve as the two poling electrodes. Note that the poling field for our thin-film tests was limited to 100 V/μm by dielectric breakdown, which is smaller than the value of 450 V/μm used in SOH devices. For the VASE measurement, the gold top electrode is removed by an etching step using an iodine (I_2)/potassium iodide (KI) solution after the poling process.

The ellipsometry data was acquired using a commercially available VASE ellipsometer (model M-2000 by J. A. Woollam Co.) [236]. For extracting the refractive indices from the raw data, we use the evaluation software supplied with the device (CompleteEASE software version 4.81) [237], modeling JRD1 as an anisotropic layer with refractive indices $n_\parallel$ and $n_\perp$ defined in the directions parallel and perpendicular to the sample surface, respectively. Note that the indices $n_\parallel$ and $n_\perp$ correspond to the coordinate system of the substrate on which the film is deposited and not to the index ellipsoid associated with an individual chromophore. The film indices $n_\parallel$ and $n_\perp$ are hence distinctively different from the ordinary and the extraordinary molecular refractive indices n_o and n_e of the chromophore. For the unpoled film we obtain $n_{\parallel,u} = 1.85$, $n_{\perp,u} = 1.76$ and $\Delta n_u = n_{\perp,u} - n_{\parallel,u} = -0.09$. Note that already the unpoled sample exhibits significant birefringence and that the refractive index $n_\parallel$ in the in-plane direction exceeds the one measured in the surface-normal direction, $n_\parallel > n_\perp$. We attributed this phenomenon to chromophore-surface interactions, which favor orientation of chromophores parallel to the substrate surface, thus increasing $n_\parallel$ and decreasing $n_\perp$. Upon poling, the birefringence reduces slightly and we obtain $n_{\parallel,p} = 1.83$, $n_{\perp,p} = 1.77$ and $\Delta n_p = n_{\perp,p} - n_{\parallel,p} = -0.06$. This change is attributed to an increased chromophore alignment perpendicular to the interface induced by the poling field. The comparison between unpoled and poled thin-

film samples indicates that the birefringence induced by chromophore-surface interactions is of the same magnitude as the poling-induced birefringence.

For determining the EO coefficient r_{33} from the in-device EO figure of merit $n^3 r_{33}$, we need to know the in-device refractive index $n = n_x$ seen by the dominant electric field (E_x) of the optical quasi-TE mode, see Figure A.2 for a definition of the coordinate system. Since a direct measurement of the birefringence in the slot is not possible, we rely on an estimated value of n_x. In this context, it is important to avoid any underestimation of n_x, which would lead to an overestimation of r_{33}. The findings obtained from the characterization of birefringence in the thin film suggest that, after deposition, chromophores in SOH devices are predominantly aligned in the zy-plane, parallel to the slot sidewalls, forced by a strong influence of surface-chromophore interactions within the nanoscopic slot. In the slot, the influence of these interactions is even stronger than in our thin-film samples, and we hence expect an in-device refractive index n_x that does not exceed the value of $n_{\perp,\mathrm{u}} = 1.76$ measured in the unpoled thin film. Poling of the SOH modulator leads to a re-orientation of some of the chromophores along the x-direction, which would increase the refractive index again. However, this re-orientation only affects a rather small fraction of the overall number of chromophores – for our highest EO activity of $n^3 r_{33} = 2300$ pm/V, the acentric order parameter amounts to $\langle cos^3 \vartheta \rangle < 0.2$. We may hence assume that the in-device refractive index n_x is still close to the value of $n_{\perp,\mathrm{p}} = 1.77$ measured in the poled thin film and does very likely not exceed the average value of $n = \frac{1}{2}(n_{\|,\mathrm{p}} + n_{\perp,\mathrm{p}}) \approx 1.80$, which agrees well with the previously published "isotropic" refractive index of JRD1 of $n = 1.81$, which was obtained from an ellipsometry measurement, in which JRD1 was modeled as an isotropic layer [100]. To calculate r_{33} we therefore use the value of $n = 1.81$, which simplifies the comparison with previously published EO coefficients of JRD1 [100].

Using the in-device EO figure of merit $n^3 r_{33} = 2300$ pm/V and the estimated in-device refractive index of JRD1 of 1.81, we obtain $r_{33} = 390$ pm/V. Note that this value has to be taken with caution, since the refractive index may still be subject to large uncertainties.
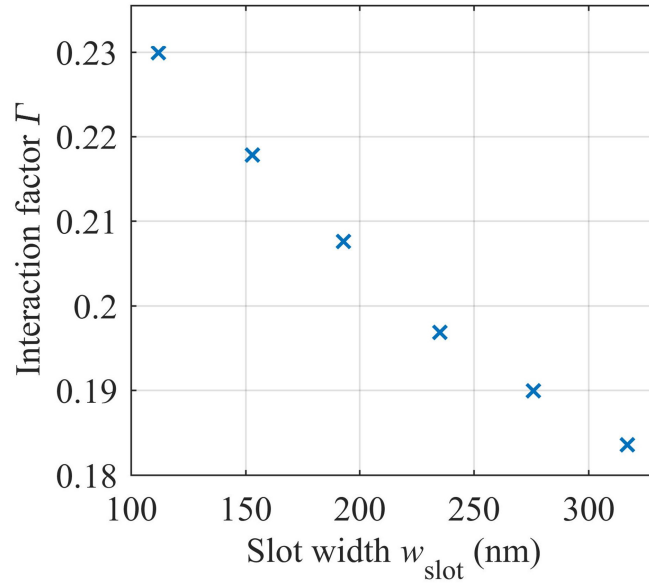
Figure A.4: Interaction factor Γ as a function of the slot width w_{slot} for an in-device refractive index of $n = 1.81$. Γ decreases with increasing slot width as the overlap between the optical and the RF mode decreases for wider slots.

A.5 Error estimation of in-device r_{33} and $n^3 r_{33}$

We identify the uncertainty of the slot width measurement and the uncertainty of the in-device refractive index as the two main reasons for errors in the reported values of r_{33} and $n^3 r_{33}$. The slot widths were obtained by analyzing 70 top-view SEM micrographs for which we estimate a measurement accuracy of $\Delta_w = \pm 10$ nm. The accuracy of the in-device refractive index we estimate to $\Delta_n = \pm 0.1$. Note that the inaccuracy in refractive index Δ_n leads to an inaccuracy in the interaction factor Γ, see Eq. (A.6). For the investigation of this effect, we plot the interaction factor Γ as a function of the refractive index n in Figure A.5. We can see that Γ increases with increasing n. Using the etsimated value of $n \approx 1.81$ as a reference, and assuming $\Delta_n = \pm 0.1$, we find for the interaction factor an error of $\Delta_\Gamma = 0.011$. Combining the above listed effects we obtain $n^3 r_{33} = (2300 \pm 170)$ pm/V and $r_{33} = (390 \pm 70)$ pm/V for the error bounds of the in-device EO figure of merit and the in-device EO coefficient, respectively. The relative error for $n^3 r_{33}$ is smaller compared to the respective error of r_{33} since the uncertainty of the refractive index Δ_n enters the calculation for the error of
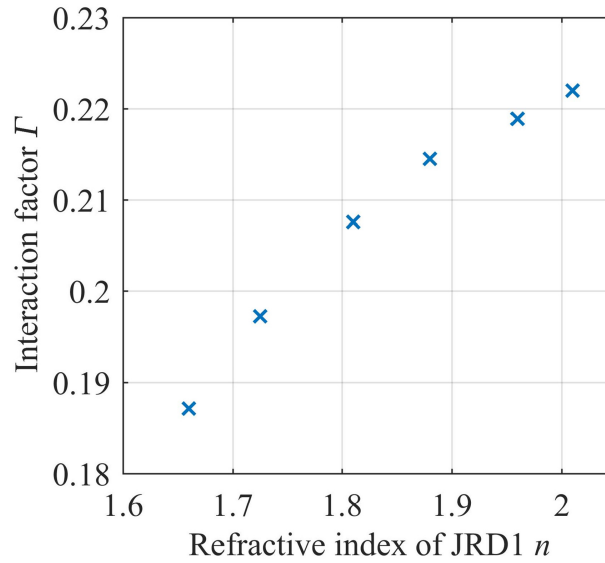
Figure A.5: Interaction factor Γ as a function of the refractive index n of JRD1 for a device with slot width of 190 nm. For a variation of the in-device refractive index of $n = 1.81\pm0.1$, the field interaction factor varies only by $\Gamma = 0.208\pm0.011$, corresponding to a relative change of 5 %.

$n^3 r_{33}$ only indirectly via Δ_Γ whereas both Δ_n and Δ_Γ have to be considered for the calculation of the uncertainty of r_{33}.

Note that the uncertainty in slot width $\Delta_w = \pm10$ nm induces an additional uncertainty of the interaction factor Γ, see Figure A.5. However, since the induced relative changes are about only 1 % we neglect this effect.

A.6 Material processing and device functionalization

For applying the JRD1 chromophore to the silicon chip, the organic material is first dissolved in 1,1,2-trichloroethane (TCE) and stirred for 3 hours to ensure good mixing. For material deposition on the silicon chip, we employ a micro dispenser setup consisting of a glass capillary with an inner tip diameter of 30 μm. The position of the capillary can be adjusted by a computer controlled 3D translation stage. We rely on capillary forces to fill the needle with the solution. On touching the surface, the solution wets the chip over a limited region with a radius of about 15 μm. For functionalizing the modulators, we

translate the capillary along the Mach-Zehnder arms to obtain a uniform coverage of the silicon slot waveguides. For drying of the deposited solution, the chip is heated to 60 °C for 30 min. Subsequently, the device is stored in a high vacuum (10^{-4} mbar) for 12 h at room temperature in order to remove the remaining solvent.

[end of supplementary information of paper [J1]]

B.   Low-loss, small footprint SOH modulators for high-speed signaling

The following content was published as the appendix to the journal article [J2]. To fit the structure and layout of this document, it was adapted accordingly.

[start of supplementary information of paper [J2]]

B.1   Determination of phase-shifter insertion loss

To determine the phase-shifter insertion loss, we investigated SOH devices on nominally identical MZM dies from four different positions of a 200 mm wafer, which we label Die 1, Die 2, Die 3, and Die 4. Each die contains four imbalanced SOH MZM with 280 μm-long phase shifters. For each device, we extract the dB-values of the phase-shifter loss $a_{PS}(\lambda_i)$ at wavelengths λ_i of constructive interference by subtracting the attenuation of the two grating couplers ($2a_{GC}(\lambda_i)$), the two MMI splitters ($2a_{MMI}(\lambda_i)$), the strip waveguides (a_{Strip}) and the two mode converters ($2a_{Conv}$) from the total measured attenuation ($a_{tot}(\lambda_i)$) of the respective device. Subsequently, an average of $a_{PS}(\lambda_i)$ over the set of wavelengths λ_i gives the mean phase-shifter loss $\overline{a}_{PS}$, see Chapter 4. For the grating couplers, the MMI splitters, and the mode converters, the attenuations are obtained from measurements of nominally identical reference structures fabricated in the same production run. The propagation loss of the strip waveguides is obtained from specifications of the SiP foundry. Table B.1 summarizes the values and the standard deviations of the loss contributions obtained for the various building blocks. Note that these loss contributions are generally wavelength-dependent, which is taken into account when estimating

$a_{PS}(\lambda_i)$. For simplicity, Table B.1 only specifies the values for the loss contributions a_{MMI}, a_{GC}, and $a_{GC,2}$ and the associated standard deviations at a fixed wavelength of 1560 nm. The losses a_{Strip} and a_{Conv} are assumed to be wavelength-independent for the investigated wavelength range. For a_{tot}, we picked the wavelength λ_i of constructive interference that is closest to 1560 nm and indicate the used value of λ_i in Table B.1.

The measurement of the grating coupler (GC) test structure is particularly important since the associated attenuation is by far the largest of all components. Due to general fabrication tolerances, there are variations in GC performance across the wafer, and we hence measure a_{GC} for each die separately and use a test structure directly next to the respective SOH MZM. Each MZM die also contains a test structure for the MMI insertion loss a_{MMI} consisting of 4, 8, and 12 concatenated MMI couplers, which are accessed via grating couplers. A fit of the losses measured for these coupler sequences allows extracting the attenuation per coupler. This measurement also provides an additional value for the grating coupler attenuation $a_{GC,2}$. For all MZM dies, $a_{GC,2}$ and a_{GC} agree very well, and the mean relative deviations of the associated dB-values do not exceed 3 % in the investigated wavelength range. This result indicates that there is only little intra-die variation of the GC performance and that the losses a_{GC} obtained from the GC test structure can be safely used as a reference. For measuring the insertion losses of the strip-to-slot converters, we use a dedicated test structure on a fifth die, which is obtained from the same wafer as the four MZM dies. The test structure comprises 2, 4, 8, and 10 concatenated pairs of strip-to-slot and slot-to-strip converters. A fit to the measured data gives the attenuation per converter.

The error bounds for the measured attenuations a_{MMI}, a_{Conv}, and $a_{GC,2}$, are obtained from the least-squares fits of the associated linear model to the respective measurement data. For a_{Strip}, we rely on the uncertainty specified by the manufacturer. The error bounds for a_{tot} and a_{GC} correspond to a statistical error obtained by measuring the very same structure three times, starting the alignment of the fibers from independent positions.

Table B.1. Loss contributions obtained for the various building blocks. The losses a_{MMI}, a_{GC}, and $a_{GC,2}$ are specified at the wavelength of 1560 nm. The total loss a_{tot} is specified at the wavelength λ_i of constructive interference, which is closest to 1560 nm. The quantity σ_{meas} reflects the total measurement uncertainty of individual $a_{PS}(\lambda_i)$ taking into account the uncertainties of the individual loss contributions, and $\sigma_{a_{PS}}$ represents the measured standard deviation of $a_{PS}(\lambda_i)$. The value specified for σ_{meas} refers to the respective wavelength λ_i of constructive interference closest to 1560 nm. All losses are specified in dB.

Die 1

a_{MMI}	a_{GC}	$a_{GC,2}$	MZM#	λ_i (nm)	$a_{tot}(\lambda_i)$	$\sigma_{meas}(\lambda_i)$	$\overline{a}_{PS} \pm \sigma_{a_{PS}}$
0.27 ± 0.01	5.52 ± 0.09	5.48 ± 0.06	1	1557	13.08 ± 0.23	0.34	0.75 ± 0.13
			2	1554	13.63 ± 0.06	0.18	0.74 ± 0.30
			3	1561	12.44 ± 0.24	0.30	0.48 ± 0.16
			4	1560	12.59 ± 0.05	0.20	0.55 ± 0.08

Die 2

a_{MMI}	a_{GC}	$a_{GC,2}$	MZM#	λ_i (nm)	$a_{tot}(\lambda_i)$	$\sigma_{meas}(\lambda_i)$	$\overline{a}_{PS} \pm \sigma_{a_{PS}}$
0.28 ± 0.01	5.14 ± 0.09	5.01 ± 0.04	1	1563	12.96 ± 0.06	0.12	1.78 ± 0.12
			2	1561	12.81 ± 0.07	0.17	1.83 ± 0.25
			3	1558	11.75 ± 0.08	0.18	0.41 ± 0.14
			4	1562	11.67 ± 0.08	0.14	0.46 ± 0.07

Die 3

a_{MMI}	a_{GC}	$a_{GC,2}$	MZM#	λ_i (nm)	$a_{tot}(\lambda_i)$	$\sigma_{meas}(\lambda_i)$	$\overline{a}_{PS} \pm \sigma_{a_{PS}}$
0.27 ± 0.01	4.36 ± 0.06	4.21 ± 0.05	1	1563	10.03 ± 0.06	0.11	0.51 ± 0.28
			2	1563	10.21 ± 0.08	0.12	0.53 ± 0.19
			3	1564	9.57 ± 0.05	0.10	0.03 ± 0.31
			4	1564	9.68 ± 0.27	0.28	0.21 ± 0.32

Die 4

a_{MMI}	a_{GC}	$a_{GC,2}$	MZM#	λ_i (nm)	$a_{tot}(\lambda_i)$	$\sigma_{meas}(\lambda_i)$	$\overline{a}_{PS} \pm \sigma_{a_{PS}}$
0.27 ± 0.01	4.93 ± 0.02	4.78 ± 0.02	1	1554	12.12 ± 0.07	0.10	0.64 ± 0.13
			2	1555	12.23 ± 0.10	0.14	0.70 ± 0.25
			3	1563	11.10 ± 0.08	0.12	0.01 ± 0.36
			4	1559	11.46 ± 0.07	0.11	0.30 ± 0.28

Die 5

a_{Conv}
$0.10 \pm$ 0.02

Specified by silicon photonic foundry

a_{Strip}
$0.32 \pm$ 0.06

The phase-shifter losses $a_{\mathrm{PS}}(\lambda_i)$ are associated with a wavelength-dependent measurement error σ_{meas}, corresponding to the blue error bars in Fig. 3(a). For each wavelength λ_i, this error is determined as the root of the summed error squares of the various contributions according to Eq. (4.1). Note that, for simplicity, Table B.1 specifies σ_{meas} only for the wavelength λ_i of constructive interference, which is closest to 1560 nm. The wavelength-averaged phase-shifter loss $\overline{a}_{\mathrm{PS}}$ along with the measured standard deviation $\sigma_{a_{\mathrm{PS}}}$ of $a_{\mathrm{PS}}(\lambda_i)$ is specified in the last column of Table B.1.

B.2 State-of-the-art EO modulators

Table B.2 gives an overview on state-of-the-art EO modulators, comparing the phase shifter length L, the π-voltage-length product $U_\pi L$, the loss-efficiency product $a U_\pi L$, the phase-shifter attenuation a_{PS}, and the achieved data rates. The SOH modulators presented in this work (last row) stand out due to a unique combination of low optical loss, high modulation efficiency and small footprint, as well as demonstrated performance in high-speed data transmission. Small phase-shifter insertion loss is also offered by thin-film LiNbO$_3$ (Row 1) [132], InP (Row 2) [133] or hybrid BaTiO$_3$-based devices (Row 7) [14], but these modulators feature either smaller modulation efficiency [132,133] quantified by larger $U_\pi L$-products or are limited in the demonstrated data rate [14]. Moreover, the SOH MZM presented in this work can be co-integrated with standard SiP circuits while offering better performance than conventional pn-depletion-type silicon modulators.

Table B.2. Performance metrics of state-of-the-art Mach-Zehnder and IQ modulators. If the reported modulation efficiency depends on the operating point of the device, we specify a range of values for the $U_\pi L$ product. In case the data rate is not given in the respective publication, we specify the line rate. The SOH modulators presented in this work (last row) stand out due to a unique combination of low optical loss, high modulation efficiency and small footprint, as well as demonstrated performance in high-speed data transmission. The associated performance parameters are close to those of best-in-class competing devices, indicated in bold.

	Technology	Ref.	L (mm)	$U_\pi L$ (Vmm)	$aU_\pi L$ (VdB)	a_{PS} (dB)	Data rate (Gbit/s)	Modulation format
1	Thin film LiNbO$_3$	[132]	5	22	**0.4**	**0.1**	175	8-ASK
2	InP	[133]	4	6	0.9	0.6	**373**	16QAM
3	Si depl. type	[238]	3	3.4…5.5	8.5…13.8	7.5	32 (line rate)	OOK
4	Si depl. type	[142]	4.8	38.4	34.4	4.3	157	PAM4
5	Si depl. type	[130]	2.8	25	32.1	3.6	93	PAM4
6	Si depl. type	[71]	2	4.6…9.4	5.8…11.9	2.5	24 (line rate)	OOK
7	Si/BaTiO$_3$ Hybrid	[14]	1	2.3	1.3	0.6	25 (line rate)	OOK
8	Si/IIIV Hybrid	[113]	0.25	0.9	3.6	1.0	32 (line rate)	OOK
9	POH	[138]	**0.02**	0.24	190	16	50	QPSK
10	POH	[239]	0.025	**0.13**	65	12.5	333	16QAM
11	CC-SOH	[141]	1	1.3	N/A.	N/A	167	PAM4
12	SOH	[140]	1.5	0.32	1.2	5.8	40	OOK
13	SOH	[151]	1.5	2.2	3.7	2.5	40	OOK
14	SOH	[152]	0.6	0.9	2.1	1.4	133	16QAM
15	SOH	This work	0.28	0.41	1.0	0.7	187	PAM4

[end of supplementary information of paper [J2]]

C. Measurement techniques for χ⁽²⁾ of thin-film materials based on second-harmonic generation

The following content was published as the supplementary information to the journal article [J4]. To fit the structure and layout of this document, it was adapted accordingly.

Artur Hermans,* **Clemens Kieninger**,* Kalle Koskinen, Andreas Wickberg, Eduardo Solano, Jolien Dendooven, Martti Kauranen, Stéphane Clemmen, Martin Wegener, Christian Koos, and Roel Baets, "On the determination of $\chi^{(2)}$ in thin films: a comparison of one-beam second-harmonic generation measurement methodologies," *Sci. Rep.* **7**, 1–13 (2017).
DOI: https://doi.org/10.1038/srep44581
*These authors contributed equally to this work.

[start of supplementary information of paper [J4]]

C.1 Glass reference measurement

Figure C.1 shows a reference measurement for a blank BOROFLOAT® 33 substrate (500 µm thickness) conducted at the Optics Laboratory, Tampere
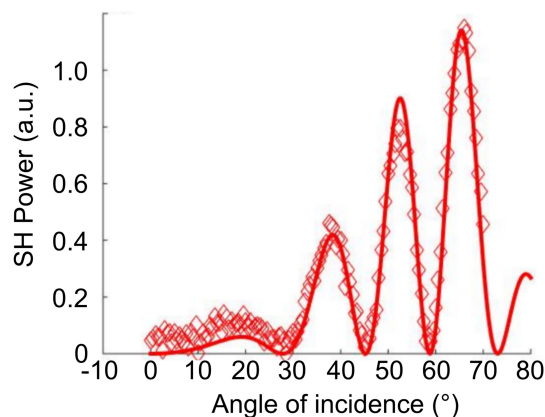
Figure C.1: Reference measurement Tampere University of Technology.
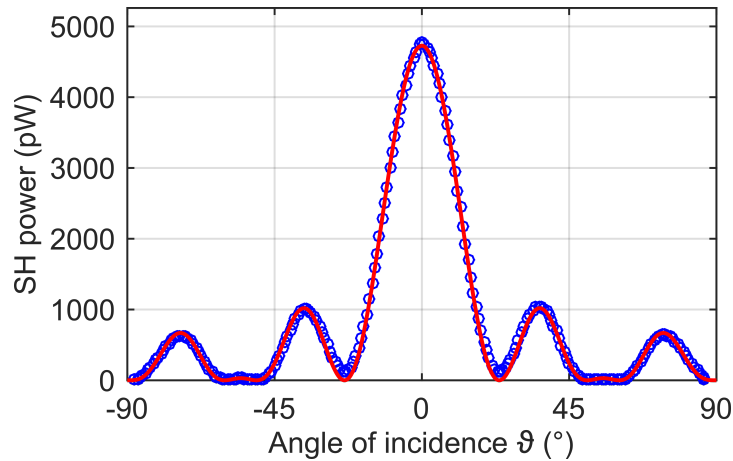
Figure C.2: Reference measurement on Y-cut quartz plate.

University of Technology. The horizontal axis represents the incidence angle ϑ (in degrees) and the vertical axis shows the SH power $P_{2\omega}$ (in arbitrary units). Both the incident fundamental wave and the generated SH wave are p-polarized. The fitted $\chi_s^{(2)}$ values are $\chi_{s,zzz} = 43\times10^{-22}$ m²/V and $2\chi_{s,xxz} + \chi_{s,zxx} = 18\times10^{-22}$ m²/V when referenced against quartz with known second-order nonlinearity $\chi_{xxx}^{SiO_2} = 0.6$ pm/ V.

C.2   Quartz crystal reference measurement

A typical Maker fringe calibration measurement and fit of a Y-cut quartz plate is shown in Figure C.2. The p-polarized SH power is recorded as a function of the angle of incidence ϑ for p-polarized fundamental beam with an excitation power $P_\omega = 100$ mW. The theoretical model for the fit is also given by Eq. (6.4) in Chapter 6. However, it has to be noted that the quartz plate is not supported upon a substrate. This can be accounted for by replacing the refractive index of the substrate by the refractive index of air. The effective susceptibility for the Y-cut quartz crystal reads

$$\chi_{eff}^p = \chi_{xxx}^{SiO_2}\left(\cos(\theta_{f,2\omega})\left(\cos^2(\theta_{f,\omega}) - \sin^2(\theta_{f,\omega})\right) - 2\sin(\theta_{f,2\omega})\sin(\theta_{f,\omega})\cos(\theta_{f,\omega})\right) \text{ (C.1)}$$

with $\chi_{xxx}^{SiO_2} = 0.6$ pm/ V [211]. There are two free fitting parameters. The first one is the thickness d_f of the quartz plate which determines the position of the individual Maker fringes. Note that fitting the thickness is a quite common

approach in the evaluation of Maker fringe experiments [188]. The second fitting parameter is $\alpha = 1/(A^{(\text{spot})}\Delta\tau^2 f_{\text{rep}}^2)$ that is needed for the evaluation of Eq. (6.4) in Chapter 6. The fitting results are $d_{\text{f}} = (119.486 \pm 0.007)$ μm and $\alpha = (2.340 \pm 0.007)\, 10^{18}$ m^{-2}. For three consecutive measurements on different spots of the quartz plate the following mean values and corresponding standard deviations are obtained $d_{\text{f}} = (119.24 \pm 0.22)$ μm and $\alpha = (2.338 \pm 0.015)\, 10^{18}$ m^{-2}. Since the standard deviations of the fitting results for an individual measurement, as well as for consecutive measurements are negligible it can be assumed that the calibration measurement itself introduces insignificant error on the $\chi^{(2)}$ tensor elements of the nanolaminates. Note that due to the symmetry of the data relative to $\vartheta = 0°$ it can be excluded that the angle of incidence on the sample was calibrated incorrectly. Additionally, due to the good agreement between data and fit in magnitude and position of the individual Maker fringes it can be assumed that the quartz plate is not rotated out of focus during the measurement.

C.3 Comparison of different theoretical models for glass substrate measurements

Figure C.3 shows measurement and fitting for a blank BOROFLOAT® 33 substrate with known $\chi_{\text{s}}^{(2)}$. For incidence angles larger than 70° there is a clear discrepancy between the fitted curve and the measurement when reflections are not included. When reflections are included a good fit is also obtained for the larger angles. We only include single reflections at the glass-air interfaces, not multiple reflections within the substrate (so no Fabry-Pérot type effects). See Ref. [204,207] for more details.

The model without reflections is described by (see also Chapter 6)

$$E_{2\omega,\text{total}} = E_{2\omega,\text{front}} + E_{2\omega,\text{back}}$$

$$= -j\frac{\omega(t_{\text{a-s},\omega}^{\text{p}})^2 t_{\text{s-a},2\omega}^{\text{p}} E_{\omega,\text{in}}^2}{2cn_{\text{s},2\omega}\cos(\theta_{\text{s},2\omega})}\chi_{\text{s,eff}}^{\text{glass}}\left[\exp\left(-j\frac{2\omega n_{\text{s},2\omega}\cos(\theta_{\text{s},2\omega})}{c}d_{\text{s}}\right)\right.$$

$$\left. - \exp\left(-2j\frac{\omega n_{\text{s},\omega}\cos(\theta_{\text{s},\omega})}{c}d_{\text{s}}\right)\right],$$

(C.2)

with

$$\chi_{\text{s,eff}}^{\text{glass}} = \chi_{\text{s},xxz}^{\text{glass}} \sin(2\theta_{\text{s},\omega})\cos(\theta_{\text{s},2\omega}) + \chi_{\text{s},xxz}^{\text{glass}} \sin(\theta_{\text{s},2\omega})\cos^2(\theta_{\text{s},\omega})$$
$$+ \chi_{\text{s},xxz}^{\text{glass}} \sin^2(\theta_{\text{s},\omega})\sin(\theta_{\text{s},2\omega}),$$

(C.3)

The notation is the same as in Chapter 6.

The model with single reflections is described by

$$E_{2\omega,\text{total}} = E_{2\omega,\text{front}} + E_{2\omega,\text{back}}$$

$$= -j\frac{\omega(t_{\text{a-s},\omega}^{\text{p}})^2 t_{\text{s-a},2\omega}^{\text{p}} E_{\omega,\text{in}}^2}{2cn_{\text{s},2\omega}\cos(\theta_{\text{s},2\omega})} \exp\left(-j\frac{2\omega n_{\text{s},2\omega}\cos(\theta_{\text{s},2\omega})}{c}d_{\text{s}}\right)$$

$$\times \left[(1 - r_{\text{s-a},2\omega}^{\text{p}})\chi_{\text{s},xxz}^{\text{glass}}\sin(2\theta_{\text{s},\omega})\cos(\theta_{\text{s},2\omega})\right.$$

$$+ (1 + r_{\text{s-a},2\omega}^{\text{p}})\chi_{\text{s},zxx}^{\text{glass}}\sin(\theta_{\text{s},2\omega})\cos^2(\theta_{\text{s},\omega})$$

$$\left.+ (1 + r_{\text{s-a},2\omega}^{\text{p}})\chi_{\text{s},zzz}^{\text{glass}}\sin^2(\theta_{\text{s},\omega})\sin(\theta_{\text{s},2\omega})\right]$$

$$+ j\frac{\omega(t_{\text{a-s},\omega}^{\text{p}})^2 t_{\text{s-a},2\omega}^{\text{p}} E_{\omega,\text{in}}^2}{2cn_{\text{s},2\omega}\cos(\theta_{\text{s},2\omega})} \exp\left(-j\frac{2\omega n_{\text{s},\omega}\cos(\theta_{\text{s},\omega})}{c}d_{\text{s}}\right)$$

$$\times \left[(1 - (r_{\text{s-a},\omega}^{\text{p}})^2)\chi_{\text{s},xxz}^{\text{glass}}\sin(2\theta_{\text{s},\omega})\cos(\theta_{\text{s},2\omega})\right.$$

$$+ (1 - r_{\text{s-a},\omega}^{\text{p}})^2 \chi_{\text{s},zxx}^{\text{glass}}\sin(\theta_{\text{s},2\omega})\cos^2(\theta_{\text{s},\omega})$$

$$\left.+ (1 + r_{\text{s-a},\omega}^{\text{p}})^2 \chi_{\text{s},zzz}^{\text{glass}}\sin^2(\theta_{\text{s},\omega})\sin(\theta_{\text{s},2\omega})\right].$$

(C.4)

Here, $r_{i\text{-}j}^{\text{p}}$ are the Fresnel reflection coefficients (for p-polarized light) propagating from medium i to j.

To include temporal walk-off effects we model the laser light as 100 fs (FWHM) sech^2 pulses

$$P_{2\omega} = K_2 \int_{-\infty}^{\infty} \left| E_{2\omega,\text{front}} \operatorname{sech}^2\left(\frac{t}{\frac{\Delta\tau}{2\ln(1+\sqrt{2})}}\right) + E_{2\omega,\text{back}} \operatorname{sech}^2\left(\frac{(t+t_{\text{walk-off}})}{\frac{\Delta\tau}{2\ln(1+\sqrt{2})}}\right) \right|^2 dt,$$

(C.5)

with $\Delta\tau$ the FWHM pulse duration and $t_{\text{walk-off}}$ the walk-off time.
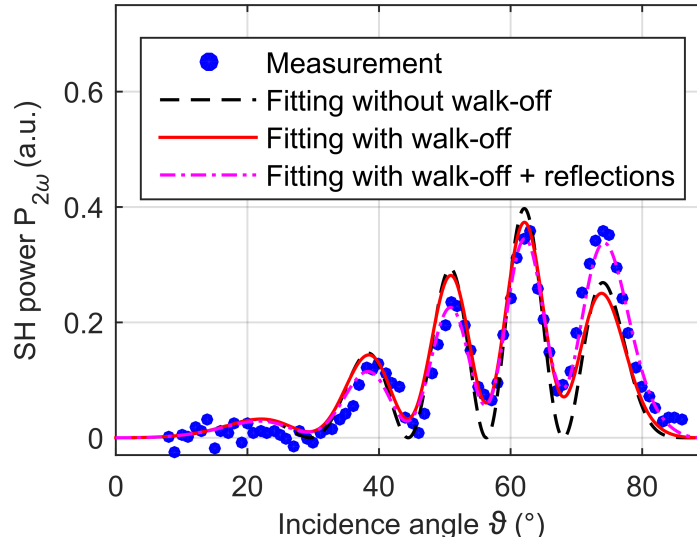
Figure C.3: SH power obtained from glass substrate. Various theoretical models are used for fitting.

C.4   Comparison of different theoretical models for the ABC-type thin-film measurements

Figure C.4 (a) shows the measurement and fitting for the ITA sample. The full red line is obtained using the relatively simple model described in the main paper. The dashed purple line is the result of fitting with a more advanced model that takes into account the birefringence of the nonlinear film, the multiple reflections inside the nonlinear thin film and the single reflections in the substrate, the finite thickness of the thin film and the temporal walk-off in the substrate. The thin film contribution is modelled according to the transfer matrix formalism described in [189]. The matrix formalism is implemented in MATLAB. Though correct and very complete, the matrix formalism is not very transparent and prone to coding errors. For the contribution of the back glass-air interface we used the second term of Eq. (C.4). In the fitting we assume that $\chi_{xxz}^{\mathrm{ABC}} = \chi_{zxx}^{\mathrm{ABC}} = \chi_{\mathrm{sum}}^{\mathrm{ABC}} / 3$. This is necessary even for the advanced model. If we do not use this approximation, the relative uncertainties on the off-diagonal components can go above 100% and the results become essentially meaningless. By eliminating one fitting parameter, we can significantly reduce the uncertainty on the final results.
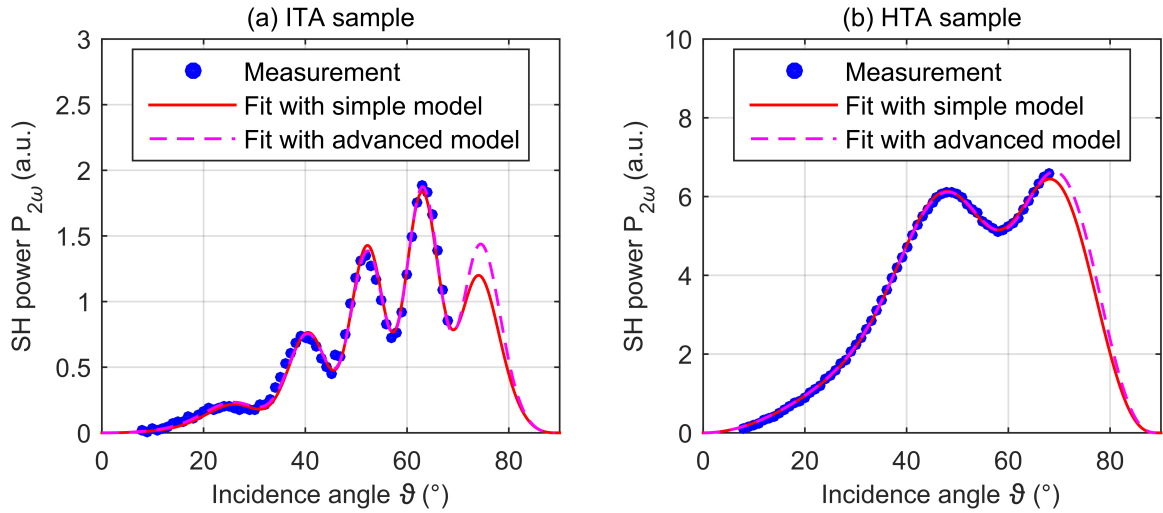
Figure C.4: Comparison of different theoretical models for the ABC-type thin film measurements. **(a,b)** SH power as a function of incidence angle obtained from ITA, HTA sample.

The fitting results are (with standard errors): $\chi_{\text{sum}}^{\text{ABC}} = (0.21 \pm 0.01)\,\text{pm/V}$, $\chi_{zzz}^{\text{ABC}} = (0.97 \pm 0.05)\,\text{pm/V}$ and $d_{\text{s}} = (498.26 \pm 0.16)\,\mu\text{m}$, for the simple model and $\chi_{\text{sum}}^{\text{ABC}} = (0.23 \pm 0.01)\,\text{pm/V}$, $\chi_{zzz}^{\text{ABC}} = (0.80 \pm 0.04)\,\text{pm/V}$ and $d_{\text{s}} = (498.24 \pm 0.14)\,\mu\text{m}$, for the more advanced model.

The same procedure is repeated for the HTA sample (see Figure C.4 (b)).

The fitting results are (with standard errors): $\chi_{\text{sum}}^{\text{ABC}} = (0.60 \pm 0.01)\,\text{pm/V}$, $\chi_{zzz}^{\text{ABC}} = (0.70 \pm 0.01)\,\text{pm/V}$ and $d_{\text{s}} = (170.31 \pm 0.04)\,\mu\text{m}$, for the simple model and $\chi_{\text{sum}}^{\text{ABC}} = (0.597 \pm 0.005)\,\text{pm/V}$, $\chi_{zzz}^{\text{ABC}} = (0.63 \pm 0.01)\,\text{pm/V}$ and $d_{\text{s}} = (169.97 \pm 0.02)\,\mu\text{m}$, for the more advanced model.

The advanced model yields slightly different results, but the discrepancy is within the error margins (standard error and systematic error due to angular uncertainty).
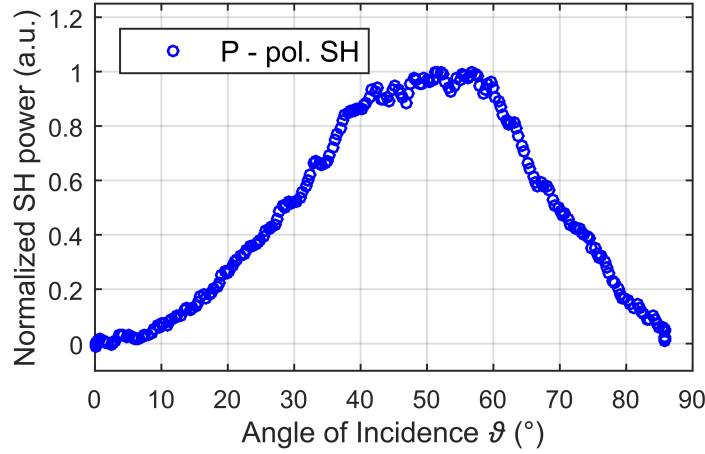
C.5 Interference fringes of s-polarized SH for *φ* = 45° in KIT setup

Figure C.5 displays the normalized s-polarized SH power as a function of the angle of incidence ϑ for fixed pump polarization $\varphi = 45°$ obtained from (a) the
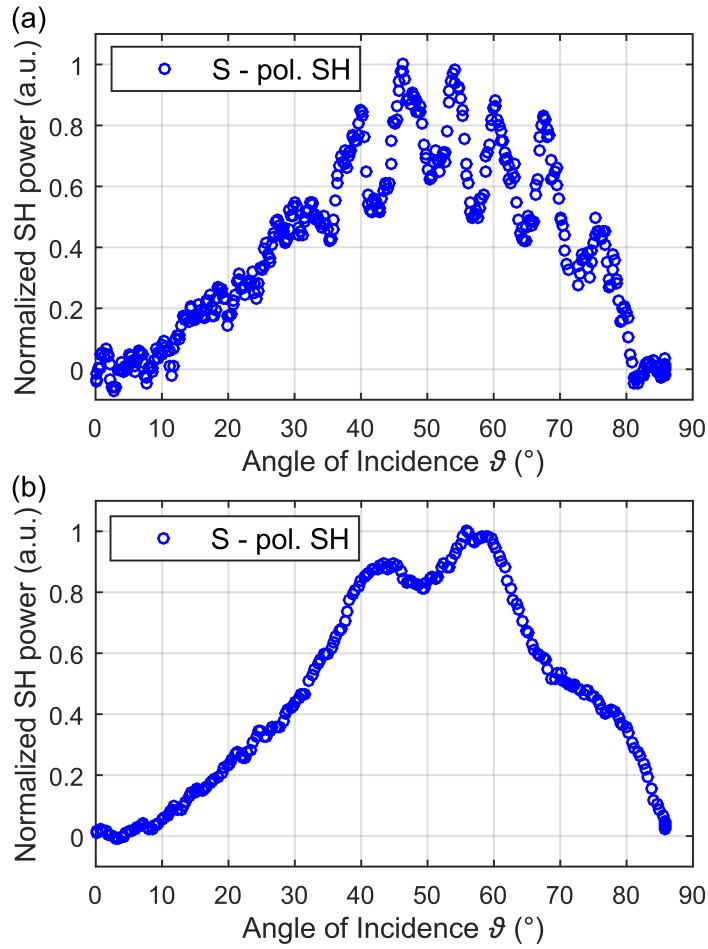
Figure C.5: s-polarized SH power obtained from **(a)** the ITA sample and **(b)** the HTA sample. The input polarization is fixed at $\varphi = 45°$.

ITA sample and (b) the HTA sample, respectively. For this measurement configuration only the elements χ_{xxz}^{ABC} and $\chi_{s,xxz}^{glass}$ contribute to the SH power. The very pronounced interference fringes for the ITA sample can explain why the determined values of χ_{xxz} vary for varying angle of incidence in Table 6.2. On the other hand, there are only minor interference fringes for the HTA sample, which results in minor changes in the determined values of χ_{xxz} for the specific angles of incidence.

Figure C.6: p-polarized SH power obtained from the HTA sample. The input polarization is fixed at $\varphi = 0°$.

C.6 Interference fringes of p-polarized SH for $\varphi = 0°$ in KIT setup

Figure C.6 shows the normalized p-polarized SH power as a function of the angle of incidence ϑ for fixed pump polarization $\varphi = 0°$ obtained from the HTA sample. For this measurement configuration only the elements $\chi_{zxx}^{\mathrm{ABC}}$ and $\chi_{\mathrm{s},zxx}^{\mathrm{glass}}$ contribute to the SH power. There are no interference fringes visible for the HTA sample. Therefore it can be concluded that $\chi_{\mathrm{s},zxx}^{\mathrm{glass}}$ is much smaller than $\chi_{zxx}^{\mathrm{ABC}}$. This finding explains why the determined values for $\chi_{zxx}^{\mathrm{ABC}}$ for the HTA sample do not vary depending on the angle of incidence, as listed in Table 6.2. Unfortunately, a corresponding measurement on the ITA sample could not be performed since the level of generated SH power is too close to the detection limit of the setup.

Table C.1. ALD deposition parameters for the HTA sample.

Precursor for	Aluminum	Titanium	Hafnium	Oxygen
Temperature (°)	Not heated	80	75	Not heated
Pulse duration (s)	0.015	0.1	0.15	0.015
Wait time after pulse (s)	20	See below	20	20

C.7   ALD deposition parameters for the HTA sample

The parameters used for ALD of the HTA sample are summarized in Table C.1. The vacuum valve was closed before the insertion of the titanium precursor and reopened two seconds later; subsequently the chamber was flushed for 20 s with 100 sccm of argon.

[end of supplementary information of paper [J4]]

# D.   Second-order optical nonlinear ZnO/Al₂O₃ nanolaminates

The following content was published as the supplementary information to the journal article [J5]. To fit the structure and layout of this document, it was adapted accordingly.

A. Wickberg*, **C. Kieninger**, C. Sürgers, S. Schlabach, X. Mu, C. Koos and M. Wegener, "Second-Harmonic Generation from ZnO/Al$_2$O$_3$ Nanolaminate Optical Metamaterials Grown by Atomic-Layer Deposition," *Adv. Opt. Mater.* **4**, 1203–1208 (2016).
DOI: https://doi.org/10.1002/adom.201600200
*These authors contributed equally to this work.

[start of supplementary information of paper [J5]]
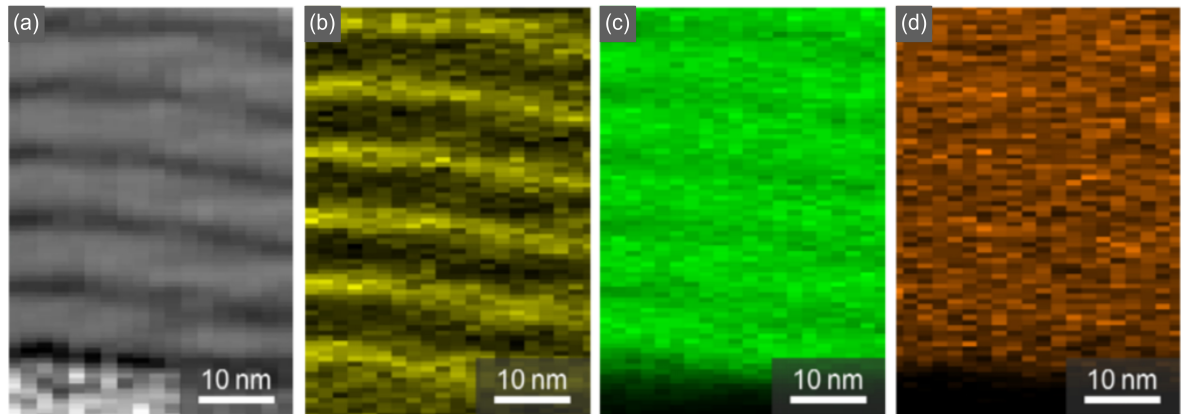
Figure D.1: (a) Same as panel (c) in Figure 7.1. **(b-d)** are elemental maps derived from STEM-EDX measurements corresponding to the integrated signal at the Al-K (b), the Zn-K (c) and the O-K (d) edge.

[end of supplementary information of paper [J5]]

E.   Bibliography

[1]   M. Smit, K. Williams & J. Van Der Tol, "Past, Present, and Future of InP-Based Photonic Integration," *APL Photonics* **4**, 050901 (2019).

[2]   G. E. Hoefler, Y. Zhou, M. Anagnosti, A. Bhardwaj, P. Abolghasem, A. James, S. Luna, P. Debackere, A. Dentai, T. Vallaitis, P. Liu, M. Missey, S. Corzine, P. Evans, V. Lal, M. Ziari, D. Welch, F. Kish, J. S. Suelzer, P. S. Devgan & N. G. Usechak, "Foundry Development of System-On-Chip InP-Based Photonic Integrated Circuits," *IEEE J. Sel. Top. Quantum Electron.* **25**, (2019).

[3]   M. O. Manasreh, *InP and Related Compounds Materials, Applications and Devices* (CRC Press, 2000).

[4]   I. Kaminow, T. Li & A. E. Willner, *Optical Fiber Telecommunications: Components and Subsystems: Sixth Edition* **VIA**, (Elsevier Inc., 2013).

[5]   F. Boeuf, S. Cremer, E. Temporiti, M. Fere, M. Shaw, C. Baudot, N. Vulliet, T. Pinguet, A. Mekis, G. Masini, H. Petiton, P. Le Maitre, M. Traldi & L. Maggi, "Silicon Photonics R&D and Manufacturing on 300-mm Wafer Platform," *J. Light. Technol.* **34**, 286–295 (2016).

[6]   R. W. Boyd, *Nonlinear optics* (Academic Press, 2008).

[7]   R. A. Soref & B. R. Bennett, "Electrooptical Effects in Silicon," *IEEE J. Quantum Electron.* **23**, 123–129 (1987).

[8]   J. Witzens, "High-Speed Silicon Photonics Modulators," *Proc. IEEE* **106**, 2158–2182 (2018).

[9]   A. Rao, A. Patil, P. Rabiei, A. Honardoost, R. DeSalvo, A. Paolella & S. Fathpour, "High-Performance and Linear Thin-Film Lithium Niobate Mach–Zehnder Modulators on Silicon up to 50 GHz," *Opt. Lett.* **41**, 5700 (2016).

[10]   S. Jin, L. Xu, H. Zhang & Y. Li, "LiNbO3 Thin-Film Modulators Using Silicon Nitride Surface Ridge Waveguides," *IEEE Photon. Technol. Lett.* **28**, 736–739 (2016).

[11]   P. O. Weigel, J. Zhao, K. Fang, H. Al-Rubaye, D. Trotter, D. Hood, J. Mudrick, C. Dallo, A. T. Pomerene, A. L. Starbuck, C. T. DeRose, A. L. Lentine, G. Rebeiz & S. Mookherjea, "Bonded Thin Film Lithium Niobate Modulator on a Silicon Photonics Platform Exceeding 100 GHz 3-dB Electrical Modulation Bandwidth," *Opt. Express* **26**, 23728 (2018).

[12] M. He, M. Xu, Y. Ren, J. Jian, Z. Ruan, Y. Xu, S. Gao, S. Sun, X. Wen, L. Zhou, L. Liu, C. Guo, H. Chen, S. Yu, L. Liu & X. Cai, "High-Performance Hybrid Silicon and Lithium Niobate Mach–Zehnder Modulators for 100 Gbit/s and Beyond," *Nat. Photonics* **13**, 359–364 (2019).

[13] N. Boynton, H. Cai, M. Gehl, S. Arterburn, C. Dallo, A. Pomerene, A. Starbuck, D. Hood, D. C. Trotter, T. Friedmann, C. T. DeRose & A. Lentine, "A Heterogeneously Integrated Silicon Photonic/Lithium Niobate Travelling Wave Electro-Optic Modulator," *Opt. Express* **28**, 1868 (2020).

[14] F. Eltes, C. Mai, D. Caimi, M. Kroh, Y. Popoff, G. Winzer, D. Petousi, S. Lischke, J. Elliott Ortmann, L. Czornomaz, L. Zimmermann, J. Fompeyrine & S. Abel, "A BaTiO$_3$-Based Electro-Optic Pockels Modulator Monolithically Integrated on an Advanced Silicon Photonics Platform," *J. Light. Technol.* **37**, 1456–1462 (2019).

[15] C. Koos, J. Leuthold, W. Freude, M. Kohl, L. Dalton, W. Bogaerts, A. L. Giesecke, M. Lauermann, A. Melikyan, S. Koeber, S. Wolf, C. Weimann, S. Muehlbrandt, K. Koehnle, J. Pfeifle, W. Hartmann, Y. Kutuvantavida, S. Ummethala, R. Palmer, D. Korn, L. Alloatti, P. C. Schindler, D. L. Elder, T. Wahlbrink & J. Bolten, "Silicon-Organic Hybrid (SOH) and Plasmonic-Organic Hybrid (POH) Integration," *J. Light. Technol.* **34**, 256–268 (2016).

[16] S. Wolf, H. Zwickel, C. Kieninger, M. Lauermann, W. Hartmann, Y. Kutuvantavida, W. Freude, S. Randel & C. Koos, "Coherent Modulation up to 100 GBd 16QAM Using Silicon-Organic Hybrid (SOH) Devices," *Opt. Express* **26**, 220–232 (2018).

[17] S. Wolf, H. Zwickel, W. Hartmann, M. Lauermann, Y. Kutuvantavida, C. Kieninger, L. Altenhain, R. Schmid, J. Luo, A. K.-Y. Jen, S. Randel, W. Freude & C. Koos, "Silicon-Organic Hybrid (SOH) Mach-Zehnder Modulators for 100 Gbit/s on-off Keying," *Sci. Rep.* **8**, 2598 (2018).

[18] H. Zwickel, S. Wolf, C. Kieninger, Y. Kutuvantavida, M. Lauermann, T. de Keulenaer, A. Vyncke, R. Vaernewyck, J. Luo, A. K.-Y. Jen, W. Freude, J. Bauwelinck, S. Randel & C. Koos, "Silicon-Organic Hybrid (SOH) Modulators for Intensity-Modulation / Direct-Detection Links With Line Rates of up to 120 Gbit/s," *Opt. Express* **25**, 23784–23800 (2017).

[19] R. Dinu, D. Jin, G. Yu, B. Chen, D. Huang, H. Chen, A. Barklund, E.

Miller, C. Wei & J. Vemagiri, "Environmental Stress Testing of Electro–Optic Polymer Modulators," *J. Light. Technol.* **27**, 1527–1532 (2009).

[20] Min-Cheol Oh, Hua Zhang, Cheng Zhang, H. Erlig, Yian Chang, B. Tsap, D. Chang, A. Szep, W. H. Steier, H. R. Fetterman & L. R. Dalton, "Recent Advances in Electrooptic Polymer Modulators Incorporating Highly Nonlinear Chromophore," *IEEE J. Sel. Top. Quantum Electron.* **7**, 826–835 (2001).

[21] L. Alloatti, C. Kieninger, A. Froelich, M. Lauermann, T. Frenzel, K. Köhnle, W. Freude, J. Leuthold, M. Wegener & C. Koos, "Second-Order Nonlinear Optical Metamaterials: ABC-Type Nanolaminates," *Appl. Phys. Lett.* **107**, 121903 (2015).

[22] S. Clemmen, A. Hermans, E. Solano, J. Dendooven, K. Koskinen, M. Kauranen, E. Brainis, C. Detavernier & R. Baets, "Atomic Layer Deposited Second-Order Nonlinear Optical Metamaterial for Back-End Integration With CMOS-Compatible Nanophotonic Circuitry," *Opt. Lett.* **40**, 5371 (2015).

[23] E. G. Sauter, *Nonlinear optics* (Wiley, 1996).

[24] W. Voigt, *Lehrbuch der Kristallphysik Lehrbuch der Kristallphysik* (Vieweg+Teubner Verlag, 1966).

[25] P. Butcher, *Nonlinear optical phenomena* (Ohio State University, 1965).

[26] A. Hermans, C. Kieninger, K. Koskinen, A. Wickberg, E. Solano, J. Dendooven, M. Kauranen, S. Clemmen, M. Wegener, C. Koos & R. Baets, "On the Determination of $\chi(2)$ in Thin Films: A Comparison of One-Beam Second-Harmonic Generation Measurement Methodologies," *Sci. Rep.* **7**, 1–13 (2017).

[27] P. A. Franken, A. E. Hill, C. W. Peters & G. Weinreich, "Generation of Optical Harmonics," *Phys. Rev. Lett.* **7**, 118–119 (1961).

[28] L. McDonagh & R. Wallenstein, "Low-Noise 62 W CW Intracavity-Doubled TEM00 Nd:YVO4 Green Laser Pumped at 888 nm," *Opt. Lett.* **32**, 802 (2007).

[29] Q. H. Xue, Q. Zheng, Y. K. Bu, F. Q. Jia & L. S. Qian, "High-Power Efficient Diode-Pumped Nd:YVO4/LiB3O5 457 nm Blue Laser With 46 W of Output Power," *Opt. Lett.* **31**, 1070 (2006).

[30] G. P. Agrawal, *Fiber-Optic Communication Systems: Fourth Edition* (Wiley, 2017).

[31] L. R. Dalton, P. Günter, M. Jazbinsek & O. P. Kwon, *Organic Electro-Optics and Photonics: Molecules, Polymers and Crystals* (Cambridge University Press, 2015).

[32] R. L. Sutherland, D. G. Mclean & S. Kirkpatrick, *Handbook of Nonlinear Optics* (CRC Press, 2003).

[33] W. N. Herman & L. M. Hayden, "Maker Fringes Revisited: Second-Harmonic Generation From Birefringent or Absorbing Materials," *J. Opt. Soc. Am. B* **12**, 416 (1995).

[34] R. J. St. Pierre, D. W. Mordaunt, H. Injeyan, J. G. Berg, R. C. Hilyard, M. E. Weber, M. G. Wickham, G. M. Harpole & R. Senn, "Diode Array Pumped Kilowatt Laser," *IEEE J. Sel. Top. Quantum Electron.* **3**, 53–58 (1997).

[35] D. Woll, B. Beier, K.-J. Boller, R. Wallenstein, M. Hagberg & S. O'Brien, "1 W of Blue 465-nm Radiation Generated by Frequency Doubling of the Output of a High-Power Diode Laser in Critically Phase-Matched LiB3O5," *Opt. Lett.* **24**, 691 (1999).

[36] J. J. De Yoreo, A. K. Burnham & P. K. Whitman, "Developing KH_3PO_4 and KD_2PO_4 Crystals for the World's Most Powerful Laser," *Int. Mater. Rev.* **47**, 113–152 (2002).

[37] D. H. Jundt, G. A. Magel, M. M. Fejer & R. L. Byer, "Periodically Poled $LiNbO_3$ for High-Efficiency Second-Harmonic Generation," *Appl. Phys. Lett.* **59**, 2657–2659 (1991).

[38] E. L. Wooten, K. M. Kissa, A. Yi-Yan, E. J. Murphy, D. A. Lafaw, P. F. Hallemeier, D. Maack, D. V. Attanasio, D. J. Fritz, G. J. McBrien & D. E. Bossi, "Review of Lithium Niobate Modulators for Fiber-Optic Communications Systems," *IEEE J. Sel. Top. Quantum Electron.* **6**, 69–82 (2000).

[39] S. Abel, F. Eltes, J. E. Ortmann, A. Messner, P. Castera, T. Wagner, D. Urbonas, A. Rosa, A. M. Gutierrez, D. Tulli, P. Ma, B. Baeuerle, A. Josten, W. Heni, D. Caimi, L. Czornomaz, A. A. Demkov, J. Leuthold, P. Sanchis & J. Fompeyrine, "Large Pockels Effect in Micro- and Nanostructured Barium Titanate Integrated on Silicon," *Nat. Mater.* **18**, 42–47 (2019).

[40] C. V. McLaughlin, L. M. Hayden, B. Polishak, S. Huang, J. Luo, T. D. Kim & A. K. Y. Jen, "Wideband 15 THz Response Using Organic Electro-Optic Polymer Emitter-Sensor Pairs at Telecommunication

Wavelengths," *Appl. Phys. Lett.* **92**, 151107 (2008).

[41] W. Jin, P. V. Johnston, D. L. Elder, A. F. Tillack, B. C. Olbricht, J. Song, P. J. Reid, R. Xu, B. H. Robinson & L. R. Dalton, "Benzocyclobutene Barrier Layer For Suppressing Conductance in Nonlinear Optical Devices During Electric Field Poling," *Appl. Phys. Lett.* **104**, 243304 (2014).

[42] W. Jin, P. V. Johnston, D. L. Elder, K. T. Manner, K. E. Garrett, W. Kaminsky, R. Xu, B. H. Robinson & L. R. Dalton, "Structure–Function Relationship Exploration for Enhanced Thermal Stability and Electro-Optic Activity in Monolithic Organic NLO Chromophores," *J. Mater. Chem. C* **4**, 3119–3124 (2016).

[43] T. Baehr-Jones, B. Penkov, J. Huang, P. Sullivan, J. Davies, J. Takayesu, J. Luo, T. D. Kim, L. Dalton, A. Jen, M. Hochberg & A. Scherer, "Nonlinear Polymer-Clad Silicon Slot Waveguide Modulator With a Half Wave Voltage of 0.25 V," *Appl. Phys. Lett.* **92**, 163303 (2008).

[44] Y. Enami, Y. Jouane, J. Luo & A. K.-Y. Jen, "Enhanced Conductivity of Sol-Gel Silica Cladding for Efficient Poling in Electro-Optic Polymer/TiO_2 Vertical Slot Waveguide Modulators," *Opt. Express* **22**, 30191 (2014).

[45] X. Piao, X. Zhang, Y. Mori, M. Koishi, A. Nakaya, S. Inoue, I. Aoki, A. Otomo & S. Yokoyama, "Nonlinear Optical Side-Chain Polymers Post-Functionalized with High-β Chromophores Exhibiting Large Electro-Optic Property," *J. Polym. Sci. A Polym. Chem.* **49**, 47–54 (2011).

[46] H. Xu, F. Liu, D. L. Elder, L. E. Johnson, Y. de Coene, K. Clays, B. H. Robinson & L. R. Dalton, "Ultrahigh Electro-optic Coefficients, High Index of Refraction, and Long-term Stability from Diels-Alder Crosslinkable Binary Molecular Glasses," *Chem. Mater.* **32**, 1408–1421 (2020).

[47] M. Stähelin, C. A. Walsh, D. M. Burland, R. D. Miller, R. J. Twieg & W. Volksen, "Orientational Decay in Poled Second-Order Nonlinear Optical Guest-Host Polymers: Temperature Dependence and Effects of Poling Geometry," *J. Appl. Phys.* **73**, 8471–8479 (1993).

[48] D. Jin, H. Chen, A. Barklund, J. Mallari, G. Yu, E. Miller & R. Dinu, "EO Polymer Modulators Reliability Study," in *Organic Photonic Materials and Devices XII* **7599**, 75990H (SPIE, 2010).

[49] Y. Kuo, J. Luo, W. H. Steier, L. Fellow & A. K-Y Jen, "Enhanced Thermal Stability of Electrooptic Polymer Modulators Using the Diels–

Alder Crosslinkable Polymer," *IEEE Photon. Technol. Lett.* **18**, 175–177 (2006).

[50] D. W. Van Krevelen & K. Te Nijenhuis, *Properties of Polymers* (Elsevier Inc., 2009).

[51] T. Goodson & C. H. Wang ', "Dipolar Orientational Relaxation in Guest/Host Amorphous Polymer Probed by Second Harmonic Generation," *Macromolecules* **26**, 1837–1840 (1993).

[52] H. L. Hampsch, J. Yang, G. K. Wong & J. M. Torkelson, "Dopant Orientation Dynamics in Doped Second-Order Nonlinear Optical Amorphous Polymers. 1. Effects of Temperature Above and Below T_g in Corona-Poled Films," *Macromolecules* **23**, 3640–3647 (1990).

[53] D. Jungbauer, I. Teraoka, D. Y. Yoon, B. Reck, J. D. Swalen, R. Twieg & C. G. Willson, "Second-Order Nonlinear Optical Properties and Relaxation Characteristics of Poled Linear Epoxy Polymers with Tolane Chromophores," *J. Appl. Phys.* **69**, 8011–8017 (1991).

[54] M. T. Cicerone & M. D. Ediger, "A New Technique for Measuring Ultraslow Molecular Reorientation Near and Below the Glass Transition," *J. Chem. Phys.* **97**, 2156–2159 (1992).

[55] Telcordia, "GR-468-CORE: Generic Reliability Assurance Requirements for Optoelectronic Devices Used in Telecommunications Equipment," (2004). Available at: https://telecom-info.njdepot.ericsson.net/site-cgi/ido/docs.cgi?ID=SEARCH&DOCUMENT=GR-468&.

[56] L. R. Dalton, P. A. Sullivan & D. H. Bale, "Electric Field Poled Organic Electro-optic Materials: State of the Art and Future Prospects," *Chem. Rev.* **110**, 25–55 (2010).

[57] G. Gupta, W. H. Steier, Y. Liao, J. Luo, L. R. Dalton & A. K. Y. Jen, "Modeling Photobleaching of Optical Chromophores: Light-Intensity Effects in Precise Trimming of Integrated Polymer Devices," *J. Phys. Chem. C* **112**, 8051–8060 (2008).

[58] Y. Shi, W. Wang, W. Lin, D. J. Olson & J. H. Bechtel, "Double-End Crosslinked Electro-Optic Polymer Modulators With High Optical Power Handling Capability," *Appl. Phys. Lett.* **70**, 1342–1344 (1997).

[59] M. E. DeRosa, M. He, J. S. Cites, S. M. Garner & Y. R. Tang, "Photostability of High $\mu\beta$ Electro-Optic Chromophores at 1550 nm," *J. Phys. Chem. B* **108**, 8725–8730 (2004).

[60] D. Rezzonico, M. Jazbinsek, P. Günter, C. Bosshard, D. H. Bale, Y. Liao, L. R. Dalton & P. J. Reid, "Photostability Studies of π-Conjugated Chromophores With Resonant and Nonresonant Light Excitation for Long-Life Polymeric Telecommunication Devices," *J. Opt. Soc. Am. B* **24**, 2199 (2007).

[61] G. V. M. Williams, Y. Kutuvantavida, S. Janssens, S. G. Raymond, M. T. T. Do, M. D. H. Bhuiyan, J. W. Quilty, N. Denton & A. J. Kay, "The Effects of Excited State Lifetime, Optical Intensity, and Excited State Quenchers on the Photostability of Zwitterionic Chromophores," *J. Appl. Phys.* **110**, 083524 (2011).

[62] S. Beutner, B. Bloedorn, T. Hoffmann & H. D. Martin, "Synthetic Singlet Oxygen Quenchers," *Methods Enzymol.* **319**, 226–241 (2000).

[63] S. M. George, "Atomic Layer Deposition: An Overview," *Chem. Rev.* **110**, 111–131 (2010).

[64] O. Sneh, R. B. Clark-Phelps, A. R. Londergan, J. Winkler & T. E. Seidel, "Thin Film Atomic Layer Deposition Equipment for Semiconductor Processing," *Thin Solid Films* **402**, 248–261 (2002).

[65] R. L. Puurunen, "Surface Chemistry of Atomic Layer Deposition: A Case Study for the Trimethylaluminum/ Water Process," *J. Appl. Phys* **97**, 121301 (2005).

[66] D. N. Nikogosyan, *Nonlinear Optical Crystals: A Complete Survey* (Springer-Verlag, 2005).

[67] D. Feng, S. Liao, H. Liang, J. Fong, B. Bijlani, R. Shafiiha, B. J. Luff, Y. Luo, J. Cunningham, A. V. Krishnamoorthy & M. Asghari, "High Speed GeSi Electro-Absorption Modulator at 1550 nm Wavelength on SOI Waveguide," *Opt. Express* **20**, 22224 (2012).

[68] P. Dong, S. Liao, D. Feng, H. Liang, D. Zheng, R. Shafiiha, C.-C. Kung, W. Qian, G. Li, X. Zheng, A. V. Krishnamoorthy & M. Asghari, "Low Vpp, Ultralow-Energy, Compact, High-Speed Silicon Electro-Optic Modulator," *Opt. Express* **17**, 22484–22490 (2009).

[69] L. B. Soldano & E. C. M. Pennings, "Optical Multi-Mode Interference Devices Based on Self-Imaging: Principles and Applications," *J. Light. Technol.* **13**, 615–627 (1995).

[70] R. Palmer, *Silicon Photonic Modulators for Low-power Applications* (KIT Scientific Publishing, 2015).

[71] Z. Yong, W. D. Sacher, Y. Huang, J. C. Mikkelsen, Y. Yang, X. Luo, P. Dumais, D. Goodwill, H. Bahrami, G.-Q. Lo, E. Bernier & J. K. Poon, "Efficient Single-Drive Push-Pull Silicon Mach-Zehnder Modulators with U-Shaped PN Junctions for the O-Band," in *Optical Fiber Communication Conference* Tu2H.2 (OSA, 2017).

[72] J. Fujikata, S. Takahashi, M. Takahashi, M. Noguchi, T. Nakamura & Y. Arakawa, "High-Performance MOS-Capacitor-Type Si Optical Modulator and Surface-Illumination-Type Ge Photodetector for Optical Interconnection," *Jpn. J. Appl. Phys.* **55**, 04EC01 (2016).

[73] J.-H. Han, F. Boeuf, J. Fujikata, S. Takahashi, S. Takagi & M. Takenaka, "Efficient Low-Loss InGaAsP/Si Hybrid MOS Optical Modulator," *Nat. Photonics* **11**, 486–490 (2017).

[74] L. Chen, P. Dong & Y.-K. Chen, "Chirp and Dispersion Tolerance of a Single-Drive Push–Pull Silicon Modulator at 28 Gb/s," *IEEE Photon. Technol. Lett.* **24**, 936–938 (2012).

[75] F. Eltes, M. Kroh, D. Caimi, C. Mai, Y. Popoff, G. Winzer, D. Petousi, S. Lischke, J. E. Ortmann, L. Czornomaz, L. Zimmermann, J. Fompeyrine & S. Abel, "A Novel 25 Gbps Electro-Optic Pockels Modulator Integrated on an Advanced Si Photonic Platform," in *Technical Digest - International Electron Devices Meeting, IEDM* 24.5.1-24.5.4 (Institute of Electrical and Electronics Engineers Inc., 2018).

[76] P. Stark, F. Eltes, Y. Baumgartner, D. Caimi, Y. Popoff, N. Meier, L. Czornomaz, J. Fompeyrine, B. Offrein & S. Abel, "Heterogeneous Co-Integration of BTO/Si and III-V Technology on a Silicon Photonics Platform," in *Optical Fiber Communication Conference (OFC) 2020* T3B.3 (OSA, 2020).

[77] H. Sato, H. Miura, F. Qiu, A. M. Spring, T. Kashino, T. Kikuchi, M. Ozawa, H. Nawata, K. Odoi & S. Yokoyama, "Low Driving Voltage Mach-Zehnder Interference Modulator Constructed From an Electro-Optic Polymer on Ultra-Thin Silicon With a Broadband Operation," *Opt. Express* **25**, 768–775 (2017).

[78] F. Qiu, H. Sato, D. Spring, Andrew M. Maeda, M. Ozawa, K. Odoi, I. Aoki, A. Otomo & S. Yokoyama, "Ultra-Thin Silicon/Electro-Optic Polymer Hybrid Waveguide Modulators," *Appl. Phys. Lett.* **107**, (2015).

[79] L. Guo-Wei, J. Hong, F. Qiu, T. Spring, Andrew M. Kashino, J. Oshima, M. Ozawa & S. Nawata, Hideyuki Yokoyama, "High-Temperature-

Resistant Silicon-Polymer Hybrid Modulator Operating at up to 200 Gbit s^{-1} for Energy-Efficient Datacentres and Harsh-Environment Applications," *Nat. Commun.* **11**, 4224 (2020).

[80] H. Zwickel, S. Singer, C. Kieninger, Y. Kutuvantavida, N. Muradyan, T. Wahlbrink, S. Yokoyama, S. Randel, W. Freude & C. Koos, "A Verified Equivalent-Circuit Model for Slot-Waveguide Modulators," *Opt. Express* **28**, 12951–12976 (2019).

[81] L. Alloatti, R. Palmer, S. Diebold, K. P. Pahl, B. Chen, R. Dinu, M. Fournier, J.-M. Fedeli, T. Zwick, W. Freude, C. Koos & J. Leuthold, "100 GHz Silicon–Organic Hybrid Modulator," *Light Sci. Appl.* **3**, e173 (2014).

[82] J. Witzens, T. Baehr-Jones & M. Hochberg, "Design of Transmission Line Driven Slot Waveguide Mach-Zehnder Interferometers and Application to Analog Optical Links," *Opt. Express* **18**, 16902 (2010).

[83] N. J. Parsons, A. C. O'Donnell & K. K. Wong, "Design Of Efficient And Wideband Travelling-Wave Modulators," in *Integrated Optical Circuit Engineering III* **0651**, 148 (SPIE, 1986).

[84] I. P. Kaminow, T. Li & A. E. Willner, *Optical Fiber Telecommunications V B : systems and networks* (Elsevier Academic Press, 2013).

[85] A. Khilo, S. J. Spector, M. E. Grein, A. H. Nejadmalayeri, C. W. Holzwarth, M. Y. Sander, M. S. Dahlem, M. Y. Peng, M. W. Geis, N. A. DiLello, J. U. Yoon, A. Motamedi, J. S. Orcutt, J. P. Wang, C. M. Sorace-Agaskar, M. A. Popović, J. Sun, G.-R. Zhou, H. Byun, J. Chen, J. L. Hoyt, H. I. Smith, R. J. Ram, M. Perrott, T. M. Lyszczarz, E. P. Ippen & F. X. Kärtner, "Photonic ADC: Overcoming the Bottleneck of Electronic Jitter," *Opt. Express* **20**, 4454 (2012).

[86] M. Lauermann, C. Weimann, A. Knopf, W. Heni, R. Palmer, S. Koeber, D. L. Elder, W. Bogaerts, J. Leuthold, L. R. Dalton, C. Rembe, W. Freude & C. Koos, "Integrated Optical Frequency Shifter in Silicon-Organic Hybrid (SOH) Technology," *Opt. Express* **24**, 11694 (2016).

[87] G. Raybon, J. Cho, A. Adamiecki, P. Winzer, A. Konczykowska, F. Jorge, J.-Y. Dupuy, M. Riet, B. Duval, K. Kim, S. Randel, D. Pilori, B. Guan, N. K. Fontaine & E. Burrows, "Single Carrier High Symbol Rate Transmitter for Data Rates up to 1.0 Tb/s," in *Optical Fiber Communication Conference* Th3A.2 (OSA, 2016).

[88] C. Haffner, W. Heni, Y. Fedoryshyn, B. Baeuerle, A. Josten, Y. Salamin, R. Bonjour, C. Hoessbacher, A. Emboras, D. L. Elder, P. Leuchtmann, D.

Hillerkuss, L. R. Dalton, C. Hafner & J. Leuthold, "Ultra-Compact Plasmonic IQ-Modulator," in *2015 European Conference on Optical Communication (ECOC)* 1–3 (IEEE, 2015).

[89] V. Katopodis, P. Groumas, Z. Zhang, R. Dinu, E. Miller, A. Konczykowska, J.-Y. Dupuy, A. Beretta, A. Dede, J. H. Choi, P. Harati, F. Jorge, V. Nodjiadjim, M. Riet, G. Cangini, A. Vannucci, N. Keil, H.-G. Bach, N. Grote, H. Avramopoulos & C. Kouloumentas, "Polymer Enabled 100Gbaud Connectivity for Datacom Applications," *Opt. Commun.* **362**, 13–21 (2016).

[90] P. C. Schindler, D. Korn, C. Stamatiadis, M. F. OKeefe, L. Stampoulidis, R. Schmogrow, P. Zakynthinos, R. Palmer, N. Cameron, Y. Zhou, R. G. Walker, E. Kehayas, S. Ben-Ezra, I. Tomkos, L. Zimmermann, K. Petermann, W. Freude, C. Koos & J. Leuthold, "Monolithic GaAs Electro-Optic IQ Modulator Demonstrated at 150 Gbit/s With 64QAM," *J. Light. Technol.* **32**, 760–765 (2014).

[91] Y. Ogiso, J. Ozaki, Y. Ueda, N. Kashio, N. Kikuchi, E. Yamada, H. Tanobe, S. Kanazawa, H. Yamazaki, Y. Ohiso, T. Fujii & M. Kohtoku, "Over 67 GHz Bandwidth and 1.5 V Vπ InP-Based Optical IQ Modulator With n-i-p-n Heterostructure," *J. Light. Technol.* **35**, 1450–1455 (2017).

[92] C. Koos, J. Brosi, M. Waldow, W. Freude & J. Leuthold, "Silicon-on-Insulator Modulators for Next-Generation 100 Gbit/s-Ethernet," in *33rd European Conference and Exhibition on Optical Communication - ECOC 2007* 1–2 (IEE, 2007).

[93] R. Ding, T. Baehr-Jones, Y. Liu, R. Bojko, J. Witzens, S. Huang, J. Luo, S. Benight, P. Sullivan, J.-M. Fedeli, M. Fournier, L. Dalton, A. Jen & M. Hochberg, "Demonstration of a Low VπL Modulator with GHz Bandwidth Based on Electro-Optic Polymer-Clad Silicon Slot Waveguides," *Opt. Express* **18**, 15618–23 (2010).

[94] A. Melikyan, L. Alloatti, A. Muslija, D. Hillerkuss, P. C. Schindler, J. Li, R. Palmer, D. Korn, S. Muehlbrandt, D. Van Thourhout, B. Chen, R. Dinu, M. Sommer, C. Koos, M. Kohl, W. Freude & J. Leuthold, "High-Speed Plasmonic Phase Modulators," *Nat. Photonics* **8**, 229–233 (2014).

[95] C. Haffner, W. Heni, Y. Fedoryshyn, J. Niegemann, A. Melikyan, D. L. Elder, B. Baeuerle, Y. Salamin, A. Josten, U. Koch, C. Hoessbacher, F. Ducry, L. Juchli, A. Emboras, D. Hillerkuss, M. Kohl, L. R. Dalton, C. Hafner & J. Leuthold, "All-Plasmonic Mach–Zehnder Modulator Enabling Optical High-Speed Communication at the Microscale," *Nat.*

Photonics **9**, 525–528 (2015).

[96] A. Melikyan, K. Koehnle, M. Lauermann, R. Palmer, S. Koeber, S. Muehlbrandt, P. C. Schindler, D. L. Elder, S. Wolf, W. Heni, C. Haffner, Y. Fedoryshyn, D. Hillerkuss, M. Sommer, L. R. Dalton, D. Van Thourhout, W. Freude, M. Kohl, J. Leuthold & C. Koos, "Plasmonic-Organic Hybrid (POH) Modulators for OOK and BPSK Signaling at 40 Gbit/s," *Opt. Express* **23**, 9938–9946 (2015).

[97] P. O. Weigel, M. Savanier, C. T. DeRose, A. T. Pomerene, A. L. Starbuck, A. L. Lentine, V. Stenger & S. Mookherjea, "Lightwave Circuits in Lithium Niobate through Hybrid Waveguides with Silicon Photonics.," *Sci. Rep.* **6**, 22301 (2016).

[98] S. Abel, T. Stöferle, C. Marchiori, D. Caimi, L. Czornomaz, M. Stuckelberger, M. Sousa, B. J. Offrein & J. Fompeyrine, "A Hybrid Barium Titanate–Silicon Photonics Platform for Ultraefficient Electro-Optic Tuning," *J. Light. Technol.* **34**, (2016).

[99] S. Koeber, R. Palmer, M. Lauermann, W. Heni, D. L. Elder, D. Korn, M. Woessner, L. Alloatti, S. Koenig, P. C. Schindler, H. Yu, W. Bogaerts, L. R. Dalton, W. Freude, J. Leuthold & C. Koos, "Femtojoule Electro-Optic Modulation Using a Silicon–Organic Hybrid Device," *Light Sci. Appl.* **4**, e255 (2015).

[100] W. Heni, C. Haffner, D. L. Elder, A. F. Tillack, Y. Fedoryshyn, R. Cottier, Y. Salamin, C. Hoessbacher, U. Koch, B. Cheng, B. Robinson, L. R. Dalton & J. Leuthold, "Nonlinearities of Organic Electro-Optic Materials in Nanoscale Slots and Implications for the Optimum Modulator Design," *Opt. Express* **25**, 2627 (2017).

[101] C. Hoessbacher, A. Josten, B. Baeuerle, Y. Fedoryshyn, H. Hettrich, Y. Salamin, W. Heni, C. Haffner, C. Kaiser, R. Schmid, D. L. Elder, D. Hillerkuss, M. Möller, L. R. Dalton & J. Leuthold, "Plasmonic Modulator With >170 GHz Bandwidth Demonstrated at 100 GBd NRZ," *Opt. Express* **25**, 1762 (2017).

[102] C. Xiong, W. H. P. Pernice, J. H. Ngai, J. W. Reiner, D. Kumah, F. J. Walker, C. H. Ahn & H. X. Tang, "Active Silicon Integrated Nanophotonics: Ferroelectric BaTiO$_3$ Devices," *Nano Lett.* **14**, 1419–1425 (2014).

[103] B. Baeuerle, C. Hoessbacher, W. Heni, Y. Fedoryshyn, A. Josten, C. Haffner, T. Watanabe, D. L. Elder, L. R. Dalton & J. Leuthold, "Driver-

Less Sub 1 Vpp Operation of a Plasmonic-Organic Hybrid Modulator at 100 GBd NRZ," in *Optical Fiber Communication Conference* M2I.1 (OSA, 2018).

[104] R. Palmer, S. Koeber, D. L. Elder, M. Woessner, W. Heni, D. Korn, M. Lauermann, W. Bogaerts, L. Dalton, W. Freude, J. Leuthold & C. Koos, "High-Speed, Low Drive-Voltage Silicon-Organic Hybrid Modulator Based on a Binary-Chromophore Electro-Optic Material," *J. Light. Technol.* **32**, 2726–2734 (2014).

[105] C. Haffner, W. Heni, D. L. Elder, Y. Fedoryshyn, N. Đorđević, D. Chelladurai, U. Koch, K. Portner, M. Burla, B. Robinson, L. R. Dalton & J. Leuthold, "Harnessing Nonlinearities Near Material Absorption Resonances for Reducing Losses in Plasmonic Modulators," *Opt. Mater. Express* **7**, 2168 (2017).

[106] A. F. Tillack & B. H. Robinson, "Toward Optimal EO Response from ONLO Chromophores: A Statistical Mechanics Study of Optimizing Shape," *J. Opt. Soc. Am. B* **33**, E121 (2016).

[107] W. Heni, Y. Kutuvantavida, C. Haffner, H. Zwickel, C. Kieninger, S. Wolf, M. Lauermann, Y. Fedoryshyn, A. F. Tillack, L. E. Johnson, D. L. Elder, B. H. Robinson, W. Freude, C. Koos, J. Leuthold & L. R. Dalton, "Silicon–Organic and Plasmonic–Organic Hybrid Photonics," *ACS Photonics* **4**, 1576–1590 (2017).

[108] R. D. Dureiko, D. E. Schuele & K. D. Singer, "Modeling Relaxation Processes in Poled Electro-Optic Polymer Films," *J. Opt. Soc. Am. B* **15**, 338–350 (1998).

[109] J. Luo, S. Huang, Z. Shi, B. M. Polishak, X.-H. Zhou & A. K. Jen, "Tailored Organic Electro-optic Materials and Their Hybrid Systems for Device Applications †," *Chem. Mater.* **23**, 544 (2011).

[110] L. R. Dalton, D. Lao, B. C. Olbricht, S. Benight, D. H. Bale, J. A. Davies, T. Ewy, S. R. Hammond & P. A. Sullivan, "Theory-Inspired Development of New Nonlinear Optical Materials and Their Integration into Silicon Photonic Circuits and Devices," *Opt. Mater.* **32**, 658–668 (2010).

[111] M. Sprave, R. Blum & M. Eich, "High Electric Field Conduction Mechanisms in Electrode Poling of Electro-Optic Polymers," *Appl. Phys. Lett.* **69**, 2962–2964 (1996).

[112] S. Huang, T.-D. Kim, J. Luo, S. K. Hau, Z. Shi, X.-H. Zhou, H.-L. Yip &

A. K.-Y. Jen, "Highly Efficient Electro-Optic Polymers Through Improved Poling Using a Thin TiO2-Modified Transparent Electrode," *Appl. Phys. Lett.* **96**, 243311 (2010).

[113] T. Hiraki, T. Aihara, K. Hasebe, K. Takeda, T. Fujii, T. Kakitsuka, T. Tsuchizawa, H. Fukuda & S. Matsuo, "Heterogeneously Integrated III–V/Si MOS Capacitor Mach–Zehnder Modulator," *Nat. Photonics* **11**, 482–485 (2017).

[114] A. Rao, A. Patil, J. Chiles, M. Malinowski, S. Novak, K. Richardson, P. Rabiei & S. Fathpour, "Heterogeneous Microring and Mach-Zehnder Modulators Based on Lithium Niobate and Chalcogenide Glasses on Silicon," *Opt. Express* **23**, 22746 (2015).

[115] F. Eltes, D. Caimi, F. Fallegger, M. Sousa, E. O'Connor, M. D. Rossell, B. Offrein, J. Fompeyrine & S. Abel, "Low-Loss BaTiO $_3$ –Si Waveguides for Nonlinear Integrated Photonics," *ACS Photonics* **3**, 1698–1703 (2016).

[116] S. Wolf, M. Lauermann, P. Schindler, G. Ronniger, K. Geistert, R. Palmer, S. Kober, W. Bogaerts, J. Leuthold, W. Freude & C. Koos, "DAC-Less Amplifier-Less Generation and Transmission of QAM Signals Using Sub-Volt Silicon-Organic Hybrid Modulators," *J. Light. Technol.* **33**, 1425–1432 (2015).

[117] M. Lauermann, R. Palmer, S. Koeber, P. C. Schindler, D. Korn, T. Wahlbrink, J. Bolten, M. Waldow, D. L. Elder, L. R. Dalton, J. Leuthold, W. Freude & C. Koos, "Low-Power Silicon-Organic Hybrid (SOH) Modulators for Advanced Modulation Formats," *Opt. Express* **22**, 29927 (2014).

[118] M. Lauermann, S. Wolf, P. C. Schindler, R. Palmer, S. Koeber, D. Korn, L. Alloatti, T. Wahlbrink, J. Bolten, M. Waldow, M. Koenigsmann, M. Kohler, D. Malsam, D. L. Elder, P. V. Johnston, N. Phillips-Sylvain, P. A. Sullivan, L. R. Dalton, J. Leuthold, W. Freude & C. Koos, "40 GBd 16QAM Signaling at 160 Gb/s in a Silicon-Organic Hybrid Modulator," *J. Light. Technol.* **33**, 1210–1216 (2015).

[119] X. Wang, C.-Y. Lin, S. Chakravarty, J. Luo, A. K.-Y. Jen & R. T. Chen, "Effective In-Device r33 of 735 pm/V on Electro-Optic Polymer Infiltrated Silicon Photonic Crystal Slot Waveguides," *Opt. Lett.* **36**, 882 (2011).

[120] Y. Enami, C. T. Derose, D. Mathine, C. Loychik, C. Greenlee, R. A.

Norwood, T. D. Kim, J. Luo, Y. Tian, A. K.-Y. Jen & N. Peyghambarian, "Hybrid Polymer/Sol–Gel Waveguide Modulators With Exceptionally large Electro–Optic Coefficients," *Nat. Photonics* **1**, 180–185 (2007).

[121] W. Freude, R. Schmogrow, B. Nebendahl, M. Winter, A. Josten, D. Hillerkuss, S. Koenig, J. Meyer, M. Dreschmann, M. Huebner, C. Koos, J. Becker & J. Leuthold, "Quality Metrics for Optical Signals: Eye diagram, Q-factor, OSNR, EVM and BER," in *2012 14th International Conference on Transparent Optical Networks (ICTON)* 1–4 (IEEE, 2012).

[122] R. Ding, T. Baehr-Jones, W.-J. Kim, B. Boyko, R. Bojko, A. Spott, A. Pomerene, C. Hill, W. Reinhardt & M. Hochberg, "Low-Loss Asymmetric Strip-Loaded Slot Waveguides in Silicon-on-Insulator," *Appl. Phys. Lett.* **98**, 233303 (2011).

[123] D. Marris-Morini, C. Baudot, J.-M. Fédéli, G. Rasigade, N. Vulliet, A. Souhaité, M. Ziebell, P. Rivallin, S. Olivier, P. Crozat, X. Le Roux, D. Bouville, S. Menezo, F. Bœuf & L. Vivien, "Low Loss 40 Gbit/s Silicon Modulator Based on Interleaved Junctions and Fabricated on 300 mm SOI Wafers.," *Opt. Express* **21**, 22471–5 (2013).

[124] A. Brimont, D. J. Thomson, F. Y. Gardes, J. M. Fedeli, G. T. Reed, J. Martí & P. Sanchis, "High-Contrast 40 Gb/s Operation of a 500 μm Long Silicon Carrier-Depletion Slow Wave Modulator," *Opt. Lett.* **37**, 3504 (2012).

[125] D. J. Thomson, F. Y. Gardes, Y. Hu, G. Mashanovich, M. Fournier, P. Grosse, J.-M. Fedeli & G. T. Reed, "High contrast 40Gbit/s optical modulation in silicon," *Opt. Express* **19**, 11507 (2011).

[126] Hoon Kim & A. H. Gnauck, "Chirp Characteristics of Dual-Drive Mach-Zehnder Modulator With a Finite DC Extinction Ratio," *IEEE Photon. Technol. Lett.* **14**, 298–300 (2002).

[127] R. Palmer, L. Alloatti, D. Korn, W. Heni, P. C. Schindler, J. Bolten, M. Karl, M. Waldow, T. Wahlbrink, W. Freude, C. Koos & J. Leuthold, "Low-Loss Silicon Strip-to-Slot Mode Converters," *IEEE Photonics J.* **5**, 2200409–2200409 (2013).

[128] Zhen Sheng, Zhiqi Wang, Chao Qiu, Le Li, A. Pang, Aimin Wu, Xi Wang, Shichang Zou & Fuwan Gan, "A Compact and Low-Loss MMI Coupler Fabricated With CMOS Technology," *IEEE Photonics J.* **4**, 2272–2277 (2012).

[129] C. Xiong, D. M. Gill, J. E. Proesel, J. S. Orcutt, W. Haensch & W. M. J. Green, "Monolithic 56 Gb/s Silicon Photonic Pulse-Amplitude Modulation Transmitter," *Optica* **3**, 1060 (2016).

[130] D. Patel, A. Samani, V. Veerasubramanian, S. Ghosh & D. V. Plant, "Silicon Photonic Segmented Modulator-Based Electro-Optic DAC for 100 Gb/s PAM-4 Generation," *IEEE Photon. Technol. Lett.* **27**, 2433–2436 (2015).

[131] X. Tu, T.-Y. Liow, J. Song, M. Yu, & G. Q. Lo, "Fabrication of Low Loss and High Speed Silicon Optical Modulator Using Doping Compensation Method," *Opt. Express* **19**, 18029 (2011).

[132] C. Wang, M. Zhang, X. Chen, M. Bertrand, A. Shams-Ansari, S. Chandrasekhar, P. Winzer & M. Lončar, "Integrated Lithium Niobate Electro-Optic Modulators Operating at CMOS-Compatible Voltages," *Nature* **562**, 101 (2018).

[133] Y. Ogiso, J. Ozaki, Y. Ueda, H. Wakita, M. Nagatani, H. Yamazaki, M. Nakamura, T. Kobayashi, S. Kanazawa, Y. Hashizume, H. Tanobe, N. Nunoya, M. Ida, Y. Miyamoto & M. Ishikawa, "80-GHz Bandwidth and 1.5-V Vπ InP-Based IQ Modulator," *J. Light. Technol.* 1–1 (2019).

[134] Y. R. Shen, *Principles of Nonlinear Optics* (Wiley-Interscience, 1984).

[135] J. E. Donehue, E. Wertz, C. N. Talicska & J. S. Biteen, "Plasmon-Enhanced brightness and photostability from single fluorescent proteins coupled to gold nanorods," *J. Phys. Chem. C* **118**, 15027–15035 (2014).

[136] S. Muehlbrandt, A. Melikyan, T. Harter, K. Köhnle, A. Muslija, P. Vincze, S. Wolf, P. Jakobs, Y. Fedoryshyn, W. Freude, J. Leuthold, C. Koos & M. Kohl, "Silicon-plasmonic internal-photoemission detector for 40 Gbit/s data reception," *Optica* **3**, 741 (2016).

[137] X. Yang, Y. Li, Z. Lou, Q. Chen & B. Li, "Optical Energy Transfer from Photonic Nanowire to Plasmonic Nanowire," *ACS Appl. Energy Mater.* **1**, 278–283 (2018).

[138] S. Ummethala, T. Harter, K. Koehnle, Z. Li, S. Muehlbrandt, Y. Kutuvantavida, J. Kemal, P. Marin-Palomo, J. Schaefer, A. Tessmann, S. K. Garlapati, A. Bacher, L. Hahn, M. Walther, T. Zwick, S. Randel, W. Freude & C. Koos, "THz-to-Optical Conversion in Wireless Communications Using an Ultra-Broadband Plasmonic Modulator," *Nat. Photonics* **13**, 519–524 (2019).

[139] M. Burla, C. Hoessbacher, W. Heni, C. Haffner, Y. Fedoryshyn, D.

Werner, T. Watanabe, H. Massler, D. L. Elder, L. R. Dalton & J. Leuthold, "500 GHz plasmonic Mach-Zehnder modulator enabling sub-THz microwave photonics," *APL Photonics* **4**, 056106 (2019).

[140] C. Kieninger, Y. Kutuvantavida, D. L. Elder, S. Wolf, H. Zwickel, M. Blaicher, J. N. Kemal, M. Lauermann, S. Randel, W. Freude, L. R. Dalton & C. Koos, "Ultra-High Electro-Optic Activity Demonstrated in a Silicon-Organic Hybrid Modulator," *Optica* **5**, 739–748 (2018).

[141] S. Ummethala, J. N. Kemal, M. Lauermann, A. S. Alam, H. Zwickel, T. Harter, Y. Kutuvantavida, L. Hahn, S. H. Nandam, D. L. Elder, L. R. Dalton, W. Freude, S. Randel, C. Koos, S. Randel, C. Koos & C. Koos, "Capacitively Coupled Silicon-Organic Hybrid Modulator for 200 Gbit/s PAM-4 Signaling," in *Conference on Lasers and Electro-Optics* JTh5B.2 (2019).

[142] A. Samani, D. Patel, M. Chagnon, E. El-Fiky, R. Li, M. Jacques, N. Abadía, V. Veerasubramanian & D. V. Plant, "Experimental Parametric Study of 128 Gb/s PAM-4 Transmission System Using a Multi-Electrode Silicon Photonic Mach Zehnder Modulator," *Opt. Express* **25**, 13252 (2017).

[143] J. Wang, S. Paesani, Y. Ding, R. Santagati, P. Skrzypczyk, A. Salavrakos, J. Tura, R. Augusiak, L. Mančinska, D. Bacco, D. Bonneau, J. W. Silverstone, Q. Gong, A. Acín, K. Rottwitt, L. K. Oxenløwe, J. L. O'Brien, A. Laing & M. G. Thompson, "Multidimensional Quantum Entanglement with Large-Scale Integrated Optics.," *Science* **360**, 285–291 (2018).

[144] X. Qiang, X. Zhou, J. Wang, C. M. Wilkes, T. Loke, S. O'Gara, L. Kling, G. D. Marshall, R. Santagati, T. C. Ralph, J. B. Wang, J. L. O'Brien, M. G. Thompson & J. C. F. Matthews, "Large-Scale Silicon Quantum Photonics Implementing Arbitrary Two-Qubit Processing," *Nat. Photonics* **12**, 534–539 (2018).

[145] C. V. Poulton, A. Yaacobi, D. B. Cole, M. J. Byrd, M. Raval, D. Vermeulen & M. R. Watts, "Coherent Solid-State LIDAR with Silicon Photonic Optical Phased Arrays," *Opt. Lett.* **42**, 4091 (2017).

[146] V. R. Almeida, Q. Xu, C. A. Barrios & M. Lipson, "Guiding and confining light in void nanostructure," *Opt. Lett.* **29**, 1209 (2004).

[147] L. Alloatti, D. Korn, R. Palmer, D. Hillerkuss, J. Li, A. Barklund, R. Dinu, J. Wieland, M. Fournier, J. Fedeli, H. Yu, W. Bogaerts, P. Dumon,

R. Baets, C. Koos, W. Freude & J. Leuthold, "42.7 Gbit/s Electro-Optic Modulator in Silicon Technology," *Opt. Express* **19**, 11841 (2011).

[148] M. Gehl, C. Long, D. Trotter, A. Starbuck, A. Pomerene, J. B. Wright, S. Melgaard, J. Siirola, A. L. Lentine & C. Derose, "Operation of high-speed silicon photonic micro-disk modulators at cryogenic temperatures," *Optica* **4**, (2017).

[149] F. Eltes, G. E. Villarreal-Garcia, D. Caimi, H. Siegwart, A. A. Gentile, A. Hart, P. Stark, G. D. Marshall, M. G. Thompson, J. Barreto, J. Fompeyrine & S. Abel, "An Integrated Cryogenic Optical Modulator," *arXiv:1904.10902v1 [physics.app-ph]* (2019).

[150] P. Pintus, Z. Zhang, S. Pinna, M. A. Tran, A. Jain, M. J. Kennedy, L. Ranzani, M. Soltani & J. E. Bowers, "Characterization of Heterogeneous InP-on-Si Optical Modulators Operating Between 77 K and Room Temperature," *APL Photonics* **4**, 100805 (2019).

[151] C. Kieninger, Y. Kutuvantavida, H. Miura, J. N. Kemal, H. Zwickel, F. Qiu, M. Lauermann, W. Freude, S. Randel, S. Yokoyama & C. Koos, "Demonstration of Long-Term Thermally Stable Silicon-Organic Hybrid Modulators at 85 °C," *Opt. Express* **26**, 27955 (2018).

[152] H. Zwickel, J. N. Kemal, C. Kieninger, Y. Kutuvantavida, J. Rittershofer, M. Lauermann, W. Freude, S. Randel & C. Koos, "Electrically Packaged Silicon-Organic Hybrid (SOH) I/Q-Modulator for 64 GBd Operation," *Opt. Express* **26**, 34580 (2018).

[153] J. Degallaix, R. Flaminio, D. Forest, M. Granata, C. Michel, L. Pinard, T. Bertrand & G. Cagnoli, "Bulk optical absorption of high resistivity silicon at 1550 nm," *Opt. Lett.* **38**, 2047 (2013).

[154] Y. Sato, "A Method of Self-Recovering Equalization for Multilevel Amplitude-Modulation Systems," *IEEE Trans. Commun.* **23**, 679–682 (1975).

[155] F. Chang, K. Onohara & T. Mizuochi, "Forward Error Correction for 100 G Transport Networks," *IEEE Commun. Mag.* **48**, S48–S55 (2010).

[156] H. K. Li, K. Y. Fong, H. Zhu, Q. Li, S. Wang, S. Yang, Y. Wang & X. Zhang, "Valley optomechanics in a monolayer semiconductor," *Nature Photonics* **13**, 397–401 (2019).

[157] X. Yang & B. Li, "Monolayer MoS2 for nanoscale photonics," *Nanophotonics* Preprint DOI: 10.1515/nanoph-2019-0533 (2020).

[158] G. T. Reed & C. E. Jason Png, "Silicon Optical Modulators," *Mater. Today* **8**, 40–50 (2005).

[159] H. Yu, M. Pantouvaki, J. Van Campenhout, D. Korn, K. Komorowska, P. Dumon, Y. Li, P. Verheyen, P. Absil, L. Alloatti, D. Hillerkuss, J. Leuthold, R. Baets & W. Bogaerts, "Performance Tradeoff Between Lateral and Interdigitated Doping Patterns for High Speed Carrier-Depletion Based Silicon Modulators," *Opt. Express* **20**, 12926–12938 (2012).

[160] P. Dong, J. H. Sinsky & C. Gui, "Coplanar-Waveguide-Based Silicon Mach–Zehnder Modulator Using a Meandering Optical Waveguide and Alternating-Side PN Junction Loading," *Opt. Lett.* **41**, 4401–4404 (2016).

[161] G. T. Reed, D. J. Thomson, F. Y. Gardes, Y. Hu, J.-M. Fedeli & G. Z. Mashanovich, "High-Speed Carrier-Depletion Silicon Mach-Zehnder Optical Modulators With Lateral PN Junctions," *Front. Phys.* **2**, 77 (2014).

[162] F. Qiu, H. Miura, A. M. Spring, J. Hong, D. Maeda, M.-A. Ozawa, K. Odoi & S. Yokoyama, "An Electro-Optic Polymer-Cladded TiO2 Waveguide Modulator," *Appl. Phys. Lett.* **1091**, 173301–123302 (2016).

[163] H. Miura, F. Qiu, A. M. Spring, T. Kashino, T. Kikuchi, M. Ozawa, H. Nawata, K. Odoi & S. Yokoyama, "High Thermal Stability 40 GHz Electro-Optic Polymer Modulators," *Opt. Express* **25**, 28643–28649 (2017).

[164] P. Debye, *Polar molecules,* (The Chemical Catalog Company Inc., 1929).

[165] M. G. Kuzyk, R. C. Moore & L. A. King, "Second-Harmonic-Generation Measurements of the Elastic Constant of a Molecule in a Polymer Matrix," *J. Opt. Soc. Am. B* **7**, 64–72 (1990).

[166] K. D. Singer & L. A. King, "Relaxation Phenomena in Polymer Nonlinear Optical Materials," *J. Appl. Phys.* **70**, 3251–3255 (1991).

[167] A. Dhinojwala, G. K. Wongj & M. Torkelson, "Rotational Reorientation Dynamics of Nonlinear Optical Chromophores in Rubbery and Glassy Polymers: a-Relaxation Dynamics Probed by Second Harmonic Generation and Dielectric Relaxation," *Macromolecules* **26**, 5943–5953 (1993).

[168] D. Korn, M. Lauermann, S. Koeber, P. Appel, L. Alloatti, R. Palmer, P. Dumon, W. Freude, J. Leuthold & C. Koos, "Lasing in Silicon–Organic

Hybrid Waveguides," *Nat. Commun.* **7**, 10864 (2016).

[169] N. Lindenmann, S. Dottermusch, M. L. Goedecke, T. Hoose, M. R. Billah, T. P. Onanuga, A. Hofmann, W. Freude & C. Koos, "Connecting Silicon Photonic Circuits to Multicore Fibers by Photonic Wire Bonding," *J. Light. Technol.* **33**, 755–760 (2015).

[170] M. R. Billah, M. Blaicher, T. Hoose, P.-I. Dietrich, P. Marin-Palomo, N. Lindenmann, A. Nesic, A. Hofmann, U. Troppenz, M. Moehrle, S. Randel, W. Freude & C. Koos, "Hybrid Integration of Silicon Photonics Circuits and InP Lasers by Photonic Wire Bonding," *Optica* **5**, 876–883 (2018).

[171] "Keysight Technologies, 89600 VSA Software," Available at: https://www.keysight.com/de/de/software/application-sw/89600-vsa-software.html. (Accessed: 17th August 2018)

[172] E. Garmire, "Nonlinear Optics in Daily Life," *Opt. Express* **21**, 30544 (2013).

[173] "Lee Laser. Frequency-Doubled, Diode-Pumped Nd:YAG Laser," (2016). Available at: http://leelaser.com/ldp-3000mqg-1-50-khz-pulse-rate/. (Accessed: 10th November 2016)

[174] "Continuum Lasers. SureliteTM OPO Plus, Broadband Optical Parametric Oscillator," (2016). Available at: http://www.continuumlasers.com/index.php?option=com_contentview=articleid=652Itemid=581. (Accessed: 10th November 2016)

[175] "Coherent. Mira-OPO.," (2016). Available at: https://www.coherent.com/lasers/laser/mira-opo. (Accessed: 10th November 2016)

[176] P. G. Kwiat, K. Mattle, H. Weinfurter, A. Zeilinger, A. V Sergienko & Y. Shih, "New High-Intensity Source of Polarization-Entangled Photon Pairs," *Phys. Rev. Lett.* **75**, 4337–4341 (1995).

[177] H. Zhang, X. M. Jin, J. Yang, H. N. Dai, S. J. Yang, T. M. Zhao, J. Rui, Y. He, X. Jiang, F. Yang, G. S. Pan, Z. S. Yuan, Y. Deng, Z. B. Chen, X. H. Bao, S. Chen, B. Zhao & J. W. Pan, "Preparation and Storage of Frequency-Uncorrelated Entangled Photons From Cavity-Enhanced Spontaneous Parametric Downconversion," *Nat. Photonics* **5**, 628–632 (2011).

[178] "Oclaro. 400G Lithium Niobate Modulator," (2016). Available at: http://www.oclaro.com/product/400g-lithium-niobate-modulator/.

(Accessed: 10th November 2016)

[179] "Coherent Solutions. IQFROG, Frequency-Resolved Optical Gating Pulse Analyzer," (2016). Available at: http://www.coherent-solutions.com/frog-optical-pulse-analyzer/. (Accessed: 10th November 2016)

[180] D. Vakhshoori & S. Wang, "Integrable Semiconductor Optical Correlator, Parametric Spectrometer For Communication Systems," *J. Light. Technol.* **9**, 906–917 (1991).

[181] P. J. Campagnola & L. M. Loew, "Second-Harmonic Imaging Microscopy for Visualizing Biomolecular Arrays in Cells, Tissues and Organisms," *Nature Biotechnology* **21**, 1356–1360 (2003).

[182] P. Pantazis, J. Maloney, D. Wu & S. E. Fraser, "Second Harmonic Generating (SHG) Nanoprobes for In Vivo Imaging," *Proc. Natl. Acad. Sci. U. S. A.* **107**, 14535–14540 (2010).

[183] Y. R. Shen, "Surface Properties Probed by Second-Harmonic and Sum-Frequency Generation," *Nature* **337**, 519–525 (1989).

[184] Y. R. Shen, "Surface Nonlinear Optics: A Historical Perspective," *IEEE J. Sel. Top. Quantum Electron* **6**, 1375–1379 (2000).

[185] M. L. Calvo, V. Lakshminarayanan & B. Lamontagne, "Enabling Fabrication Technologies for Planar Waveguide Devices," in *Optical Waveguides: From Theory to Applied Technologies* 271–308 (CRC Press, 2007).

[186] J. P. George, P. F. Smet, J. Botterman, V. Bliznuk, W. Woestenborghs, D. Van Thourhout, K. Neyts & J. Beeckman, "Lanthanide-Assisted Deposition of Strongly Electro-Optic PZT Thin Films on Silicon: Toward Integrated Active Nanophotonic Devices," *ACS Appl. Mater. Interfaces* **7**, 13350–13359 (2015).

[187] Y. Ishigame, T. Suhara & H. Nishihara, "LiNbO$_3$ Waveguide Second-Harmonic-Generation Device Phase Matched With a Fan-Out Domain-Inverted Grating," *Opt. Lett.* **16**, 375 (1991).

[188] J. Jerphagnon & S. K. Kurtz, "Maker Fringes: A Detailed Comparison of Theory and Experiment for Isotropic and Uniaxial Crystals," *J. Appl. Phys.* **41**, 1667–1681 (1970).

[189] D. S. Bethune, "Optical Harmonic Generation and Mixing in Multilayer Media: Extension of Optical Transfer Matrix Approach to Include

Anisotropic Materials," *J. Opt. Soc. Am. B* **8**, 367 (1991).

[190] V. Rodriguez & C. Sourisseau, "General Maker-Fringe Ellipsometric Analyses in Multilayer Nonlinear and Linear Anisotropic Optical Media," *J. Opt. Soc. Am. B* **19**, 2650 (2002).

[191] M. Abe, I. Shoji, J. Suda & T. Kondo, "Comprehensive Analysis of Multiple-Reflection Effects on Rotational Maker-Fringe Experiments," *J. Opt. Soc. Am. B* **25**, 1616 (2008).

[192] P. D. Maker, R. W. Terhune, M. Nisenoff & C. M. Savage, "Effects of Dispersion and Focusing on the Production of Optical Harmonics," *Phys. Rev. Lett.* **8**, 21–22 (1962).

[193] Y. Fujii, S. Yoshida, S. Misawa, S. Maekawa & T. Sakudo, "Nonlinear Optical Susceptibilities of AlN Film," *Appl. Phys. Lett.* **31**, 815–816 (1977).

[194] K. D. Singer, J. E. Sohn & S. J. Lalama, "Second Harmonic Generation in Poled Polymer Films," *Appl. Phys. Lett.* **49**, 248–250 (1986).

[195] H. Cao, J. Y. Wu, H. C. Ong, J. Y. Dai & R. P. H. Chang, "Second Harmonic Generation in Laser Ablated Zinc Oxide Thin Films," *Appl. Phys. Lett.* **73**, 572–574 (1998).

[196] N. A. Sanford, A. V. Davydov, D. V. Tsvetkov, A. V. Dmitriev, S. Keller, U. K. Mishra, S. P. Denbaars, S. S. Park, J. Y. Han & R. J. Molnar, "Measurement of Second Order Susceptibilities of GaN and AlGaN," *J. Appl. Phys.* **97**, 053512 (2005).

[197] M. C. Larciprete, D. Passeri, F. Michelotti, S. Paoloni, C. Sibilia, M. Bertolotti, A. Belardini, F. Sarto, F. Somma & S. Lo Mastro, "Second Order Nonlinear Optical Properties of Zinc Oxide Films Deposited by Low Temperature Dual Ion Beam Sputtering," *J. Appl. Phys.* **97**, 023501 (2005).

[198] R. W. Terhune, P. D. Maker & C. M. Savage, "Optical Harmonic Generation in Calcite," *Phys. Rev. Lett.* **8**, 404–406 (1962).

[199] C. C. Wang & A. N. Duminski, "Second-Harmonic Generation of Light at the Boundary of Alkali Halides and Glasses," *Phys. Rev. Lett.* **20**, 668–671 (1968).

[200] C. K. Chen, T. F. Heinz, D. Ricard & Y. R. Shen, "Detection of Molecular Monolayers by Optical Second-Harmonic Generation," *Phys. Rev. Lett.* **46**, 1010–1012 (1981).

[201] R. M. Corn & D. A. Higgins, "Optical Second Harmonic Generation as a Probe of Surface Chemistry," *Chem. Rev.* **94**, 107–125 (1994).

[202] P. F. Brevet, *Surface Second Harmonic Generation* (Presses polytechniques et universitaires romandes, 1997).

[203] G. Lüpke, "Characterization of Semiconductor Interfaces by Second-Harmonic Generation," *Surface Science Reports* **35**, 75–161 (1999).

[204] T. F. Heinz, "Second-Order Nonlinear Optical Effects at Surfaces and Interfaces," in *Nonlinear Surface Electromagnetic Phenomena* **29**, 353–416 (Elsevier, 1991).

[205] S. Cattaneo, E. Vuorimaa, H. Lemmetyinen & M. Kauranen, "Advantages of Polarized Two-Beam Second-Harmonic Generation in Precise Characterization of Thin Films," *J. Chem. Phys.* **120**, 9245–9252 (2004).

[206] J. J. Maki, M. Kauranen & A. Persoons, "Surface Second-Harmonic Generation From Chiral Materials," *Phys. Rev. B* **51**, 1425–1434 (1995).

[207] J. E. Sipe, "New Green-Function Formalism for Surface Optics," *J. Opt. Soc. Am. B* **4**, 481 (1987).

[208] M. Zdanowicz, J. Harra, J. M. Mäkelä, E. Heinonen, T. Ning, M. Kauranen & G. Genty, "Second-Harmonic Response of Multilayer Nanocomposites of Silver-Decorated Nanoparticles and Silica," *Sci. Rep.* **4**, (2014).

[209] F. J. Rodriguez, F. X. Wang & M. Kauranen, "Calibration of the Second-Order Nonlinear Optical Susceptibility of Surface and Bulk of Glass," *Opt. Express* **16**, 8704 (2008).

[210] G. P. Agrawal, *Nonlinear Fiber Optics* (2001).

[211] V. G. Dmitriev, G. G. Gurzadyan & D. N. Nikogosyan, *Handbook of Nonlinear Optical Crystals* (Springer, 1999).

[212] "SCHOTT Technical Glass Solutions GmbH. SCHOTT BOROFLOAT® 33 Datasheet," (2009). Available at: http://psec.uchicago.edu/glass/borofloat_33_e.pdf. (Accessed: 1st August 2016)

[213] A. Wickberg, C. Kieninger, C. Sürgers, S. Schlabach, X. Mu, C. Koos & M. Wegener, "Second-Harmonic Generation from ZnO/Al$_2$O$_3$ Nanolaminate Optical Metamaterials Grown by Atomic-Layer Deposition," *Adv. Opt. Mater.* **4**, 1203–1208 (2016).

[214] R. C. Miller, "Optical Second Harmonic Generation in Piezoelectric Crystals," *Appl. Phys. Lett.* **5**, 17–19 (1964).

[215] M. C. Larciprete & M. Centini, "Second Harmonic Generation From ZnO Films and Nanostructures," *Appl. Phys. Rev.* **2**, 31302 (2015).

[216] G. Wang, G. K. L. Wong & J. B. Ketterson, "Redetermination of Second-Order Susceptibility of Zinc Oxide Single Crystals," *Appl. Opt.* **40**, 5436 (2001).

[217] Ü. Özgür, Y. I. Alivov, C. Liu, A. Teke, M. A. Reshchikov, S. Doğan, V. Avrutin, S. J. Cho & H. Morkọ, "A Comprehensive Review of ZnO Materials and Devices," *J. Appl. Phys.* **98**, 1–103 (2005).

[218] J. Ebothé, R. Miedzinski, V. Kapustianyk, B. Turko, B. Kulyk, W. Gruhn & I. van Kityk, "Optical SHG for ZnO Films With Different Morphology Stimulated by UV-Laser Thermotreatment," *J. Phys. Conf. Ser.* **79**, 012001 (2007).

[219] U. Griebner, R. A. Kaindl, T. Elsaesser & W. Seeber, "Frequency Doubling and Autocorrelation Studies of 20-fs Pulses Using Polycrystalline Zinc Oxide Thin Films," *Appl. Phys. B Lasers Opt.* **67**, 757–760 (1998).

[220] C. Y. Liu, B. P. Zhang, N. T. Binh & Y. Segawa, "Second Harmonic Generation in ZnO Thin Films Fabricated by Metalorganic Chemical Vapor Deposition," *Opt. Commun.* **237**, 65–70 (2004).

[221] S. W. Liu, J. L. Weerasinghe, J. Liu, J. Weaver, C. L. Chen, W. Donner & M. Xiao, "Reflective Second Harmonic Generation Near Resonance in the Epitaxial Al-doped ZnO Thin Film," *Opt. Express* **15**, 10666 (2007).

[222] U. Neumann, R. Grunwald, U. Griebner, G. Steinmeyer & W. Seeber, "Second-Harmonic Efficiency of ZnO Nanolayers," *Appl. Phys. Lett.* **84**, 170–172 (2004).

[223] U. Neumann, R. Grunwald, U. Griebner, G. Steinmeyer, M. Schmidbauer & W. Seeber, "Second-Harmonic Performance of a-Axis-Oriented ZnO Nanolayers on Sapphire Substrates," *Appl. Phys. Lett.* **87**, 1–3 (2005).

[224] G. Wang, G. T. Kiehne, G. K. L. Wong, J. B. Ketterson, X. Liu & R. P. H. Chang, "Large Second Harmonic Response in ZnO Thin Films," *Appl. Phys. Lett.* **80**, 401–403 (2002).

[225] X. Q. Zhang, Z. K. Tang, M. Kawasaki, A. Ohtomo & H. Koinuma, "Resonant Exciton Second-Harmonic Generation in Self-Assembled

ZnO Microcrystallite Thin Films," *J. Phys. Condens. Matter* **15**, (2003).

[226] X. Q. Zhang, Z. K. Tang, M. Kawasaki, A. Ohtomo & H. Koinuma, "Second Harmonic Generation in Self-Assembled ZnO Microcrystallite Thin Films," *Thin Solid Films* **450**, 320–323 (2004).

[227] H. Mohseni & T. W. Scharf, "Atomic Layer Deposition of ZnO/Al$_2$O$_3$/ZrO$_2$ Nanolaminates for Improved Thermal and Wear Resistance in Carbon-Carbon Composites," *J. Vac. Sci. Technol. A* **30**, 01A149 (2012).

[228] A. A. Chaaya, R. Viter, I. Baleviciute, M. Bechelany, A. Ramanavicius, Z. Gertnere, D. Erts, V. Smyntyna & P. Miele, "Tuning Optical Properties of Al$_2$O$_3$/ZnO Nanolaminates Synthesized by Atomic Layer Deposition," *J. Phys. Chem. C* **118**, 3811–3819 (2014).

[229] L. Karvonen, A. Säynätjoki, Y. Chen, H. Jussila, J. Rönn, M. Ruoho, T. Alasaarela, S. Kujala, R. A. Norwood, N. Peyghambarian, K. Kieu & S. Honkanen, "Enhancement of the Third-Order Optical Nonlinearity in ZnO/Al$_2$O$_3$ Nanolaminates Fabricated by Atomic Layer Deposition," *Appl. Phys. Lett.* **103**, 031903 (2013).

[230] S.-Y. Pung, K. Choy, X. Hou & C. Shan, "Preferential Growth of ZnO Thin Films by the Atomic Layer Deposition Technique," *Nanotechnology* **19**, (2008).

[231] D. M. Hausmann & R. G. Gordon, "Surface Morphology and Crystallinity Control in the Atomic Layer Deposition (ALD) of Hafnium and Zirconium Oxide Thin Films," *J. Cryst. Growth* **249**, 251–261 (2003).

[232] J. D. Dana, E. S. Dana, C. Palache, H. Berman & C. Frondel, *Dana's System of Mineralogy, Vol. I: Elements, Sulfides, Sulfosalts, Oxides* (Wiley, 1944).

[233] R. Snyder & R. Jenkins, *Introduction to X-Ray Powder Diffractometry.* (Wiley-Interscience, 2012).

[234] C. Koos, *Nanophotonic devices for linear and nonlinear optical signal processing* (Univ.-Verl. Karlsruhe, 2007).

[235] J. A. Woollam, B. D. Johs, C. M. Herzinger, J. N. Hilfiker, R. A. Synowicki & C. L. Bungay, "Overview of Variable-Angle Spectroscopic Ellipsometry (VASE): I. Basic Theory and Typical Applications," in *Optical Metrology: A Critical Review* **10294**, 1029402 (SPIE, 1999).

[236] "M-2000XI Spectroscopic Ellipsometer Hardware Manual," *J. A. Woollam Co., Inc.* (2010). Available at: www.jawoollam.com.

[237] "Complete EASE Data Analysis Manual, version 4.63, J. A. Woollam Co., Inc.," (2011). Available at: www.jawoollam.com.

[238] G. Zhou, L. Zhou, Y. Guo, L. Liu, L. Lu & and Chen J., "High-Efficiency Silicon Mach-Zehnder Modulator with U-Shaped PN Junctions," in *Conference on Lasers and Electro-Optics* JTh2A.42 (2019).

[239] W. Heni, Y. Fedoryshyn, B. Baeuerle, A. Josten, C. B. Hoessbacher, A. Messner, C. Haffner, T. Watanabe, Y. Salamin, U. Koch, D. L. Elder, L. R. Dalton & J. Leuthold, "Plasmonic IQ modulators with attojoule per bit electrical energy consumption," *Nat. Commun.* **10**, 1–8 (2019).

F.   Glossary

F.1   List of abbreviations

Al	Aluminium
Al_2O_3	Aluminum oxide
ALD	Atomic layer deposition
AWG	Arbitrary waveform generator
BBO	Beta-barium borate
BCC	Binary chromophore composite
BCOG	Binary chromophore organic glass
BER	Bit error ratio
BP	Bandpass filter
$BaTiO_3$	Barium titanate
CMOS	Complementary metal-oxide-semiconductor
CW	Continuous wave
DUV	Deep ultraviolet
ECL	External cavity laser
EDFA	Erbium doped fiber amplifier
EDX	Energy-dispersive X-ray
EO	Electro-optic
ER	Extinction ratio
FG	Function generator

FIB	Focused ion beam
FWHM	Full width half maximum
GC	Grating coupler
Ge	Germanium
GSG	Ground-signal-ground
HAADF	High-angle annular dark-field
HfO_2	Hafnium oxide
HTA	$HfO_2/TiO_2/Al_2O_3$
ILD	Interlayer dielectric
In_2O_3	Indium oxide
InGaAsP	Indium gallium arsenide phosphide
InP	Indium phosphide
ISC	Intersystem crossing
ITA	$In_2O_3/TiO_2/Al_2O_3$
KDP	Potassium dihydrogen phosphate
LBO	Lithium triborate
Le	Lens
$LiNbO_3$	Lithium niobate
LP	Longpass filter
MMA	Methyl methacrylate
MMI	Multi-mode interference
MZM	Mach-Zehnder modulator
$^{1/3}O_2$	Singlet/Triplet oxygen

OEO	Organic electro-optic
OOK	On-off keying
OPO	Optical parametric amplifier
PAM	Pulse-amplitude modulation
PBSC	Polarizing beam-splitter cube
PD	Photodiode
PIC	Photonic integrated circuit
PMT	Photomultiplier tube
POH	Plasmonic-organic hybrid
PVT	Phenyl vinylene thiophene
QCSE	Quantum-confined Stark effect
RF	Radio frequency
SH	Second-harmonic
SHG	Second-harmonic generation
Si	Silicon
SiP	Silicon photonics
SISCAP	Silicon-insulator-silicon capacitors
SOH	Silicon-organic hybrid
SOI	Silicon-on-insulator
SP	Shortpass filter
STEM	Scanning transmission electron microscopy
TFLN	Thin-film lithium niobate
TiO_2	Titanium oxide

TL	Transmission line
XRD	X-ray diffraction
ZnO	Zinc oxide

F.2   List of mathematical symbols

Greek symbols

α	Real part of propagation constant $\underline{\gamma}$
$\tilde{\alpha}$	Optical attenuation coefficient measured in 1/mm
$\hat{\alpha}$	Linear polarizability
$\alpha^{(c)}$	Chirp parameter
β	Imaginary part of propagation constant $\underline{\gamma}$
$\hat{\beta}$	First hyperpolarizability
$\underline{\gamma}$	Complex RF propagation constant
Γ	Field interaction factor
$\underline{\tilde{\Gamma}}$	Complex voltage reflection factor at the interface of an RF transmission line
$\delta_{i,j}$	Kronecker delta
$\Delta\tau$	Temporal pulse width (FWHM)
ε	Permittivity tensor
ε_0	Vacuum permittivity
η	Impermeability tensor
θ	Propagation angle
ϑ	Angle of incidence

λ_0	Vacuum wavelength
μ	Electric dipole moment
τ	Time integration variable
$\underset{\sim}{\tau}$	Mean crystallite size obtained from XRD
ϕ	Phase of the optical carrier
φ	Angle of polarization; $\varphi = 0.90$ °corresponds to s-,p-polarization
$\chi^{(n)}$	nth order electric susceptibility
ω	Angular frequency

Latin symbols

a	Propagation loss measured in dB/mm
a_i	Power attenuation of component i measured in dB
$A^{(\text{spot})}$	Laser spot area
c	Vacuum speed of light
C	Capacitance
C'	Capacitance per infinitesimal length $\varDelta z$
d	Thickness of nonlinear film
$\vec{D}(\vec{x},t)$	Electric displacement field
$\underline{\vec{D}}(\vec{x},\omega)$	Complex amplitude of electric displacement field
$\vec{E}(\vec{x},t)$	Electric field
$\underline{\vec{E}}(\vec{x},\omega)$	Complex amplitude of electric field
f_{rep}	Repetition rate of pulsed laser

$\hat{g}$	Lorentz–Onsager local field factor
G	Conductance
G'	Conductance per infinitesimal length $\varDelta z$
I_{ALD}	Number of intermediate Al_2O_3 ALD growth cycles
k_0	Vacuum wavenumber
L	Phase-shifter length
$\underset{\sim}{L}$	Inductance
$\underset{\sim}{L}'$	Inductance per infinitesimal length $\varDelta z$
M_{ALD}	Number of ALD macrocycles
n	Refractive index
P	Power
$\vec{\mathcal{P}}(\vec{x},t)$	Electric polarization
$\underline{\vec{\mathcal{P}}}(\vec{x},\omega)$	Complex amplitude of electric polarization
Q	Quality factor
r	Electro-optic tensor
$r_{i\text{-}j}^{\text{s/p}}$	Fresnel reflection coefficient from medium i to j for s/p-polarization
R	Resistance
R'	Resistance per infinitesimal length $\varDelta z$
S_{ALD}	Number of Al_2O_3 ALD seed layer growth cycles
t	Time
$t_{i\text{-}j}^{\text{s/p}}$	Fresnel transmission coefficient from medium i to j for s/p-polarization
T_{g}	Glass-transition temperature

U	Voltage
U_π	π-voltage of an MZM
w	Electrode spacing
$\vec{x}$	Space
$\underline{Z}$	Complex impedance
Z_{ALD}	Number of ZnO ALD growth cycles

Danksagung

Herzlich bedanken möchte ich mich bei allen meinen Kollegen, die diese Arbeit einerseits fachlich enorm unterstützt haben, aber auch menschlich eine große Unterstützung waren und dafür gesorgt haben, dass ich mich am IPQ immer sehr wohl gefühlt habe.

Großer Dank gilt Yasar Kutuvantavida, für die jahrelange gute und enge Zusammenarbeit, für die bereichernden Diskussionen bezüglich der Chemie der EO Chromophore und für seine große Ausdauer beim Beschichten der SOH Modulatoren. Matthias Lauermann möchte ich besonders danken, dass er mich nach der Betreuung meiner Masterarbeit sehr gut als Bürokollegen aufgenommen hat und durch sein breites Wissen im Bereich der integrierten Photonik den Beginn meiner Promotion enorm vereinfacht hat. Besonders bedanke ich mich bei Stefan Wolf, der mich bei zahlreichen Messungen unterstützt hat und immer für eine lockere Atmosphäre bei der Arbeit gesorgt hat. Ebenso bedanke ich mich besonders bei Mr. Juned Kemal für seine Unterstützung bei Messungen und deren Auswertung als auch für seine hilfreichen Tipps beim Meistern der VSA-Software. Carsten Eschenbaum danke ich besonders für die Unterstützung bei der Bewältigung des SOH-Tagesgeschäfts, dem Beschichten, Polen und Charakterisieren der SOH Bauteile. Alexander Kotz danke ich besonders für seine interessierten Fragen und seine scheinbar stete sehr gute Laune – so hat mir das Arbeiten im Büro immer großen Spaß bereitet. Stefan Singer danke ich besonders für die tatkräftige Unterstützung und seinen langen Atem bei der Organisation der HLB Klausuren. Christoph Füllner danke ich besonders für die Unterstützung bei der Durchführung und Auswertung von Experimenten und für die Tischtennispartien, bei denen wir uns stets auf Augenhöhe begegnet sind. Ich danke auch besonders Daria Kohler und Sandeep Ummethala für die Unterstützung bei der Chip-Fabrikation und insbesondere Daria für die Begleitung beim Klettern und Bouldern. Besonders bedanken möchte ich mich auch bei Philipp Trocha, für die tolle gemeinsame Zeit im und außerhalb des Instituts und für die exquisiten Mittagspausen. Besonders bedanken möchte ich mich auch bei Tobias Harter, der sich immer sehr selbstlos Zeit für fachliche und persönliche Gespräche genommen hat. Besonders bedanken möchte ich mich außerdem bei Andreas Wickberg für das Herstellen unzähliger ALD-Proben und für die langjährige persönliche Unterstützung außerhalb des Uni-Lebens. Besonders bedanken möchte ich mich auch bei Heiner Zwickel für die

List of publications

Journal publications

[J1] **C. Kieninger**, Y. Kutuvantavida, D. L. Elder, S. Wolf, H. Zwickel, M. Blaicher, J. N. Kemal, M. Lauermann, S. Randel, W. Freude, L. R. Dalton & C. Koos, "Ultra-High Electro-Optic Activity Demonstrated in a Silicon-Organic Hybrid Modulator," *Optica* **5**, 739–748 (2018).

[J2] **C. Kieninger**, C. Füllner, H. Zwickel, Y. Kutuvantavida, J. Kemal, C. Eschenbaum, D. Elder, L. Dalton, W. Freude, S. Randel, and C. Koos, "Silicon-Organic Hybrid (SOH) Mach-Zehnder Modulators for 100 GBd PAM4 Signaling With Sub-1 dB Phase-Shifter Loss," *Opt. Express* **28**, 24693–24707 (2020).

[J3] **C. Kieninger**, Y. Kutuvantavida, H. Miura, J. N. Kemal, H. Zwickel, F. Qiu, M. Lauermann, W. Freude, S. Randel, S. Yokoyama & C. Koos, "Demonstration of Long-Term Thermally Stable Silicon-Organic Hybrid Modulators at 85 °C," *Opt. Express* **26**, 27955 (2018).

[J4] A. Hermans*, **C. Kieninger***, K. Koskinen, A. Wickberg, E. Solano, J. Dendooven, M. Kauranen, S. Clemmen, M. Wegener, C. Koos & R. Baets, "On the Determination of $\chi^{(2)}$ in Thin Films: A Comparison of One-Beam Second-Harmonic Generation Measurement Methodologies," *Sci. Rep.* **7**, 1–13 (2017).

*These authors contributed equally to this work.

[J5] A. Wickberg*, **C. Kieninger***, C. Sürgers, S. Schlabach, X. Mu, C. Koos & M. Wegener, "Second-Harmonic Generation from ZnO/Al_2O_3 Nanolaminate Optical Metamaterials Grown by Atomic-Layer Deposition," *Adv. Opt. Mater.* **4**, 1203–1208 (2016).

*These authors contributed equally to this work.

[J6]   M. Blaicher; M. R. Billah, J. N. Kemal, T. Hoose, P. Marin-Palomo, A. Hofmann, Y. Kutuvantavida, **C. Kieninger**, P.-I. Dietrich, M. Lauermann, S. Wolf, U. Troppenz, M. Moehrle, F. Merget, S. Skacel, J. Witzens, S. Randel, W. Freude, & C. Koos, "Hybrid multi-chip assembly of optical communication engines by in situ 3D nano-lithography," *Light Sci. Appl.* **9**, 71 (2020).

[J7]   H. Zwickel, S. Singer, **C. Kieninger**, Y. Kutuvantavida, N. Muradyan, T. Wahlbrink, S. Yokoyama, S. Randel, W. Freude & C. Koos, "A Verified Equivalent-Circuit Model for Slot-Waveguide Modulators," *Opt. Express* **28**, 12951–12976 (2019).

[J8]   H. Zwickel, J. N. Kemal, **C. Kieninger**, Y. Kutuvantavida, J. Rittershofer, M. Lauermann, W. Freude, S. Randel & C. Koos, "Electrically Packaged Silicon-Organic Hybrid (SOH) I/Q-Modulator for 64 GBd Operation," *Opt. Express* **26**, 34580 (2018).

[J9]   S. Wolf, H. Zwickel, W. Hartmann, M. Lauermann, Y. Kutuvantavida, **C. Kieninger**, L. Altenhain, R. Schmid, J. Luo, A. K.-Y. Jen, S. Randel, W. Freude & C. Koos, "Silicon-Organic Hybrid (SOH) Mach-Zehnder Modulators for 100 Gbit/s on-off Keying," *Sci. Rep.* **8**, 2598 (2018).

[J10] S. Wolf, H. Zwickel, **C. Kieninger**, M. Lauermann, W. Hartmann, Y. Kutuvantavida, W. Freude, S. Randel & C. Koos, "Coherent Modulation up to 100 GBd 16QAM Using Silicon-Organic Hybrid (SOH) Devices," *Opt. Express* **26**, 220–232 (2018).

[J11] H. Zwickel, S. Wolf, **C. Kieninger**, Y. Kutuvantavida, M. Lauermann, T. de Keulenaer, A. Vyncke, R. Vaernewyck, J. Luo, A. K.-Y. Jen, W. Freude, J. Bauwelinck, S. Randel & C. Koos, "Silicon-Organic Hybrid (SOH) Modulators for Intensity-Modulation / Direct-Detection Links With Line Rates of up to 120 Gbit/s," *Opt. Express* **25**, 23784–23800 (2017).

[J12] W. Heni, Y. Kutuvantavida, C. Haffner, H. Zwickel, **C. Kieninger**, S. Wolf, M. Lauermann, Y. Fedoryshyn, A. F. Tillack, L. E. Johnson, D. L. Elder, B. H. Robinson, W. Freude, C. Koos, J. Leuthold & L. R. Dalton, "Silicon–Organic and Plasmonic–Organic Hybrid Photonics," *ACS Photonics* **4**, 1576–1590 (2017).

Conference publications

[C1] **C. Kieninger**, C. Füllner, H. Zwickel, Y. Kutuvantavida, J. N. Kemal, C. Eschenbaum, D. L. Elder, L. R. Dalton, W. Freude, S. Randel, and C. Koos, "SOH Mach-Zehnder Modulators for 100 GBd PAM4 Signaling with Sub-1 dB Phase-Shifter Loss," in *Optical Fiber Communications Conference and Exhibition* (2020), paper Th3C.3.

[C2] **C. Kieninger**, Y. Kutuvantavida, J. N. Kemal, H. Zwickel, H. Miura, S. Randel, W. Freude, S. Yokoyama, and C. Koos, "Demonstration of Long-Term Thermal Stability of a Silicon-Organic Hybrid (SOH) Modulator at 85 °C," in *Conference on Lasers and Electro-Optics* (2018), paper SM3B.3.

[C3] **C. Kieninger**, Y. Kutuvantavida, H. Zwickel, S. Wolf, M. Lauermann, D. Elder, L. Dalton, W. Freude, S. Randel, C. Koos, "Record-High In-Device Electro-Optic Coefficient of 359 pm/V in a Silicon-Organic Hybrid (SOH) Modulator," in *Conference on Lasers and Electro-Optics* (2017), paper STu3N.2.

[C4] H. Zwickel, J. N. Kemal, **C. Kieninger**, Y. Kutuvantavida, M. Lauermann, J. Rittershofer, R. Pajković, D. Lindt, S. Randel, W. Freude, and C. Koos, "Electrically Packaged Silicon-Organic Hybrid Modulator for Communication and Microwave Photonic Applications," in *Conference on Lasers and Electro-Optics* (2018), paper SM3B.1.

[C5] C. Koos, S. Randel, W. Freude, L. R. Dalton, S. Wolf, **C. Kieninger**, Y. Kutuvantavida, M. Lauermann, D. L. Elder, S. Muehlbrandt, H. Zwickel, A. Melikyan, T. Harter, S. Ummethala, M. R. Billah, M. Blaicher, P.-I. Dietrich, and T. Hoose, "Hybrid Photonic Integration and Plasmonic Devices: New Perspectives for High-Speed Communications and Ultra-Fast Signal Processing," in *CLEO Pacific Rim Conference* (2018), paper W4J.1

[C6] A. Wickberg, **C. Kieninger**, C. Sürgers, C. Koos, M. Wegener, "Second-Harmonic Generation from ZnO / Al$_2$O$_3$ Laminate Optical Metamaterials Grown by Atomic-Layer Deposition," in *Conference on Lasers and Electro-Optics* (2017), paper FM1D.2.

[C7] A. Hermans, M. V. Daele, **C. Kieninger**, J. Dendooven, S. Clemmen, C. Detavernier, C. Koos, and R. Baets, "CMOS-Compatible ALD Zinc Oxide Coating for On-Chip Second-Order Nonlinear Optical Functionalities," in *Conference on Lasers and Electro-Optics* (2017), paper SM3K.3

[C8] S. Wolf, H. Zwickel, **C. Kieninger**, Y. Kutuvantavida, M. Lauermann, J. Lutz, L. Altenhain, R. Schmid, W. Freude, C. Koos, and S. Randel, "Silicon-Organic Hybrid (SOH) IQ Modulator for 100 GBd 16QAM Operation," in *Optical Fiber Communication Conference Postdeadline Papers* (2017), paper Th5C.1.

[C9] H. Zwickel, T. De Keulenaer, S. Wolf, **C. Kieninger**, Y. Kutuvantavida, M. Lauermann, M. Verplaetse, R. Pierco, R. Vaernewyck, A. Vyncke, X. Yin, G. Torfs, W. Freude, E. Mentovich, J. Bauwelinck, and C. Koos, "100 Gbit/s Serial Transmission Using a Silicon-Organic Hybrid (SOH) Modulator and a Duobinary Driver IC," in *Optical Fiber Communication Conference* (2017), paper W4I.5

[C10] M. R. Billah, J. N. Kemal, P. Marin-Palomo, M. Blaicher, Y. Kutuvantavida, **C. Kieninger**, H. Zwickel, P. I. Dietrich, S. Wolf, T. Hoose, Y. Xu, U. Troppenz, M. Moehrle, S. Randel, W. Freude, and C. Koos, "Four-Channel 784 Gbit/s Transmitter Module Enabled by Photonic Wire Bonding and Silicon-Organic Hybrid Modulators," in *European Conference on Optical Communication* (2017), paper Th.PDP.C.1.

[C11] S. Wolf, W. Hartmann, M. Lauermann, H. Zwickel, Y. Kutuvantavida, **C. Kieninger**, W. Freude, C. Koos, "High-Speed Silicon-Organic Hybrid (SOH) Modulators," in *European Conference on Optical Communication* (2016).

[C12] H. Zwickel, S. Wolf, Y. Kutuvantavida, **C. Kieninger**, M. Lauermann, W. Freude, C. Koos, "120 Gbit/s PAM-4 signaling using a silicon-organic hybrid (SOH) Mach-Zehnder modulator," in *European Conference on Optical Communication* (2016).

[C13] L. Alloatti, **C. Kieninger**, A. Froelich, M. Lauermann, T. Frenzel, K. Koehnle, W. Freude, J. Leuthold, C. Koos, M. Wegener, "Second-

harmonic generation from atomic-scale ABC-type laminate optical metamaterials," in *Metamaterials, Metadevices, and Metasystems* (2015), paper 95440Y-95440Y-1.